# A Comparison of Structurally Connected and Multiple Spacecraft Interferometers

Derek M. Surka and Edward F. Crawley

December 1996 SERC#9-96

(Under the sponsorship of NASA)

This report is based on the unaltered thesis of Derek M. Surka submitted to the Department of Aeronautics and Astronautics in partial fulfillment of the requirements for the degree of Master of Science at the Massachusetts Institute of Technology.

# Abstract

Structurally connected and multiple spacecraft interferometers are compared in an attempt to establish the maximum baseline (referred to as the "cross-over baseline") for which it is preferable to operate a single-structure interferometer in space rather than an interferometer composed of numerous, smaller spacecraft. This comparison is made using the total launched mass of each configuration as the comparison metric.

A framework of study within which structurally connected and multiple spacecraft interferometers can be compared is presented in block diagram form. This methodology is then applied to twenty-two different combinations of trade space parameters to investigate the effects of different orbits, orientations, truss materials, propellants, attitude control actuators, onboard disturbance sources, and performance requirements on the cross-over baseline. Rotating interferometers and the potential advantages of adding active structural control to the connected truss of the structurally connected interferometer are also examined.

The minimum mass design of the structurally connected interferometer that meets all performance requirements and satisfies all imposed constraints is determined as a function of baseline. This minimum mass design is then compared to the design of the multiple spacecraft interferometer.

It is discovered that the design of the minimum mass structurally connected interferometer that meets all performance requirements and constraints in solar orbit is limited by the minimum allowable aspect ratio, areal density, and gage of the struts. In the formulation of the problem used in this study, there is no advantage to adding active structural control to the truss for interferometers in solar orbit.

The cross-over baseline for missions of practical duration (ranging from one week to thirty years) in solar orbit is approximately 400 m for non-rotating interferometers and 650 m for rotating interferometers.

# Acknowledgments

This work was sponsored by the M.I.T. Space Engineering Research Center under NASA grant NAGW-1335.

The authors would like to thank the people at the Jet Propulsion Laboratory (JPL) who helped with the disturbance modeling and who took the time to review our work and offer suggestions about the overall scope — Chester Chu, Mark Colavita, Robert Laskin, Jim Melody, and Mike Shao.

The time Prof. Kathleen Howell of Purdue University took to review our work on halo orbits was also greatly appreciated. Unfortunately, in the end, this work was not applicable to this study.

# Contents

# List of Figures

# List of Tables

# Chapter 1

# Introduction

## 1.1 Motivation and Objective

NASA and the scientific community have recently been attempting to determine the direction of future space astronomy and astrophysics research. In May of 1996, NASA created the Origins Program [1], whose purpose is to help in answering fundamental questions regarding the origins of life and the universe:

(i) Where did galaxies, stars and planets come from?

(ii) Are there worlds like the Earth around nearby stars? If so, are they habitable and is life as we know it present there?

(iii) What is the origin of the universe?

These questions are very interesting both scientifically and philosophically and one way to attempt to solve them is to obtain direct observational evidence. Very young, and hence, very distant, galaxies can be observed in an attempt to determine how they, and the stars of which they are composed, were formed. Earth-like planets can be searched for by direct observation of nearby stars.

There are two decisions that must be made when determining how to make these observations. The first is the location of the observing instrument, whether it is to be located on Earth or in space, and the second is the type of instrument, whether it

will be a single, large aperture telescope or a multiple aperture interferometer. These decisions are not necessarily independent of each other.

Earth-based observatories suffer from image degradation caused by the atmosphere. This degradation includes both distortion caused by refraction and the absorption of certain wavelengths. Earth-based infrared observatories additionally suffer from the large amount of infrared noise caused by thermal emissions. (Observations of very young galaxies must be done in the infrared because of the red-shift of their spectra caused by their high rate of apparent recession from the Earth.)

In order to be able to observe very faint objects, such as distant galaxies, large light collecting areas are desired. Large collecting areas are also desired for high angular resolution which in turn leads to more accurate astrometric measurements (such as position) and higher resolution image capability. Unfortunately, there are practical limits to the size of an aperture that can be launched into space.

One solution to this problem is to use an interferometer with multiple smaller apertures. The angular resolution is then dependent upon the separation distance of the apertures, which is also called the baseline. Greater resolution can be obtained by longer baselines and images can be taken by rotating the interferometer to fill in the image plane. The basic operating principles of interferometers are discussed in Section 1.3.

Three different groups have convened in the past five years in an attempt to determine the future needs of astronomy and astrophysics research. The Hubble Space Telescope (HST) and Beyond Committee was formed to examine the future of space-based astronomy [2]. The Space Interferometry Science Working Group (SISWG) [3] was formed in response to the recommendation of the Bahcall Report [4] for an Astrometric Interferometry Mission (AIM) which would accurately measure the positions of astronomical objects to within a few millionths of an arcsecond. Finally, the third group was charged with establishing a plan for the future Exploration of Neighboring Planetary Systems (ExNPS) [5]. The Origins Program was created in response to these three committees in an attempt to integrate their recommendations.

Each of these studies recommended the future development of large infrared interferometers. Even though there is much science that can and should be done by large ground-based telescopes and interferometers, the atmospheric and background noise effects limit their performance to well below that required for Earth-size planet detection. Furthermore, even a space-based observatory will require a baseline on the order of tens to hundreds of meters to detect Earth-sized planets, which is well beyond the practical size limit (around 10 m) of a single-aperture space-based telescope.

The one question that hasn't been answered is whether or not it is "better" to launch and operate an interferometer that is composed of one large, connected structure or an interferometer that is composed of many individual spacecraft that are flown in formation.

> Finally, there exists the option of having no metering [connecting] structure at all [for the interferometer]. For some baseline greater than 75 m, it will become cheaper to operate each telescope as an independent spacecraft flying in precise formation to produce the desired array configuration. Detailed studies will be required to establish the cross-over baseline length at which a multi-spacecraft design becomes more cost effective than a deployed or inflatable approach.[1]

*It is the objective of this research to establish a framework within which such a study can be undertaken and to provide a preliminary estimate of this cross-over baseline.*

## 1.2 Future and Proposed Missions

Before discussing the approach taken by this study in order to achieve the above objectives, the three proposed second generation missions of the Origins program will be presented. These missions will be referenced throughout this document.

---

[1] C.A. Beichman, ed., *A Road Map for the Exploration of Neighboring Planetary Systems (ExNPS)*, (Pasadena, CA: Jet Propulsion Laboratory, 1996), p. 6-3.

More information on the Origins Program can be found at the Origins web page

**http://www.hq.nasa.gov/office/oss/origins/Origins.html**

The Space Interferometry Mission (SIM) [3] was proposed by SISWG to fulfill the Bahcall report's recommendation that an interferometer be launched that could measure the position of $20^{th}$ magnitude objects to within 3-30 micro-arcseconds. SIM is a connected Michelson interferometer with a baseline of 10 m and seven 30 cm apertures. It is to be launched into a 900 km Sun-synchronous orbit. SIM's resolution will also allow it to detect Uranus-sized planets in orbit about nearby stars.

The Next Generation Space Telescope (NGST) was recommended by the HST and Beyond committee as a follow-up to HST and its objective is to study the origin of galaxies and the early universe. NGST is proposed to be a deployable, single aperture telescope operating in the near infrared range (0.5-20 $\mu$m wavelengths). It will have a diameter of 8 m and be launched into a halo orbit about the $L_2$ Lagrange point of the Sun-Earth system.

The third mission was proposed by the ExNPS team and is called Planet Finder (PF). The objective of Planet Finder is to detect the presence of Earth-like planets around the nearest 1000 stars and to determine if they are capable of supporting life as we know it. The proposed configuration of PF consists of a structurally connected Michelson, nulling interferometer with four 1.5 apertures and a baseline of 100 m. The interferometer will operate in the infrared range of wavelengths and will be operated in an orbit 5 astronomical units (AU) from the Sun in order to minimize the background noise associated with the zodiacal dust cloud.

Numerous additional missions have been proposed to demonstrate the technologies necessary for the above three missions to be successful. Optical interferometers have been successfully tested on Earth [6] but none have been tested in space. A mission demonstrating the technologies necessary to operate a space-based interferometer, such as active vibration control, is planned and one proposal for this flight is the Jet Propulsion Laboratory's Interferometric Stellar Imaging System (ISIS), a shuttle-based interferometry experiment [7].

Two freeflying interferometers have been proposed to NASA. The New Millen-

nium Interferometer (NMI) [8] is planned as the third Deep Space mission of the New Millennium program and will demonstrate autonomous formation flying of three spacecraft and the ability to perform interferometry with these spacecraft. The Multiple Spacecraft Interferometer Constellation (MUSIC) [9] is another JPL concept to demonstrate the feasibility of operating a long baseline (1-100 km) interferometer composed of numerous (sixteen) freeflyers.

Studies have been performed for each of the aforementioned missions to determine their most feasible design. These studies, however, have always assumed a priori the type of interferometer to be designed (structurally connected versus multiple spacecraft) and then optimized that design to best demonstrate the new technologies. No study has been conducted that attempts to determine, in general, under what conditions a structurally connected interferometer (SCI) is preferable over a multiple spacecraft interferometer (MSI).

## 1.3 Introduction to Stellar Interferometry

This section briefly outlines the operating principles of an interferometer used for astrometry and astronometric imaging and reviews the advantages of a space-based interferometer (from Colavita [10]). Shao and Colavita [11] provide a more detailed history and explanation of optical stellar interferometry, both ground- and space-based. They also provide an extensive list of references for more information.

Figure 1-1 shows the basic operation of a Michelson interferometer. The interferometer combines the light from two different apertures separated by a distance, $L$, equal to the baseline. The incoming light is collected by two mirrors called siderostats and is then reflected off a series of smaller mirrors until it is finally passed through a beam splitter and the light is interfered on the detector. The interference of the two beams creates a series of fringes on the detector. Two detectors are shown in the diagram.

In order for high-quality measurements to be taken, the instrument must combine light from the same wavefront. This requires that the optical path lengths of the

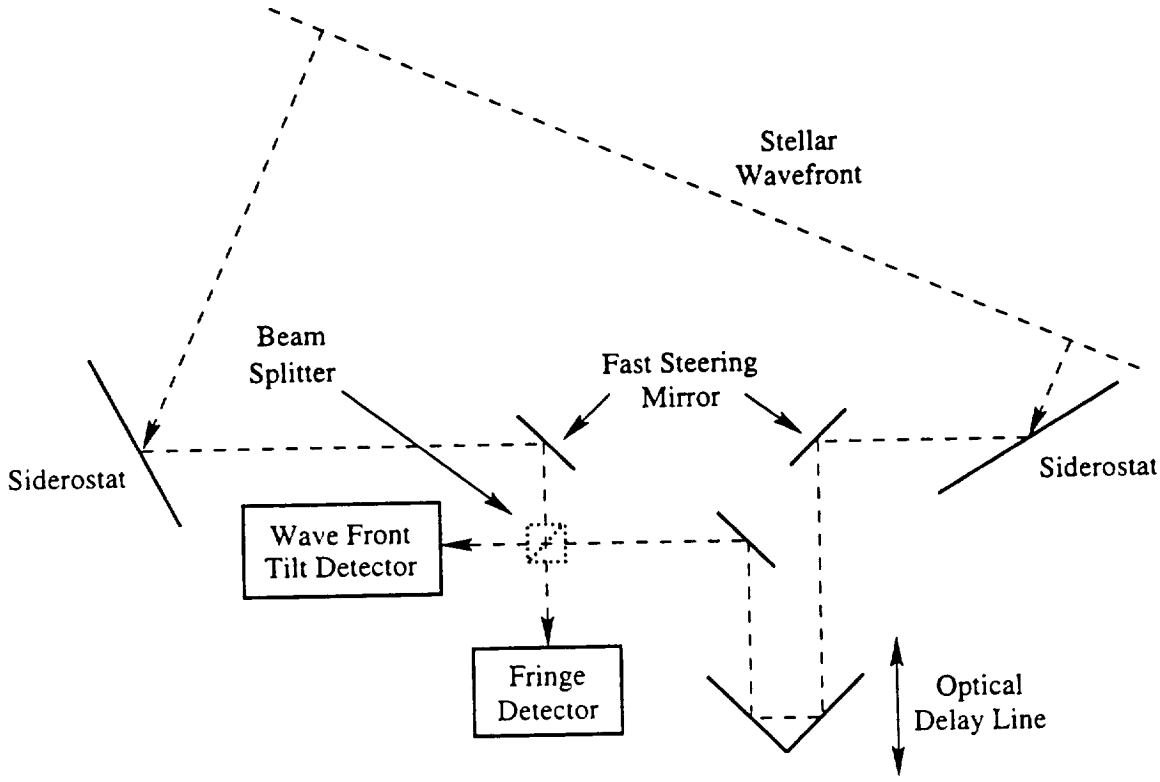


Figure 1-1: Operation of a Stellar Michelson Interferometer

two legs of the interferometer be equal to within fractions of a wavelength, typically to within $\lambda/10$, where $\lambda$ is the wavelength of observation. The optical path length difference (OPD) is controlled by moving an optical delay line (ODL) in one of the legs.

The are two additional requirements of interferometers for measurements to be accurate — minimal beam overlap difference (BOD) and wavefront tilt (WFT). There must be a large percentage of overlap of the two beams on the detector and the two beams must not be tilted relative to one another at the detector. The BOD and WFT are controlled by the operation of fast steering mirrors (FSM) in the two optical paths. The ability to maintain the OPD, BOD, and WFT to the required levels in the presence of various sources of disturbance vibration is the major challenge in interferometer operation.

The use of an interferometer to perform astrometry, the measurement of position and velocity of celestial bodies, is illustrated in Figure 1-2. Astrometry is performed

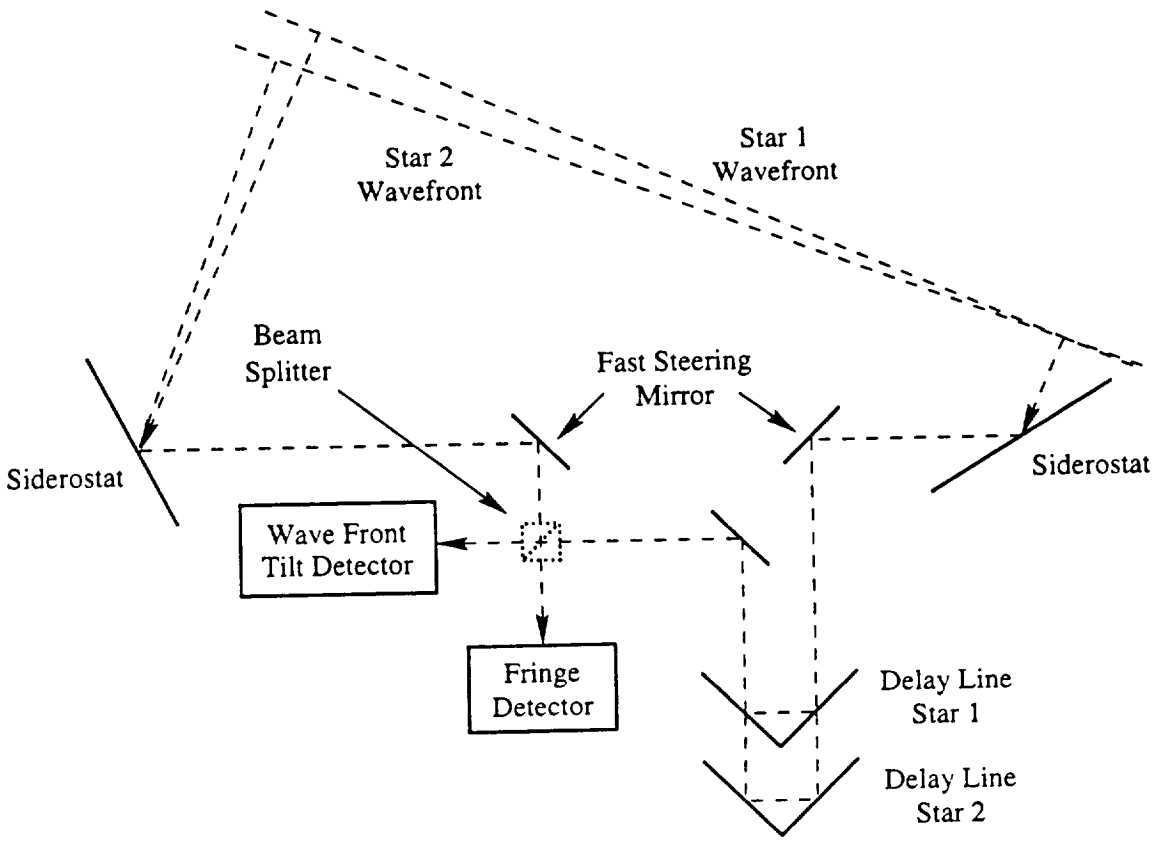


Figure 1-2: Astrometry Performed by a Michelson Interferometer

by measuring the difference in ODL position required to capture fringes on two different stars. The extra delay is a measure of the angle between the two stars. The longer the baseline, the smaller the angle between the two stars that can be measured, i.e. the greater the angular resolution. Changes in the apparent position or velocity of a star over time may indicate the presence of one or more orbiting planets.

The imaging process is shown pictorially in Figure 1-3, modified from [10]. An interferometer measures the Fourier transform of the object. For each orientation of the interferometer baseline, two points in the image plane (also called the $uv$-plane) are measured because of symmetry. The $uv$-plane can be filled in by taking measurements at many different baselines and the image can then be recreated by taking the inverse Fourier transform of the $uv$-plane.

In order to detect planets, spatial resolutions on the order of 0.038 arcseconds are required [5]. This requires a baseline on the order of 40–90 m for near-infrared

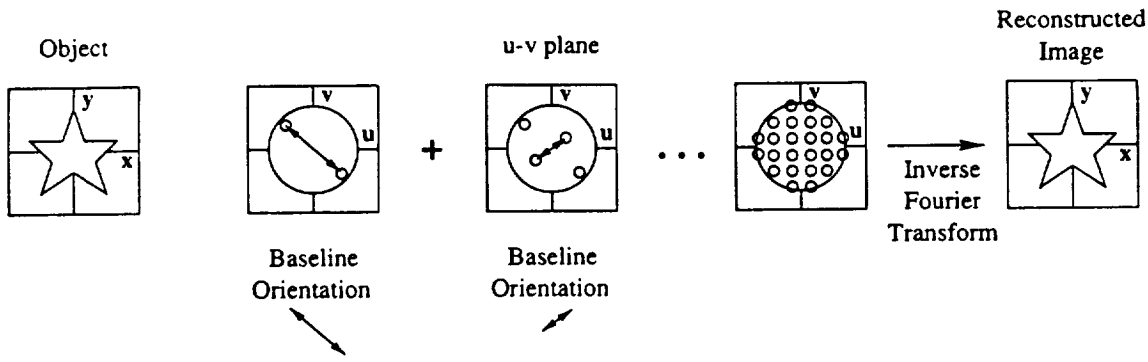


Figure 1-3: Imaging Process of a Stellar Interferometer

observations at wavelengths of 7–17 $\mu$m. This required baseline is beyond the practical size of an orbiting, single aperture telescope. Furthermore, even though larger Earth-based telescopes can be constructed, the atmospheric degradation and the background noise level prohibit them from achieving the necessary resolution. Only a space-based interferometer can achieve the level of performance required for the Origins Program.

There are two possible configurations for orbiting interferometers, as shown in Figure 1-4. The interferometer can either be composed of one large structure with the collecting optics located at opposite ends of a connecting truss and the combining optics contained within the central portion of the spacecraft, or the interferometer can be composed of individual freeflyer spacecraft flying in formation with the collecting and combining optics located on separate spacecraft. For this work, the "collecting optics" refers to the siderostats and the "combining optics" refers to all other optical components, including the fast steering mirrors, the optical delay line, and the detectors. See Figure 1-5.

There are advantages and disadvantages to each of these configurations. The connecting structure of the structurally connected interferometer (SCI) provides a passive means of maintaining the baseline to some accuracy, on the order of centimeters. However, this same structure that provides knowledge of the baseline distance also allows the propagation of vibration disturbances between the collecting and combining optics. Furthermore, the structure itself exhibits flexibility and responds to vibration disturbances.

These disturbances must either be isolated from the optics or rejected by some

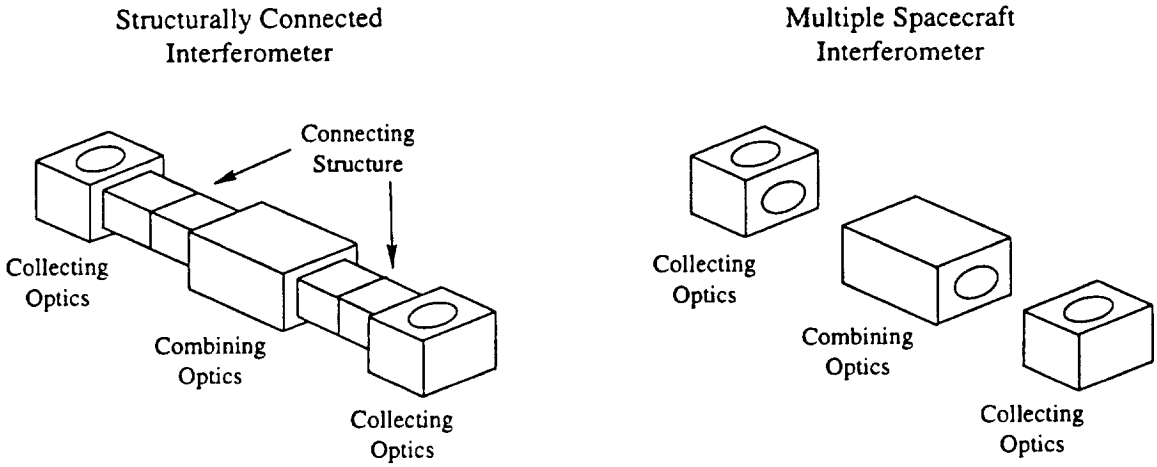


Figure 1-4: Structurally Connected and Multiple Spacecraft Interferometer Configurations

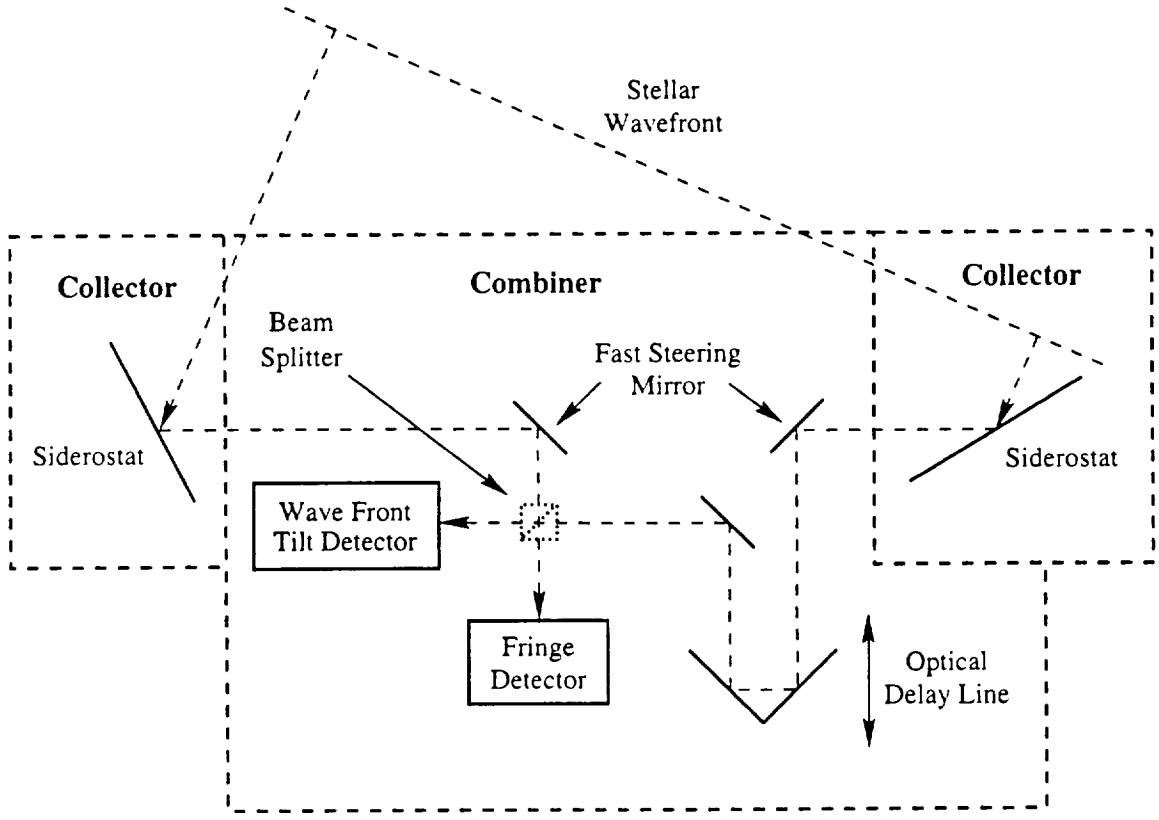


Figure 1-5: Illustration of Collecting and Combining Optics

combination of structural and/or optical control. Structural control is performed by placing actuators on the structure itself while optical control is provided by the optical delay line and the fast steering mirrors. Considerable work has been done in this area, including that done by Hyde [12], Spanos et. al. [13] and the work done on the Middeck Active Control Experiment (MACE) by MIT's Space Engineering Research Center [14]. An exhaustive list of references on this topic is provided by Hyde [12].

The main advantage of a multiple spacecraft interferometer is the possibility of longer baselines, potentially on the order of thousands of kilometers. The major disadvantage is this baseline must be actively maintained over the period of time required to make the desired measurement, which requires very precise formation flying accurate to within centimeters. Preliminary technological requirements of formation flying are presented in the preliminary designs of NMI [8] and MUSIC [9].

A third possible configuration that is not addressed in this work is the construction of an interferometer on the Moon. The Moon has the benefits of being a large, stable platform for the observing optics and of not having an atmosphere to degrade observations. However, the European Space Agency recently conducted a study [15] that compared a free-flyer interferometer with a Moon-based one and concluded, for a variety of reasons, that the free-flyer version was preferred as a near term mission.

## 1.4 Approach

As mentioned above, the primary objectives of this work are:

(i) to establish a framework of study within which a comparison of structurally connected and multiple spacecraft interferometers can be made; and

(ii) to make a preliminary estimate of the cross-over baseline, for a variety of operating parameters, beyond which it is preferable to operate a multiple spacecraft interferometer.

(iii) to investigate the advantages of adding active structural control to the SCI.

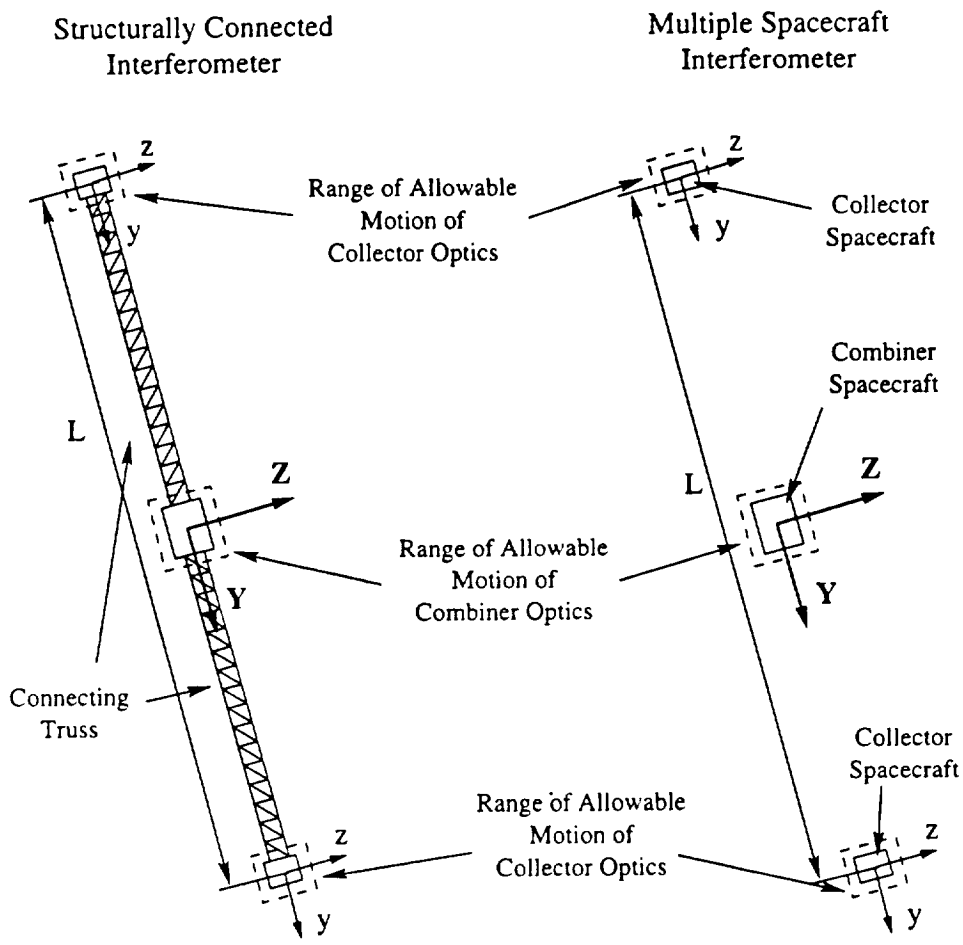


Figure 1-6: Assumed Configurations of the Structurally Connected and Multiple Spacecraft Interferometers Used in this Study

The calculation of the cross-over baseline is performed for a variety of operating parameters — such as orbit, truss material, propellant, performance requirement etc. — in an attempt to bound the range and to determine the effect of each parameter on the cross-over baseline. This calculation requires the identification of the design parameters that constrain the designs of the SCI and MSI. Future research in those areas could enable the use of a particular configuration under a wider range of operating conditions.

The potential trade space of the problem is immense, so simplifying assumptions are made to make the problem tractable. Figure 1-6 illustrates the assumed configurations of the structurally connected and multiple spacecraft interferometers used in this study.

The first and most important assumption is that a comparison of structurally connected and multiple spacecraft interferometers can be made *without a detailed analysis of the optical subsystems.* It is assumed that if the absolute positions of the collecting and combining optics are maintained within a specified range, on the order of centimeters, then the optical control subsystem alone will be able to reduce the remaining OPD to the distance required, on the order of tens to hundreds of nanometers (corresponding to a gain of 100-120 dB), and to control the WFT and BOD to the required levels.

The second assumption is that the problem can be analyzed in two dimensions instead of three. All motion of the interferometers is constrained to lie within the $YZ$-plane of the global $XYZ$ coordinate system. The axes are centered on the combiner optics with the $X$-axis along the line-of-sight of the interferometer which is out of the plane of the page, the $Y$-axis parallel to the baseline, and the $Z$-axis completing the right-handed coordinate system. Local $xyz$-axes are centered on the collector optics and are parallel to the global $XYZ$-axes.

Furthermore, only linear interferometers composed of two sets of collecting optics are analyzed. In reality, a structurally connected interferometer would probably consist of numerous collectors arranged along the structurally connecting member, as is the baseline design for SIM [3]. This interferometer would then only need to be rotated through 180 degrees to fill in the $uv$-plane. Similarly, a multiple spacecraft interferometer would probably consist of numerous spacecraft arranged along a circle so that minimal translation of each spacecraft would be required to fill in the $uv$-plane. (See the designs for MUSIC [9] or the interferometer studied by ESA [15].) As a first attempt at determining the cross-over baseline, it is believed that it is not necessary to model these more complex interferometer designs.

The final assumption is that a fair comparison of SCI's and MSI's can be made based on mass rather than the explicit calculation of cost or complexity. This allows a comparison of SCI's and MSI's to be made without requiring detailed models of the interferometers, which are not available at this early stage of decision-making. This assumption is further discussed in Chapter 2.

## 1.5 Outline

The cross-over baseline is calculated by first determining the minimum mass design of the structurally connected interferometer that meets all performance requirements and imposed constraints and then comparing this design with that of the multiple spacecraft interferometer. This process is described in the following chapters.

This report can be divided into three parts — the methodology used, the modeling of the trade space, and the comparison of the modeled interferometers.

Chapter 2 describes the methodology used in this work to make comparisons between structurally connected and multiple spacecraft interferometers. The formulation of the problem in block diagram form is presented, as well as the examined trade space and the imposed constraints. The presentation of the methodology in block diagram form makes it very easy for future investigators to input different assumptions, constraints, and models. In the end, it may be this methodology which is the greatest contribution of this work.

Chapters 3 and 4 describe the modeling of the trade space. Chapter 3 presents the modeling of the performance and operational scenario of the interferometers as well as the modeling of the interferometers themselves.

Chapter 4 describes the modeling of both the external environmental disturbances that affect the attitude of the interferometer and the onboard disturbances that might affect the interferometer's performance. All assumptions that are made in these modeling steps are also presented.

Chapters 5 and 6 present the comparisons of the modeled interferometers for 22 different combinations of trade space parameters. Each combination is referred to as a separate case. The reference case to which the results of all other cases are compared is described in Chapter 2.

Chapter 5 describes in detail the process of designing the minimum mass structurally connected interferometer that meets all performance requirements and constraints for the reference case. This minimum mass SCI design is then compared to the design of the multiple spacecraft interferometer.

Chapter 6 presents the comparisons of the SCI and MSI designs for the remaining 21 cases and explains the differences between these results and the results of the reference case.

Finally, Chapter 7 summarizes the results of this study and presents those areas where future research can be performed to determine a more accurate estimate of the cross-over baseline beyond which multiple spacecraft interferometers are preferred over structurally connected interferometers.

# Chapter 2

# Methodology

The first purpose of this work is to establish a framework of study within which structurally connected and multiple spacecraft interferometers can be compared. The second purpose is to then perform actual comparisons within this framework. This chapter addresses the first purpose, establishing the framework.

In order to determine whether it is "better" to build and operate a structurally connected interferometer (SCI) instead of a multiple spacecraft interferometer (MSI), it is first necessary to select a metric upon which the comparisons will be made.

The next step is to specify the trade space over which the study will be conducted. The trade space consists of those parameters that will be varied to determine under what operating conditions SCI's are preferable over MSI's and to what extent structural control is beneficial. To maintain a sense of realism in the trade space, it is also necessary to identify and impose constraints on various parameters, such as total mass and component size.

After the selection of the comparison metric, trade space, and constraints, the process of calculating the metric must be identified and applied. This methodology specifies the areas that need to be modeled and their interactions.

The framework of study consists of the above four steps — the selection of a metric, the specification of the trade space, the identification of constraints, and the formulation of the methodology. The first three are specific to this particular study but it is believed that the methodology formulated is general to the problem

of designing space interferometers. Different metrics, trade space, constraints, and models of components can be used with the methodology presented which potentially makes it extremely beneficial to the space interferometry community.

Section 2.1 discusses the selection and presentations of a comparison metric. Section 2.2 describes the trade space of the study, while the imposed constraints are described in Section 2.3. Finally, Section 2.4 formally presents the methodology and the areas that require modeling.

## 2.1 Comparison Metric

### 2.1.1 Metric

When selecting the configuration for an experiment to be launched into space, many times the decision is made based on cost. The configuration that achieves the same level of performance at the lowest cost is commonly chosen. It is noted that to first order for many space payloads, the cost is proportional to the total mass launched. Therefore, it is natural to look at the mass launched as the comparison metric in order to avoid the lengthy and detailed cost analysis.

The mass launched is a function of both the size of the interferometer and the mission duration. The size determines the dry mass of the interferometer while the mission duration determines the propellant mass. For this study, the total mass launched is calculated by adding the dry mass to the product of the average propellant mass rate with the mission duration.

The dry mass of the structurally connected interferometer consists of the mass of the connecting truss and the dry mass of all other subsystems, including optical, attitude determination and control, electrical, thermal, other structural, etc. Hence, the total SCI mass is

$$m_{sci} = m_{o,sci} + m_t + \dot{m}_{sci} t_m \tag{2.1}$$

where $m_t$ is the truss mass, $m_{o,sci}$ is the dry mass of all other subsystems, $\dot{m}_{sci}$ is the

average propellant mass rate and $t_m$ is the mission duration. The truss mass and average propellant mass rate are both calculated properties and vary with interferometer size. The dry mass of the other subsystems is an assumed quantity based on estimates for planned missions and does not scale with size. Inherent in this approach is the assumption that the variation with baseline of the mass of the components of the other subsystems identified above (optical, electrical, thermal, etc.) is small compared to the variation of the mass of the truss.

The total mass of the multiple spacecraft interferometer is calculated in a similar fashion.

$$m_{msi} = m_{d,msi} + \dot{m}_{msi} t_m \tag{2.2}$$

In Equation 2.2, $m_{d,msi}$ is the sum of the assumed dry masses of the three or more freeflyers and $\dot{m}_{msi}$ is the sum of the calculated average propellant mass rates for all of the maneuvering spacecraft. The dry masses are based on estimates for planned missions and do not scale with baseline.

Laskin [16] identifies a potential problem with using mass as the comparison metric. He points out that interferometers tend to be very light for their size and complexity and may not conform well to accepted notions of mass equating to dollars. The added cost of the connecting truss of an SCI may be small compared to the cost of the additional attitude control equipment required on each of the freeflyers, even if the masses are equal. The fear is that a mass comparison may unfairly penalize SCI's.

It is beyond the scope of this study to fully address this problem, since to do so requires a detailed cost analysis. This study does, however, include the additional mass of the attitude control equipment required by assuming that $m_{d,msi}$ is greater than $m_{o,sci}$. This does not address the cost issue but does make the mass comparison more realistic. One way to potentially address the cost problem without explicitly performing the cost analysis is to add non-physical penalty mass to $m_{d,msi}$ to represent the additional cost of the attitude control equipment. This is not done in this study.

Thus, the comparison metric of this study is the total launched mass. (The total launched mass is also referred to as the wet mass of the interferometer.) The minimum mass of each configuration (MSI and SCI, the latter both structurally active and passive) necessary to meet the performance requirement, subject to various constraints to maintain realizability, is compared. (As discussed in the first chapter, the performance requirement is that the interferometer design be able to constrain the absolute displacement of the collecting optics to a specified level under all disturbances present.) The next section describes the presentation of the comparison metric.

### 2.1.2 Critical Time Plots

Examination of Equations 2.1 and 2.2 reveals that given the dry masses and average propellant mass rates of the two configurations, there is at most one mission duration for which the total wet masses are equal.

$$t_{crit} = \frac{m_{o,sci} + m_t - m_{d,msi}}{\dot{m}_{msi} - \dot{m}_{sci}} \tag{2.3}$$

This mission duration will be referred to as the "critical time" throughout this work. For the various operating conditions examined in this study, the critical time is the maximum mission duration for which it is preferable to use an interferometer composed of multiple spacecraft. For missions shorter than the critical time, the total wet mass of an MSI is less than the wet mass of an SCI, so MSI's are preferable. Alternatively, for missions longer than the critical time, a structurally connected interferometer is desirable.

This interpretation of the critical time allows the different interferometer configurations to be compared without the explicit calculation of the total launched mass. This is beneficial because only one plot is necessary for a given set of operating conditions to identify the range of baselines and mission durations for which one configuration is preferred over the other. The dry masses and average propellant mass rates can be calculated as functions of interferometer baseline only, so the critical

time is also only a function of baseline. Instead of a series of plots, one for each baseline, showing the total mass of the SCI and MSI configurations as a function of mission duration, only one plot showing the critical time as a function of baseline and the above interpretation is needed to compare structurally connected and multiple spacecraft interferometers. The critical time is an "indicator" of the total launched mass metric.

The end product of this study is a plot of critical time versus baseline. As discussed in Chapter 1, the baseline is the distance between the two sets of collector optics and ranges between 10 and 1000 meters. Critical time plots are generated for both passive and active structurally connected interferometers. In this way, direct comparisons can be made between freeflyers and passive structurally connected interferometers as well as between freeflyers and actively controlled SCI's. Comparing the two critical time plots then allows indirect comparison of passive and active SCI's. Figures 2-1 through 2-3 are sample plots of dry mass, average propellant mass rate, and critical time versus baseline, respectively.

In Figure 2-1, the solid line is a plot of dry SCI mass required to meet the performance specification and all constraints. The dashed line is the dry MSI mass required to meet the same specifications. An important distance is the distance where the dry masses are equal, which occurs at 127 m as shown by the vertical dotted line. This distance will be referred to as the "equal dry mass" point throughout this work.

Similarly, in Figure 2-2, the solid line is a plot of average SCI propellant mass rate necessary to meet the requirements while the dashed line is the plot of average MSI propellant mass rate. An important distance is the distance at which the average propellant mass rates are equal, which occurs at 343 m as shown by the vertical dotted line. Similar to the equal dry mass point, this distance will be referred to as the "equal mass rate" point.

Performing the calculation in Equation 2.3 generates Figure 2-3, the plot of critical time versus baseline. The line extends from zero at the equal dry mass point to infinity at the equal mass rate point. The shaded area is the range of mission times for which the freeflyer configuration is better than the structurally connected configuration

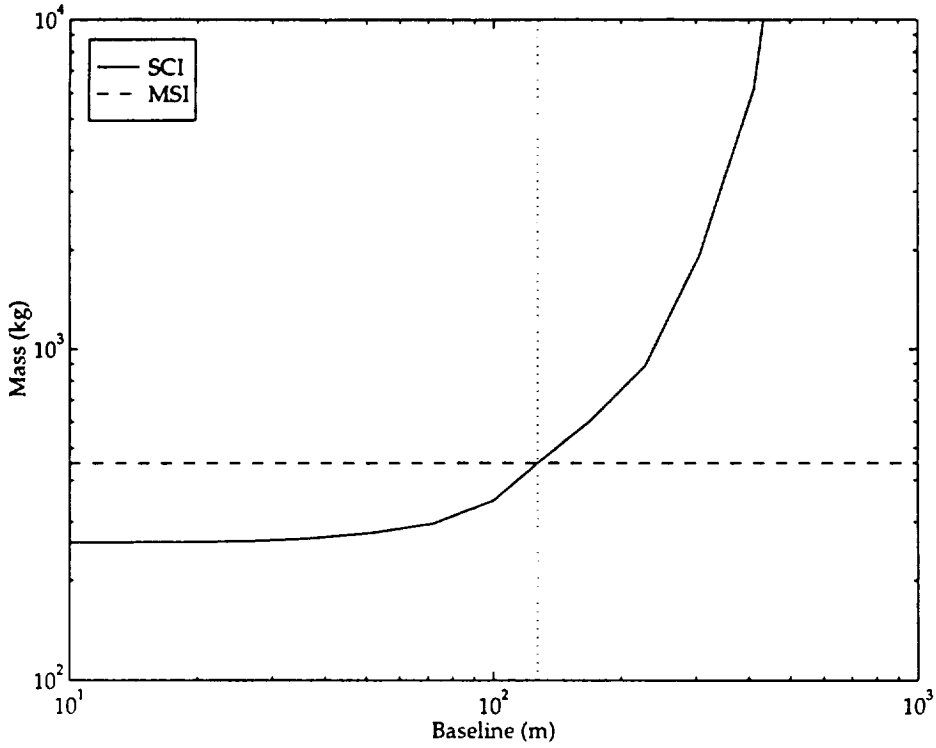


Figure 2-1: Sample Dry Mass vs Baseline Length Plot

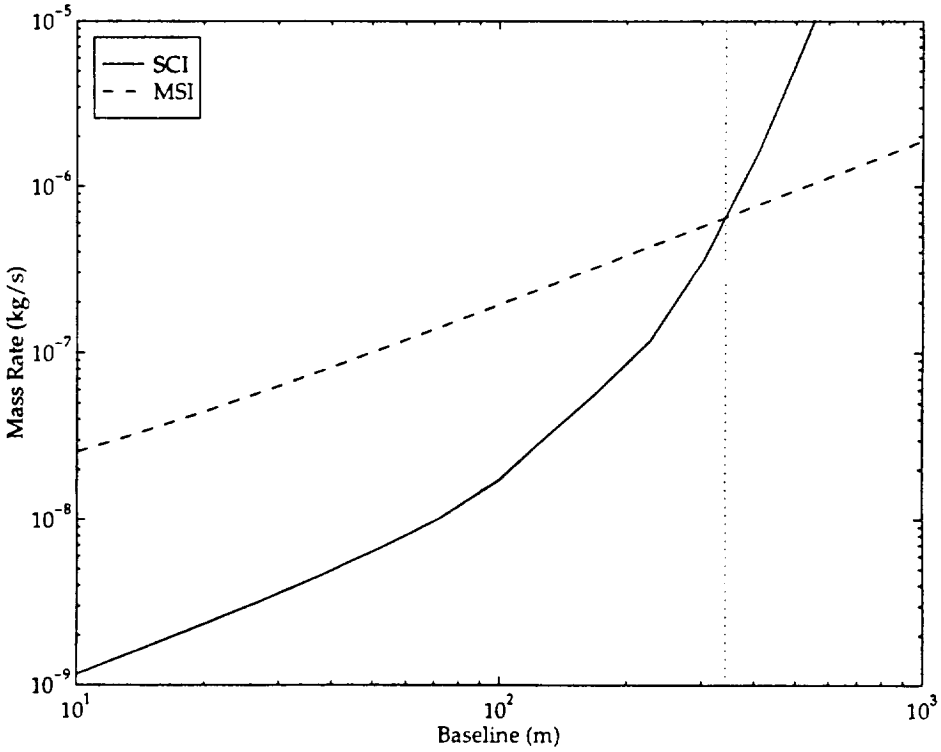


Figure 2-2: Sample Propellant Mass Rate vs Baseline Length Plot

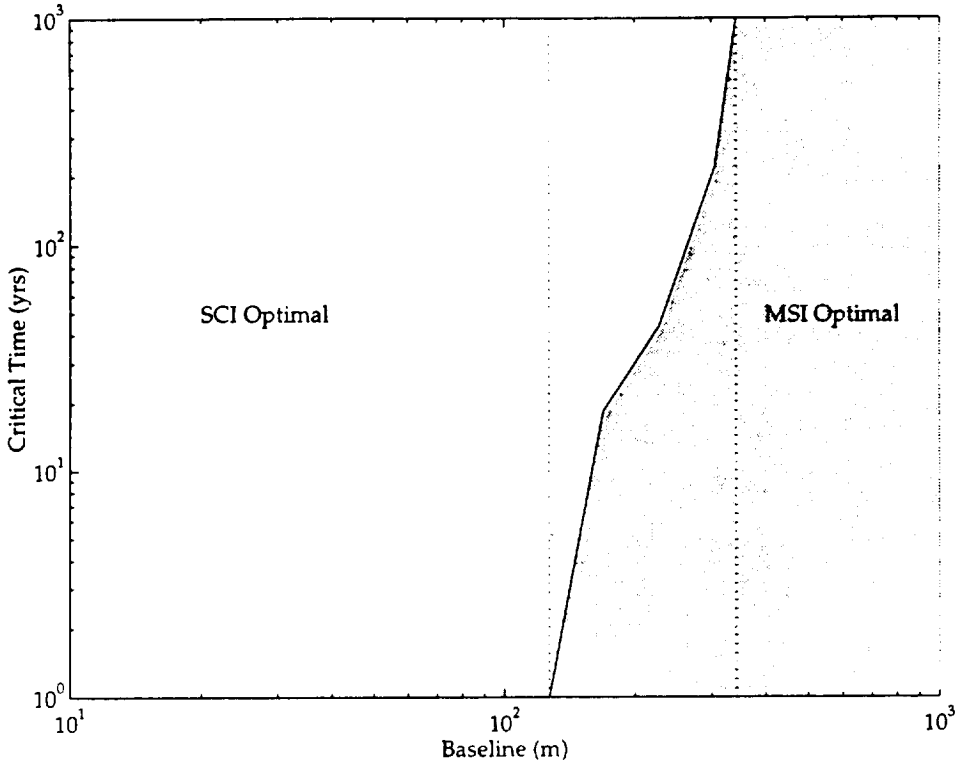


Figure 2-3: Sample Critical Time vs Baseline Length Plot

based on the mass launched metric and subject to the constraints imposed.

For baselines shorter than the equal dry mass point, a structurally connected interferometer is always optimal. This is because both the dry mass and the average propellant mass rate of the SCI are less than the corresponding MSI values. The structurally connected interferometer is initially less massive and consumes less fuel than the multiple spacecraft interferometer at every time instant so regardless of mission duration, the SCI will be optimal. Similarly, for distances above the equal mass rate point, a multiple spacecraft interferometer is always optimal because it is initially less massive and consumes less fuel than the structurally connected interferometer.

For baselines between the equal dry mass and equal mass rate points, there is a finite mission duration for which the launched mass of an SCI equals the launched mass of an MSI. Even though the SCI has greater dry mass, it requires less propellant so eventually the MSI savings in dry mass are offset by the increase in propellant mass. It is in this range of baseline lengths that it is necessary to know the intended mission

duration in order to be able to determine which configuration is best.

Figure 2-3 is typical of the shape of all critical time plots in this study. The actual values of the equal dry mass and equal mass rate points may vary but it is only between these two points that there exists a critical time plot. Table 2.1 summarizes the properties of the equal dry mass and equal mass rate points and assigns each a number that is used in Figure 2-5, the methodology block diagram.

Table 2.1: Important Critical Time Plot Parameters

| No. | Parameter | Description |
|---|---|---|
| M1 | Equal Dry Mass Point | Distance where MSI and SCI dry masses are equal<br>Below this baseline distance, SCI always better |
| M2 | Equal Mass Rate Point | Distance where MSI and SCI propellant mass rates are equal<br>Above this baseline distance, MSI always better |

## 2.2 Description of Trade Space

After determining the comparison metric, it is necessary to select the set of design parameters of interest to determine the sensitivity of the critical time. These parameters make up the trade space of the study. Table 2.2 lists those parameters that were varied in this work to determine their effects on the critical time. The baseline design value against which other variations is compared is in **boldface** type. Recall that the critical time plot compares an MSI configuration with an SCI configuration and that critical time plots are generated for both passive and active SCI's. Consequently, these trades are not explicitly listed in the trade space.

The number beside each entry is used to identify the variable parameters in the methodology block diagram, Figure 2-5. A brief description of each entry in Table 2.2 follows. More detailed descriptions and the actual values associated with each parameter can be found in Chapters 3 and 4.

(T1) Operational Scenario: Both rotating and non-rotating interferometers are studied. The rotating interferometers rotate at a constant rate while image-taking

Table 2.2: Trade Space

| Trade | Parameter | Options |
|---|---|---|
| T1 | Operational Scenario | Rotating (RPM scales with size) |
| | | **Stationary** - 5°, **15°**, 45°, 75°, 85° |
| T2 | Orbit | LEO, GEO, **1 AU**, 5.2 AU |
| T3 | Truss Material | **G/E**, Al |
| T4 | Propellant | $GN_2$, **$N_2H_4$**, PPT |
| T5 | Attitude Control | **Thrusters**, RWA |
| T6 | Thruster Location | **Tip**, Central S/C |
| T7 | Onboard Disturbances | **Thruster**, RWA, **ODL**, Thermal Snap |
| T8 | Deadband (Amp.) | 0.225 cm, **0.450 cm**, 2.250 cm |
| T9 | Performance (Amp.) | 0.25 cm, **0.50 cm**, 2.50 cm |

and this rate scales with interferometer size. The non-rotating interferometers hold a constant orientation relative to the body about which they orbit. Five different orientations are studied: 5°, **15°**, 45°, 75° and 85°. See Section 3.2.2, for a detailed description of these orientations.

(T2) Orbit: Four different orbits for the interferometers are studied:

(i) 300 km Low Earth Orbit (LEO)

(ii) 35,786 km Geosynchronous Earth Orbit (GEO)

(iii) **Solar Orbit at Earth Distance (1AU)**

(iv) Solar Orbit at Jupiter Distance (5.2 AU)

(T3) Truss Material: **Graphite/Epoxy (G/E)** and aluminum (Al) are the two different materials used for the structural truss of the SCI's.

(T4) Propellant: Three different propellants are studied: nitrogen cold gas ($GN_2$), **hydrazine ($N_2H_4$)** and pulsed plasma thrusters (PPT).

(T5) Attitude Control: Two forms of attitude control are studied:

(i) **Thrusters** - The thrusters use one of the three propellants listed above and are located at one of the two locations below.

(ii) Reaction Wheels (RWA) - Reaction wheels are used as the primary source of attitude control but still require thrusters for desaturation. As above, the thrusters use one of the three propellants listed above and are located at one of the two locations below.

(T6) Thruster Location: Two locations of the thrusters on SCI for attitude control or reaction wheel desaturation are studied:

(i) **Tip** - The thrusters are located at the tips of the connecting truss, i.e. at the location of the collecting optics.

(ii) Central Spacecraft - The thrusters are located at the edges of the central spacecraft.

(T7) Onboard Disturbances: Four different onboard disturbances are studied:

(i) **Thrusters** - If thrusters are used for primary attitude control, their disturbance spectrum is input into the plant. No thruster disturbance spectrum is input if thrusters are only used for reaction wheel desaturation.

(ii) Reaction Wheels (RWA) - If reaction wheels are used for primary attitude control, their disturbance spectrum is input into the plant. Only one of the reaction wheel or thruster disturbance spectrums is input.

(iii) **Optical Delay Line Reactuation (ODL)** - The forces exerted by the optical delay line on the spacecraft are always input into the plant.

(iv) Thermal Snap (Snap) - A thermal snap disturbance is used in conjunction with any of the above disturbances for the structurally connected interferometer. Cases are run both with and without thermal snap.

(T8) Deadband: If thrusters are used for primary attitude control, the deadband of the interferometer must be specified. For this study, the deadband is assumed to be 90% of the performance requirement. The amplitude of the linear deadband of the multiple spacecraft interferometer is set to 90% of the performance specification below (90% of 0.25 cm, **0.50 cm**, or 2.50 cm.) The angular deadband

of the structurally connected interferometer is set to limit the amplitude of the rigid body tip displacement of the truss to the same deadband specification.

(T9) Performance: As discussed in Section 1.4, the performance specification is to keep the amplitude (half peak-to-peak) of the absolute displacement of the collector and combiner optics to one of three levels: 0.25 cm, **0.50 cm**, or 2.50 cm.

Even though this is a small subset of the total number of variable parameters of the problem, this is still a very large trade space having almost 3500 combinations. In an attempt to capture the important trends in this trade space, 22 cases were selected. The selected cases are shown in Table 2.3.

The first case is the baseline case, which is a non-rotating interferometer in orbit about the sun at 1 AU and oriented at 15° from the stable gravity gradient orientation. Attitude control is provided by hydrazine thrusters located at the tips of the interconnecting truss which is made of graphite/epoxy. The onboard disturbances are the thrusters and the ODL reactuation. The $3\sigma$ absolute displacement amplitude of the collector and combiner optics is specified to be 0.50 cm (1 cm peak to peak.)

In every other case, one or two of the above trades are selectively made, as shown in Table 2.3. The baseline case is described in detail in Chapter 5 while the results of the other runs are presented in Chapter 6.

Table 2.3: Summary of Cases

| Case | T1 - Orientation | | | | | | T2 - Orbit | | | | T3 - Material | | T4 - Propellant | | | T5 - Attitude Control | | T6 - Thruster Location | | T7 - Onboard Disturbances | | | | T9 - Performance | | |
|---|---|---|---|---|---|---|---|---|---|---|---|---|---|---|---|---|---|---|---|---|---|---|---|---|---|---|
| | Rot. | 5° | 15° | 45° | 75° | 85° | LEO | GEO | 1 AU | 5.2 AU | G/E | Al | GN2 | N2H4 | PPT | Thrusters | RWA | Tip | S/C | Thruster | RWA | ODL | Thermal Snap | 0.25 cm | 0.50 cm | 2.50 cm |
| 1 | | | X | | | | | | X | | X | | | X | | X | | X | | X | | X | | | X | |
| 2 | | | X | | | | X | | | | X | | | X | | X | | X | | X | | X | | | X | |
| 3 | | | X | | | | | X | | | X | | | X | | X | | X | | X | | X | | | X | |
| 4 | | | X | | | | | | | X | X | | | X | | X | | X | | X | | X | | | X | |
| 5 | | X | | | | | | | X | | X | | | X | | X | | X | | X | | X | | | X | |
| 6 | | | | X | | | | | X | | X | | | X | | X | | X | | X | | X | | | X | |
| 7 | | | | | X | | | | X | | X | | | X | | X | | X | | X | | X | | | X | |
| 8 | | | | | | X | | | X | | X | | | X | | X | | X | | X | | X | | | X | |
| 9 | X | | | | | | X | | | | X | | | X | | X | | X | | X | | X | | | X | |
| 10 | X | | | | | | | X | | | X | | | X | | X | | X | | X | | X | | | X | |
| 11 | X | | | | | | | | X | | X | | | X | | X | | X | | X | | X | | | X | |
| 12 | X | | | | | | | | | X | X | | | X | | X | | X | | X | | X | | | X | |
| 13 | | | X | | | | | | X | | | X | | X | | X | | X | | X | | X | | | X | |
| 14 | | | X | | | | | | X | | X | | X | | | X | | X | | X | | X | | | X | |
| 15 | | | X | | | | | | X | | X | | | | X | X | | X | | X | | X | | | X | |
| 16 | | | X | | | | | | X | | X | | | X | | X | | | X | X | | X | | | X | |
| 17 | | | X | | | | | | X | | X | | | X | | X | | X | | X | | X | X | | X | |
| 18 | | | X | | | | | | X | | X | | | X | | | X | X | | | X | X | | | X | |
| 19 | | | X | | | | | | X | | X | | | X | | | X | | X | | X | X | | | X | |
| 20 | | | X | | | | | | X | | X | | | X | | | X | X | | | X | X | X | | X | |
| 21 | | | X | | | | | | X | | X | | | X | | X | | X | | X | | X | | X | | |
| 22 | | | X | | | | | | X | | X | | | X | | X | | X | | X | | X | | | | X |

## 2.3 Imposed Constraints

In this work, a minimum mass structurally connected interferometer and a multiple spacecraft interferometer are designed to meet the performance requirements specified in Chapter 1. In order to ensure that the design is realizable, constraints must be imposed on various structural and component parameters. The various constraints enforced in this trade study are summarized in Table 2.3 and described below. More detailed descriptions are given in Chapter 3. Table 2.3 also assigns to each constraint a number that is used in Figure 2-5, which is discussed in Section 2.4.

Table 2.4: Imposed Constraints

| No. | Constraint | | Value | Active |
|---|---|---|---|---|
| C1 | Dry Mass | LEO, GEO, 1 AU<br>5.2 AU | 15,400 kg<br>3850 kg | SCI |
| C2 | Truss Natural Frequency | Passive<br>Active | 1 decade above ACS BW<br>1 decade below ACS BW | SCI |
| C3 | Maximum Thrust | $GN_2$<br>$N_2H_4$<br>PPT | 1 N<br>25 N<br>5 mN | SCI<br>MSI |
| C4 | Reaction Wheel Mass | | 100 kg | SCI<br>MSI |
| C5 | Strut Minimum Thickness | | 0.5 mm (20 mils) | SCI |
| C6 | Strut Maximum Stress | G/E<br>Al | 830 kPa<br>120 kPa | SCI |
| C7 | Strut Maximum Force | | $\leq$ 1/2 buckling load | SCI |
| C8 | Propellant Percentage of Dry Mass | | $\leq$ 30% | SCI<br>MSI |

(C1) Dry Mass: Modern launchers limit the amount of mass that can be put into orbit, and the interferometers designed in this study must meet these limits. For launch into LEO, GEO, and 1 AU orbits, the limit used is 20,000 kg, based on Shuttle capabilities. A limit of 5,000 kg is used for launch into the 5.2 AU orbit (compared with the 2,500 kg and 5,800 kg masses of Galileo and Cassini, respectively.)

This total mass is composed of the dry mass of the interferometer and the propellant mass as indicated by Equations 2.1 and 2.2. Since the total mass is never explicitly calculated, 23% of this mass limit is set aside for the propellant required to counter the attitude disturbances. This corresponds to the propellant mass equaling 30% of the dry mass. No allowance is made for the mass of propellant required for orbit transfer.

Therefore, the dry mass of the interferometers must be less than or equal to 77% of the values given above, which is 15,400 kg for the LEO, GEO, and 1 AU orbits and 3,850 kg for 5.2 AU orbit.

In theory this constraint is applied to both the MSI and SCI designs, but in reality since the dry mass of the multiple spacecraft interferometer is fixed and doesn't scale with baseline, this constraint is only active on the SCI design.

(C2) Truss Natural Frequency: In order to prevent undesired excitation of flexible modes by the attitude control subsystem, traditional spacecraft design requires the first structural natural frequency of the spacecraft to be at least one decade above the attitude control bandwidth. This limit is imposed on the structurally passive SCI.

By actively controlling the structure, however, it is possible to reduce the flexible response and thereby allow the natural frequency to fall within the attitude control bandwidth. It is still desirable, however, to limit the number of modes within the bandwidth to a manageable number. In many cases this can be done by limiting the fundamental structural natural frequency to one decade below the ACS bandwidth. This limit is imposed on the active SCI.

Since the multiple spacecraft interferometer is treated as a collection of three rigid bodies, no constraint can be imposed on their structural natural frequencies.

(C3) Maximum Thrust: Present-day technology limits the maximum size of attitude control thrusters. The maximum thrust limits for the three propellants studied

are, from Larson and Wertz [17] and Olin Aerospace [18]:

(i) Nitrogen Cold Gas ($GN_2$) - 1 N

(ii) Hydrazine ($N_2H_4$) - 25 N

(iii) Pulsed Plasma Thrusters (PPT) - 5 mN

These limits are enforced on both the MSI and SCI designs.

(C4) Reaction Wheel Mass: Similar to maximum thrust, there is a maximum mass for the reaction wheels necessary to fight attitude control disturbances. In this study, the maximum mass assumed is 100 kg. This limit is enforced on both the MSI and SCI designs.

(C5) Strut Minimum Thickness: The minimum thickness of the struts that compose the SCI truss is 0.5 mm or 20 mils.

(C6) Strut Maximum Stress: The struts must not fail so it is required in this study that the maximum stress allowable is one-half the yield stress of the material used. This corresponds to 830 kPa and 120 kPa for graphite/epoxy and aluminum, respectively.

(C7) Strut Maximum Force: The struts must also not buckle so it is required that the maximum force be less than one-half the corresponding critical buckling load.

(C8) Propellant Percentage of Dry Mass: In order to not violate the assumptions made in calculating the propellant mass rate as discussed in Section 4.1.4 and for the SCI design to meet the launch mass constraints, the total propellant mass must be limited to 30% of the dry mass of the interferometer. For the multiple spacecraft interferometer, the propellant mass of each of the freeflyers must be less than or equal to 30% of its dry mass.

Unlike the other limits which are explicitly checked for when designing the minimum mass SCI (and MSI where applicable), this last constraint is enforced graphically on the critical time plot. In addition to plotting the critical time, the times at which

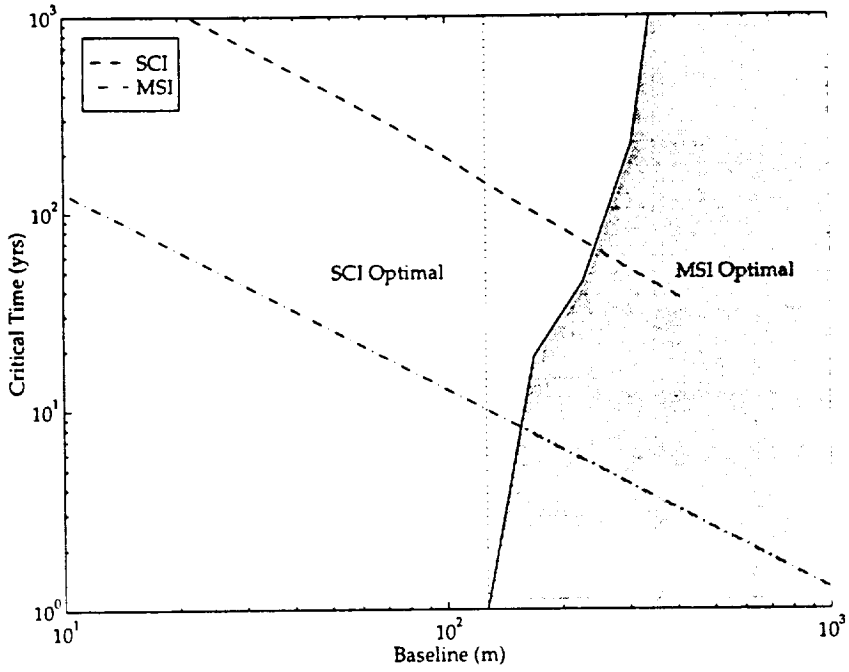


Figure 2-4: Sample Critical Time Plot with Propellant Mass Constraints

the propellant mass of the SCI and MSI equal 30% of the respective dry masses are also plotted.

For mission durations beyond this time, the propellant mass is greater than 30% of the dry mass so the Taylor series approximation to the rocket equation which is used in Section 4.1.4 to calculate the average propellant mass rate may not be accurate. Additionally, even though the dry mass of the SCI design meets the dry mass constraint, the propellant mass required may cause the total launched mass of the interferometer to be greater than the launch limits discussed above. Therefore, for mission durations beyond this time, both the total mass and the propellant mass rate should be checked and the results of this study applied carefully.

Figure 2-4 shows these mass fraction constraints. The solid line is the critical time, the dashed line is the time at which the propellant mass of the SCI equals 30% of the SCI dry mass at that baseline, and the dash-dot line is the time at which the propellant mass of one of the freeflyers of the MSI equals 30% of its corresponding dry mass. The time constraint shown for the multiple spacecraft interferometer is the minimum of the time constraints for each of the freeflyers.

## 2.4 Formal Methodology

### 2.4.1 Presentation of Methodology

There are two processes necessary to generate the critical time plots discussed in Section 2.1.2. The first is the design of the minimum mass structurally connected interferometer that meets all the performance requirements and constraints described in Sections 1.4 and 2.3, respectively. The second process is the actual calculation of the critical time plot using these minimum mass SCI's.

Traditionally, three areas need to be modeled — the performance, the plant, and the disturbances — in order to determine if a given design meets the performance requirements. In the case of the interferometer, some disturbances are dependent on its mission scenario, which includes its orbit and operating conditions. Hence, for this problem, there are four top-level areas that need to be modeled — the performance, the mission scenario, the plant and the disturbances. Chapters 3 and 4 describe the detailed modeling of these areas while this section details the interaction among them.

Each area can be subdivided as shown in Table 2.5. Each of these subdivisions is an element that needs to be modeled and corresponds to a block in Figure 2-5. The description of each element is contained in the explanation of Figure 2-5.

Figure 2-5 is the pièce de résistance of this chapter. It is the formal methodology for solving the problem of space interferometer design. As will be seen, this is a

Table 2.5: Subdivision of Modeled Areas

| Area | Elements |
|---|---|
| Performance | Performance |
| Mission Scenario | Orbit<br>Operational Scenario |
| Plant | High-Level Plant<br>Internal Plant<br>Optical Train |
| Disturbances | External/Attitude Disturbances<br>Onboard Disturbances |

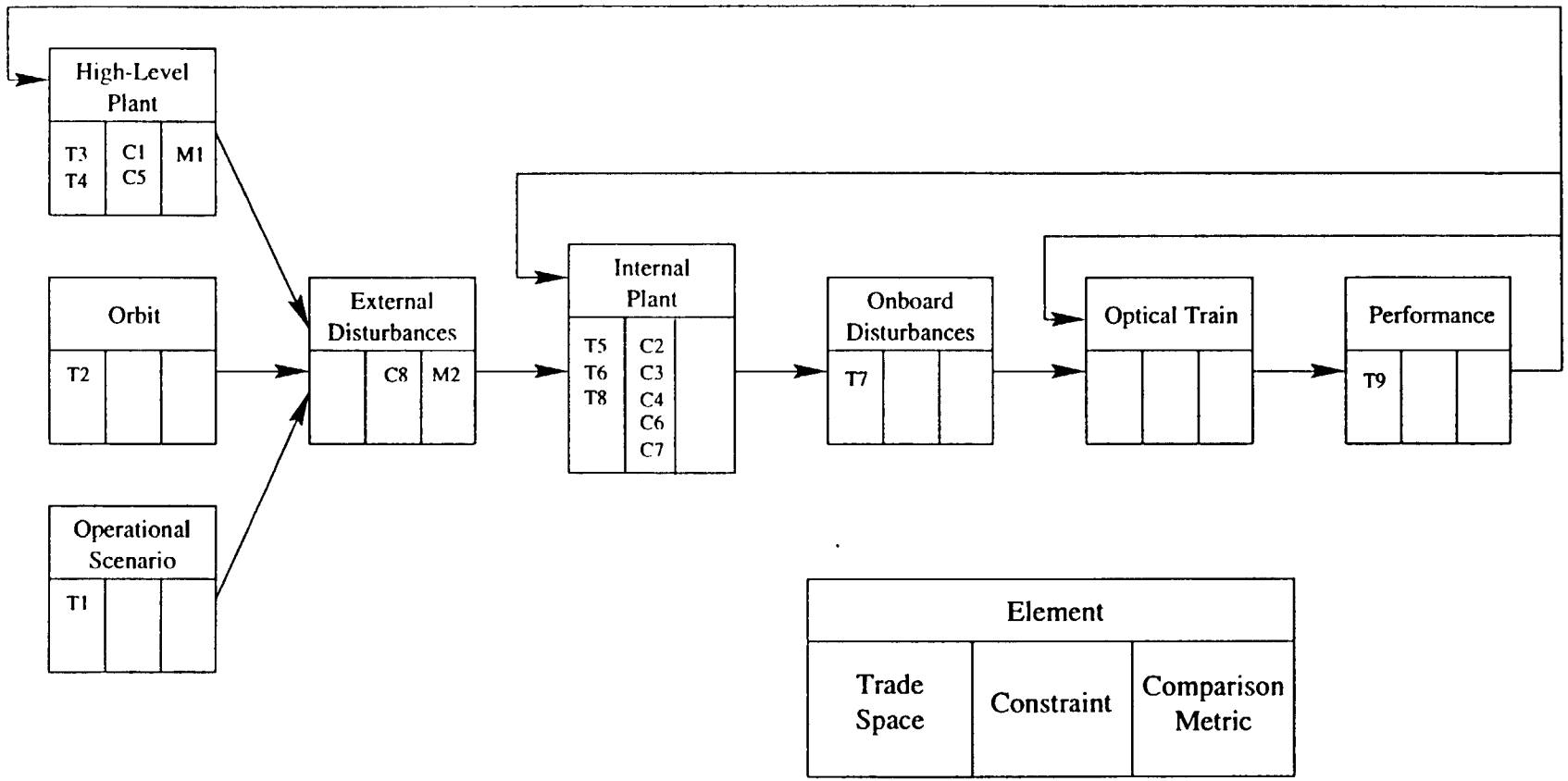


Figure 2-5: Methodology Block Diagram

general methodology and is not limited to the assumptions made in this study. It can be used to describe both the steps involved in the determination of the existence of a solution to the problem and in the calculation of the comparison metric. (In the formulation of the problem used in this study, the former refers to the determination of the minimum mass interferometer while the latter refers to the calculation of the critical time.)

Additionally, in conjunction with Tables 2.1, 2.2, and 2.3, the methodology block diagram can be used to qualitatively determine which of the comparison metrics and constraints are affected by changes in the trade space.

Each block in Figure 2-5 consists of four parts. The top row contains the name of the element that is modeled. The bottom row consists of three columns whose entry numbers correspond to the numbers in Tables 2.2, 2.1, and 2.3 respectively.

The first column indicates which of the trade space parameters are input at that stage, i.e. are contained within the scope of the element. The second column indicates which constraints can be violated at that stage while the third column indicates which comparison metrics can be calculated after modeling of the element.

The arrows between blocks indicate where the results of the modeling of one element are used as inputs to the modeling of another element. Hence, by noting where a specific trade space parameter is entered it is possible to determine which metrics and constraints *could* be affected by following the flow downstream.

It is important to note that not *all* metrics and constraints downstream will be affected. It is necessary to look at the actual modeling equations to determine which will be affected and to what degree. Table 2.6 at the end of this chapter qualitatively lists which metrics and constraints are affected by which trade space parameters for this study. The performance of the interferometer is affected by every trade space parameter except for propellant (C4). All comparison metrics and constraints are affected by the overall geometry of the SCI.

### 2.4.2 Step-by-Step Modeling Process

By illustrating the input/output relationships between the different elements, Figure 2-5 makes clear the step-by-step process that must be undertaken in order to solve the space interferometer problem. Even though the process will be described using the trade space, comparison metric and constraints for this study, it is important to remember that the process itself is general. A different trade space, a different comparison metric, different constraints, even different models of any of the elements can be used so long as they are input at the appropriate locations. The relationship between a particular trade parameter and constraint or metric may change, but the input/output relationships between the elements will not.

Below, the modeling steps of this study are described. Each description includes a brief discussion of which trade space parameters are input at this step and which comparison metrics and constraints can be calculated or checked after the modeling step. The details of how each element is modeled are in Chapters 3 and 4. The modeling of the first three steps can be performed in any order.

(i) Model High-Level Plant: The "high-level plant" is the most general level of plant modeling and includes the overall mass distribution and geometry of the interferometer. This is where decisions regarding propellant and truss material are input. This is also where the scaling of the truss parameters (such as height and cross-sectional area) with length is decided. The constraint on dry mass is imposed here.

Note that in this study, the actual scaling of the truss is calculated based on the minimum mass configuration. Once the minimum mass SCI as a function of length has been determined, the equal dry mass point of the critical time plot can be calculated here. No knowledge other than the dry masses of the SCI and MSI is required.

(ii) Select Orbit: One part of specifying the mission scenario consists of selecting the orbit of the interferometer. This is one of the trade parameters of this study.

(iii) Specify Operating Scenario: The second part of mission scenario selection consists of specifying the operating scenario of the interferometer. This is where the decision between a rotating and non-rotating interferometer is made in this study. This is also where the orientation of the non-rotating interferometer is specified.

(iv) Compute Selected External/Attitude Disturbances: Once the orbit and orientation of the interferometer and its size have been specified, the magnitudes of the environmental disturbance forces and torques can be calculated. These forces and torques affect the attitude of each independent component of the interferometer as well as the location of the freeflyers relative to each other.

The mass of propellant required to overcome these disturbance is calculated at this point. No information is needed about how often the thrusters fire or their size because the calculation is based on the conservation of momentum principle.

An important observation is that the entire critical time plot can be constructed at this stage. The equal mass rate point can be calculated and the limit on propellant mass relative to dry mass can be plotted. This particular comparison metric allows the SCI and MSI designs to be compared at a very early stage, *provided all the performance requirements and constraints are met.* The following steps need only be conducted to ensure that this is the case. Hence, these steps need to be performed when determining the minimum mass interferometer.

If a different comparison metric is chosen, such as cost, the following steps might have to be conducted, for example to size the internal components so a cost model can be run. By assuming an initial mass for the interferometer independent of the size of these components, these steps have been avoided. It will be necessary, however, to check this assumption that the mass of the reaction wheels is negligible compared to the mass of the truss.

(v) Model Internal Plant: The second level of plant modeling involves the design of the subsystems required to counteract the external disturbances. In this study,

this consists of the selection, placement and sizing of attitude control actuators. Given a different comparison metric and different assumptions, different subsystems may be designed (e.g. thermal).

Many assumptions are employed in sizing the components and the reader is referred to Chapter 3 for details. If thrusters are used for primary attitude control, one specification that must be made is the allowable deadband of the spacecraft. In this study, the allowable deadband is equal to the performance specification, but this need not always be the case.

Once the actuators are sized, the limits on their size, the interaction between the frequencies of the structure and attitude control subsystem, and the strength of the truss struts can be checked.

(vi) Compute Selected Onboard Disturbances: The subsystems designed above may generate their own disturbances, such as mechanical vibrations, that could affect the performance of the interferometer. These disturbances are identified and modeled at this step.

(vii) Model Optical Train: In order to calculate whether the performance requirement is met, a model must be developed that takes the onboard disturbances as inputs and outputs the level of performance achieved. The performance requirement for an interferometer is commonly given in optical terms so this step consists of assembling an integrated model of the structure and the optical components.

It is believed that a first-order estimate of the critical time can be achieved without this detailed modeling of the optical train, as is discussed in Section 1.4. Therefore, there is no modeling of the optical train in this study. The performance can be computed by running the onboard disturbances through the structural model of the interferometer designed in Step 1.

(viii) Compute Performance: The onboard disturbances are input into the appropriate model specified in the above step and the resulting performance is computed and

compared to the requirement. For this study, the performance that is calculated at this step is the absolute displacement of the collector and combiner optics.

If the performance requirement is not met, there are three possible ways to improve performance, indicated by the three feedback loops in Figure 2-5.Improved optical control is indicated by the loop back to the optical train modeling, but this option is not modeled here. The second option is to modify the internal plant to alter the onboard disturbances, which includes isolation and the selection of different actuators. Only the effect of different actuators is examined in this study. Finally, the overall geometry of the interferometer can be altered in an attempt to modify stiffness and/or reduce the external disturbances that determine the size of internal components.

Active structural control would traditionally be included in the integrated modeling of the optical train. Since the optical components are not modeled in this study, generalized effects of structural control are included by modifying the frequency constraint and increasing the damping ratio of the truss, as described in Section 3.3.1.

For each case in Table 2.3, the following procedure was performed to generate the plots of critical time versus baseline.

First, a wide range of possible scalings of the SCI truss was selected. These scalings are described in Chapter 3.

Second, all of the above modeling steps were performed for each scaling over the entire range of baselines. This was done to determine if that particular truss scaling could meet all constraints and satisfy the performance requirement. Typically, a scaling would be able to satisfy all constraints for some baselines but not for others.

Third, the truss scaling that satisfied all the constraints and requirements and minimized the truss mass *for a particular baseline* was selected as the "optimal" scaling for that baseline. This process was repeated for each baseline in the range. The result was the determination of the minimum mass structurally connected interferometer as a function of baseline.

Note that since the dry mass of the multiple spacecraft interferometer is an assumed quantity and is independent of baseline, there is no need to determine the minimum mass MSI that will satisfy all requirements and constraints. Either the

assumed multiple spacecraft interferometer will or will not satisfy the requirements and constraints. To determine if the requirements and constraints are met, all of the above modeling steps were performed for the multiple spacecraft interferometer design.

Finally, the critical time plot was generated by comparing the MSI design with the "optimal" scaling of the SCI and performing the calculation in Equation 2.3. Once again, it is important to note that all of the quantities in Equation 2.3 can be determined after only the first four modeling steps described above, *provided all the performance requirements and constraints are met.* All of the modeling steps had to be initially performed to confirm this.

## 2.5 Summary

This chapter first described the selection of the comparison metric for this study. The metric used is mass and the comparison of the SCI and MSI configurations is done through the generation of a critical time plot. The critical time is the time at which the masses of the two configurations are equal. Two important parameters that characterize the critical time plot are the equal dry mass and equal mass rate points, which are summarized in Table 2.1.

Sections 2.2 and 2.3 then described the trade space and imposed constraints of the study. The results are summarized in Tables 2.2 and 2.3, respectively.

Finally, Section 2.4 presented the organization of the problem in block diagram form. Figure 2-5 shows the interaction between the various model blocks and can be used in conjunction with Tables 2.1, 2.2 and 2.3 to qualitatively determine which comparison metrics and constraints are affected by changes in the trade space. Table 2.6 explicitly lists which trade parameters affect which metrics and constraints for this study.

Table 2.6: Metrics and Constraints Affected by Trade Parameters

| Trade Parameter | Affected Metrics and Constraints | | | | | | | | | |
|---|---|---|---|---|---|---|---|---|---|---|
| | M1 | M2 | C1 | C2 | C3 | C4 | C5 | C6 | C7 | C8 |
| T1 | | X | | X | X | X | | X | X | X |
| T2 | | X | | X | X | X | | X | X | X |
| T3 | X | X | X | X | X | X | | X | X | X |
| T4 | | | | | X | | | | | X |
| T5 | | | | X | | | | X | X | |
| T6 | | | | | X | | | X | X | |
| T7 | performance only | | | | | | | | | |
| T8 | | | | X | X | | | X | X | |
| T9 | | | | X | X | | | X | X | |

# Chapter 3

# Performance, Mission Scenario, and Plant Modeling

This chapter describes the modeling of three of the four areas identified in Table 2.5. The fourth area, the disturbance modeling, is described in Chapter 4.

The performance of the various interferometer configurations is calculated in the frequency domain. Section 3.1 describes how this is accomplished. The two aspects of mission scenario modeling — the selection of an orbit and the specification of the operating scenario — are discussed in Section 3.2.

The third area modeled in this chapter is the plant itself. As discussed in Chapter 2, the modeling of the plant can be subsequently broken down into three sub-areas. The first is referred to as the "high-level plant" and includes the overall geometry of the interferometer. The second area that is modeled is the selection and placement of attitude control actuators and is referred to as the "internal plant." The modeling of the optical train is the third area that can be modeled in the formulation of the problem as presented in Chapter 2. However, as discussed in Chapter 2, the optical train is *not* modeled in this work. Only the high-level and internal plant modeling are discussed in detail in this chapter. The high-level plant is described in Section 3.3 and the internal plant is described in Section 3.4.

## 3.1 Performance Modeling

### 3.1.1 Performance Cost Requirement

As discussed in Section 1.4 and shown in Figure 3-1, the performance requirement is to maintain the absolute displacement of the collector and combiner optics within the range specified in both the $y$- and $z$- directions. (The range shown in Figure 3-1 is exaggerated.) The allowable range is specified as one of the trade space parameters (T9). The maximum amplitude of the allowable displacement, $d_{max}$, is one of the following three values — 0.25 cm, 0.50 cm, or 2.50 cm. The reference case maximum amplitude is 0.50 cm.

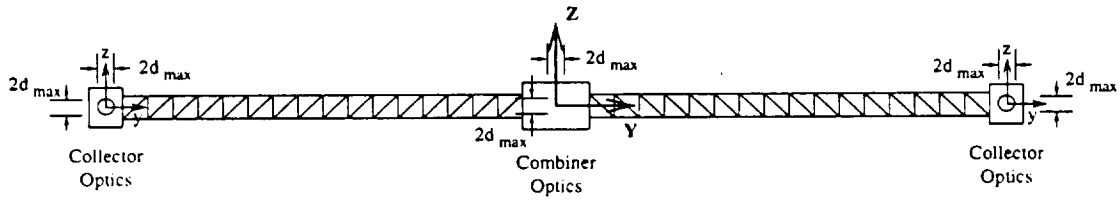


Figure 3-1: Range of Allowable Motion of Collector and Combiner Optics

In order to determine if this performance requirement is met, the allowable maximum displacement must be allocated between the deterministic rigid body motion within a deadband and the "stochastic" motion caused by the onboard disturbances. Figure 3-2 illustrates this allocation for the reference case where thrusters are selected for attitude control.

The dashed line is the deterministic motion of the collector due to the constant

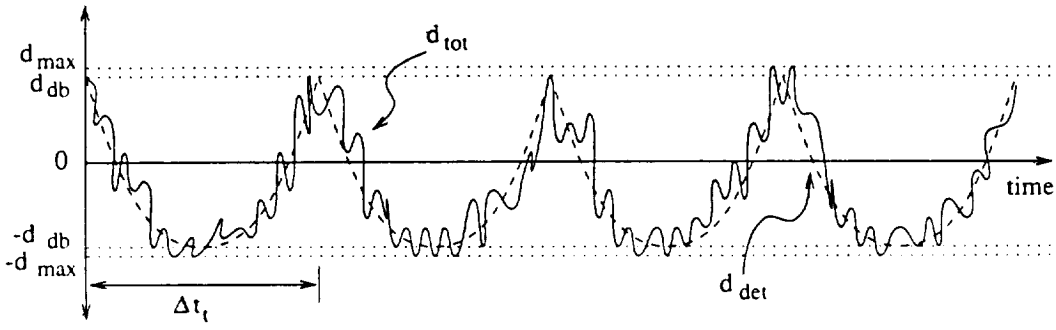


Figure 3-2: Sample Collector Displacement

disturbance acting on the spacecraft (a disturbance torque on the SCI or a differential acceleration of the MSI) and the thrusters firing with a period of $\Delta t_t$. The amplitude of the deterministic motion equals the amplitude of the deadband specified in trade space parameter (T8). In this study, the deadband amplitude, $d_{db}$, is equal to 90% of the performance requirement.

$$d_{db} = 0.9 d_{max} \tag{3.1}$$

The solid line in Figure 3-2 is the actual collector displacement, $d_{tot}$, which is the summation of the deterministic displacement, $d_{det}$, and the displacement, $d_{stoc}$, caused by the onboard disturbances described in Section 4.2.

$$d_{tot} = d_{det} + d_{stoc} \tag{3.2}$$

It is this total displacement that must be less than the maximum allowable displacement at all times.

$$d_{tot} \leq d_{max} \; \forall \; t$$

Since the deterministic displacement is known a priori from the specification of the deadband, the enforced stochastic performance requirement, $z_{req}$, is defined as

$$z_{req} = d_{max} - d_{db} \tag{3.3}$$

This requirement is treated stochastically as a $3\sigma$ bound on the amplitude of the displacement caused by the onboard disturbances

$$3\sigma_z \leq z_{req} \tag{3.4}$$

The subscript $z$ is used to illustrate the fact that the displacement is the performance. The computation of the standard deviation of the actual performance, $\sigma_z$, is explained in Section 3.1.2. Table 3.1 summarizes the stochastic performance requirements for

Table 3.1: Stochastic Performance Requirements (All values in cm)

| $d_{max}$ (T9) | SCI $z_{req}$ | | MSI $z_{req}$ |
|---|---|---|---|
| | Attitude Control Actuators (T5) | | |
| | Thrusters | Reaction Wheels | |
| 0.25 | 0.025 | 0.25 | 0.025 |
| 0.50 | 0.050 | 0.50 | 0.050 |
| 2.50 | 0.250 | 2.50 | 0.250 |

the SCI and MSI.

If thrusters are selected as the attitude control actuators for the SCI, the deadband amplitude is defined by Equation 3.1. If reaction wheels are selected as the SCI attitude control actuators, the deadband amplitude is zero and the enforced stochastic performance requirement is equal to $d_{max}$, specified as a trade space parameter (T9).

Reaction wheels can only reject the individual disturbance torques on the freeflyers composing the MSI, so thrusters must always be used on the freeflyers to control the displacement of the collector and combiner optics in the $y$- and $z$-directions. Hence, the stochastic performance requirement for the MSI is given by Equation 3.3 with a deadband defined by Equation 3.1.

### 3.1.2 Calculation of Performance Cost

For the structurally connected interferometer, $d_{stoc}$ of Equation 3.2 is composed of the sum of the flexible response to the deterministic thruster firing and both the rigid body and flexible responses to the "stochastic" onboard disturbances — the optical delay line reactuation, the reaction wheel imbalances, and thermal snap. Since these disturbances are treated stochastically, the structural response is also stochastic. In order to be able to sum the response to these disturbances and the flexible response to the thruster firing in a coherent fashion, *the flexible response to the thruster firing is treated as a stochastic process even though it is caused by a deterministic disturbance.* The onboard disturbances that are active for each case examined in this work is a trade space parameter (T7) and are presented in Table 2.3.

There is no flexible response for the multiple spacecraft interferometer, so $d_{stoc}$ of the individual freeflyers of the MSI consists of only the stochastic rigid body response to the optical delay line and reaction wheel disturbances.

In this study, the actual performance cost of the designed interferometer is calculated through the use of transfer functions in the frequency domain. For each disturbance, the performance of the interferometer, $Z_i(\omega)$, is calculated by multiplying the disturbance spectrum, $W_i(\omega)$ in units/$\sqrt{\text{Hz}}$, by the structural transfer function from the location of the disturbance to the location of the performance, $G_{zw}(\omega)$, for each frequency point in the range of interest.

$$Z_i(\omega) = G_{zw}(\omega)W_i(\omega)$$

The frequency range of interest for this study is $10^{-6}$ to $10^4$ Hz.

Since the various disturbance sources are assumed to be uncorrelated, the total performance cost is the summation of the squares of the absolute values of the individual performances.

$$J_z(\omega) = \sum_{i=1}^{n} |Z_i(\omega)|^2$$

The standard deviation, $\sigma_z$, of the absolute displacement is the square root of the area under the cost curve.

$$\sigma_z = \sqrt{\int_{\omega_1}^{\omega_2} J_z(\omega) d\omega}$$

Three times the standard deviation must be less than the stochastic performance requirement, as given by Equation 3.4.

Section 3.3 describes the modeling of the performance to disturbance transfer functions for both the structurally connected and the multiple spacecraft interferometers. The modeling of the spectra of the various disturbances is described in Section 4.2.

## 3.2 Mission Scenario

### 3.2.1 Orbit

Four representative orbits of the interferometer were selected to be studied — a 300 km altitude Low Earth Orbit (LEO), a 35,786 km altitude geosynchronous orbit (GEO), a solar orbit at 1 AU (the distance between the Earth and the Sun), and a solar orbit at 5.2 AU (the distance between Jupiter and the Sun.)

These orbits were selected to characterize the potential orbits of future missions. The orbits baselined for the proposed missions described in Chapter 1 are shown in Table 3.2.

Table 3.2: Baseline Orbits for Proposed Missions

| Mission Type | Mission | Orbit |
|---|---|---|
| SCI | SIM<br>Planet Finder | Earth Orbit at 900 km altitude<br>Solar Orbit at 5 AU |
| MSI | NMI<br>MUSIC | Solar Orbit at 1 AU<br>Solar Orbit at 1.01 AU (Sun-Earth $L_2$ point) |
| Telescope | NGST | Solar Orbit at 1.01 AU (Sun-Earth $L_2$ point) |

The 300 km altitude Low Earth Orbit selected is not baselined as the orbit for any long-term mission. This orbit was chosen to be studied in order to determine the effects a worst-case disturbance environment has on the "optimal" interferometer design. It is more typical of the orbit of a shuttle-based experiment, which would be neither long duration nor long baseline.

### 3.2.2 Operational Scenario

The operational scenario of an interferometer consists of the daily maneuvers required to obtain the desired images. These operations include the order and number of images or measurements taken, and the lengths of time required for each image and for repositioning. These operations determine the mass of propellant required for the mission. It is therefore necessary to model them in some fashion.

Unfortunately, mission planning is very complex and very mission dependent. In an attempt to achieve an estimate of the propellant mass, this study makes some simplifying assumptions regarding the operational scenario of the interferometer.

As discussed in Section 1.4, the first assumption made involves constraining all motion of the interferometer to lie within the $YZ$-plane, the plane of the orbit. Both rotating and non-rotating interferometers are examined within this plane.

In order to model non-rotating interferometers, one of five possible orientations is assumed to be maintained for the duration of the mission. The possible orientations are 5°, 15°, 45°, 75°, and 85° off the stable gravity gradient orientation. The reference case orientation of 15° is shown in Figure 3-3. (The reference case is Case 1 of Table 2.3.) Fifteen degrees was selected for the reference case because the gravity gradient torque is one-half the maximum value, which occurs at 45°.

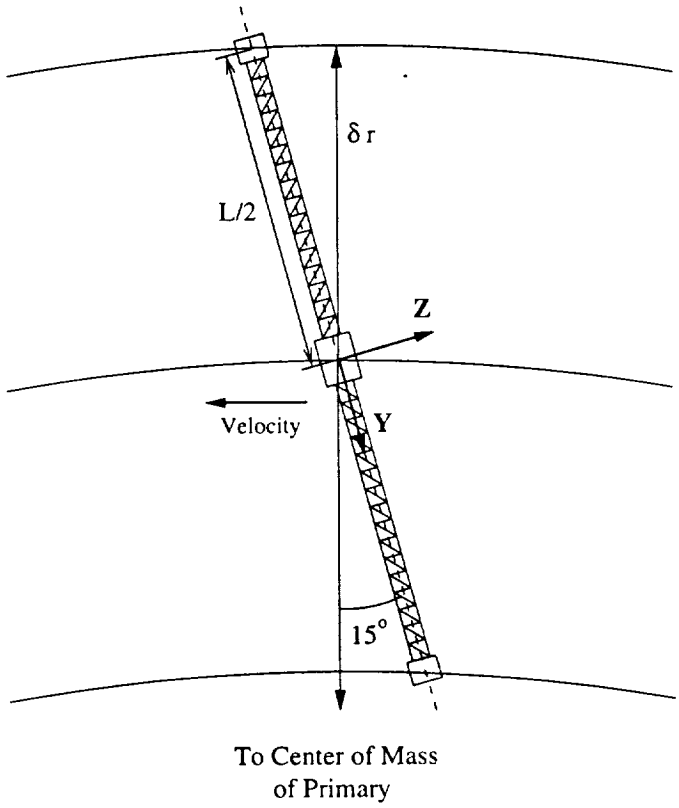


Figure 3-3: Reference Case Orientation

It is assumed that by holding the orientation constant throughout the mission, the propellant mass rate calculated is representative of the average over the entire

mission, which includes the propellant necessary for both disturbance rejection and interferometer reorientation. If the examination of a variety of orientations does not reveal significant differences in the propellant mass rate calculated, then this assumption is valid. It will be seen in Chapter 6 that this is the case. The calculation of the average propellant mass rate is presented in Section 4.1.4.

The rotation rate of the interferometer is assumed to be 1 revolution per hour for a 10 m baseline. This rate scales inversely as the square-root of the baseline which gives the following equation for the rotation rate $\omega_{rot}$ in radians per second

$$\omega_{rot} = \frac{2\pi}{3600}\sqrt{\frac{10}{L}}$$

where $L$ is the baseline.

This scaling matches the proposed rotation rates of SIM and Planet Finder. The Stellar Interferometry Mission has a proposed baseline of 10 m and a rotation rate of 180° in 30 minutes while the Terrestrial Planet Finder has a proposed baseline of 75 m and a rotation rate of 180° in 90 minutes.

## 3.3 High-Level Plant Modeling

The first level of plant modeling consists of the overall layout of the interferometer and includes the selection of the material and propellant used. Both the structurally connected and multiple spacecraft interferometer layouts are specified as a function of baseline. These layouts can then be used to calculate the equal dry mass point of the critical time plot. These layouts are also used to generate the structural transfer functions, $G_{zw}$, necessary to compute the performance as discussed in Section 3.1.

Sections 3.3.1 and 3.3.2 describe the modeling of the structurally connected and multiple spacecraft interferometers, respectively. Section 3.3.3 discusses the various propellants examined in this study.

### 3.3.1 Structurally Connected Interferometer

#### Overall Geometry

The overall geometry of the structurally connected interferometer is shown in Figure 3-4. The line of sight of the interferometer in Figure 3-4 is out of the plane of the page, along the $X$-axis.

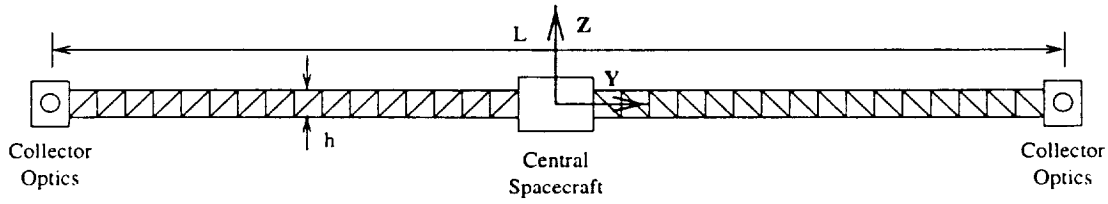


Figure 3-4: Overall Geometry of Structurally Connected Interferometer

At the center of the interferometer is the central spacecraft which houses the combining optics as well as most of the other subsystems necessary for the operation of the interferometer. The collecting optics are located at opposite ends of the connecting truss, which corresponds to a baseline of $L$. For long baselines, the length of the truss is approximately equal to the baseline. The height of the truss is denoted as $h$ in the figure. The depth of the truss is assumed to be equal to the height.

The truss is assumed to be composed of cubic bays with side length equal to $h$. Each bay consists of four longerons, four diagonal struts, and a square batten frame with one diagonal. Figure 3-5 shows a typical truss bay.

One way to characterize such a truss is to use the three independent parameters length, $L$, cross-sectional area, $A$, and radius of gyration, $r$, each a dimensional quantity. The method used in this work is to characterize the truss by one dimensional quantity, the length, $L$, and two non-dimensional quantities — the aspect ratio, $AR$, and the areal density, $\upsilon$.

The aspect ratio is defined as the ratio of the truss length to the truss height (or width, since the cross-section is square.)

$$AR = \frac{L}{h}$$

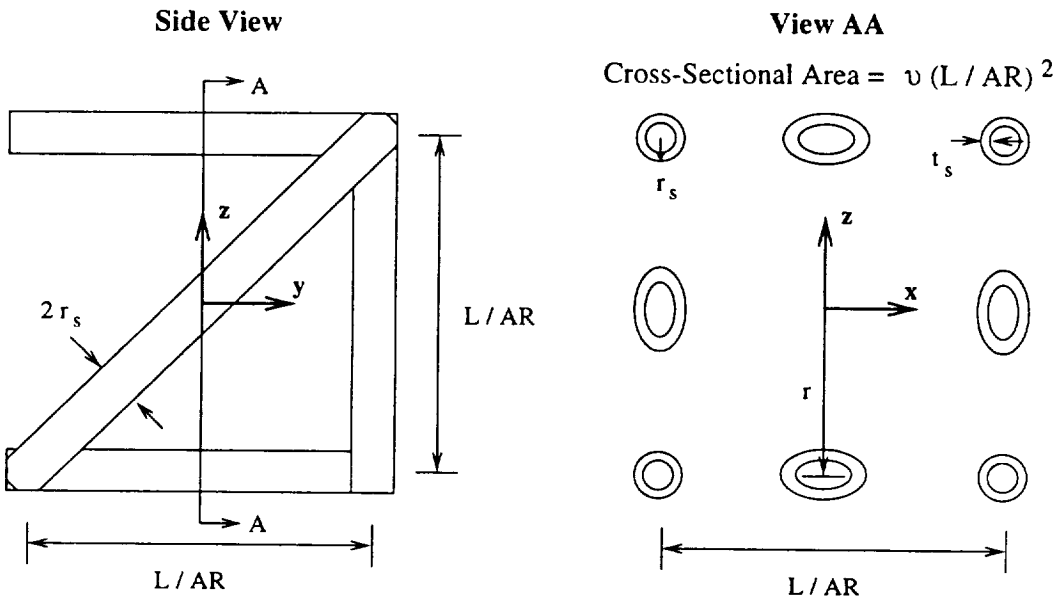


Figure 3-5: Typical Truss Bay

where $h$ is the height of the truss.

The areal density is a measure of the truss cross-sectional area as a fraction of the cross-sectional area of a solid beam with the same height and width as the truss. Hence, the total cross-sectional area of the truss is

$$A = \upsilon h^2 = \upsilon \left( \frac{L}{AR} \right)^2 \tag{3.5}$$

The area moment of inertia of the truss is calculated assuming only the four longerons contribute to the stiffness of the truss. Additionally, from Figure 3-5, the radius of gyration is assumed to be equal to half the height of the truss. Therefore,

$$I = \frac{A}{2} r^2 = \frac{\upsilon}{8} \left( \frac{L}{AR} \right)^4 \tag{3.6}$$

In order to maintain realistic values of the aspect ratio and areal density parameters, three actual trusses were used as a reference. These reference trusses are shown in Table 3.3. The Middeck 0-gravity Dynamics Experiment (MODE) was a deployable truss flown on STS-48 and STS-62 to study the dynamics of deployable truss

Table 3.3: Important Parameters of Example Trusses

| Parameter | MODE | SADE | ISIS | SCI Model |
|---|---|---|---|---|
| Length | 72 in | 385 in | 25 m | $10 - 1000$ m |
| Height | 8 in | 55 in | 0.3 m | - |
| Cross-Sectional Area | $0.12\,\text{in}^2$ | $3.5\,\text{in}^2$ | $7 \times 10^{-4}\,\text{m}^2$ | - |
| Aspect Ratio | 9 | 7 | 83 | $10 - 1000$ |
| Areal Density $\upsilon$ | $\frac{1}{530}$ | $\frac{1}{860}$ | $\frac{1}{130}$ | $\frac{1}{1000} - 1$ |

structures in zero-gravity [19]. The Structural Assembly Demonstration Experiment (SADE) was a proposed Space Shuttle experiment designed to test the assembly and deployment of structures in space [20]. The third truss was MIT's model of the design for JPL's proposed Interferometric Stellar Imaging System (ISIS) [7].

Also shown in Table 3.3 are the allowable ranges of the parameters for the SCI model used in this study. For each baseline, the aspect ratio is varied from 10 to 1000 and the areal density from 1/1000 to 1 to determine if there exists a minimum mass SCI that meets all performance requirements and constraints.

The mass of the truss can be calculated from

$$m_t = (8 + 5\sqrt{2}) L_s A_s \rho N \tag{3.7}$$

where $L_s$ and $A_s$ are the length and cross-sectional area of an individual strut calculated below, $\rho$ is the density of the truss material, and $N$ is the number of bays which, for cubic bays, is equal to the aspect ratio.

$$N = AR$$

The truss material is a trade parameter (T3) and two materials are examined — graphite/epoxy and aluminum. The relevant properties of each material are listed in Table 3.4. Graphite/Epoxy is the reference case material.

In addition to the truss mass, there are three concentrated masses in the SCI model — two at the tips and one at the center representing the mass of the collector

Table 3.4: Truss Material Properties

| Property | Graphite/Epoxy | Aluminum |
|---|---|---|
| Young's Modulus, $E$ (GPa) | 276 | 70 |
| Density, $\rho$ (kg/m$^3$) | 1744 | 2700 |
| Yield Strength, (MPa) | 1660 | 240 |
| Coefficient of Thermal Expansion, $\alpha$ (per °C) | $2 \times 10^{-6}$ | $22 \times 10^{-6}$ |

optics and the mass of the central spacecraft, respectively. The collector optics are assumed to have a mass of 30 kg apiece while the central spacecraft has a mass of 200 kg, which includes the combiner optics. The summation of these three masses equals the dry mass of all non-structural subsystems as discussed in Section 2.1.

$$m_{o,sci} = 2m_o + m_{cnt}$$

where $m_{o,sci}$ is the dry mass of all non-structural subsystems in Equation 2.1, and $m_o$ and $m_{cnt}$ are the masses of the collector optics and the central spacecraft, respectively.

The total dry mass of the SCI is then

$$m_{d,sci} = 2m_o + m_{cnt} + m_t \tag{3.8}$$

The mass moment of inertia of the central spacecraft is also modeled as a lumped parameter at the central node of the finite element model. The central spacecraft is assumed to have dimensions of 2.0 m × 2.5 m × 2.0 m which gives mass moments of inertia about the $x$- and $z$-axes of 171 kg·m$^2$ and about the $y$-axis of 133 kg·m$^2$. These moments of inertia will be denoted by $I_{xx,cnt}$, $I_{zz,cnt}$, and $I_{yy,cnt}$, respectively.

The projected side area of the truss, which is necessary for the calculation of the solar pressure and aerodynamic drag disturbance torques, can also be calculated by examining Figure 3-5.

$$A_t = 2(3 + \sqrt{2})L_s r_s N$$

where $r_s$ is the radius of an individual strut calculated in Section 3.3.1 below. Adding this area to the area of one face of the central spacecraft

$$A_{cnt} = 5\,\mathrm{m}^2$$

gives the total projected area of the SCI in both the $XY$- and $YZ$-planes.

$$A_{sci} = 2(3+\sqrt{2})L_s r_s N + 5 \tag{3.9}$$

These projected areas are equal because all interferometer dimensions in the $X$-direction have equal dimensions in the $Z$-direction. In other words, the height and depth of the truss are equal as are the height and depth of the central spacecraft. This area is used in Sections 4.1.2 and 4.1.3 to calculate the solar pressure and aerodynamic drag torques on the interferometer.

The overall mass moments of inertia of the interferometer are also needed to calculate the gravity gradient torque in Section 4.1.1 and to size the attitude control actuators in Section 3.4. The mass moments of inertia are

$$I_{xx} = \frac{1}{12}m_t L^2 + 2m_o L^2 + I_{xx,cnt} \tag{3.10a}$$

$$I_{yy} = \frac{1}{6}m_t \left(\frac{L}{AR}\right)^2 + I_{yy,cnt} \tag{3.10b}$$

$$I_{zz} = \frac{1}{12}m_t L^2 + 2m_o L^2 + I_{zz,cnt} \tag{3.10c}$$

where $I_{ii}$ is the mass moment of inertia about the $i$th axis of the interferometer.

### Strut Geometry

In order to enforce the constraints on minimum gage (C5), maximum stress (C6), and buckling (C7), the geometry of the individual struts that compose the truss must be modeled. The minimum gage constraint can be enforced immediately after the scaling of the strut is determined. The maximum stress and buckling constraints can only be imposed after the modeling of the internal plant, discussed in Section 3.4.

As can be seen from Figure 3-5, the length of one strut is equal to the length of one bay. Therefore,

$$L_s = \frac{L}{AR} \tag{3.11}$$

Additionally, the cross-sectional area of one strut must equal one-eighth the total cross-sectional area of the truss. Using Equation 3.5

$$A_s = \frac{1}{8} v \left(\frac{L}{AR}\right)^2 \tag{3.12}$$

Each strut is assumed to be a tube with radius $r_s$ and thickness $t_s$. Therefore, the strut area must equal

$$A_s = \pi(r_s^2 - (r_s - t_s)^2) \tag{3.13}$$

Setting Equations 3.12 and 3.13 equal to each other allows one to solve for the strut thickness given the radius

$$t_s = r_s - \sqrt{r_s^2 - \frac{v}{8\pi}\left(\frac{L}{AR}\right)^2} \tag{3.14}$$

This thickness must be greater than the minimum gage allowable, which is 0.5 mm (20 mils).

The minimum radius of a strut is assumed to scale from 1 mm for a 1 cm deep

truss to 1 cm for a 1 m deep truss. Therefore,

$$r_{s,min} = 10^{-2}\sqrt{\frac{L}{AR}} \tag{3.15}$$

As the cross-sectional area of the truss varies, the strut radius is assumed to be equal to this minimum radius and the thickness is scaled using Equation 3.14 to give the desired area. Note that there will be some minimum areal density for which the required thickness equals the minimum gage.

$$\upsilon_{min} = 8\pi(r_{s,min}^2 - (r_{s,min} - t_{s,min})^2)\left(\frac{AR}{L}\right)^2$$

which upon substitution of Equation 3.15 becomes

$$\upsilon_{min} = 8\pi t_{s,min}\left(\frac{AR}{L}\right)^2\left(t_{s,min} - 2\times 10^{-2}\sqrt{\frac{L}{AR}}\right) \tag{3.16}$$

Smaller areal densities result in the minimum gage constraint being violated.

There is also a maximum areal density for which the required thickness equals the radius of the strut.

$$\upsilon_{max} = 8\pi r_{s,min}^2\left(\frac{AR}{L}\right)^2$$

which upon substitution of Equation 3.15 becomes

$$\upsilon_{max} = 8\times 10^{-4}\pi\frac{AR}{L} \tag{3.17}$$

For larger areal densities, the individual struts are assumed to be solid rods and the radius is scaled to give the desired cross-sectional area.

$$r_s = \frac{L}{AR}\sqrt{\frac{\upsilon}{8\pi}} \tag{3.18}$$

The scaling of the radius and thickness as functions of baseline, aspect ratio, and

areal density are then

$$r_s = \begin{cases} 10^{-2}\sqrt{\frac{L}{AR}} & \upsilon \leq \upsilon_{max} \\ \frac{L}{AR}\sqrt{\frac{\upsilon}{8\pi}} & \upsilon > \upsilon_{max} \end{cases} \tag{3.19}$$

$$t_s = \begin{cases} 10^{-2}\sqrt{\frac{L}{AR}}\left(1 - \sqrt{1 - \frac{10^4 \upsilon L}{8\pi AR}}\right) & \upsilon \leq \upsilon_{max} \\ r_s & \upsilon > \upsilon_{max} \end{cases} \tag{3.20}$$

It must be noted that this scaling of the individual struts is only consistent with the modeling of the overall truss area moment of inertia, $I$, and the projected truss area, $A_t$, for a sparse truss. For trusses with large areal densities, this strut scaling causes physical interference between the struts. It will be seen, however, that the selection of the minimum-mass truss leads to a sparse truss so this logic problem can be ignored.

### Finite Element Model

The structurally connected interferometer is modeled in finite elements as a Bernoulli-Euler beam of length $L$ equal to the baseline. The finite element model is composed of ten beam elements. Each element has six degrees of freedom — two translations and one rotation at each end — which is consistent with constraining the motion of the interferometer to lie in a plane. Two of the elements have lengths equal to one strut, $L_s$, and are necessary for the thermal snap disturbance. The other eight elements are all equal in length and are much longer than the previous two. The length of these elements, $L_e$, is calculated from the relation

$$L = 8L_e + 2L_s$$

A representation of the finite element model of the structurally connected interferometer is shown in Figure 3-6. Figure 3-6 shows all the nodes and local degrees of freedom of the model with a schematic of the interferometer in the background.

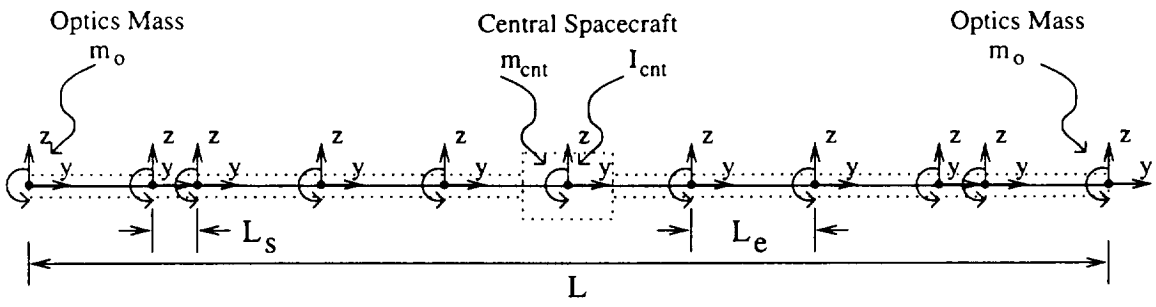


Figure 3-6: Finite Element Model of the Structurally Connected Interferometer

The cross-sectional properties of the finite-element beam are designed to give equivalent stiffness characteristics of the truss. In other words, the cross-sectional area, $A$, and area moment of inertia, $I$, of the beam must equal those of the truss.

The finite element mass and stiffness matrices are used in conjunction with the assumed structural modal damping to generate a state space model of the SCI in the standard form

$$\begin{aligned} \dot{\mathbf{q}} &= \mathbf{A}\,\mathbf{q} + \mathbf{B_w}\,\mathbf{w} \\ \mathbf{z} &= \mathbf{C_z}\,\mathbf{q} + \mathbf{D_{zw}}\,\mathbf{w} \end{aligned} \tag{3.21}$$

where $\mathbf{q}$ represents the modal coordinates of the system, $\mathbf{w}$ is the set of disturbance inputs, and $\mathbf{z}$ is the vector of performance outputs.

The system described by Equation 3.21 contains both rigid body and flexible modes and can be rewritten as

$$\begin{aligned} \begin{bmatrix} \dot{\mathbf{q}}_\mathbf{r} \\ \dot{\mathbf{q}}_\mathbf{f} \end{bmatrix} &= \begin{bmatrix} \mathbf{A_r} & \mathbf{0} \\ \mathbf{0} & \mathbf{A_f} \end{bmatrix} \begin{bmatrix} \mathbf{q_r} \\ \mathbf{q_f} \end{bmatrix} + \begin{bmatrix} \mathbf{B_{wr}} \\ \mathbf{B_{wf}} \end{bmatrix} \mathbf{w} \\ \mathbf{z} &= \begin{bmatrix} \mathbf{C_{zr}} & \mathbf{C_{zf}} \end{bmatrix} \begin{bmatrix} \mathbf{q_r} \\ \mathbf{q_f} \end{bmatrix} + \mathbf{D_{zw}}\,\mathbf{w} \end{aligned} \tag{3.22}$$

where the subscripts $\mathbf{r}$ and $\mathbf{f}$ refer to the rigid body and flexible modes, respectively. Only the first five flexible modes are kept in the model.

The structural transfer functions, $G_{zw}$, used to determine the response of the SCI

to the optical delay line, reaction wheel, and thermal snap disturbances are generated using the state-space model of Equation 3.22. As discussed in Section 3.1.2, only the flexible response to the thruster input is desired, so the structural transfer functions used with this disturbance are generated from the following state-space model which keeps only the flexible modes.

$$\begin{aligned} \dot{\mathbf{q}}_\mathbf{r} &= \mathbf{A_r}\,\mathbf{q_r} + \mathbf{B_{wr}}\,\mathbf{w} \\ \mathbf{z} &= \mathbf{C_{zr}}\,\mathbf{q_r} + \mathbf{D_{zw}}\,\mathbf{w} \end{aligned} \tag{3.23}$$

Both the passive and actuated structurally connected interferometers are modeled in the above fashion. The only difference in the modeling is that the passive truss is assumed to have 0.1% modal damping while the actuated truss is assumed to have 10% modal damping.

### 3.3.2 Multiple Spacecraft Interferometer

The MSI freeflyers are each modeled after the preliminary design of the New Millennium Interferometer [8, 21]. Each spacecraft is modeled as a cube with a side length of 1.7 m. The combiner spacecraft has a dry mass, $m_{comb}$, of 200 kg and the two collector spacecraft each have a dry mass, $m_{coll}$, of 125 kg. The combiner spacecraft is assumed to have mass moments of inertia about the $x$- and $z$-axes of 90 kg·m$^2$ and about the $y$-axis of 80 kg·m$^2$. The collector spacecraft are each assumed to have mass moments of inertia about the $x$- and $z$-axes of 60 kg · m$^2$ and about the $y$-axis of 55 kg·m$^2$.

The mass and geometry of the freeflyers does not scale with baseline. The summation of these three masses equals the total dry mass of the multiple spacecraft interferometer as discussed in Section 2.1.

$$m_{d,msi} = 2m_{coll} + m_{comb} \tag{3.24}$$

where $m_{d,msi}$ is the total dry mass in Equation 2.2. The equal dry mass point can be

calculated by equating Equation 3.8 with Equation 3.24.

The freeflyers are treated as rigid bodies. The structural transfer function used to compute the stochastic response of the central combiner spacecraft is just that of a mass equal to 200 kg. The state space representation of the Hill-Clohessy-Wiltshire equations described in Section 4.1.1 is used to calculate the performance of the collector spacecraft under the influence of the stochastic disturbances presented in Section 4.2. The Hill-Clohessy-Wiltshire equations describe the relative motion of bodies in neighboring orbits.

### 3.3.3 Propellant

The propellant used for attitude control and station keeping of the structurally connected and multiple spacecraft interferometers is one of the trade parameters (T4). Specific impulse, $I_{sp}$, varies with propellant and determines the mass of propellant required. The various propellants examined in this study and their specific impulses are listed in Table 3.3.3 [22]. Also given in Table 3.3.3 are the assumed maximum attitude control thrusts for each propellant taken from Larson and Wertz [17] and Olin Aerospace [18]. Hydrazine is the reference case propellant.

Table 3.5: Properties of Various Propellants

| Propellant | $I_{sp}$ (seconds) | Maximum Thrust (N) |
|---|---|---|
| Cold Gas ($N_2$) | 60 | 1 |
| Hydrazine ($H_2O_4$) | 210 | 25 |
| Pulsed Plasma Thrusters (PPT) | 1000 | $5 \times 10^{-3}$ |

### 3.3.4 Summary of High-Level Plant Modeling

The previous three subsections (Sections 3.3.1 – 3.3.3) described the high-level modeling of the structurally connected and multiple spacecraft interferometers. Figure 3-7 shows the block diagram of the steps performed. The numbers in parentheses refer to equation numbers in this chapter while blocks in **bold** indicate where trade space

parameters are input, imposed constraints are checked, or comparison metrics are calculated.

Many assumptions were presented in the high-level modeling of the structurally connected and multiple spacecraft interferometers. Table 3.3.4 summarizes the important assumptions in the baseline designs of these two configurations.

Table 3.6: Baseline Structural Parameters

| Structural Parameter | | Baseline | |
|---|---|---|---|
| | | SCI | MSI |
| Central Spacecraft Dimensions | | $2.0 \times 2.5 \times 2.0$ m | - |
| Freeflyer Dimensions | | - | $1.7 \times 1.7 \times 1.7$ m |
| Collector Mass | | 30 kg | 125 kg |
| Combiner Mass | | 200 kg | 200 kg |
| Collector Moments of Inertia | $I_{xx}$ | - | 60 kg·m$^2$ |
| | $I_{yy}$ | | 55 kg·m$^2$ |
| | $I_{zz}$ | | 60 kg·m$^2$ |
| Combiner Moments of Inertia | $I_{xx}$ | 171 kg·m$^2$ | 90 kg·m$^2$ |
| | $I_{yy}$ | 133 kg·m$^2$ | 80 kg·m$^2$ |
| | $I_{zz}$ | 171 kg·m$^2$ | 90 kg·m$^2$ |
| Structural Damping Ratio | Passive | 0.1% | - |
| | Actuated | 10% | |

After the overall geometries of the interferometers have been determined, the equal dry mass point of the critical time plot can be calculated (M1) and the maximum dry mass (C1) and minimum gage (C5) constraints can be checked. Additionally, these high-level models are necessary to calculate the attitude disturbances in Section 4.1.

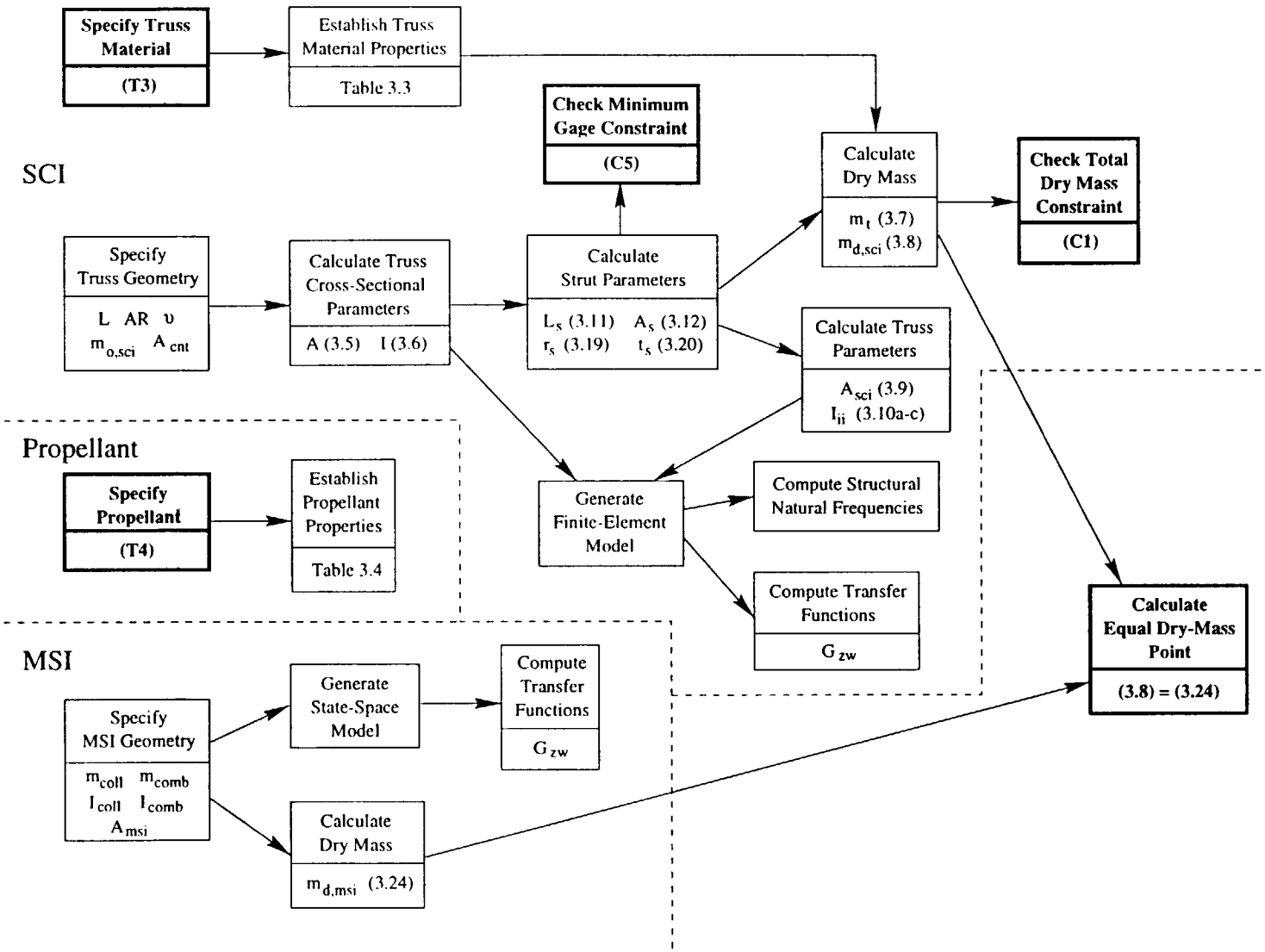


Figure 3-7: High-Level Plant Modeling Block Diagram

## 3.4 Internal Plant Modeling

The second level of plant modeling consists of the modeling of the internal subsystems of the interferometer. For this study, this consists of the sizing of the attitude control actuators necessary to counter the attitude disturbances described in Section 4.1. Thrusters are necessary to compensate for the differential motion associated with the multiple spacecraft interferometer while, in this study, either thrusters or reaction wheels can be used to overcome the disturbance torques on the structurally connected interferometer. The decision to use attitude control thrusters or reaction wheels is one of the trade parameters of this study (T5).

The sizing of the attitude control thrusters is presented in Section 3.4.1 while the sizing of the reaction wheels is described in Section 3.4.2. Block diagrams showing the steps performed to model the internal plant are presented in Figures 3-13 and 3-14 for the structurally connected and the multiple spacecraft interferometers, respectively.

### 3.4.1 Attitude Control Thrusters

If thrusters are used as the primary source of attitude control, there are two possible methods to size them. Either the thrusters are sized to be able to counteract the external disturbances, or the thrusters are sized to be able to meet the slew requirements of the instrument. Typically both the thruster size necessary to reject the disturbances and the thruster size necessary to satisfy the slew requirements are calculated. These two sizes are then compared and the larger is selected as the design thruster size. This is the procedure followed in this work.

The sizing of the thrusters refers to the determination of four parameters — the thrust $F_t$, the thrust firing time $t_t$, the period of the thrust cycle $\Delta t_t$, and the duty cycle $\xi_t$. Only three of these parameters are independent since the duty cycle is defined as the ratio of thrust firing time to the thrust cycle period.

$$\xi_t = \frac{t_t}{\Delta t_t} \tag{3.25}$$

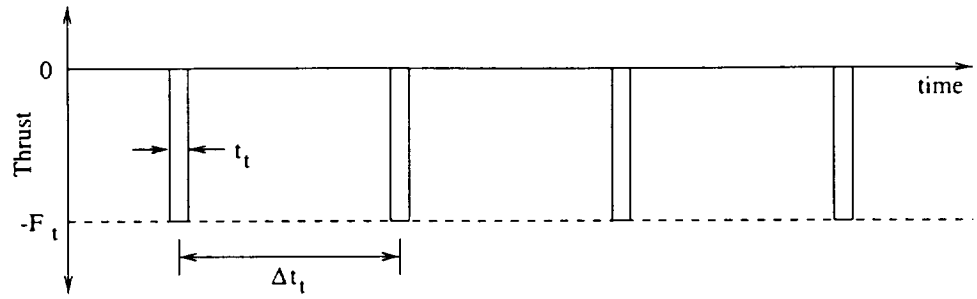


Figure 3-8: Sample Thrust Firing Sequence for Disturbance Rejection

Figure 3-8 shows the relation of these four parameters for a sample thruster firing sequence for disturbance rejection. The bandwidth of the attitude control system in Hz is defined to be

$$f_{acs} = \frac{1}{\Delta t_t} \tag{3.26}$$

The thrusters modeled in this study are assumed to always fire in pairs and to exert either a pure rotation about, or a pure translation of, the center of mass of the spacecraft. These pure rotations and translations are ideal models and are normally not physically realizable because of the misalignment or mismatch of the thrusters. This non-ideal coupling of rotational and translational motion is ignored in this work.

### Thruster Sizing for Disturbance Rejection

The derivation of thruster sizing for disturbance rejection presented in this section closely follows that of London [22]. The derivation is presented for a constant force disturbance, $F_d$, acting on a mass, $m$, which causes linear motion. It is desired to maintain the displacement of the mass within a deadband of amplitude $x_{db}$ ($2x_{db}$ peak-to-peak). The duty cycle is assumed to be $\xi_t$ and the thruster force, $F_t$, and frequency $f_{acs}$ are to be determined. Figure 3-9 shows the thrust and displacement profiles as a function of time for this derivation.

By the conservation of momentum principle, the total impulse imparted to the spacecraft by the thrusters during the period of thrusting must equal the impulse

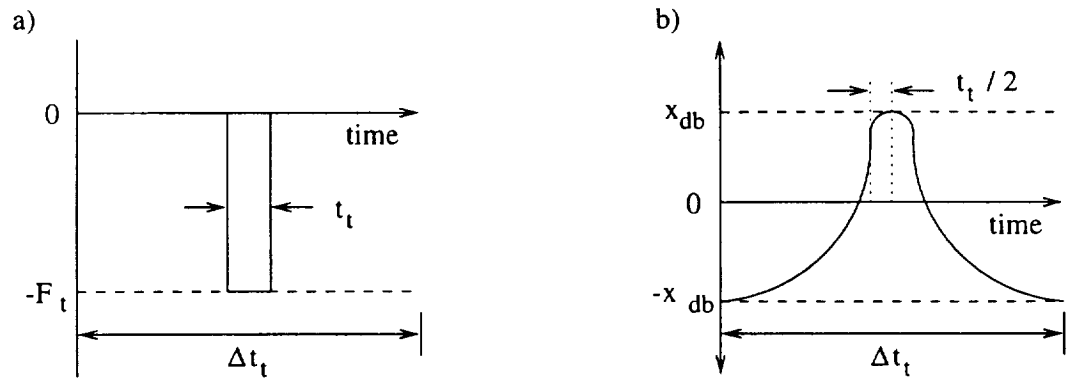


Figure 3-9: Plots of a) Thrust and b) Displacement vs Time for Disturbance Rejection Thruster Sizing

imparted by the disturbance force over the entire thrust cycle period.

$$2F_t t_t = F_d \Delta t_t$$

The factor of 2 is a result of the assumption that two thrusters fire simultaneously. Therefore, the thruster force required is

$$F_t = \frac{F_d}{2\xi_t} \tag{3.27}$$

Using the relation,

$$x(t) = x(0) + \dot{x}(0)t + \frac{1}{2}\ddot{x}t^2$$

the following expression can be written for the position at time $\Delta t_t/2$

$$x_{db} = -x_{db} + \frac{1}{2}\left(\frac{F_d}{m}\right)\left(\frac{\Delta t_t - t_t}{2}\right)^2 + \frac{F_d}{m}\left(\frac{\Delta t_t - t_t}{2}\right)\left(\frac{t_t}{2}\right) + \frac{1}{2}\left(\frac{F_d - 2F_t}{m}\right)\left(\frac{t_t}{2}\right)^2 \tag{3.28}$$

The time between firings can be found by the substitution of Equations 3.25 and 3.27

into Equation 3.28

$$\Delta t_t = \sqrt{\frac{16\, x_{db}\, m}{F_d(1-\xi_t)}} \tag{3.29}$$

Using the conservation of angular momentum and following the same procedure as above, equations similar to Equations 3.27 and 3.29 can be derived for a constant torque disturbance, $\tau_d$, acting on a body with a mass moment of inertia $I_{ii}$. The half-angle deadband is $\theta_{db}$.

$$2\tau_t = \frac{\tau_d}{\xi_t} \tag{3.30}$$

$$\Delta t_t = \sqrt{\frac{16\, \theta_{db}\, I_{ii}}{t_d(1-\xi_t)}} \tag{3.31}$$

The required force of one thruster is therefore

$$F_t = \frac{\tau_d}{2\xi_t L_t} \tag{3.32}$$

where $L_t$ is the moment arm of the thruster and is one of the trade parameters (T6) of this study.

### Thruster Sizing for Slew Requirements

The attitude control thrusters can also be sized to be able to meet the slew requirements of the instrument. As above, the derivation is presented for linear motion. The equivalent results for angular motion are presented after the derivation.

The desire is to move a mass $m$ initially at rest through a distance $x_{slew}$ and to bring it to rest in a total time of $t_{slew}$. Figure 3-10 shows the thrust and displacement profiles as a function of time for this derivation.

External disturbance forces are ignored and the thruster duty cycle is assumed to be $\xi_t$. The following equation relates the slew time, $t_{slew}$, to the thrust cycle

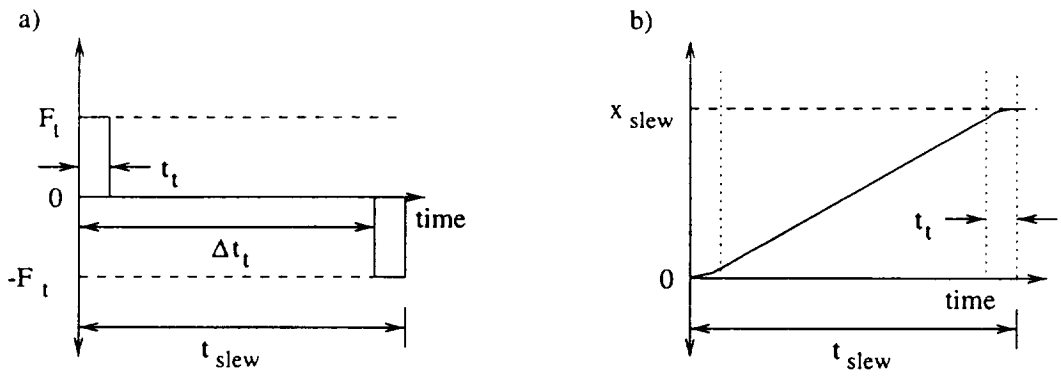


Figure 3-10: Plots of a) Thrust and b) Displacement vs Time for Slew Requirement Thruster Sizing

period, $\Delta t_t$.

$$t_{slew} = (1 + \xi_t)\Delta t_t \tag{3.33}$$

Therefore

$$t_t = \frac{\xi_t\, t_{slew}}{1 + \xi_t} \tag{3.34}$$

Classical mechanics and Figure 3-10 can be used to determine the following equation for the final displacement

$$x_{slew} = \left(\frac{2F_t}{m}\right) t_t^2 + \left(\frac{2F_t}{m}\right) t_t(t_{slew} - 2t_t) \tag{3.35}$$

The thruster force can be found by substitution of Equation 3.34 into Equation 3.35

$$F_t = \frac{(1 + \xi_t)^2}{\xi_t} \left(\frac{m x_{slew}}{2t_{slew}^2}\right) \tag{3.36}$$

The equivalent equation for the thruster force required to rotate a body of inertia $I_{ii}$ through an angle $\theta_{slew}$ in a time $t_{slew}$ is

$$F_t = \frac{(1 + \xi_t)^2}{\xi_t} \left(\frac{I_{ii}\theta_{slew}}{2L_t t_{slew}^2}\right) \tag{3.37}$$

### Selection of Thruster Size

In order to calculate the required thruster sizes for disturbance rejection using Equations 3.27 and 3.32, values for the duty cycle, deadband, and thruster moment arm must be specified. For this study, the duty cycle for disturbance rejection is assumed to be 1% and the deadband and thruster moment arm are trade parameters (T8 and T6, respectively). An orientation of 45° is assumed for the rotating interferometer in order to determine the magnitudes of the attitude disturbances used in the disturbance rejection calculations. The calculation of these disturbances is described in Section 4.1.

Similarly, in order to calculate the thruster sizes necessary to satisfy slew requirements using Equations 3.36 and 3.37, values for the duty cycle, slew distance, slew time, and thruster moment arm must be specified. For this study, the duty cycle for slew is assumed to be 10% and the thruster moment arm is a trade parameter (T6). If the thrusters are located at the tips, the moment arm is equal to one-half the baseline. If the thrusters are located on the central spacecraft, the moment arm is equal to one-half the length of the central spacecraft, which is 1.25 m.

$$\mathrm{L}_t = \begin{cases} 1.25\,\mathrm{m} & \text{located on central spacecraft} \\ L/2 & \text{located at tips} \end{cases}$$

It is also assumed that the interferometer must slew through an angle of 20° in a time of $\sqrt{L/100}$ hrs. This corresponds to a slew rate that scales from 19 minutes for a 10 m baseline to 3 hours and 10 minutes for a 1000 m baseline. The 20° slew angle requires a linear displacement of $(L/2)\sin 20°$ of the collector spacecraft of the multiple spacecraft interferometer. Table 3.7 summarizes the parameters required to size the thrusters.

The formal procedure for sizing the thrusters of the multiple spacecraft interferometer is presented in Figure 3-14 at the end of this chapter. The thruster size required for differential acceleration compensation / disturbance rejection is calculated from Equation 3.27. The thruster size required to satisfy the slew requirements

Table 3.7: Thruster Sizing Parameters

| Parameter | | Disturbance Rejection | Slew |
|---|---|---|---|
| Duty Cycle $\xi_t$ | | 1% | 10% |
| Deadband Amplitude (T8) | Linear $x_{db}$ (cm)<br>Angular $\theta_{db}$ (rads) | 0.25, **0.50**, 2.50<br>$\frac{x_{db}}{(L/2)}\left(\frac{1}{100}\right)\left(\frac{\text{m}}{\text{cm}}\right)$ | - |
| Slew | Displacement $x_{slew}$ (m)<br>Angle $\theta_{slew}$ (degs) | - | $(L/2)\sin\theta_{slew}$<br>20 |
| Slew Time $t_{slew}$ (hrs) | | - | $\sqrt{L/100}$ |

is calculated from Equation 3.36. These two thrust levels are then compared and the larger is set as the thruster design size. The maximum thrust constraint (C3) is enforced by comparing the thruster size to the maximum allowable thrust level given in Table 3.3.3.

A similar procedure is followed to size the thrusters of the structurally connected interferometer and is shown in Figure 3-13. The thruster size required for disturbance rejection is calculated from Equation 3.32. The thruster size required to satisfy the slew requirements is calculated from Equation 3.37. These two thrust levels are then compared and the larger is set as the thruster design size, $F_t$.

If the thrust required to reject disturbances is larger, this thrust level is substituted into Equation 3.36 to calculate the actual duty cycle for the slew maneuver. This duty cycle is then substituted into Equation 3.33 to calculate the actual thrust cycle period, $\Delta t_t$, of the slew maneuver.

On the other hand, if the thrust required to satisfy the slew requirements is larger, this thrust level is substituted into Equation 3.27 to calculate the actual duty cycle for disturbance rejection. This duty cycle is then substituted into Equation 3.31 to calculate the actual thrust cycle period of the disturbance rejection firings.

The shorter of the two thrust cycle periods calculated from Equations 3.33 and 3.31 for the design thruster size is then substituted into Equation 3.26 to calculate the bandwidth of the attitude control system, $f_{acs}$. This frequency is then compared to the fundamental structural frequency computed from the finite element model in

order to enforce the frequency constraint (C2). The maximum thrust constraint (C3) is enforced by comparing the thruster size to the maximum allowable thrust level given in Table 3.3.3.

### 3.4.2 Reaction Wheels

As with the sizing of the attitude control thrusters, there are two possible methods to size reaction wheels. Either the wheels are sized to be able to meet the momentum storage requirements (disturbance rejection over time), or the wheels are sized to be able to meet the slew requirements of the instrument. For all the reaction wheel cases examined in this work, meeting the slew requirements is the design driver of the wheel.

For this study, all spacecraft motion is constrained to the orbital plane so there is only one axis about which rotation can occur. This section describes the modeling of a reaction wheel with its spin axis coincident with this axis of rotation. It is assumed that all disturbance torques and slew maneuvers are about this axis.

The reaction wheel is modeled as a solid ring of stainless steel with a radius of gyration denoted by $r_w$. The cross-section is square and has a thickness equal to one-tenth the radius. Figure 3-11 shows the top and side views of the modeled wheel.

The torque exerted on the spacecraft by the reaction wheel is proportional to the angular acceleration of the wheel, $\alpha_w$ and its mass moment of inertia about the spin axis, $I_w$.

$$\tau_w = I_w \alpha_w \tag{3.38}$$

For the reaction wheel geometry of Figure 3-11,

$$I_w = m_w r_w^2 \tag{3.39}$$

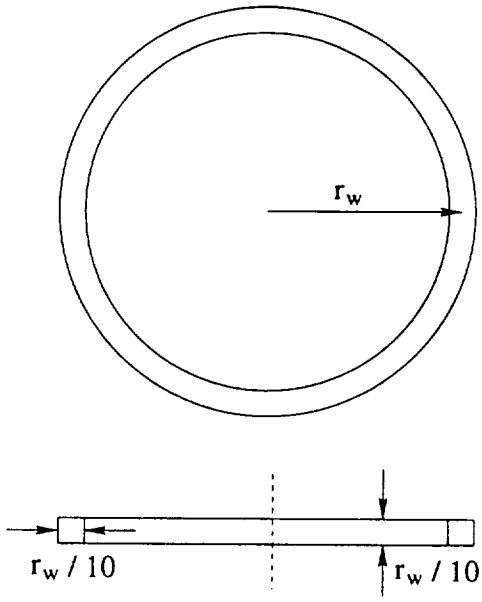


Figure 3-11: Model Reaction Wheel Geometry

where $m_w$ is the mass of the wheel and is calculated from

$$m_w = 2\pi\rho_w \frac{r_w^3}{100} \tag{3.40}$$

The density of the wheel, $\rho_w$, is 7860 kg/m$^3$.

With this geometry, there are two parameters that determine the size of the reaction wheel — the radius $r_w$ and the angular acceleration $\alpha_w$. An additional design constraint is placed on the reaction wheels to keep the maximum circumferential stress constant. For a wheel with the geometry of Figure 3-11 where the thickness is small compared to the radius, the maximum circumferential stress is

$$\sigma_{max} = \rho_w r_w^2 \omega_{w,max}^2 \tag{3.41}$$

where $\omega_{w,max}$ is the maximum rotational rate of the wheel. Given the maximum allowable stress, the Equation 3.41 defines the radius as a function of maximum wheel speed.

$$r_w = \frac{1}{\omega_{w,max}} \sqrt{\frac{\sigma_{max}}{\rho_w}} \tag{3.42}$$

Table 3.8: Major Characteristics of Hubble Reaction Wheel (HR195)

| Parameter | HR195 Value |
|---|---|
| Angular Momentum | 264.2 Nms |
| Output Torque | 0.7 Nm |
| Wheel Speed | 3000 RPM |
| Outside Diameter | 0.65 m |

Table 3.9: Derived Parameters of Hubble Reaction Wheel

| Parameter | Value |
|---|---|
| Rotor Density $\rho_w$ | 7860 kg/m$^3$ |
| Rotor Radius $r_w$ | 0.325 m |
| Moment of Inertia $I_w$ | 0.84 kgm$^2$ |
| Rotor Mass $m_w$ | 7.95 kg |
| Max Internal Stress $\sigma_{max}$ | 81.9 MPa |

Substitution of Equations 3.42 and 3.40 into Equation 3.39 gives the moment of inertia of the wheel as a function of maximum wheel speed and maximum circumferential stress.

$$I_w = \frac{2\pi}{100\omega_{w,max}^5}\sqrt{\frac{\sigma_{max}^5}{\rho_w^3}} \tag{3.43}$$

The maximum circumferential stress for this study was calculated by applying Equation 3.41 to the Hubble reaction wheels and is given in Table 3.9. Table 3.8 presents the major characteristics of these wheels, taken from Honeywell specification sheets [23].

Table 3.9 presents the values of parameters that were derived based on the values in Table 3.8 and assuming the radius of the rotor to be equal to one-half the outside diameter.

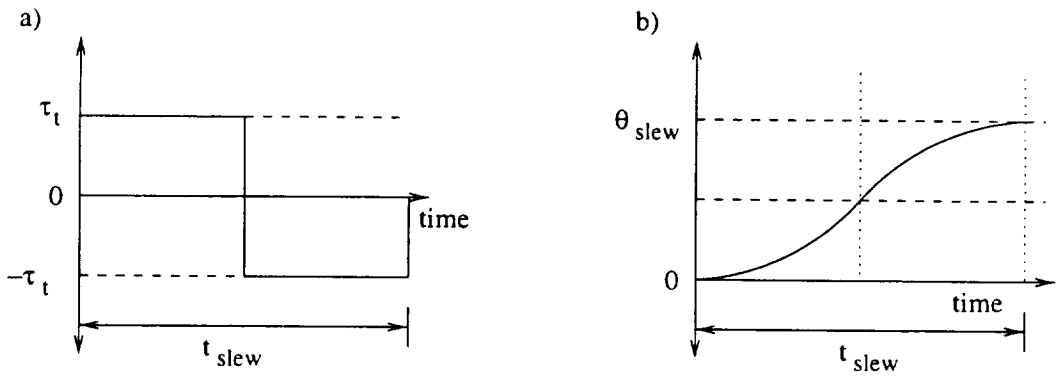


Figure 3-12: Plots of a) Thrust and b) Displacement vs Time for Slew Requirement Reaction Wheel Sizing

### SCI Reaction Wheel Sizing for Slew Requirements

As is the case with attitude control thruster sizing, reaction wheels can be sized either for disturbance rejection or for slew maneuvers. It is first necessary to determine which of these two requirements dominates the wheel size. In this study, reaction wheels are only considered for 1 AU solar orbits (See Table 2.3) where the slew requirements drive the design of the reaction wheels. For other orbits, such as LEO, the disturbance rejection requirement drives the reaction wheel design so the sizing process is different than that used in this study.

The same slew requirements as in Section 3.4.1 are used to size the reaction wheels. It is assumed that the wheel accelerates to its maximum speed in half the time of the slew and then decelerates at the same rate. The constant angular acceleration of the wheel during the slew maneuver is then

$$\alpha_{w,slew} = \frac{\omega_{w,max}}{t_{slew}/2} \tag{3.44}$$

Figure 3-12 shows the reaction wheel torque and spacecraft angular displacement profiles as a function of time for this derivation.

Using classical mechanics and Figure 3-12

$$\frac{1}{2}\theta_{slew} = \frac{1}{2}\alpha_{sci}\left(\frac{t_{slew}}{2}\right)^2 \tag{3.45}$$

where $\alpha_{sci}$ is the spacecraft angular acceleration during the slew maneuver. The spacecraft angular acceleration is related to the angular acceleration of the wheel by

$$\alpha_{sci} = \frac{I_w}{I_{xx}} \alpha_w \tag{3.46}$$

Upon substitution of Equations 3.46, 3.44 and 3.43 into Equation 3.45, the maximum wheel speed is

$$\omega_{w,max}^4 = \frac{\pi \, t_{slew}}{100 \, \theta_{slew} I_{xx}} \sqrt{\frac{\sigma_{max}^5}{\rho_w^3}} \tag{3.47}$$

This maximum wheel speed is substituted into Equation 3.42 to determine the radius of the reaction wheel. The mass of the reaction wheel is then calculated by substituting the radius into Equation 3.40. The maximum reaction wheel mass constraint (C4) is enforced by comparing this mass to the maximum allowable, 100 kg.

### Determination of Reaction Wheel Saturation Time

In order to reject the disturbance torques and maintain a constant orientation, the torque exerted by the reaction wheel must equal the total disturbance torque on the spacecraft. Denoting the time required for the wheel to reach its maximum rotational rate by $t_{sat}$ and substituting Equation 3.39 into the equation for the torque exerted by the reaction wheel, Equation 3.38, gives

$$\tau_d = m_w \, r_w^2 \, \frac{\omega_{w,max}}{t_{sat}} \tag{3.48}$$

The saturation time is solved for by substituting the maximum rotational rate from Equation 3.47 into the above equation.

$$t_{sat} = \frac{2\pi}{100 \, \omega_{w,max}^4 \, \tau_d} \sqrt{\frac{\sigma_{max}^5}{\rho_w^3}} \tag{3.49}$$

The reaction wheel must be desaturated after reaching the maximum rotational rate. Thrusters are used for desaturation in this study and the frequency at which

the thrusters fire is

$$f_{acs} = \frac{1}{t_{sat}}$$

This frequency is compared to the fundamental structural frequency computed from the finite element model in order to enforce the frequency constraint (C2).

The size of the thrusters necessary for desaturation is dependent on their location and the desaturation time. Recalling, however, that this is another conservation of angular momentum problem, the thruster size can be determined very easily. The total angular impulse imparted to the spacecraft by the thrusters during desaturation must equal the angular impulse imparted by the disturbance torque over the sum of the saturation and desaturation times.

$$2\tau_t \, t_{desat} = \tau_d(t_{desat} + t_{desat})$$

If the thrust duty cycle is defined as

$$\xi_t = \frac{t_{desat}}{t_{desat} + t_{desat}}$$

then the thruster force is given by Equation 3.32. In this study, it is assumed that if reaction wheels are selected as the primary source of attitude control, then the desaturation thrust duty cycle will be selected such that the required thrust size does not violate the maximum thrust constraint (C3).

### MSI Reaction Wheel Sizing

Reaction wheels for the multiple spacecraft interferometer are only sized for momentum storage since the reorientation maneuver must be done by thrusters. The maximum rotation rate is solved for by assuming the saturation time is ten times the thruster firing period, $\Delta t_t$, necessary for thrusters to reject the disturbance torque on

an individual spacecraft which is given by Equation 3.31.

$$t_{sat} = 10\sqrt{\frac{16\theta_{max,msi} I_{xx}}{\tau_d(1-\xi_t)}} \tag{3.50}$$

where $\theta_{max,msi}$ is assumed to be 1 arcmin, $I_{xx}$ is the spacecraft mass moment of inertia about the $x$-axis given in Table 3.3.4, and the disturbance rejection duty cycle, $\xi_t$), is 1%. This saturation time is then substituted into the following equation for the reaction wheel speed which is derived by rearranging Equation 3.49.

$$\omega_{w,max}^4 = \frac{2\pi}{100\, t_{sat}\, \tau_d}\sqrt{\frac{\sigma_{max}^5}{\rho_w^3}} \tag{3.51}$$

The reaction wheel mass constraint (C4) is checked but is never violated in this study since the disturbance torques on the individual freeflyers are very small.

### 3.4.3 Induced Internal Stresses

Once the attitude control components have been sized and located, it is necessary to determine whether the strut maximum stress (C6) and strut buckling (C7) constraints are met on the structurally connected interferometer. The torque exerted on the spacecraft by the firing of thrusters or the acceleration of the reaction wheel induces internal moments in the truss which must be transmitted as forces by the individual struts.

In order to estimate the forces within a strut, an approach based on statics is first used to estimate the maximum induced moment in the truss, which will be denoted $M_{max}$. It is assumed that this moment is transmitted only by the four longerons and not by the diagonals in a bay. From the bay geometry presented in Figure 3-5, the magnitude of the induced force in each of the four longerons is

$$F_{s,max} = \frac{M_{max}}{4}\left(\frac{2AR}{L}\right) \tag{3.52}$$

This force must be less than one-half the critical buckling load, $F_{crit}$

$$F_{crit} = \frac{\pi^2 E I_s}{L_s^2} \tag{3.53}$$

where $I_s$ and $L_s$ are the strut cross-sectional area moment of inertia and length, respectively, and are calculated in Section 3.3.1.

The maximum induced normal stress is

$$\sigma_{s,max} = \frac{F_{s,max}}{A_s} \tag{3.54}$$

and this stress must be less than one-half the yield stress of the strut material. This corresponds to 830 MPa and 120 MPa for graphite/epoxy and aluminum, respectively.

### Calculation of Maximum Induced Moment

The maximum moment is induced during a slew maneuver and is dependent on the form of attitude control and the location of the thrusters, as discussed below. The inertia of the interferometer is modeled as an opposing virtual force distributed along the truss and an estimate of the internal moment is made by balancing this inertial force with the externally applied forces.

If reaction wheels are used as the primary source of attitude control, the maximum moment is induced at the root of the truss and is approximately equal to

$$M_{max} \simeq \frac{1}{2}(I_{xx} - I_{cnt})\alpha_{sci} \tag{3.55}$$

where $I_{xx}$ is the total mass moment of inertia of the interferometer, $I_{cnt}$ is the mass moment of inertia of the central spacecraft, and $\alpha_{sci}$ is the angular acceleration of the interferometer during the slew maneuver and is calculated from Equation 3.46.

If thrusters are used as the primary source of attitude control, the maximum moment is dependent upon the thruster location. If the thrusters are located on the central spacecraft, the maximum moment is induced at the root of the truss and is also approximately given by Equation 3.55. In this case, the angular acceleration of

the interferometer, $\alpha_{sci}$, is given by

$$\alpha_{sci} = \frac{2F_t L_t}{I_{xx}} \tag{3.56}$$

where $F_t$ is the thruster force and $L_t$ is the thruster moment arm and is equal to one-half the length of the central spacecraft.

If the thrusters are located at the ends of the truss, the maximum moment is induced at the ends of the truss and is approximately

$$M_{max} \simeq \frac{F_t L}{2} - m_o \alpha_{sci} \left(\frac{L}{2}\right)^2$$

Upon substitution of Equation 3.56 for the angular acceleration of the interferometer, this becomes

$$M_{max} \simeq \left(1 - \frac{m_o L^2}{2I_{xx}}\right)\left(\frac{F_t L}{2}\right) \tag{3.57}$$

### 3.4.4 Summary of Internal Plant Modeling

The last part of this chapter presented the modeling of the internal plant, which for this study, consisted of the sizing of the attitude control actuators. Figure 3-13 shows the block diagram of the steps performed for the structurally connected interferometer while Figure 3-14 is the MSI block diagram. The numbers in parentheses refer to equation numbers in this chapter while blocks in **bold** indicate where trade space parameters are input, or imposed constraints are checked.

This level of plant modeling is necessary to ensure that all constraints on strength and realistic component size are met. The design of the internal plant also determines the size of onboard disturbances that could affect performance. The modeling of the disturbance spectra associated with the size of the attitude control actuators is discussed in the next chapter in Section 4.2.

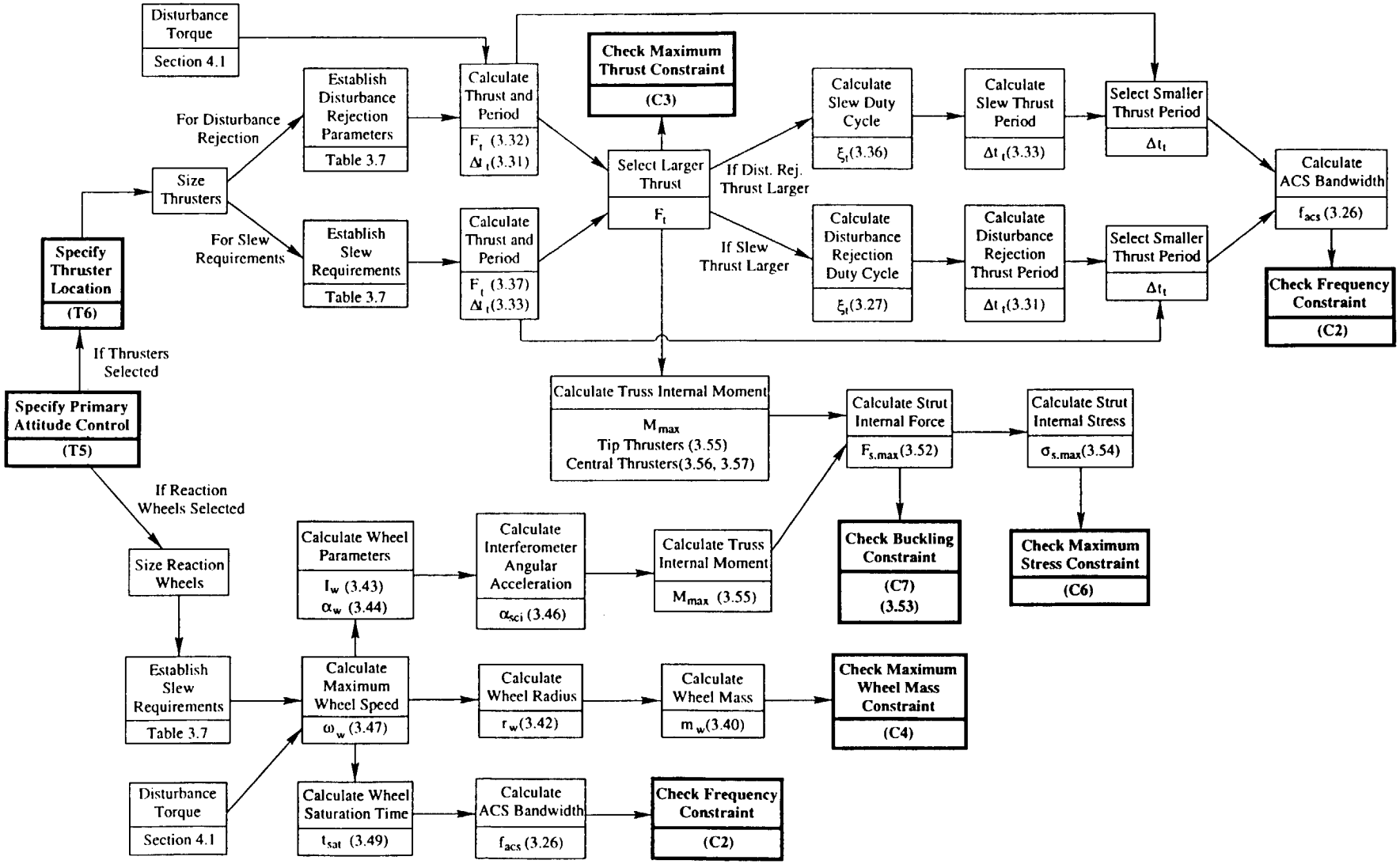


Figure 3-13: SCI Internal Plant Modeling Block Diagram

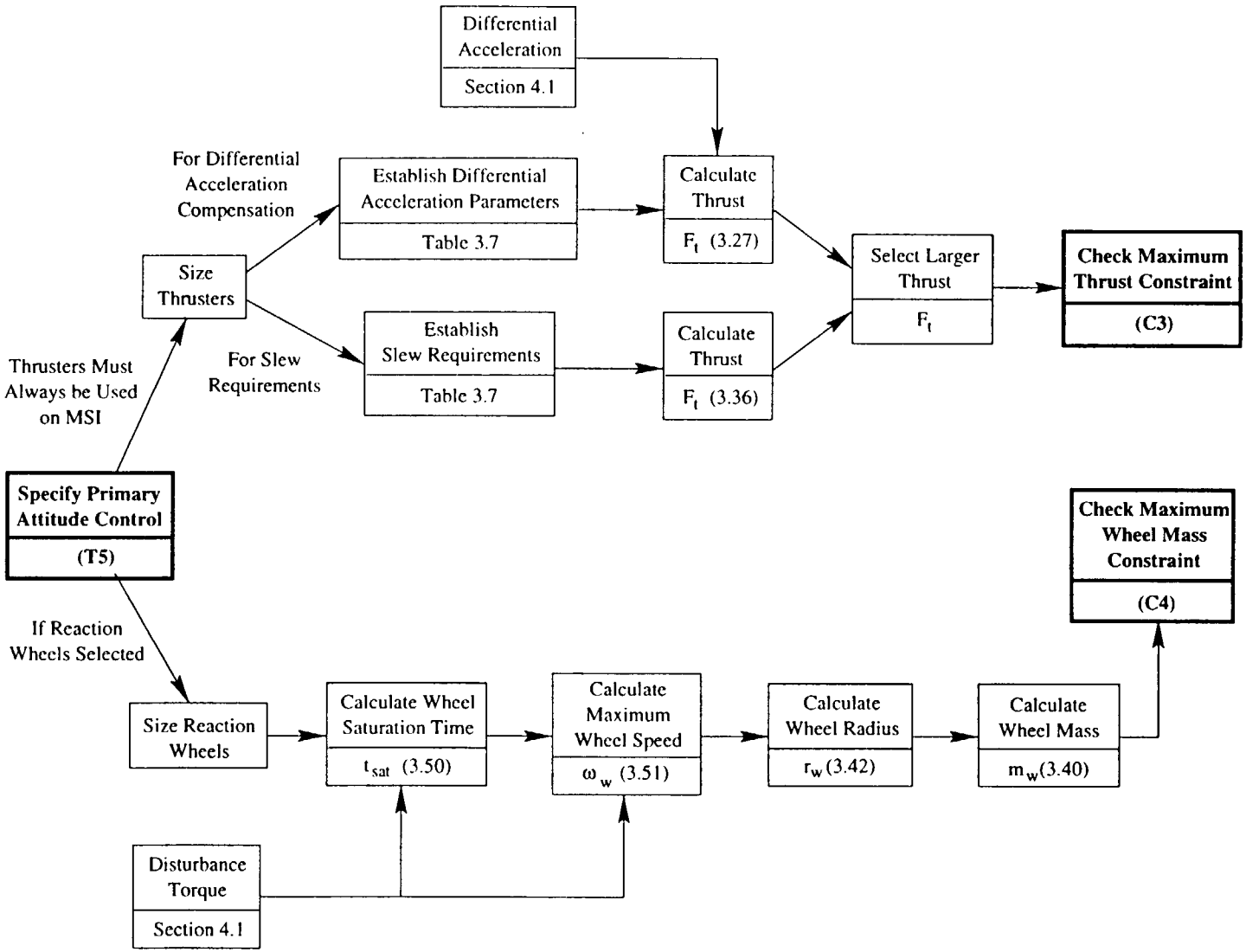


Figure 3-14: MSI Internal Plant Modeling Block Diagram

# Chapter 4

# Disturbance Modeling

As discussed in Chapter 2, two sets of disturbances are modeled in this formulation of the problem. The first set includes those disturbances that are the result of the interaction between the spacecraft and the space environment and affect its overall attitude. Hence, they are referred to as "external/attitude disturbances." The second set is referred to as "onboard disturbances" because these are disturbances that are generated by components onboard the plant.

Section 4.1 describes the three attitude disturbances used in this study — gravity gradient disturbances, solar radiation pressure and aerodynamic drag. The magnitude of these disturbances determines the size of the attitude control subsystem as well as the propellant mass rate. The calculation of this rate is described in Section 4.1.4. Section 4.2 describes the onboard disturbances that are input to the plant to determine if the performance requirement is met. These disturbances are thruster forces, reaction wheel mechanical noise, optical delay line reactuation force and thermal snap.

More information regarding spacecraft disturbances can be found in Hughes [24], French and Griffin [25], Larson and Wertz [17], and Eyerman and Shea [26].

## 4.1 External/Attitude Disturbances

The space environment interacts with spacecraft in many different ways ranging from the imposition of torques to the impingement of both charged and uncharged particles on the body. The main external disturbances of interest for the preliminary design of a space interferometer are those disturbances that cause some error in the overall pointing of the instrument. (This does not mean, however, that the other disturbances such as micro-meteoroidal impact and space radiation can be ignored or can not be catastrophic to the mission.)

For single, connected spacecraft, this pointing error is a result of the angular motion caused by the environmental disturbance torques. For a separated spacecraft interferometer, in addition to the disturbance torques on the individual spacecraft, the environment also causes relative motion between the spacecraft. In most cases, compensating for this relative motion requires more fuel than overcoming the individual disturbance torques, so these individual disturbance torques are neglected in this study. Figure 4-1 shows the attitude disturbance torques on the structurally connected interferometer while Figure 4-2 shows the relative motion between the spacecraft of the MSI caused by the external disturbance forces.

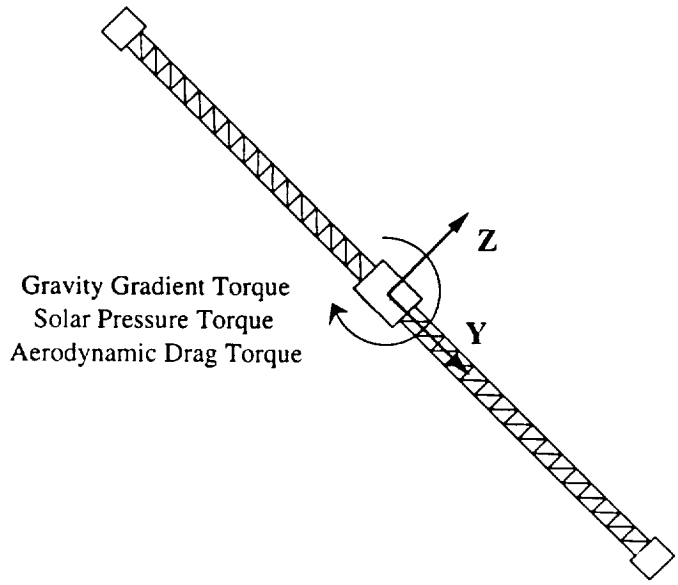


Figure 4-1: SCI Attitude Disturbance Torques

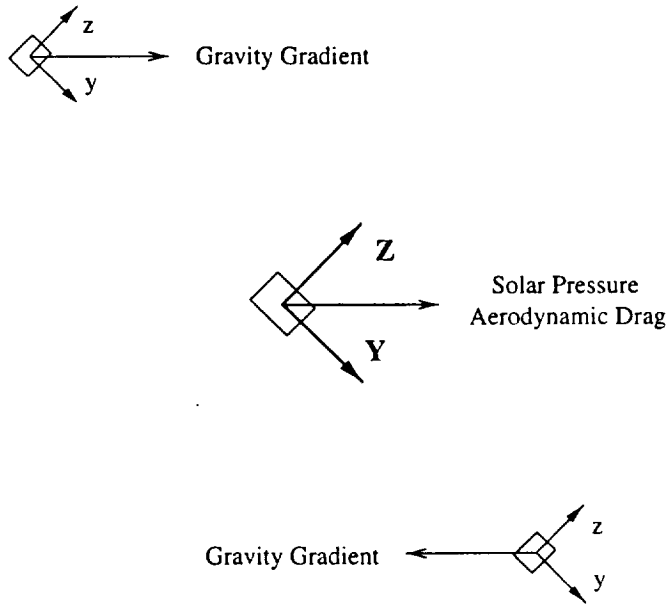


Figure 4-2: MSI Relative Motion Caused by External Disturbance Forces

Expressions for both the disturbance torque and relative motion forces are derived below. For this study, all disturbance torques are assumed to be about the $X$-axis of the interferometer and all relative motion is in the $YZ$-plane of the orbit.

### 4.1.1 Gravity Gradient Disturbances

The dependence of the gravitational force on distance causes a spacecraft in orbit about a star or a planet to experience a gradient of gravitational force. If a spacecraft is oriented such that none of its principal axes are aligned with this gradient, there is a net torque imposed on the spacecraft. (The star or planet about which the spacecraft orbits will be referred to as the "primary" throughout this chapter.) Similarly, there is relative motion between two bodies in orbit about a common primary (if the two bodies are not in the same orbit initially) because the body closer to the primary experiences a larger gravitational force.

### Gravity Gradient Torques on Individual Satellites

From Hughes [24], the expression for the resulting torque on a single spacecraft oriented as shown in Figure 4-3 is

$$\tau_g = \frac{3\mu}{R^3}\hat{u}_c \times \mathbf{I} \cdot \hat{u}_c$$

where $\mu$ is the gravitational constant of the primary body (equal to the product of the universal gravitational constant, $G$, and the mass of the body), $R$ is the distance between the centers of mass of the spacecraft and the primary, $\hat{u}_c$ is a unit vector from the center of mass of the spacecraft to the primary mass center, and $\mathbf{I}$ is the spacecraft inertia dyadic.

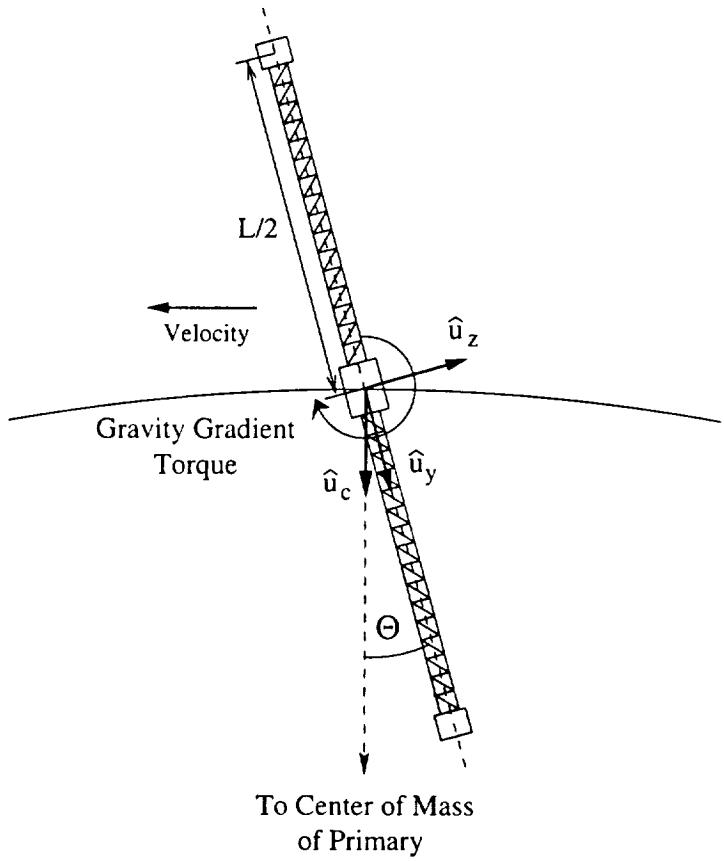


Figure 4-3: Spacecraft Orientation for Gravity Gradient Torque Calculation

Assuming principal axes for the spacecraft, the inertia dyadic is

$$\mathbf{I} = I_{xx}\hat{u}_x\hat{u}_x + I_{yy}\hat{u}_y\hat{u}_y + I_{zz}\hat{u}_z\hat{u}_z$$

where $\hat{u}_x, \hat{u}_y \text{and} \hat{u}_z$ are unit vectors in the directions of the principal axes and $I_{ii}$ is the mass moment of inertia about the $i$th axis.

This study only allows displacement in the plane of the orbit (the $YZ$-plane), so the disturbance torque is about the $X$-axis of the interferometer. The torque equation reduces to

$$\tau_g = \frac{3\mu}{2R^3}|I_{zz} - I_{yy}|\sin(2\theta) \tag{4.1}$$

where $\theta$ is the angle shown in Figure 4-3 and is one of the trade space parameters.

### Relative Motion of Satellites in Nearby Orbits

The linearized equations of relative motion between two satellites in orbit about a common primary are known as the Hill-Clohessy-Wiltshire Equations. These equations are valid for small separation distance between the satellites (small as compared to the distance to the center of the primary) and are derived in Prussing and Conway [27]. They are derived in a rotating reference frame with its origin at the center of mass of one of the satellites and rotating at the orbital rate of that spacecraft. See Figure 4-4. Note that it is not necessary that the origin of the reference frame be located at the center of mass of one of the satellites. Any orbit can be selected as the reference and the motion of each satellite relative to this rotating reference frame can be calculated using the Hill-Clohessy-Wiltshire Equations.

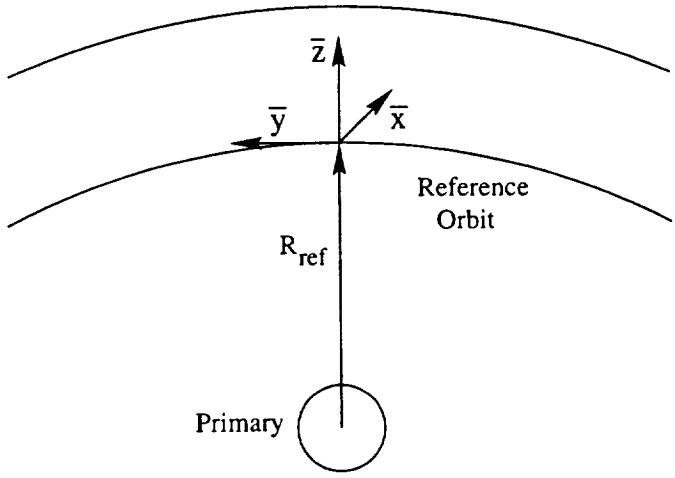


Figure 4-4: Axis System for Hill-Clohessy-Wiltshire Equations

The Hill-Clohessy-Wiltshire Equations are

$$\ddot{\bar{x}} = \Omega^2 \bar{x} + a_{\bar{x}} \tag{4.2a}$$

$$\ddot{\bar{y}} = -2\Omega \dot{\bar{z}} + a_{\bar{y}} \tag{4.2b}$$

$$\ddot{\bar{z}} = 3\Omega^2 \bar{z} + 2\Omega \dot{\bar{y}} + a_{\bar{z}} \tag{4.2c}$$

where $\bar{z}$ is radially outwards, $\bar{y}$ is in the direction of motion, and $\bar{x}$ is perpendicular to the orbit plane and completes the right-handed coordinate system. The accelerations $a_{\bar{x}}$, $a_{\bar{y}}$, and $a_{\bar{z}}$ are external accelerations acting on the second satellite in the $\bar{x}$, $\bar{y}$, and $\bar{z}$ directions. The orbital frequency, $\Omega$, of the reference satellite is calculated from the relation

$$\Omega^2 = \frac{\mu}{R^3}$$

Setting all derivatives equal to zero in Equations 4.2a-c gives the accelerations

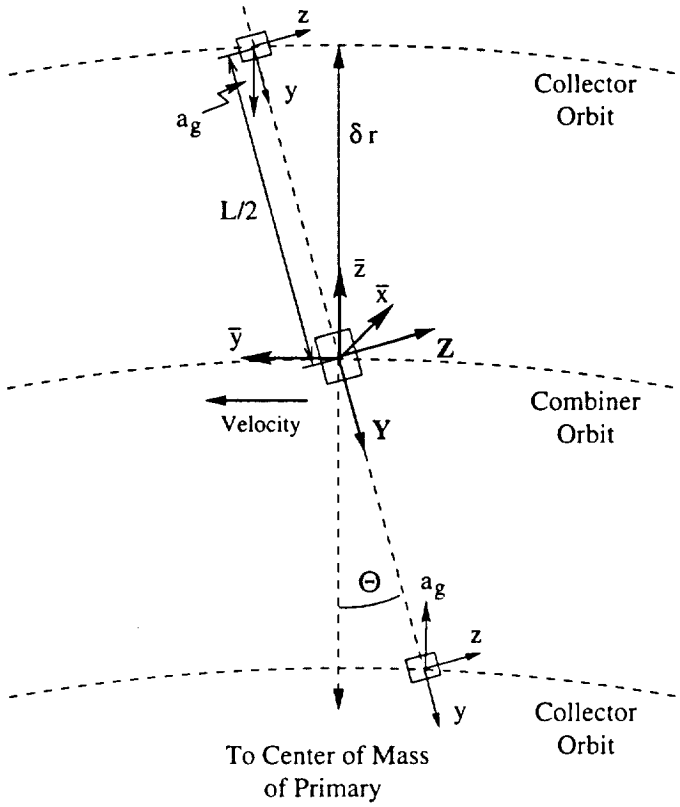


Figure 4-5: MSI Orientation for Hill-Clohessy-Wiltshire Equations

required to have no relative motion between the two satellites.

$$a_{\bar{x}} = -\Omega^2 \bar{x} \tag{4.3a}$$

$$a_{\bar{z}} = -3\Omega^2 \bar{z} \tag{4.3b}$$

In this study, the MSI is composed of three satellites that are collinear and share a common orbit plane, i.e. $\bar{x} = 0$, as shown in Figure 4-5. The central combiner spacecraft is taken as the reference so that each collector spacecraft requires an acceleration $a_g$ of magnitude

$$|a_g| = 3L\Omega^2_{combiner} \cos\theta \tag{4.4}$$

but in opposite radial directions.

### 4.1.2 Solar Radiation Pressure

Solar radiation consists of photons, which, upon impact with the surface of a spacecraft, exchange momentum with that surface. This momentum exchange leads to a net pressure force on the spacecraft. From Griffin and French [25], the solar pressure force on a spacecraft oriented as shown in Figure 4-6 is

$$\mathbf{F}_{sp} = \frac{P_s}{c} A_{\perp_{sp}} (1 + K)(-\hat{S})$$

where $P_s$ is the solar radiation intensity at the orbit of interest, $c$ is the speed of light, $K$ is the reflectance of the spacecraft (assumed to be 0.4), and $A_{\perp_{sp}}$ is the projected spacecraft area normal to the unit sun vector, $\hat{S}$.

For separated spacecraft of different masses, this force causes differential motion. (This is the primary NMI disturbance [21].)

If there is an offset between the center of the solar pressure and the center of mass of the spacecraft ($c_p/c_g$ offset), a disturbance torque is produced according to

$$\tau_{sp} = \mathbf{r}_{cpsp} \times \mathbf{F}_{sp}$$

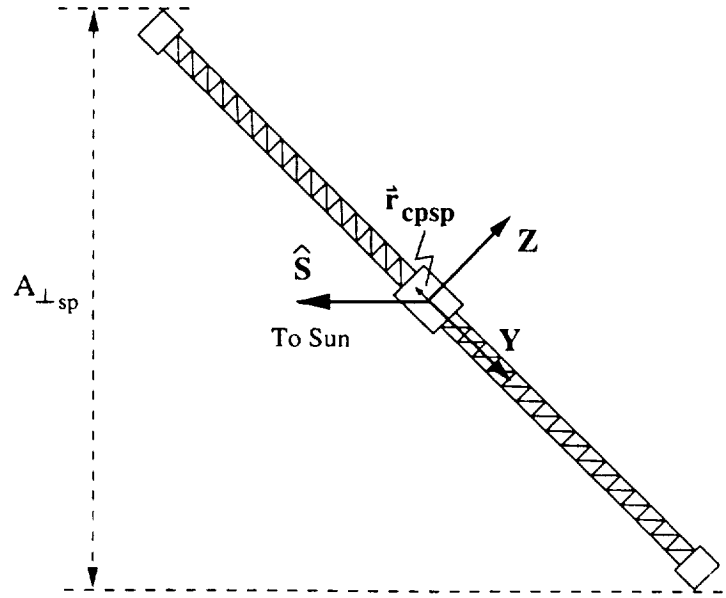


Figure 4-6: Spacecraft Orientation for Solar Pressure Force and Torque Calculation

For this study, the projected area of the SCI in Earth orbit is assumed to be equal to $A_{sci}$ from Equation 3.9 since the orientation of the interferometer relative to the Sun is unknown. In solar orbit, the interferometer has a constant orientation relative to the Sun so the projected area is equal to $A_{sci}\sin\theta$, where $\theta$ is the angle shown in Figure 4-3. The $c_p/c_g$ offset is assumed to be 0.05% of the baseline. Therefore, the solar pressure torque is

$$\tau_{sp} = 1.4\frac{P_s}{c}A_{sci}(5\times10^{-4}L) \tag{4.5}$$

in Earth orbit and

$$\tau_{sp} = 1.4\frac{P_s}{c}A_{sci}(5\times10^{-4}L)\sin\theta \tag{4.6}$$

in solar orbit.

A decision was made to scale the $c_p/c_g$ offset with baseline instead of keeping it a constant 5 cm. If the offset were constant, the solar torque would vary from ten times greater to ten times less than those calculated as the baseline increased from 10 m to 1000 m. It will be seen from the critical time plots in Chapter 6 that the critical range of baselines is greater than 100 m so the scaling of the $c_p/c_g$ offset is a worst-case scenario.

The projected area of each of the freeflyer spacecraft is equal to the area of one face, denoted by $A_{msi}$. Because the projected areas are equal, the solar pressure forces on each of the spacecraft are also equal. The resulting acceleration of the combiner spacecraft is less than the acceleration of either of the collector spacecraft because the combiner spacecraft is more massive. A compensatory acceleration equal to

$$a_{sp} = 1.4\frac{P_s}{c}A_{msi}\left(\frac{1}{m_{coll}} - \frac{1}{m_{comb}}\right) \tag{4.7}$$

must be applied to the combiner spacecraft to maintain the interferometer configuration. The solar torques on the individual satellites are neglected.

### 4.1.3 Aerodynamic Drag

In Earth orbit, spacecraft experience drag due to interaction with the particles composing the atmosphere. A detailed discussion of atmospheric drag can be found in Hughes [24]. The drag force exerted on a spacecraft oriented as shown in Figure 4-7 is

$$\mathbf{F}_{ad} = \frac{1}{2}\rho_a V^2 A_{\perp_{ad}} C_D(-\hat{V})$$

where $\rho_a$ is the atmospheric density, $V$ is the spacecraft velocity equal to $\Omega R$, $\hat{V}$ is a unit vector in the direction of the velocity in the reference frame of the spacecraft, $A_{\perp_{ad}}$ is the projected area of the spacecraft perpendicular to the velocity vector, and $C_D$ is the coefficient of drag and assumed to equal 2.

The aerodynamic drag torque is then

$$\tau_a = \mathbf{r}_{cpad} \times \mathbf{F}_{ad}$$

where $\mathbf{r}_{cpad}$ is the vector from the spacecraft center of mass to the center of aerody-

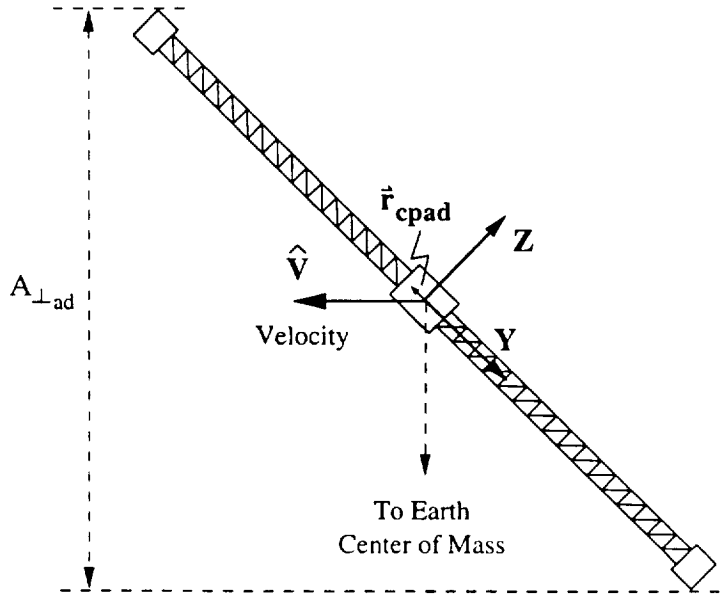


Figure 4-7: Spacecraft Orientation for Aerodynamic Drag Force and Torque Calculation

namic pressure.

The calculation of the drag torque and combiner acceleration to overcome drag are similar to the above calculations for the solar pressure disturbance. The same projected areas and $c_p/c_g$ offset are assumed. Therefore, the SCI aerodynamic drag torque is

$$\tau_{ad} = \rho_a(\Omega R)^2 A_{sci}(5 \times 10^{-4} L) \tag{4.8}$$

The required combiner acceleration is

$$a_{sp} = \rho_a(\Omega R)^2 A_{msi}\left(\frac{1}{m_{coll}} - \frac{1}{m_{comb}}\right) \tag{4.9}$$

Again, the individual drag torques are neglected.

### 4.1.4 Propellant Mass Rate Calculation

After the external disturbances have been calculated, the average propellant mass rate necessary to reject those disturbances can be computed. For a static orientation, this average rate is independent of the choice of attitude control actuators (thrusters or reaction wheels) or the thruster duty cycle. Reaction wheels eventually saturate and the angular momentum they have stored must be dumped, which in this study requires the firing of thrusters. When the thrusters fire, they must impart the same amount of angular momentum to the spacecraft as the external disturbance did in the period of time since the last firing. Since the propellant mass is dependent upon the momentum imparted, knowledge of the size and duty cycle of the thrusters is not needed to calculate an average rate. Only the thruster location is necessary to perform this calculation.

The mass of propellant necessary for a mission is dependent upon the total $\Delta V$ required. The relationship is given by the rocket equation

$$m_p = m_i(1 - e^{\Delta V/I_{sp}g})$$

where $m_p$ is the propellant mass, $m_i$ is the initial wet spacecraft mass, and $g$ is the gravitational acceleration of Earth at sea-level, $9.81\,\mathrm{m/s^2}$.

For small $\Delta V$, this can be approximated using a Taylor expansion and noting that $m_i \Delta V \simeq F_t t_t$

$$m_p \simeq \frac{F_t t_t}{I_{sp} g}$$

where $F_t$ is the thruster force and $t_t$ is the time of thrusting. It is this approximation that requires the constraint on propellant mass being less than or equal to 30% of the dry spacecraft mass.

Recalling that the momentum imparted by the thrusters must equal the momentum imparted by the disturbance and that the disturbance force acts over all time, the average propellant mass rate is

$$\dot{m}_p \simeq \frac{F_d}{I_{sp} g} \tag{4.10}$$

where $F_d$ is the disturbance force. The equivalent relation for a disturbance torque is

$$\dot{m}_p \simeq \frac{\tau_d}{L_t I_{sp} g} \tag{4.11}$$

where $\tau_d$ is the disturbance torque and $L_t$ is the thruster moment arm. Equations 4.10 and 4.11 are used to calculate the propellant mass rates for the separated spacecraft and structurally connected interferometers, respectively. Disturbance torques about the individual freeflyer spacecraft are neglected in the calculation of the MSI propellant rate because the propellant required to overcome them is much less than that required to compensate for the differential motion, at all orbits and orientations. For the MSI, the mass rate is calculated for each of the freeflyers and the rates are then summed. The 30% limit is placed on each individual spacecraft.

### Rotating Interferometers

For structurally connected interferometers that rotate, the average disturbance torque is calculated by integrating the disturbance torque magnitude over one rotation and dividing by the period of rotation. This average torque is then used in Equation 4.11. For reaction wheels, this method leads to a conservative estimate of propellant use because the wheels may not saturate.

For rotating multiple spacecraft interferometers, the differential acceleration of the central combiner spacecraft due to solar pressure and aerodynamic drag is the same as in the non-rotating case because the projected areas of the individual spacecraft are assumed to be the same as in the non-rotating case.. The thruster force required on one of the collector craft can be found by setting the desired motion as described by the Hill-Clohessy- Wiltshire equations to be sinusoidal at the rotation rate, $\omega$. Letting $\bar{x} = 0$, $\bar{y} = L\sin(\omega t)$ and $\bar{z} = L\cos(\omega t)$ in Equations 4.2a-c gives the following expressions for the required accelerations as a function of time. (Once again, no displacement is allowed out of the plane of the orbit.)

$$a_{\bar{x}} = 0$$

$$a_{\bar{y}} = -L(2\Omega\omega + \omega^2)\sin(\omega t)$$

$$a_{\bar{z}} = -L(3\Omega^2 + 2\Omega\omega + \omega^2)\cos(\omega t)$$

Integrating the magnitudes of these accelerations over one rotation and dividing by the period gives the average accelerations required in each direction.

$$\bar{a}_{\bar{y}} = \frac{2}{\pi}L(2\Omega\omega + \omega^2)$$

$$\bar{a}_{\bar{z}} = \frac{2}{\pi}L(3\Omega^2 + 2\Omega\omega + \omega^2)$$

An upper bound on the average total force required can be found by adding the average $\bar{y}$ and $\bar{z}$ accelerations and multiplying by the collector mass.

$$F_t \leq \frac{2}{\pi} m_{coll} L(3\Omega^2 + 4\Omega\omega + 2\omega^2) \tag{4.12}$$

Notice that if the rotation rate is much less than the orbital rate ($\omega \ll \Omega$) Equation 4.12 reduces to

$$F_t \leq \frac{4}{\pi} m_{coll} L\omega^2$$

which is slightly larger than the magnitude of the radial force required to maintain an object of mass $m_{coll}$ rotating at a rate equal to $\omega$. (The discrepancy is due to the fact that in this formulation the thrusters fire in the $\bar{y}$ and $\bar{z}$ directions as opposed to in the local $y$ directions. See Figure 4-5.) Only in Earth orbit where the rotation rate is not necessarily much less than the orbital rate do the thrusters also have to fight the gravity gradient.

### 4.1.5 Attitude Disturbance Summary

The first half of this chapter presented the equations for the attitude control force and torque disturbances that are used to size the ACS components as well as determine the average propellant mass rate. The assumptions made in modeling these disturbances are summarized in Table 4.1. Component sizing was discussed in the previous chapter (Section 3.4) while the calculation of the average propellant mass rate was described in Section 4.1.4.

Table 4.1: Summary of Attitude Disturbance Assumptions

| Disturbance Parameter | Assumption |
|---|---|
| Orientation of Interferometer | Contained within plane of orbit |
| SCI Projected Area | Earth orbit $A_{sci}$, Solar orbit $A_{sci} \sin\theta$ (eq. 3.9) |
| MSI Projected Area | One face = $1.7\,\mathrm{m}^2$ |
| SCI $c_p/c_g$ Offset | $5 \times 10^{-5} L$ |
| Coefficient of Drag | 2 |
| Reflectance | 0.4 |

## 4.2 Onboard Disturbances

The performance of an interferometer can be affected by the unwanted spacecraft vibrations caused by the operation of onboard components. Eyerman and Shea [26] provide an extensive overview of these internal disturbance sources. This study only includes those internal disturbances which are of primary importance for the operation of space interferometers. These include the components required to compensate for the external disturbances discussed above (reaction wheels and/or control thrusters), the motion of the optical delay line (ODL), and the thermal snap of the SCI truss.

After selecting those disturbances that will be active for a particular case (trade space parameter T7), models of the disturbance spectra are generated and input to the plant at the appropriate location, as shown in Figures 4-8 and 4-9.

All four disturbances can be input to the finite- element model of the SCI to determine their effect on tip displacement. Only the reaction wheel, and ODL reac-

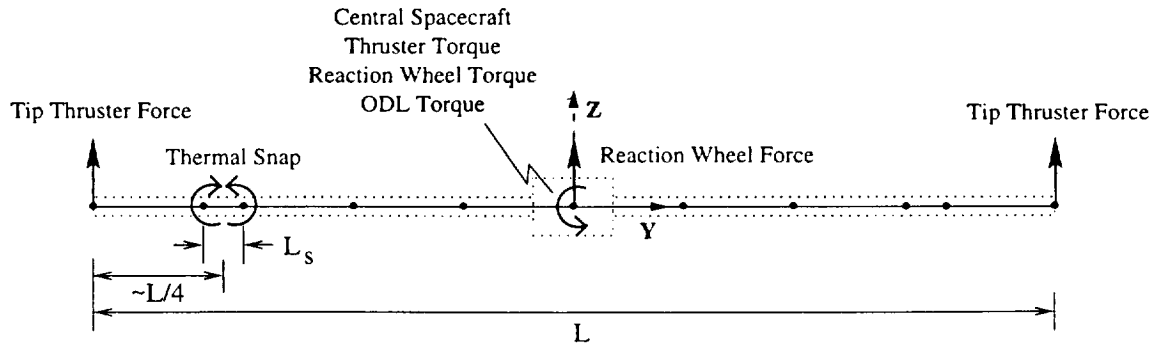


Figure 4-8: Location of Onboard Disturbances for SCI

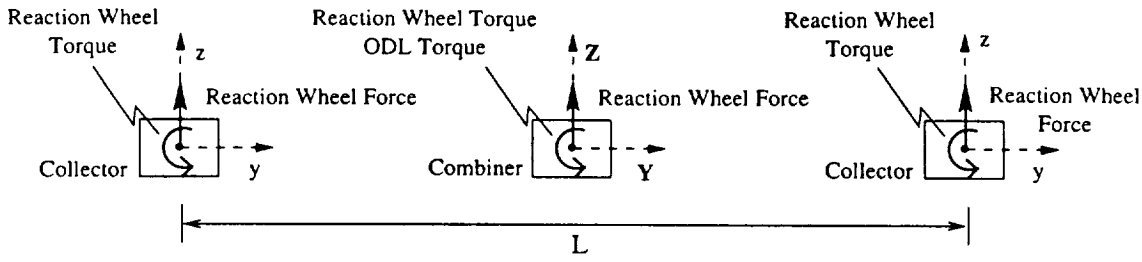


Figure 4-9: Location of Onboard Disturbances for MSI

tuation spectra can be input to the models of the freeflyers, but as will be seen in the next chapter, as expected, the onboard disturbances have negligible effect on the displacement of the spacecraft. This section discusses the modeling of these disturbance spectra.

### 4.2.1 Attitude Control Thrusters

The attitude control thrusters were sized in Section 3.4.1 and it was found that the time spectrum of the firing can be characterized by three parameters — the thruster force $F_t$, the time between firings $\Delta t_t$, and the length of time of one firing $t_t$ (or, equivalently, the duty cycle $\xi_t$). An overbound of the spectrum of this firing history is input as a disturbance to the finite-element model of the SCI that contains only flexible modes in order to determine the flexible response, as was discussed in Section 3.1.

It is important to note that this modeling of the attitude control thrusters in the frequency domain is done in an attempt to estimate the effects of the non-linear bang-bang control on the structurally connected interferometer without performing the numerically intensive calculation of the time history. In this study, the time history of the firing of the attitude control thrusters is assumed to be equal to that determined analytically for a rigid spacecraft with no flexibility and no other disturbance sources.

In reality, however, the spacecraft is not rigid and a real-time control system would determine when the thrusters fire. Sensors would be used to measure either the tip displacement or the orientation angle of the central spacecraft and whenever these measurements exceeded the allowable values, the thrusters would fire. This firing

history would most likely not be equal to the analytically predetermined time history used in this study.

If the flexible response and the effects of the other disturbances are small, the difference between the two thruster firing time histories will be small and the response calculated in this study will be representative of the real response. On the other hand, if the flexible response and the effects of the other disturbances are large, the difference between the two thruster time histories will be large and the response calculated in this study will not be representative of the real response.

This is not a problem in this study, however, because, as will be seen in Chapters 5 and 6, very few of the cases in this study have large enough responses to have performance limited designs. Furthermore, when the response is greater than the performance requirement as given by Equations 3.3 and 3.4, that particular SCI design is not allowed as the minimum-mass design.

In other words, every minimum-mass design of the SCI meets the performance requirement and therefore, has a small flexible response and response to the other disturbances. Consequently, the actual firing time history will only vary slightly from the firing time history used in this study. SCI designs that don't meet the performance requirement of this study, may be able to meet the performance requirement in reality by firing the thrusters at a greater rate than that assumed a priori in this study. This possibility is not examined, however.

A plot of a sample thruster spectrum and its overbound is presented in normalized units in Figure 4-10. The disturbance spectrum is a convolution of the spectrum of a single pulse of height $F_t$ and width $t_t$, which is flat out to a frequency of $1/t_t$ and then rolls off at $-1$, and the harmonics of the firing frequency $1/\Delta t_t$. The overbound has a 1-pole rolloff at $1/t_t$ and is scaled to have the same RMS force as the actual spectrum.

Keeping the overbound RMS equal to the spectrum RMS without modeling the spikes at the harmonics of the firing frequency means that the model will underestimate the effect on the performance at those frequencies. It will also overestimate the effect at other frequencies. The net error can be neglected for this initial system-level

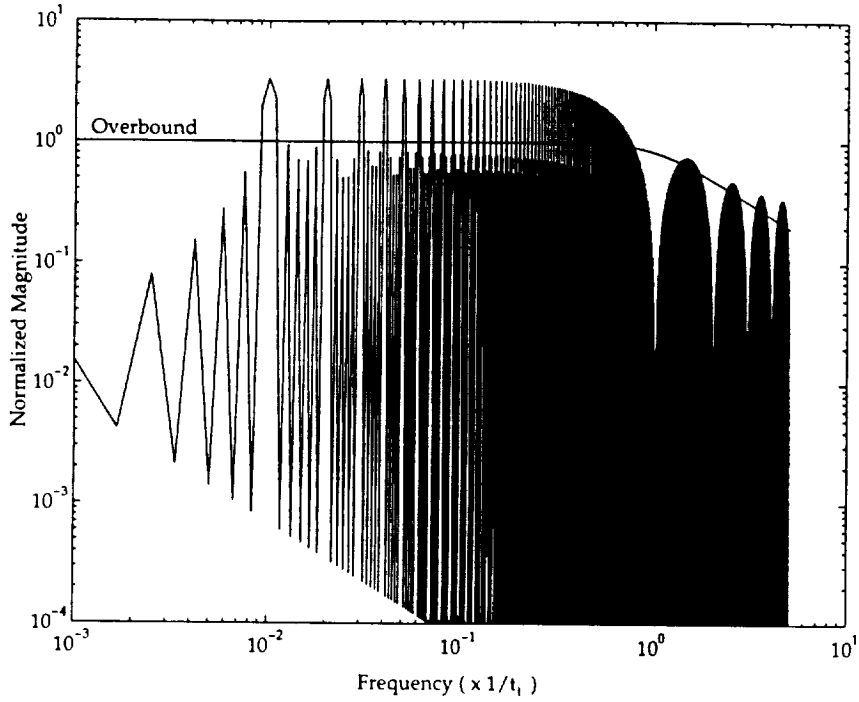


Figure 4-10: Sample Thruster Disturbance Spectrum and Overbound ($t_t = \Delta t_t/100$)

study.

For the structurally connected interferometer, this overbound of the disturbance spectrum is input as a force at the tips of the truss or as a moment about the central node dependent on the location of the thrusters, as shown in Figure 4-8. No thruster disturbance spectrum is input to the model if reaction wheels are used as primary attitude control actuators because it is assumed that the image-taking occurs between the thruster firings to dump the angular momentum stored by the reaction wheels. Therefore, these firings do not affect the performance of the interferometer.

As discussed in Section 3.1, no thruster disturbance spectrum is input to the model of the multiple spacecraft interferometer because the individual spacecraft are treated as rigid bodies which have a deterministic displacement known a priori from the specification of the deadband. The spectrum is not necessary to determine the individual spacecraft response to the thruster firings.

### 4.2.2 Reaction Wheels

Reaction wheels compensate for disturbance torques by spinning up and slowing down, exerting a compensatory torque on the spacecraft in so doing. However, due to imperfections in the design and construction of the wheel, variations in the torque about the spin axis as well as forces in the radial and axial directions are also imparted to the spacecraft.

Characterization of these disturbances was performed by Davis et al. [28] for the reaction wheels used on the Hubble Space Telescope. The spectrum of the disturbance had force spikes at various harmonics of the wheel speed with the amplitudes of these forces at low frequencies (less than 100 Hz) being proportional to the wheel mass and the square of the wheel speed.

Melody [29] then fit an analytical solution to this data to create a broadband disturbance spectrum for a Hubble-type wheel with a uniformly distributed random speed between 0 and $\omega_w$ revolutions per minute. A sample spectrum is shown in normalized units in Figure 4-11.

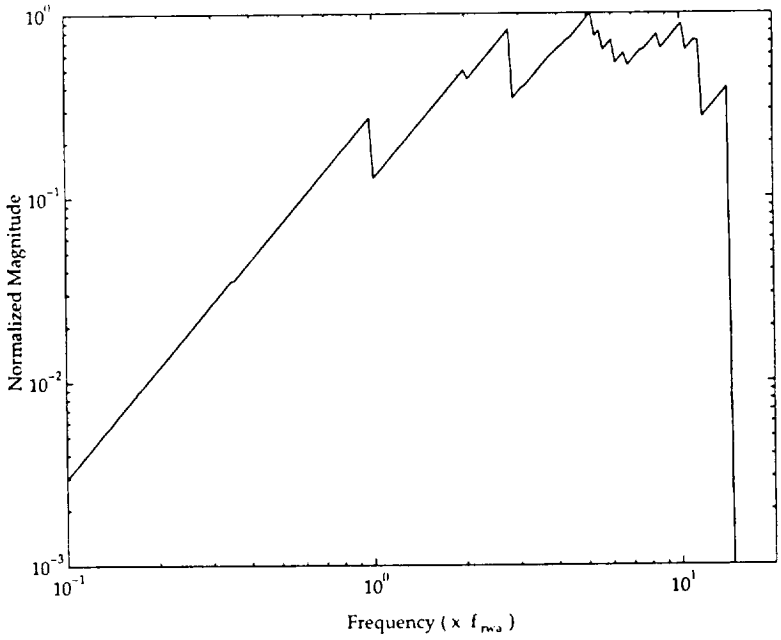


Figure 4-11: Sample Reaction Wheel Axial Force Disturbance Spectrum for Wheel Speeds Between 0 and $60 f_{rwa}$ RPM

In order to generate the disturbance spectra for the reaction wheels used in this study, the broadband Hubble spectra need to be scaled. (One disturbance spectrum is generated for each of the axial and two radial forces as well as for the disturbance torque.) This is to account for the difference in size and speed between the reaction wheels designed in Section 3.4.2 and the Hubble wheels.

To scale the spectra, the disturbance force amplitudes are assumed to be proportional to some radius of imbalance, as well as to the wheel mass and the square of the wheel speed. This radius of imbalance is assumed to scale linearly with the radius of the wheel. Therefore, since the scaling of the spectra with wheel speed is accounted for in Melody's model, the magnitude of the spectrum generated must be multiplied by $m_w r_w / m_{Hub}\, r_{Hub}$.

Similarly, the disturbance torque amplitudes are assumed to be proportional to the mass moment of inertia of the wheel about its spin axis. Hence, the magnitude of the torque spectrum must be multiplied by $m_w r_w^2 / m_{Hub}\, r_{Hub}^2$.

The broadband reaction wheel spectra generated by Melody's analytical model and scaled in the manner described above, are used directly in this study. The modeled spectra are not overbound. Additionally, all of the reaction wheel disturbances are assumed to be uncorrelated.

For the structurally connected interferometer, the reaction wheel spectra are input at the central node, as shown in Figure 4-8. It is assumed that there is one wheel for each of the $X$-, $Y$-, and $Z$-axes so one axial force spectrum and two radial force spectra are input in the $Z$-direction. No spectra are input in the $Y$-direction because it is the $Z$-direction response that is the most sensitive. If the performance requirement is met in the $Z$-direction, it will also be met in the $Y$-direction. The torque spectrum is input about the $X$-axis.

For the multiple spacecraft interferometer, one axial force spectrum and two radial force spectra are input in the $z$-direction of each spacecraft, as shown in Figure 4-9. The torque spectrum is also input about the $x$-axis.

### 4.2.3 Optical Delay Line Reactuation

The movement of the optical delay line to compensate for optical pathlength differences transmits forces to the structure at the points where the ODL is mounted. A model of these forces was created by Masters [7] for a 2 cm stroke ODL. The magnitude of the disturbance forces is dependent on the size and stroke of the ODL. In this study, the size and stroke of the ODL are taken to be constant over all baselines so this disturbance remains constant and does not scale.

The spectrum of the model reactuation disturbance force used in this study is shown in Figure 4-12. A worst case moment arm of 12.7 cm (5 in) between the location of the force and the center of mass of the spacecraft is assumed. (This is the same moment arm as was used in the ISIS study [7].)

For the structurally connected interferometer, the resulting torque is input about the central node of the finite-element model, as shown in Figure 4-8. For the multiple spacecraft interferometer, the resulting torque is input about the $x$-axis of the combiner spacecraft, as shown in Figure 4-9. Note that this disturbance, then, has no effect on the displacement performance of the combiner spacecraft. This is not a problem because in reality, the optical delay line would be designed to ensure that the forces it exerts on the spacecraft do not cause the performance requirement to be violated.

### 4.2.4 Thermal Snap

The differential thermal expansion of struts in the truss can cause the phenomenon of thermal snap to occur. When the force due to constrained thermal expansion in a strut becomes too large, there is some mechanism by which the strut slips and releases some of its energy into the rest of the truss structure. This energy release occurs through a nearly impulsive force, thereby causing unwanted vibrations in the structure.

Even though thermal snap has been observed to occur for many years, the mechanism by which it occurs is unknown. The model proposed by Kim [30] claims the

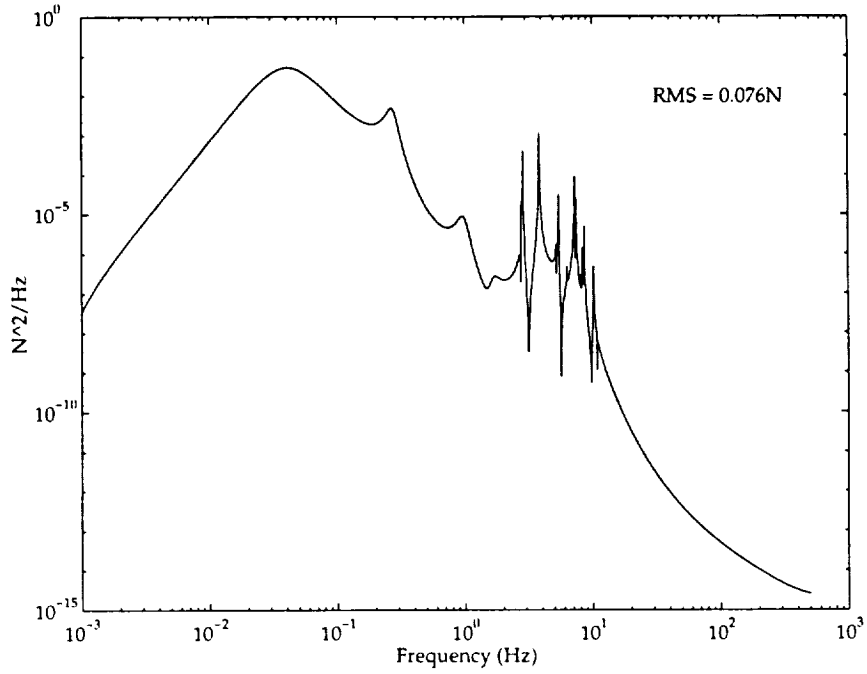


Figure 4-12: Optical Delay Line Disturbance Force Spectrum

magnitude of the force imparted to the rest of the structure is equal to the difference between the static and dynamic friction forces at the location of the slip.

$$F_{sn} = F_{stat} - F_{dyn}$$

For lack of experimental determination of the force imparted to the rest of the structure, three different values for the thermal snap force are used in this study — 10%, 1%, and 0.1% of the buckling load of one of the struts of the truss. Therefore,

$$F_{sn} = n\frac{\pi E I_s}{L_s} \tag{4.13}$$

where $n$ is the fraction of the buckling load (one of 0.1, 0.01, or 0.001), $E$ is the modulus of elasticity, $I_s$ is the cross-sectional area moment of inertia of the strut and $L_s$ is the strut length. The scaling of a strut is described in Section 3.3.1.

The rate at which thermal snap occurs depends on the thermal and stiffness properties of the strut as well as on the orbit and orientation of the spacecraft. This study assumes as a worst-case that the thermal snap occurs at a frequency of 1 Hz.

The thermal snap frequency will be denoted by $f_{sn}$. The time history of the force exerted on the structure is shown in Figure 4-13.

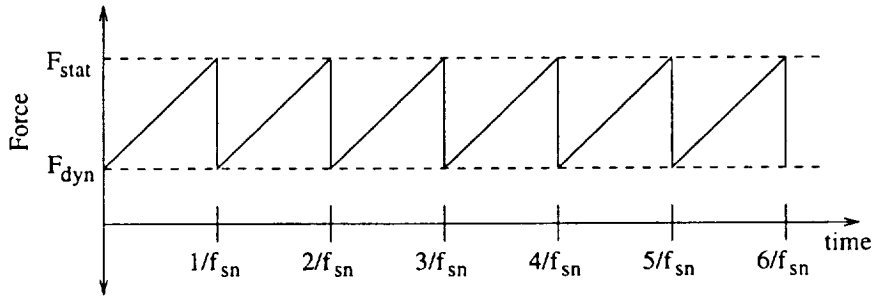


Figure 4-13: Sample Time Profile of Thermal Snap

The spectrum of this time history is then overbound by setting the RMS force of the overbound equal to the RMS force of the time history. Both the disturbance spectrum and its overbound are shown in normalized units in Figure 4-14. The overbound rolls off at $-1$ after the snap frequency.

The overbound of the disturbance spectrum is converted to a moment by multiplying by half the truss height, which is the distance of one strut from the neutral

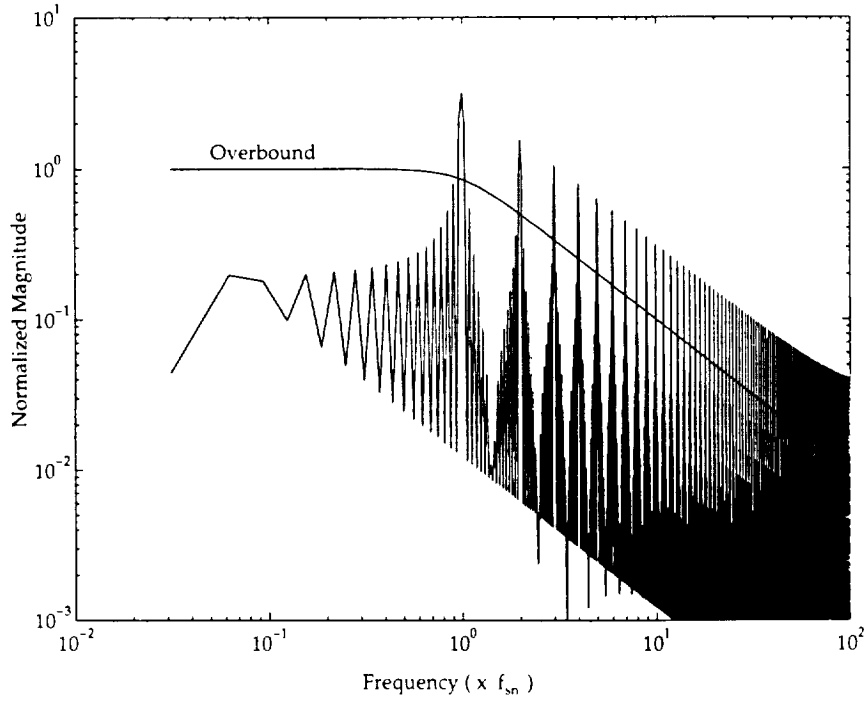


Figure 4-14: Sample Thermal Snap Disturbance Spectrum

axis of the truss. This disturbance is then input to the SCI finite-element model as shown in Figure 4-8. A pair of opposite moments are input at the two nodes located a distance $L/4$ from the tip of the truss. Thermal snap is not a disturbance for the multiple spacecraft interferometer.

### 4.2.5 Onboard Disturbance Summary

The second half of this chapter discussed the modeling of the disturbance spectra of the four onboard disturbances that are used in this study — attitude control thrusters, reaction wheels, optical delay line reactuation, and thermal snap. These disturbances are input to the plant to determine their effects on the performance of the interferometer.

Overbounds of the disturbance spectra of the attitude control thruster and the thermal snap models are input to the model of the structurally connected interferometer. The scaled, broadband disturbance spectra generated by Melody's analytical model of the reaction wheels [29] and the spectrum of the optical delay line reactuation modeled by Masters [7] are input to the models of both the SCI and MSI. Figures 4-8 and 4-9 show where these spectra are input to the models of the SCI and MSI, respectively.

The selection of the disturbances that are input to the plant is one of the trade space parameters (T7). The effect of these disturbances on the performance of the interferometer is discussed in the next two chapters.

# Chapter 5

# Reference Case Results

This chapter presents the results of the reference case. The reference case is a non-rotating interferometer in orbit about the sun at 1 AU and oriented at 15° from the stable gravity gradient orientation. Attitude control is provided by hydrazine thrusters located at the tips of the interconnecting truss which is made of graphite/epoxy. The onboard disturbances are the thrusters and the ODL reactuation. The absolute displacement amplitude of the collector and combiner optics is specified to be 0.50 cm.

Results for both passive and active structurally connected interferometers are presented in this chapter. This chapter uses the passive SCI case to demonstrate how the minimum mass SCI is calculated as a function of baseline and how the critical time plots are generated. This passive SCI case is also used to illustrate and explain the various plots that characterize the design of the interferometer.

The first step in calculating the critical time plot consists of the determination of the minimum mass structurally connected interferometer. Section 5.1 introduces the passive baseline case and Section 5.2 presents the three-dimensional surface plots that are used to determine if there exists a minimum mass SCI that meets all performance requirements and constraints. Section 5.3 then presents some sample calculations of the minimum mass configuration for various baselines.

The final minimum mass design of the passive truss is presented and explained in Section 5.4 and the MSI freeflyer design is described in Section 5.5. The critical time plot is generated from these designs and is presented in Section 5.6. Finally,

the structurally active SCI is discussed in Section 5.7. This section also describes the differences between the passive and active SCI designs.

## 5.1 Introduction to the Passive Reference Case

The determination of the minimum mass structurally connected interferometer that meets all the performance requirements and constraints requires considerable calculation. Ten logarithmically spaced aspect ratios between 10 and 1000 and areal densities between 1/1000 and 1 are specified giving a total of 100 possible combinations for the truss geometry for each baseline. For each of these combinations, the performance and the parameters necessary to enforce the constraints (such as total dry mass, attitude control component size, internal truss force, etc.) are calculated as functions of baseline using the appropriate equations in Chapters 3 and 4.

As examples of these calculations, the plots of total dry mass (Equation 3.8) and strut thickness (Equation 3.20) for a truss with an aspect ratio of 600 and an areal density of 1/100 are presented in Figures 5-1 and 5-2. In each figure, the dashed line is the constraint value.

From Figure 5-1, it can be seen that for this combination of aspect ratio and areal density, the total dry mass constraint of the interferometer (C1) is violated for all baselines greater than 548 m, at which the mass exceeds the limit of 15,400 kg. For short baselines less than 50 m, the total dry mass is set by the masses of the central spacecraft and the collector optics, which are denoted by $m_{cnt}$ and $m_o$ in Equation 3.8. Beyond 150 m, the truss mass is dominant and the $L^3$ dependence of this mass for a constant areal density and aspect ratio can be seen. (The $L^3$ dependence is a result of the substitution of Equations 3.11 and 3.12 into Equation 3.7.)

Figure 5-2 shows the strut thickness as a function of baseline as calculated by Equation 3.20. The minimum gage constraint (C5) is violated for all baselines *less* than 48 m, at which the gage drops below the limit of 0.5 mm. The kink in the curve between 100 and 200 meters is due to the fact that at a baseline of 150 m, the maximum areal density of Equation 3.17 is equal to 1/100. For baselines longer than 150 m,

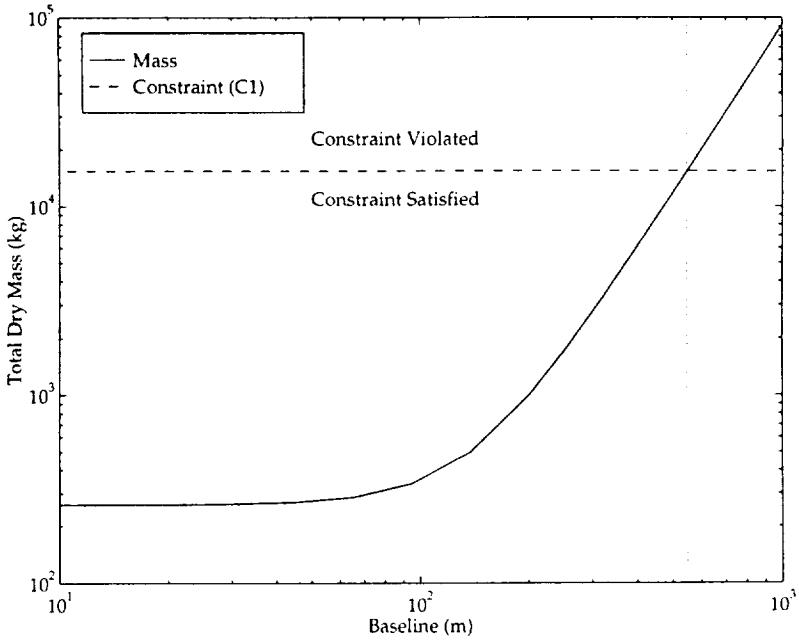


Figure 5-1: Total Dry Mass vs Baseline for an Aspect Ratio of 600 and an Areal Density of 1/100

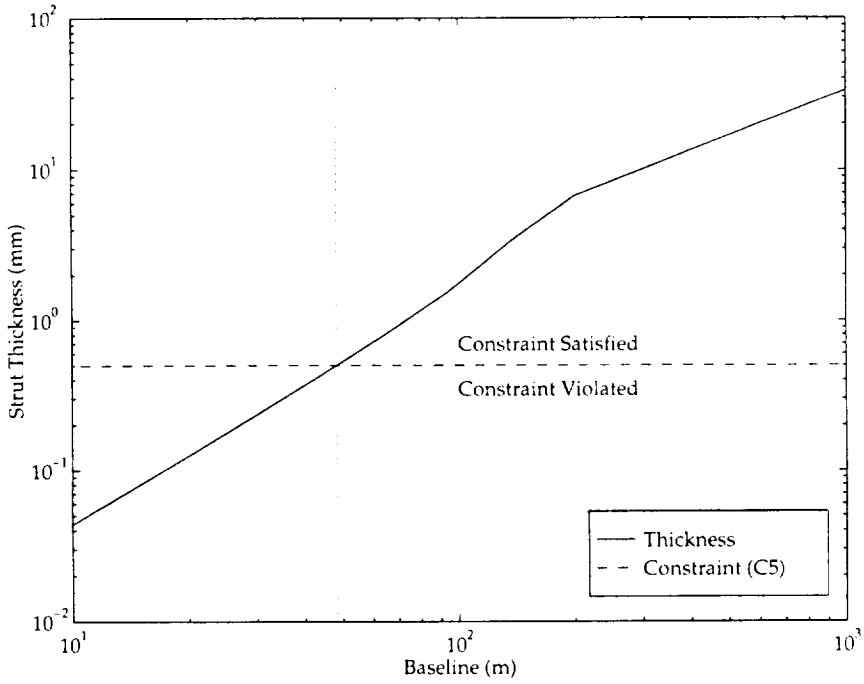


Figure 5-2: Strut Thickness vs Baseline for an Aspect Ratio of 600 and an Areal Density of 1/100

the maximum areal density of Equation 3.17 is less than 1/100 so the strut is a solid rod. For baselines shorter than 150 m, the maximum areal density of Equation 3.17 is greater than 1/100 so the strut has a thickness given by Equation 3.20.

For completeness, the remaining constraint and performance plots of the sample truss with an aspect ratio of 600 and an areal density of 1/100 are presented in Figures 5-3 through 5-7. In each figure, the dashed line is the constraint value.

Figure 5-3 shows the first truss natural frequency as a function of baseline as calculated from the finite-element model generated in Section 3.3.1. The first structural frequency of the interferometer is plotted as the solid line while the dash-dot line is the attitude control bandwidth. The first natural frequency must be at least one decade above this bandwidth, and this constraint (C2) is represented by the dashed line. Even though the natural frequency does not violate this constraint for this particular combination of aspect ratio, 600, and areal density, 1/100, it is apparent that for a different combination, the constraint could be violated twice because of the U-shape of the curve. The constraint could be violated once for a minimum baseline and once for a maximum baseline.

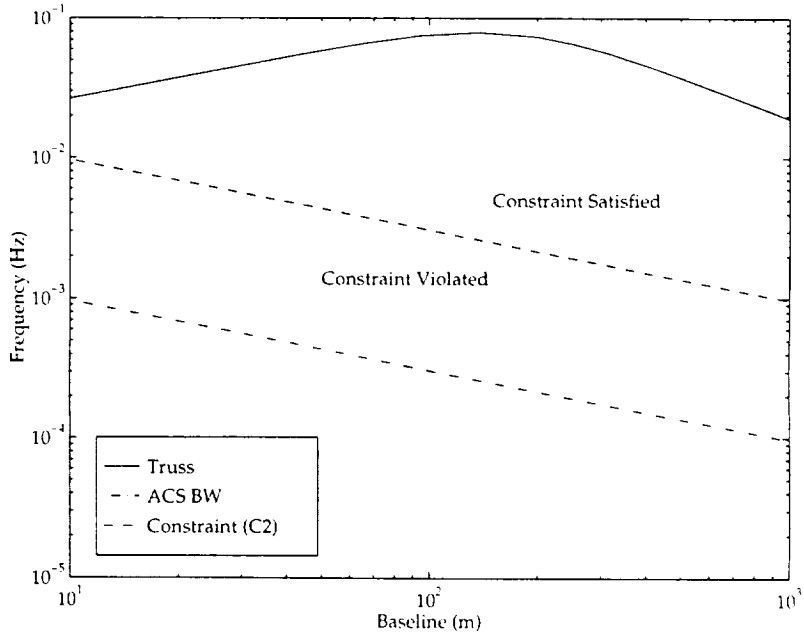


Figure 5-3: Truss Natural Frequency vs Baseline for $AR = 600$ and $\epsilon = 1/100$

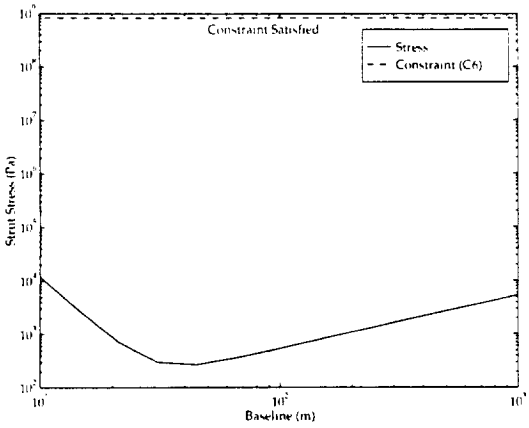


Figure 5-4: Internal Strut Stress vs Baseline for an Aspect Ratio of 600 and an Areal Density of 1/100

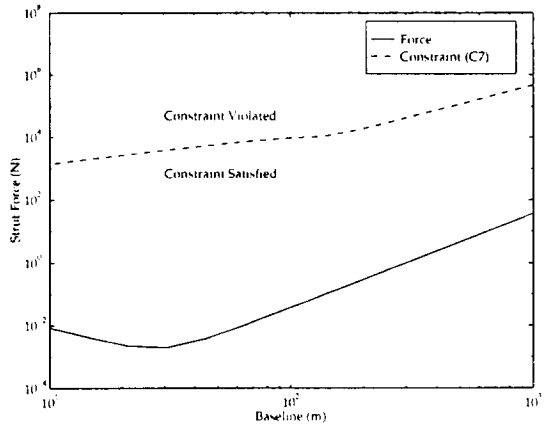


Figure 5-5: Internal Strut Force vs Baseline for an Aspect Ratio of 600 and an Areal Density of 1/100

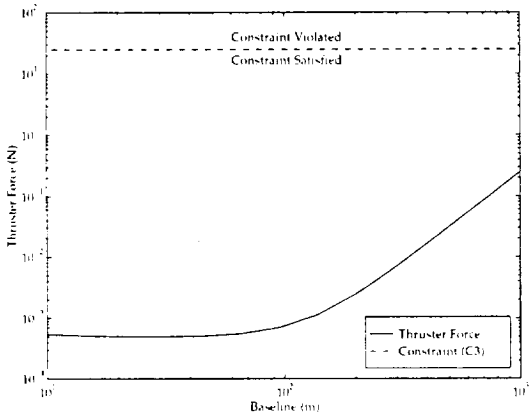


Figure 5-6: Thruster Force vs Baseline for an Aspect Ratio of 600 and an Areal Density of 1/100

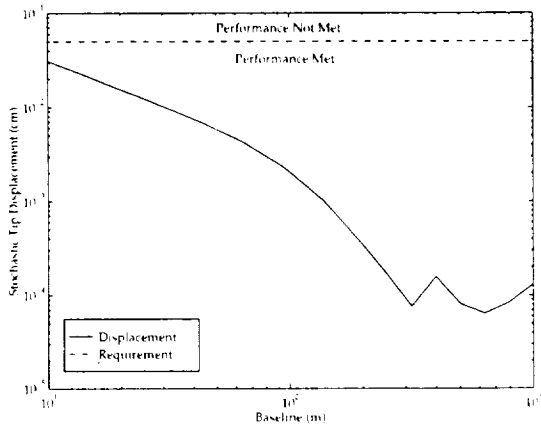


Figure 5-7: Performance vs Baseline for an Aspect Ratio of 600 and an Areal Density of 1/100

The internal strut stress and internal strut force curves are also U-shaped, as can be seen in Figures 5-4 and 5-5. Similar to the natural frequency curve, the strut stress and force curves do not violate the respective constraints for this combination of aspect ratio, 600, and areal density, 1/100. The calculation of the internal strut stress and force was described in Section 3.4.3.

The curves of thruster force and performance as functions of baseline are presented in Figures 5-6 and 5-7, respectively. Both the thruster force constraint (C3) and the performance requirement are satisfied for all baselines for this combination of aspect ratio, 600, and areal density, 1/100. The calculation of the thruster force was described in Section 3.4.1 while the performance calculation was described in Section 3.1.2.

Similar plots can be generated for the performance and for all other constraints for each of the 100 combinations of areal density and aspect ratio. However, the only important information conveyed by those curves is the baseline at which the constraint is violated or the performance not met. Therefore, each curve can be characterized by that baseline. An overall surface plot of these lengths as a function of aspect ratio and areal density can then be assembled. These surface plots will be referred to as "constraint surface plots".

As discussed above, the truss frequency and strut strength curves are U-shaped and could cross the respective constraint lines in two locations. Therefore, the frequency and strength curves are characterized by two baselines — a minimum and a maximum baseline. Between these two baselines, the constraint is met. For clarity, the surface plot of the minimum baseline will be referred to as the "lower" frequency/stress/buckling surface plot and the surface plot of the maximum baseline will be referred to as the "upper" frequency/stress/buckling surface plot.

## 5.2 Constraint Surface Plots

This section presents the process of constructing the constraint surface plots which are used to determine the minimum mass SCI. (Recall that the problem formulation

is to minimize the mass of the SCI subject to meeting the performance requirement and satisfying the imposed constraint.) There are a total of eleven constraint surface plots — one for the performance requirement, one for each of the imposed constraints C1, C3, C4, and C5 (dry mass, maximum thrust, reaction wheel mass, and minimum gage), and two for each of the strut strength constraints C6 and C7 (maximum internal stress and buckling, respectively) and two for the natural frequency constraint C2.

Seven of the surface plots — dry mass (C1), upper frequency (C2), thrust (C3), reaction wheel mass (C4), upper stress (C6), upper buckling (C7), and performance — represent the *maximum* baseline for which that constraint is met as a function of aspect ratio and areal density. For baselines shorter than this length, the constraint is met; for baselines longer than this length, that particular combination of aspect ratio and areal density can not meet the constraint.

As an example of this type of *maximum* surface plot, the dry mass (C1) constraint surface is plotted in Figure 5-8. The dry mass surface plot is interpreted in the following way. In order to meet the dry mass constraint (C1), the geometry of the truss must lie *below* the surface of Figure 5-8. The geometry of the truss consists of the specification of the areal density ($x$-axis of Figure 5-8), the aspect ratio ($y$-axis) and the baseline ($z$-axis).

It is important to note that this dry mass constraint surface is common to *all* cases in Table 2.3. As illustrated by the methodology block diagram, Figure 2-5, and discussed in Section 3.3, the dry mass of the interferometer is only dependent upon the baseline, the aspect ratio, and the areal density.

Of the eleven constraint surface plots, the other four plots — minimum gage (C5), lower frequency (C2), lower stress (C6), and lower buckling (C7) — represent the *minimum* baseline for which that constraint is met and are interpreted in the opposite fashion. For baselines longer than this length, the constraint is met; for baselines shorter than this length, that particular combination of aspect ratio and areal density can not meet the constraint.

As an example of this type of *minimum* surface plot, the minimum gage constraint surface is plotted in Figure 5-9. In order to meet the minimum gage constraint (C5),

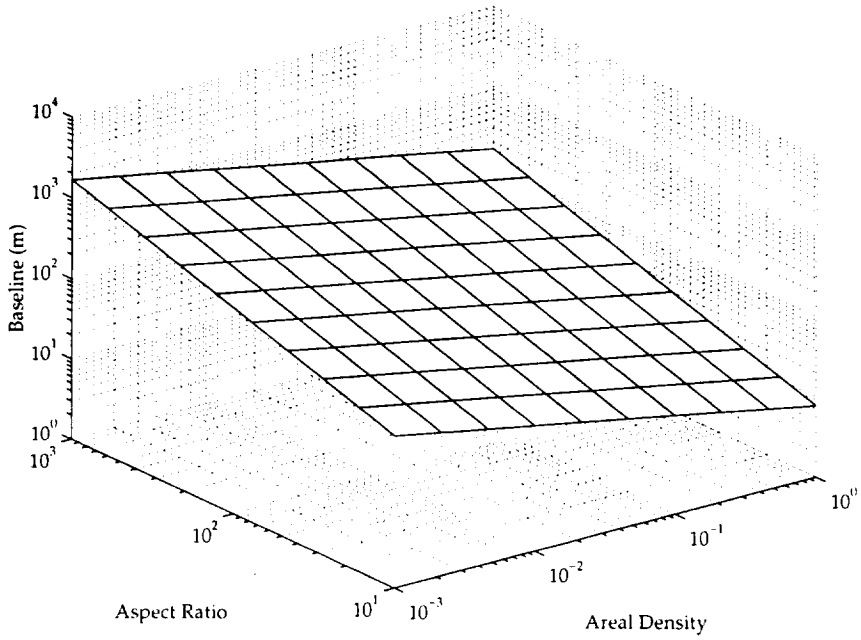


Figure 5-8: Dry Mass (C1) Constraint Surface (Satisfied Below Surface, Violated Above)

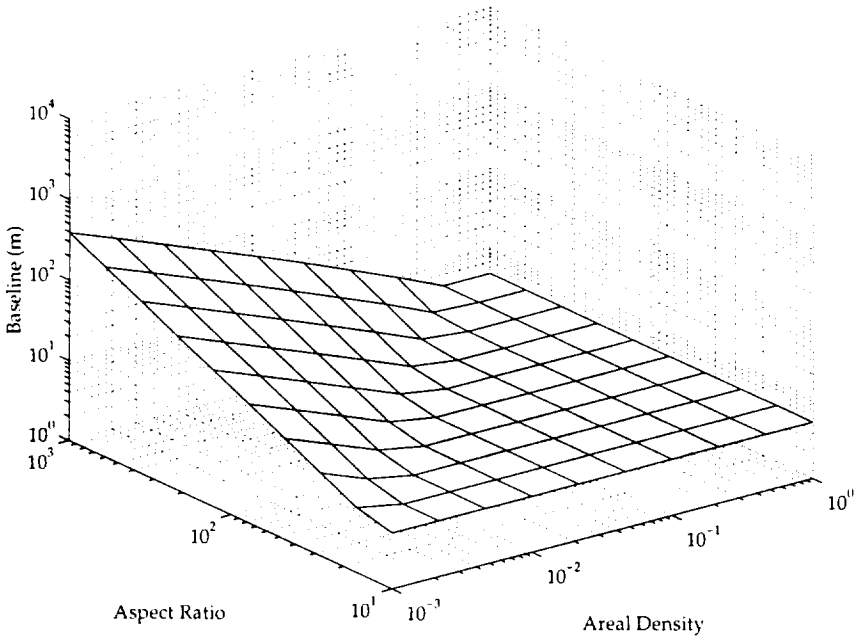


Figure 5-9: Minimum Gage (C5) Constraint Surface (Satisfied Above Surface, Violated Below)

the geometry of the truss must lie *above* the surface of Figure 5-9. Again, it is important to note that this minimum gage constraint surface is common to *all* cases in Table 2.3. As illustrated by the methodology block diagram, Figure 2-5, and discussed in Section 3.3.1, the thickness of an interferometer strut is only dependent upon the baseline, the aspect ratio, and the areal density.

The flattening off of the surface at a baseline of 5 m is an artificial construct of the computation of the surface. For each of the 100 combinations of aspect ratio and areal density, the baseline was increased from 5 m to 2000 m to determine the baseline at which each of the constraints was violated. For a minimum type constraint like the minimum gage constraint, if the constraint were not violated for any baseline in that range, the limit was set to be the minimum value, 5 m. If the constraint were violated for every baseline in that range, the limit was set to the maximum baseline, 2000 m.

Similarly, for a maximum type constraint like the dry mass or thrust constraints, the limit was set to the maximum baseline, 2000 m, if the constraint were not violated for any baseline checked and the limit was set to the minimum baseline, 5 m, if the constraint were violated for every baseline.

Consequently, baselines of 5 m and 2000 m on the constraint surface plots should not be interpreted as actual limits. They should be interpreted as indications that the constraint is either met for all or for none of the baselines in the range.

The eight remaining constraint surface plots for the passive SCI reference case are presented in Figures 5-10 through 5-15. (There is no reaction wheel mass constraint surface for the reference case because reaction wheels are not used.)

Figure 5-10 indicates that the performance requirement is met for all truss geometries, while Figure 5-11 and 5-12 indicate that there are some truss geometries for which the maximum thrust (C3) and natural frequency (C2) constraints are not met. Figures 5-14 through 5-17 illustrate that the strength constraints (C6 and C7) are met for all truss geometries.

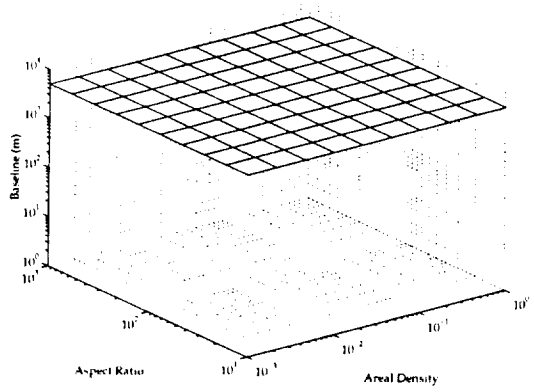


Figure 5-10: Performance Requirement Surface (Satisfied Below Surface, Violated Above)

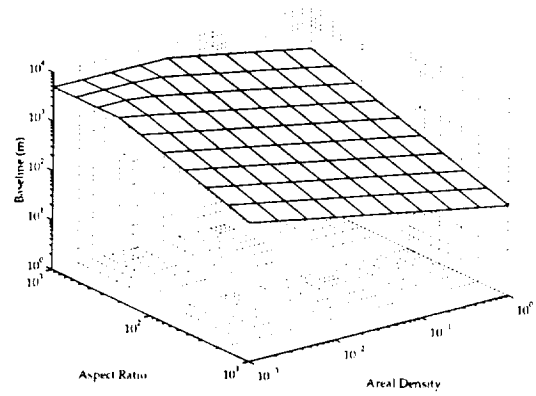


Figure 5-11: Maximum Thrust (C3) Constraint Surface (Satisfied Below Surface, Violated Above)

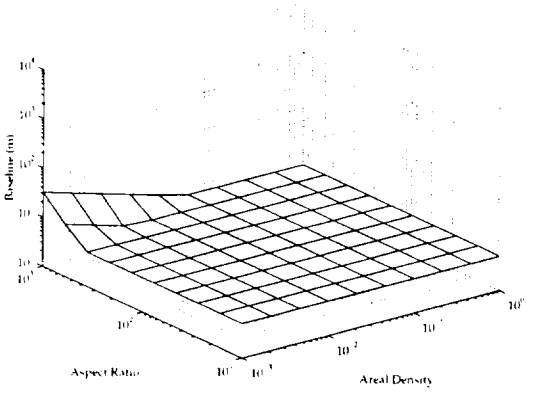


Figure 5-12: Lower Frequency (C2) Constraint Surface (Satisfied Above Surface, Violated Below)

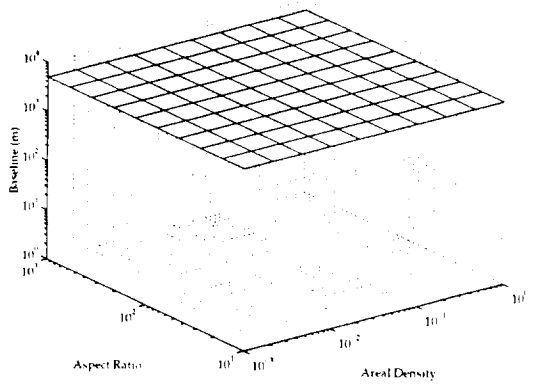


Figure 5-13: Upper Frequency (C2) Constraint Surface (Satisfied Below Surface, Violated Above)

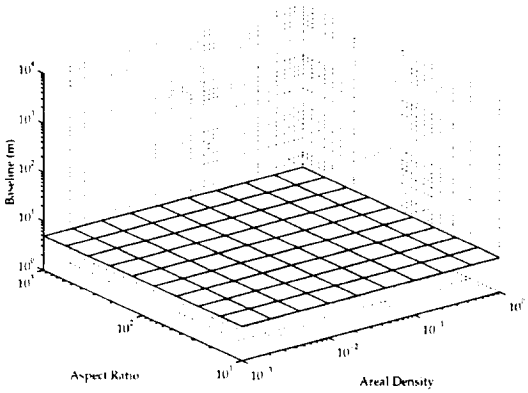


Figure 5-14: Lower Stress (C6) Constraint Surface (Satisfied Above Surface, Violated Below)

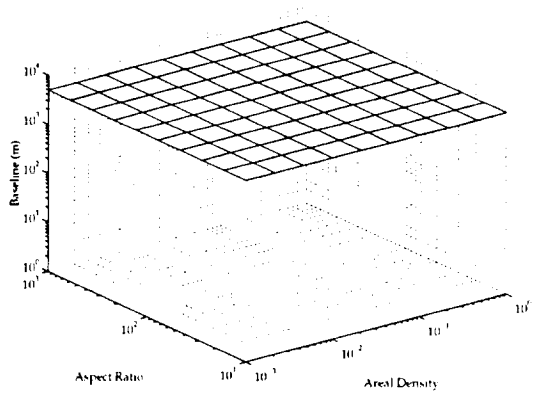


Figure 5-15: Upper Stress (C6) Constraint Surface (Satisfied Below Surface, Violated Above)

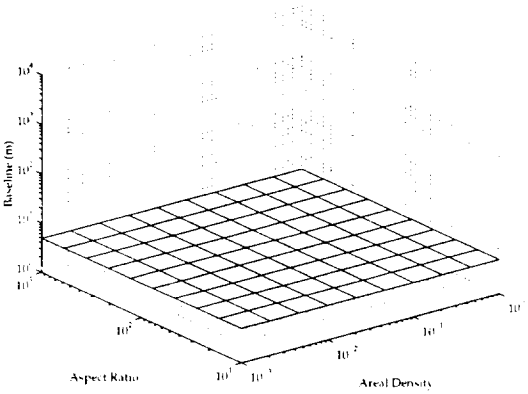


Figure 5-16: Lower Buckling (C7) Constraint Surface (Satisfied Above Surface, Violated Below)

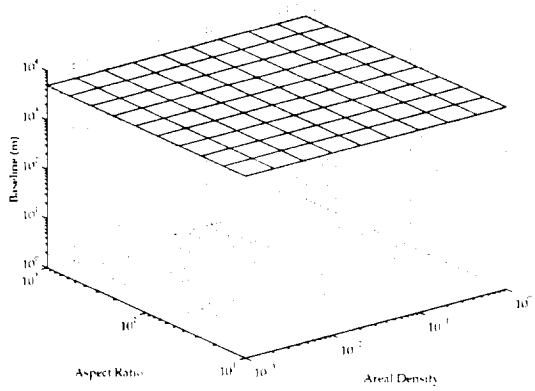


Figure 5-17: Upper Buckling (C7) Constraint Surface (Satisfied Below Surface, Violated Above)

## 5.3 Determination of Minimum Mass SCI

The truss geometries that meet all requirements and constraints are located within the volume that is common to all of the above constraint surface plots, i.e. below the lowest of the maximum constraint surface plots and above the highest of the minimum constraint surface plots. The optimum SCI is determined by identifying, for each baseline, that combination of aspect ratio and areal density that lies within this constraint volume and that gives the minimum total dry mass of the SCI.

An easy way to visualize this process is by plotting for a given baseline, on the same graph, the intersection of each of the constraint surfaces with the surface of constant baseline. Figure 5-18 is an example of such a plot for a baseline of 10 m. Notice that there are only three lines in Figure 5-18 — one in the lower right corner that corresponds to the intersection of the dry mass (C1) constraint surface with the 10 m constant baseline surface, another in the middle of the figure that corresponds to the intersection of the minimum gage (C5) constraint surface with the same constant baseline surface, and a third in the upper left corner that corresponds to the lower

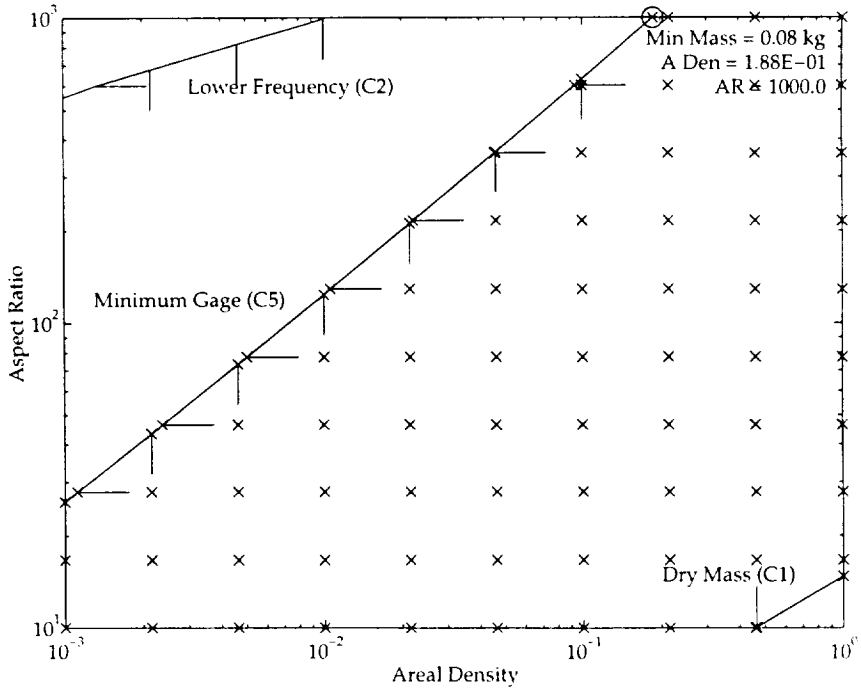


Figure 5-18: Minimum Mass Truss Calculation for 10m Baseline

frequency (C2) constraint surface. None of the other constraint surfaces are active at 10 m, and therefore do not intersect with the 10 m constant baseline surface.

Figure 5-18 is interpreted in the following way. The only constraints which limit the acceptable combinations of aspect ratio and areal density are the dry mass (C1), frequency (C2) and minimum gage (C5) constraints. The performance requirement and all other constraints are met for all combinations of aspect ratio and areal density for a 10 m baseline. Each of the lines in Figure 5-18 indicates the combinations of aspect ratio and areal density for which the calculated parameter value is equal to the value of the corresponding constraint. The side of that bound that is allowed must be interpreted from the constraint surface plots, Figures 5-8, 5-12, and 5-9 for the dry mass (C1), frequency (C2) and minimum gage (C5) constraints, respectively.

The ticks on each of the lines indicate the area of possible combinations of aspect ratio and areal density for which the constraint is met. For the lower frequency (C2) and minimum gage (C5) constraints, combinations of aspect ratios and areal densities toward the lower right corner of Figure 5-18 are allowed. For the dry mass (C1) constraint, combinations of aspect ratios and areal densities toward the upper left corner of Figure 5-18 are allowed.

The crosses (x) in Figure 5-18 then indicate the zone of possible combinations for which all performance requirements and constraints are met. This area of acceptable combinations is bounded by the "active" constraints for this baseline. In this case, the active constraints are the dry mass (C1) and minimum gage (C5) constraints.

The truss mass corresponding to each of the acceptable combinations is calculated using Equation 3.7. The combination of aspect ratio and areal density that gives the minimum truss mass (and therefore the minimum dry mass) is indicated by a circle. For a 10 m baseline, the minimum mass SCI has an aspect ratio of 1000 and an areal density of 0.19. An important point to be made about the minimum mass geometry is that for this baseline, the minimum mass geometry is only limited by the minimum gage constraint.

The above process is carried out for a range of baselines from 10 m to 1000 m. Illustrations of the calculations of the minimum mass passive SCI for baselines of

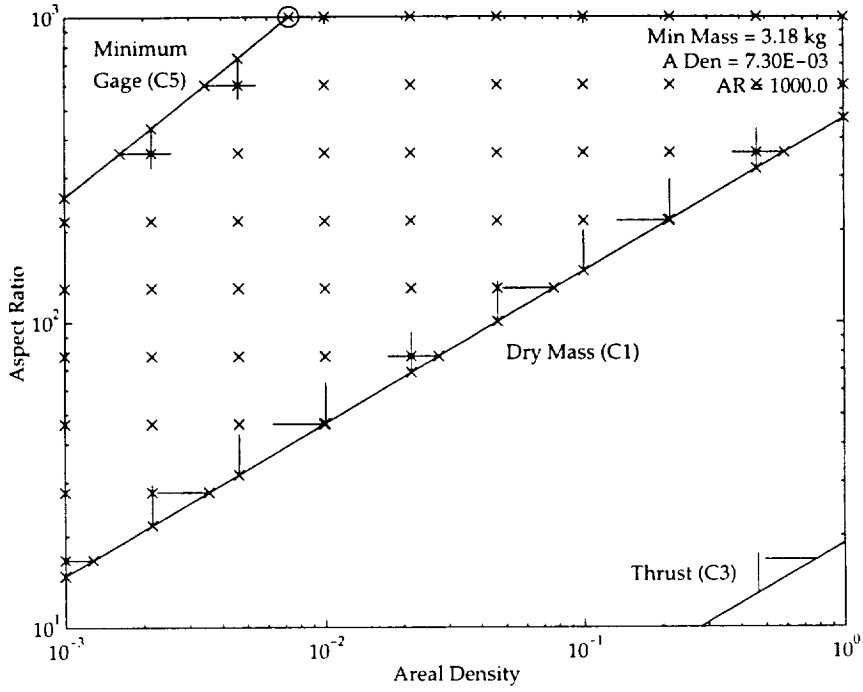


Figure 5-19: Minimum Mass Truss Calculation for 100m Baseline

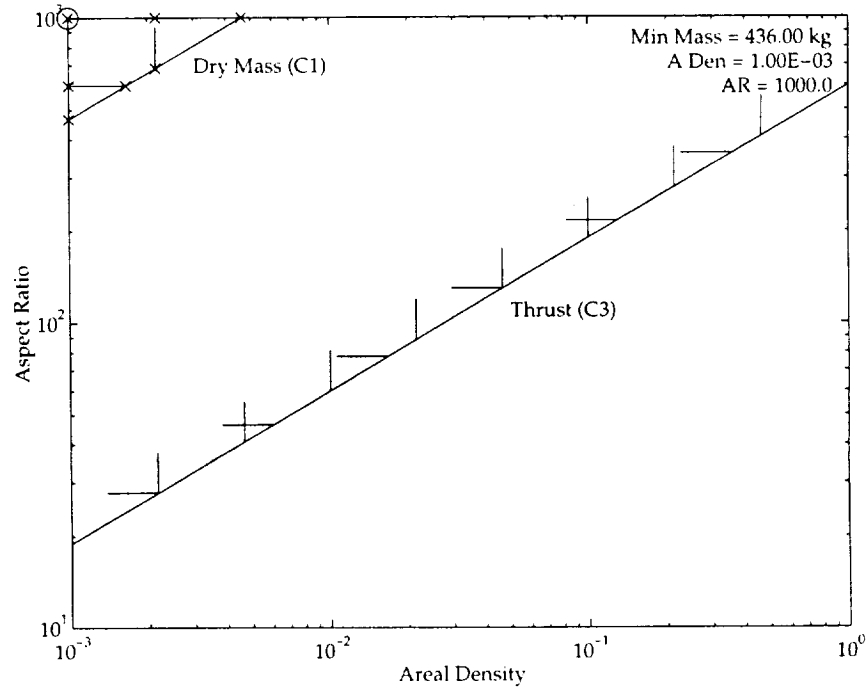


Figure 5-20: Minimum Mass Truss Calculation for 1000m Baseline

100 m and 1000 m are shown in Figures 5-19 and 5-20, respectively.

It can be seen from Figures 5-19 and 5-20 that as the baseline increases, the frequency (C2) and minimum gage (C5) constraints relax while the dry mass (C1) constraint becomes more stringent. In fact, the frequency (C2) and minimum gage (C5) constraints relax so much that the frequency constraint (C2) is met by all combinations of aspect ratio and areal density for a 100 m baseline and the minimum gage constraint (C5) is satisfied by all combinations for a baseline of 1000 m. The maximum thrust constraint (C3) also appears in Figures 5-19 and 5-20 but this constraint is never active. Only the minimum gage (C5) and total dry mass (C1) constraints are ever active.

The minimum mass geometry, however, is still limited by the minimum gage constraint (C5) for the 100 m baseline and by the limits placed on the allowable aspect ratio and areal density for the 1000 m baseline. This is an important conclusion. The minimum mass of a passive truss necessary to meet the performance requirement and the imposed constraints for the reference case is only limited by minimum gage (C5), aspect ratio and areal density constraints. None of the other requirements, including performance, frequency, and strength, are active factors.

## 5.4 Minimum Mass SCI Results for the Passive Reference Case

This section presents the design of the passive SCI as a function of baseline for the reference case which was determined using the method described in the previous section. This section also presents the corresponding values of performance and constraint parameters as proof that this optimal design does meet all performance requirements and constraints.

The first four figures presented in this section (Figures 5-21 through 5-24) describe the high-level modeling of the plant for this reference case. Figures 5-21 and 5-22 present the truss aspect ratio and areal density as functions of baseline. The aspect

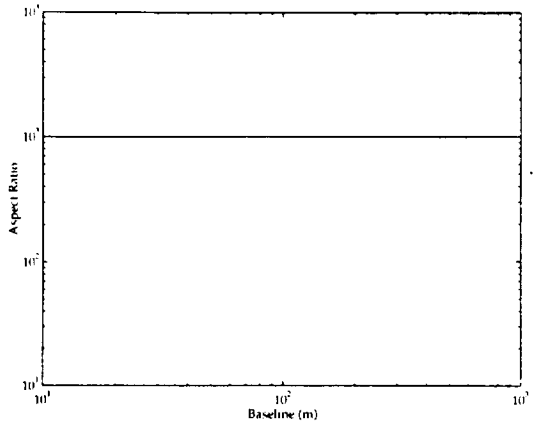


Figure 5-21: Minimum Mass SCI Aspect Ratio

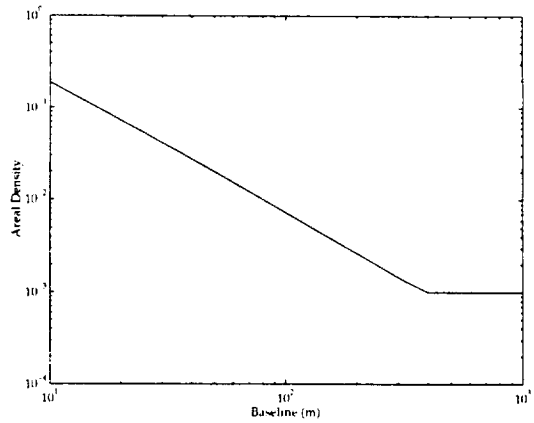


Figure 5-22: Minimum Mass SCI Areal Density

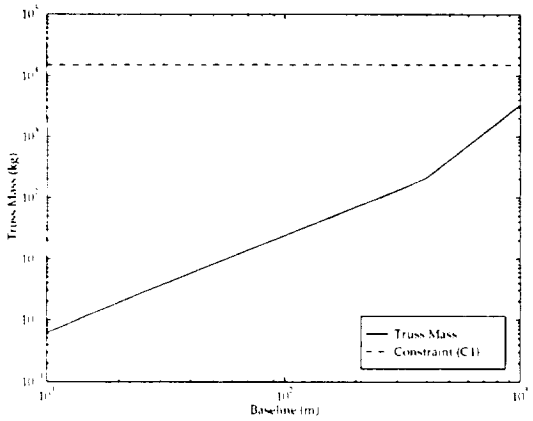


Figure 5-23: Minimum Mass SCI Truss Mass

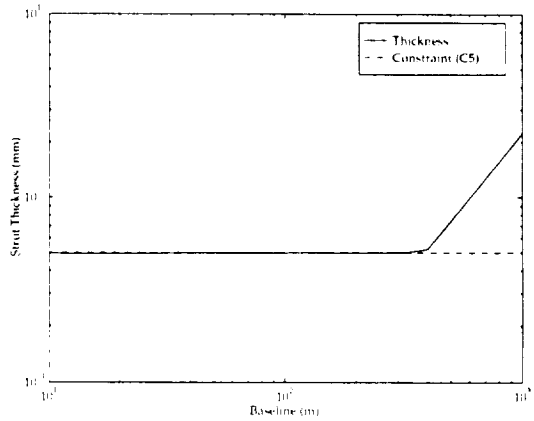


Figure 5-24: Minimum Mass SCI Strut Thickness

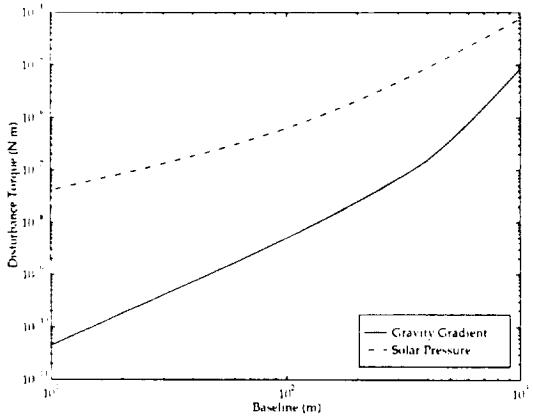


Figure 5-25: Minimum Mass SCI Attitude Disturbance Torques

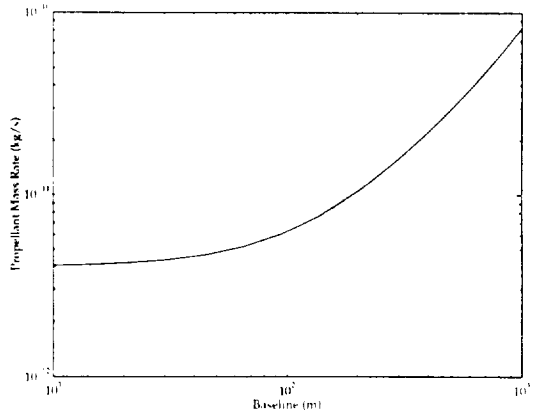


Figure 5-26: Minimum Mass SCI Average Propellant Mass Rate

ratio is constant at the maximum allowable value, 1000, while the areal density decreases from 1/5.33 to the minimum allowable value of 1/1000 at a baseline of 400 m.

This scaling of aspect ratio and areal density with baseline and Equation 3.7 give the truss mass shown in Figure 5-23. The dashed line is the maximum truss mass that satisfies the total dry mass constraint (C1) and the truss mass never reaches this value.

As discussed in Section 2.4.2, the minimum strut thickness constraint (C5) is imposed during the modeling of the high-level plant, and Figure 5-24 shows the strut thickness of the minimum mass passive SCI as a function of baseline. The dashed line is the minimum allowable thickness (C5) and it can be seen that the designed strut has the minimum thickness for all baselines less than 400 m.

The aspect ratio, areal density and strut thickness curves presented (Figures 5-21, 5-22, and 5-24) also illustrate another way to determine those constraints that limit the design of the structurally connected interferometer. For baselines less than 400 m, the design is limited by the minimum gage constraint (C5) and the maximum allowable aspect ratio. This can be inferred because the values of the strut thickness and truss aspect ratio for the minimum mass SCI equal the imposed limits on these parameters for baselines in this range. Similarly, for baselines greater than 400 m, the truss design is limited by the minimum areal density and maximum aspect ratio allowable.

The next two plots presented in this section (Figures 5-25 and 5-26) illustrate the modeling of the external/attitude disturbances acting on the minimum mass SCI. Figure 5-25 presents the external disturbance torques acting on the interferometer. These disturbances were calculated using the equations described in Section 4.1.

The solid line is the disturbance torque due to the gravity gradient caused by the sun and the dashed line is the solar pressure disturbance torque. Not unexpectedly, the solar pressure torque dominates.

As discussed in Section 2.4.2, the average propellant mass rate can be calculated with knowledge of the disturbance torques, the location of the attitude control thrusters and the propellant. Figure 5-26 presents the average propellant mass rate

for this reference case. The average propellant mass rate was calculated from the equations in Section 4.1.4.

The modeling of the internal plant is illustrated by the next four figures — Figures 5-27 through 5-30. The required thrust is shown in Figure 5-27. The solid line is the thruster size required to meet the slew requirements described in Section 3.4.1. The dash-dot line is the thruster size required for disturbance rejection as described in Section 3.4.1. The dashed line is the maximum thrust constraint (C3). The thrusters are sized to meet the slew requirements and the thrust levels required are over 3 orders of magnitude less than the maximum allowable.

Figure 5-28 presents the frequency constraint (C2). The fundamental structural frequency of the interferometer is calculated from the finite element model and is plotted as the solid line. There are two frequencies associated with the attitude control subsystems as discussed in Section 3.4.1. The thrusting frequency required to reject the disturbances of Figure 5-25 is plotted as the dash-dot line while the thrusting frequency associated with the slew maneuver is plotted as the dotted line.

The first natural frequency of the SCI must be at least one decade above the maximum of these two frequencies, and this limit is plotted as the dashed line. For this reference case, the thrusting frequency associated with slew maneuvers is dominant and the fundamental structural frequency of the minimum mass SCI is always greater than a decade above this frequency.

Figures 5-29 and 5-30 present the strength constraints on the individual struts, as calculated in Section 3.4.3. Figure 5-29 presents the maximum induced normal stress in one strut (C6) while Figure 5-30 presents the maximum induced normal force (C7). In each figure, the calculated parameter value is the solid line while the dashed line is the constraint. The strength constraints are easily met.

The last two figures of this section present the calculated performance of the minimum mass SCI. Figure 5-31 shows the stochastic displacement in bending (the $z$-direction) of one of the tips of the truss. (The performance levels of each tip are equal because of the symmetry of the problem.) The dashed line is the performance requirement, $z_{req}$ from Table 3.1, which is met for all baselines.

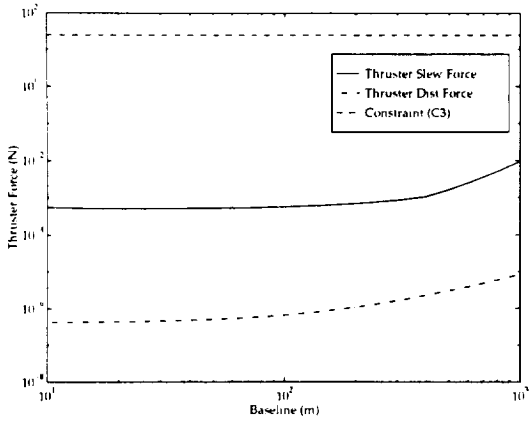


t

Figure 5-27: Minimum Mass SCI Attitude Control Thruster Size

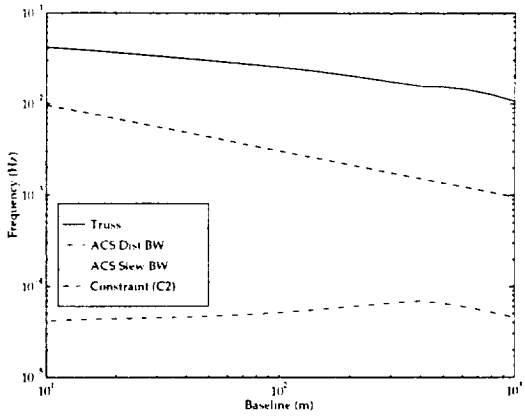


Figure 5-28: Minimum Mass SCI Fundamental Frequencies

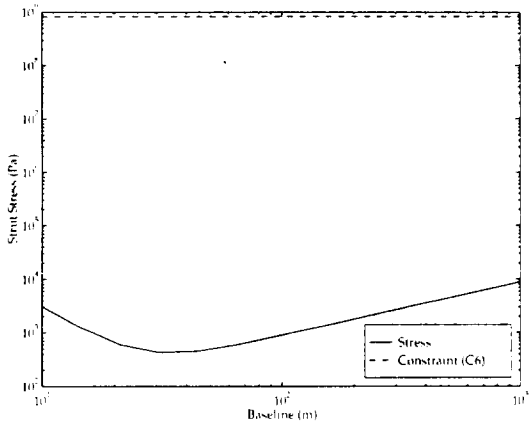


Figure 5-29: Minimum Mass SCI Strut Internal Stress

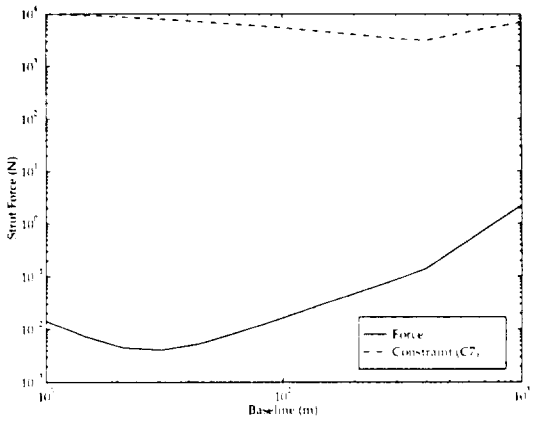


Figure 5-30: Minimum Mass SCI Strut Normal Force

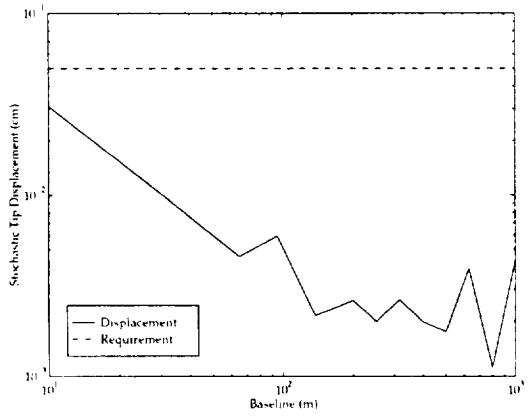


Figure 5-31: Minimum Mass SCI Stochastic Tip Displacement


Figure 5-32: Minimum Mass SCI Central Spacecraft Stochastic Displacement

Figure 5-32 shows the stochastic displacement in the $z$-direction of the central spacecraft of the SCI as a solid line. The dashed line is the performance requirement, $z_{req}$ from Table 3.1, which is met for all baselines.

## 5.5 MSI Reference Case Results

This section presents the multiple spacecraft interferometer design for the reference case. The figures in this section illustrate that all performance requirements and constraints are satisfied.

The external/attitude disturbances acting on the MSI are displayed in Figures 5-33 and 5-34. Figure 5-33 presents the differential acceleration of the freeflyers caused by the external disturbances. The solid line represents the differential acceleration due to the gravity gradient and described by Equations 4.3a and 4.3b which are the solutions of the Hill-Clohessy-Wiltshire equations. The dash-dot line represents the differential acceleration caused by solar pressure.

Figure 5-34 presents the attitude disturbance torques on a collector spacecraft. Again, the solid line is the gravity gradient torque while the dash-dot line is the solar pressure torque.

Since these torque levels are very small, the total propellant mass rate as presented in Figure 5-35 is dominated by the propellant required to compensate for the differential accelerations of the spacecraft. Additionally, the thruster sizing is determined by the slew requirements and the compensation of the differential acceleration, not the rejection of this disturbance torque.

The differential accelerations and attitude disturbance torques determine the average propellant mass rate of the MSI. Figure 5-35 presents the propellant mass rate required to compensate for the differential acceleration (solid line) and to reject the attitude disturbance torques (dash-dot line). The total propellant mass rate is the sum of these two rates and is dominated by the differential acceleration contribution.

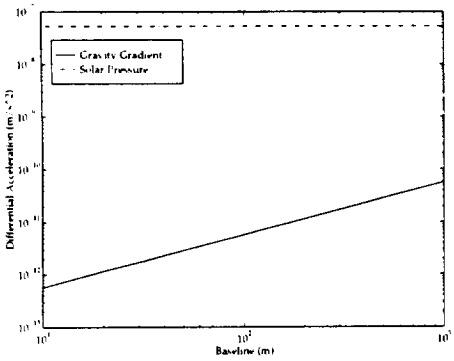


Figure 5-33: MSI Differential Acceleration

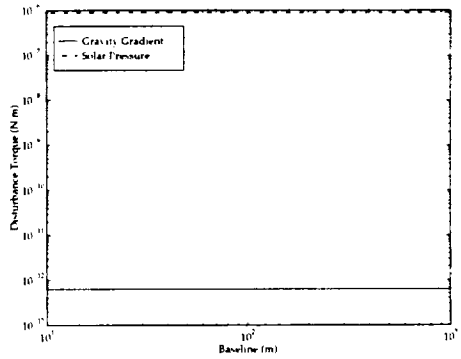


Figure 5-34: MSI Solar Pressure Disturbance Torque

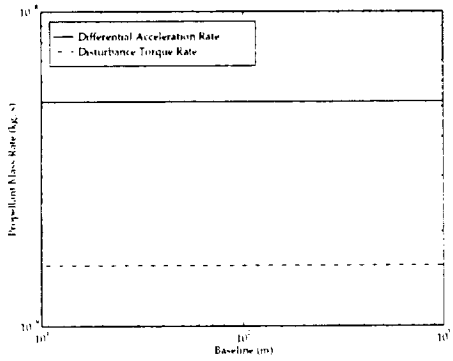


Figure 5-35: MSI Average Propellant Mass Rate

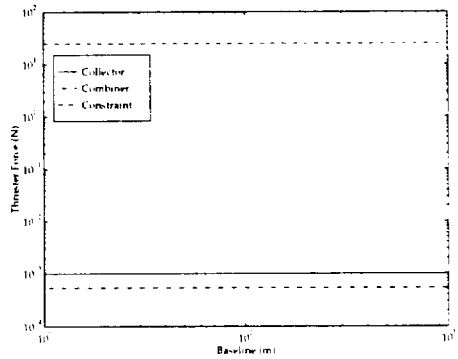


Figure 5-36: MSI Thruster Size

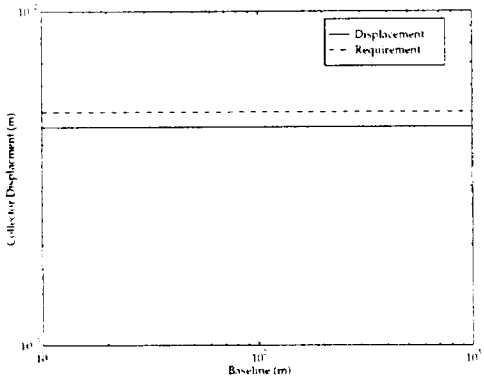


Figure 5-37: MSI Collector Performance

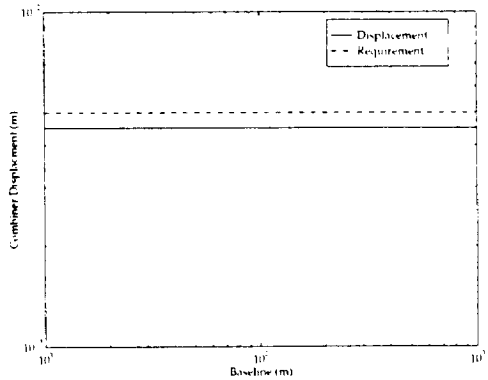


Figure 5-38: MSI Combiner Performance

The required thrust for the MSI is shown in Figure 5-36. The solid line is the collector thruster size and the dash-dot line is the combiner thruster size. The collector thruster is sized to meet the slew requirements. The combiner thruster is sized to compensate for the differential acceleration due to solar pressure. The thrust levels required are over four orders of magnitude less than the maximum allowable, illustrated by the dashed line.

Finally, the performance of the individual spacecraft is presented in Figures 5-37 and 5-38. Figure 5-37 shows the maximum displacement of a collector spacecraft relative to its desired orbit as described by the Hill-Clohessy-Wiltshire equations 4.2a-c. This displacement is in the direction of the orbital velocity.

Figure 5-38 shows the maximum displacement of the combiner spacecraft relative to its desired orbit as a result of the differential solar pressure acceleration. This displacement is directed along the vector from the spacecraft to the Sun.

In both figures, the performance requirement is plotted as a dashed-line. This performance requirement is met for all baselines. Note that in the reference case, as discussed in Section 4.2, there are no stochastic force disturbances input to the MSI freeflyers, so the performance shown in Figures 5-37 and 5-38 is the rigid body motion of the spacecraft between the limits of the deadband. There is only a stochastic torque disturbance caused by the ODL reactuation input to the combiner spacecraft, but this has no effect on the displacement of the combiner spacecraft. As was discussed in Section 4.2.3, the optical delay line would be designed to ensure that it did not cause the combiner spacecraft to exceed the maximum allowable displacement.

## 5.6 Baseline Critical Time Plot

This section presents the critical time plot for the reference case with a passive structurally connected interferometer. It is important to recall from Section 2.1.2 that the critical time plot is generated from only the total dry mass plots and the average propellant mass rate plots of the SCI and MSI.

The total dry masses of the minimum mass SCI and MSI are plotted in Figure 5-

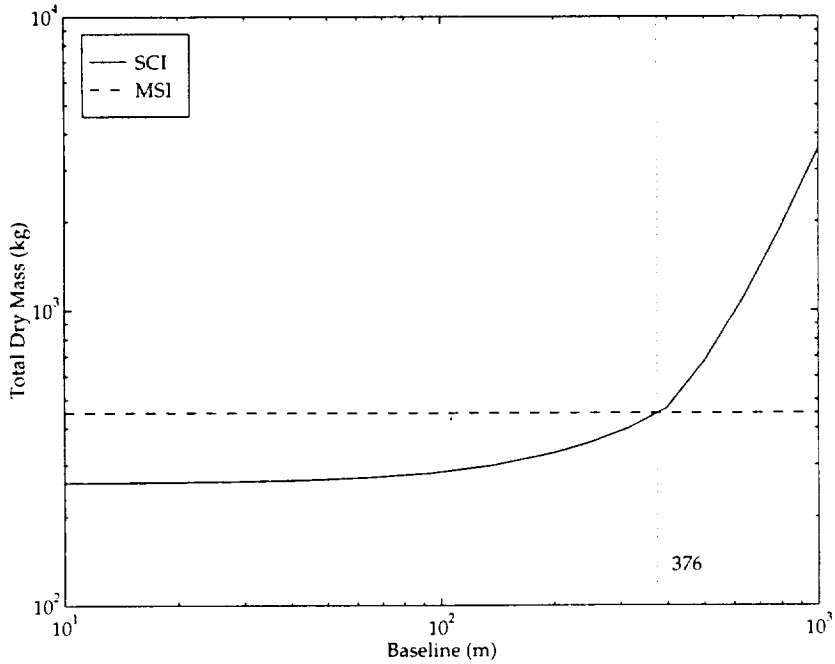


Figure 5-39: SCI and MSI Total Dry Masses versus Baseline

39. The solid line is the dry mass of the SCI, $m_{d,sci}$ given by Equation 3.8, while the dashed line is the MSI dry mass, $m_{d,msi}$. From Figure 5-39, the equal dry mass point is 376 m.

The average propellant mass rates of the minimum mass SCI and MSI are plotted in Figure 5-40. The solid line is the propellant mass rate of the SCI, $\dot{m}_{sci}$, while the dashed line is the MSI propellant mass rate, $\dot{m}_{msi}$. For this case, the propellant mass rate of the SCI is always less than that of the multiple spacecraft interferometer for all baselines.

Use of Equation 2.3 generates the critical time plot shown in Figure 5-41. The structurally connected interferometer is the optimal design for all baselines less than 376 m, the equal dry mass point. For baselines longer than this, there is a finite time shown by the solid line below which the MSI is the optimal design.

Looking at the scale of the graph, however, this critical time ranges from 1 to over 10,000 years! The freeflyer design is optimal for all baselines longer than 376 m for a one week mission and for all baselines longer than 403 m for a thirty year mission. This is shown more explicitly in Figure 5-42 where the critical time scale is presented

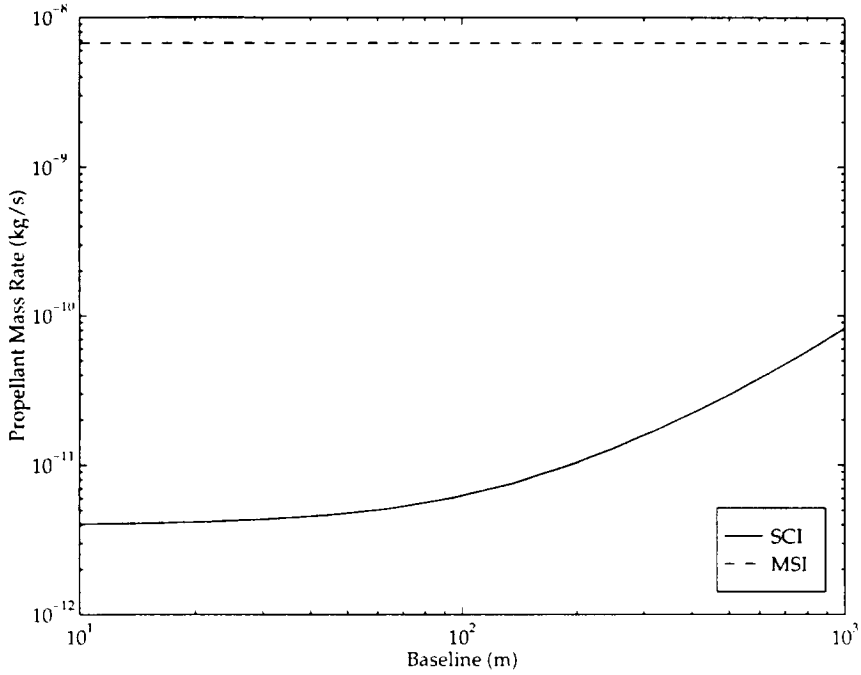


Figure 5-40: SCI and MSI Average Propellant Mass Rates versus Baseline

for realistic mission lengths ranging from one week to thirty years.

The critical time curve presented in Figure 5-42 has a very steep slope because the propellant mass rates are so small. Even though the propellant mass rate of the MSI is greater than that of the SCI, the absolute magnitude of the MSI propellant mass rate is so small that it would take a *very* long time for the extra propellant mass required for the MSI to equal the extra structural mass of the SCI.

Also shown in Figure 5-41 as the dash-dot line, is the propellant mass fraction constraint (C8) for the MSI. Once again, however, this constraint which indicates that for missions longer than 367 years the propellant mass fraction of the combiner spacecraft is greater than 30%, is well beyond the range of reasonable mission durations. The mass fraction constraint of the SCI is even greater than this time. Therefore, all requirements and constraints are met for the reference case design and the critical time plot is given by Figure 5-42.

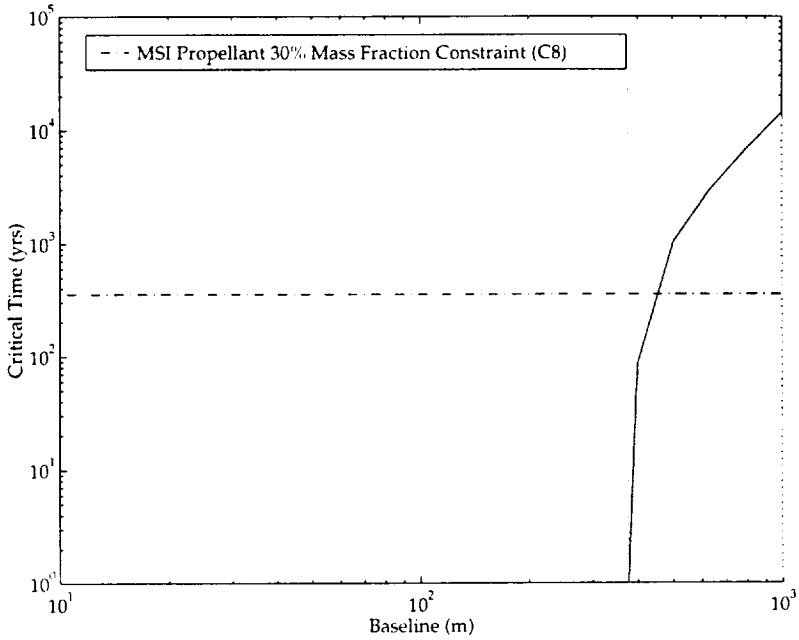


Figure 5-41: Critical Time Plot for the Passive Reference Case

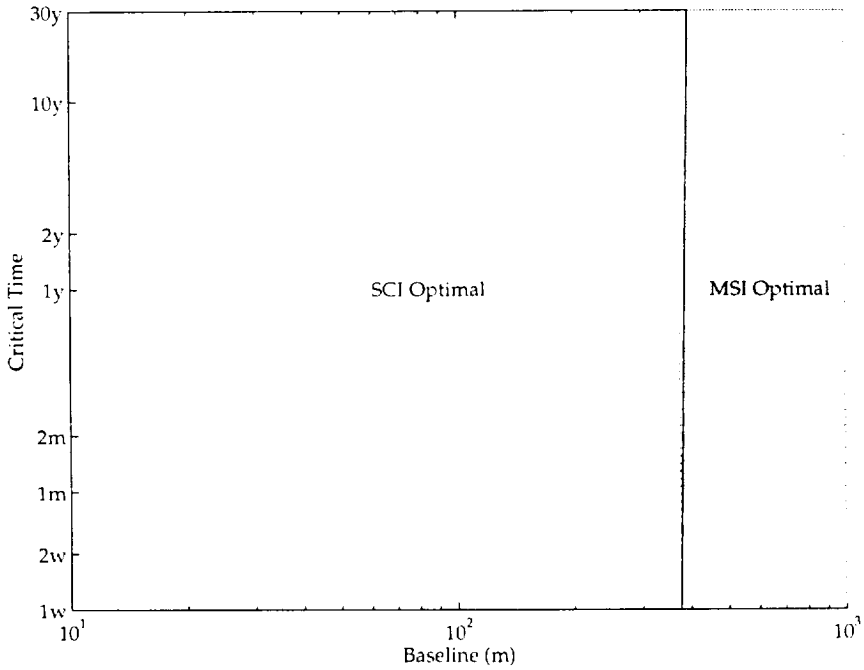


Figure 5-42: Practical Critical Time Plot for the Passive Reference Case

## 5.7 Structurally Actuated Reference Case Design

The addition of active structural control to the truss of the structurally connected interferometer is modeled in this study by relaxing the frequency constraint (C2) and by increasing the structural damping. Increasing the structural damping will only affect the achieved performance of the interferometer and will not affect any of the imposed constraints. Therefore, the addition of active structural control only alters the frequency and performance surface plots of Section 5.2 (Figures 5-12, 5-13, and 5-10.)

Furthermore, the addition of active structural control can only improve these surface plots. Since the upper frequency constraint, Figure 5-13, and the performance requirement, Figure 5-10, are satisfied for all 100 combinations of aspect ratio and areal density for the passive reference case, this constraint and requirement are also satisfied for every combination for the actuated reference case. The only constraint surface plot that is different from those of the passive reference case is the lower frequency surface plot. This is presented in Figure 5-43. Adding active structural control has caused the frequency constraint to be met for all combinations of aspect ratio and areal density.

It is important to recall that this lower frequency constraint was not active in the minimum mass SCI design of the passive reference case. Relaxing this constraint,therefore, does not affect the minimum mass SCI design of the actuated reference case. The design of the minimum mass truss is still limited by the minimum gage constraint and the allowable aspect ratio and areal density so the design is exactly the same as that presented above in Section 5.4. Additionally, the critical time plot is also the same as that in Figure 5-41 and Figure 5-42.

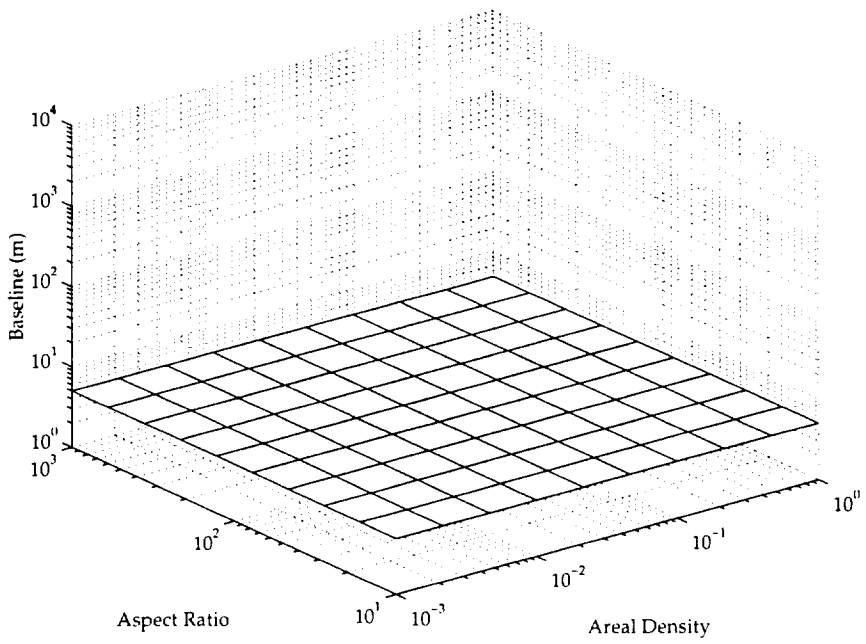


Figure 5-43: Lower Frequency Constraint Surface for Actuated Reference Case

## 5.8 Summary

The design of the minimum mass SCI that meets all performance requirements and constraints for the passive reference case was presented and it was found that the design is limited by the minimum gage constraint and the allowable aspect ratio and areal density. The critical time plot for this passive reference case was presented in Figure 5-42. From this plot, it was determined that a structurally connected interferometer is optimal for all baselines less than 376 m for a one week mission and for all baselines less than 403 m for a thirty year mission. A multiple spacecraft interferometer is optimal for longer baselines.

Since the minimum mass SCI for the passive reference case is limited by the minimum gage constraint and not by performance or frequency, the addition of active structural control can not reduce the mass of the truss necessary. Therefore, there is no benefit to adding active structural control to the interconnecting truss for the reference case.

# Chapter 6

# Non-Reference Case Results

This chapter presents the results of the remaining 21 cases of Table 2.3 in an attempt to determine the effects of the various trade parameters on the mission critical time. In order to present the results in a concise fashion, the cross-over baseline for a mission duration of ten years is presented for both the passive and actuated structurally connected interferometer configurations for each of the 21 cases. The cross-over baseline is that distance beyond which a freeflyer configuration is preferred to a structurally connected interferometer. These cross-over baselines are compared to those of the reference case and selected plots are presented to explain the differences. All plots of the dependence on baseline of dry mass, average propellant mass rate, and critical time can be found in Appendix A.

Sections 6.2 – 6.4 discuss the effects of different mission scenarios on the critical time. Different orbits and orientations as well as rotating interferometers are examined. Sections 6.5 – 6.7 discuss the effects of different onboard disturbances and changes to the plant. Different truss materials and propellants are examined, as are different locations of the thrusters and the use of reaction wheels. The inclusion of thermal snap as a disturbance source is also discussed. Finally, Section 6.8 examines the effects of changing the performance requirement.

## 6.1 Cross-Over Baseline Plots

The cross-over baseline is an alternate interpretation of the critical time plot. When planning future interferometry missions, it may be more convenient to determine the maximum baseline for which an SCI is less massive than an MSI for a given mission duration, than to determine the maximum mission duration for a given baseline. This maximum baseline will be referred to as the "cross-over baseline" for the specified mission duration.

Figure 6-1 presents the critical time plot of the passive SCI reference case discussed in Chapter 5 and shows the cross-over baseline for a mission duration of ten years. The critical time plot can either be interpreted as having a cross-over baseline of 397 m for a ten year mission duration or it can be interpreted as having a critical time of 10 years for a baseline of 397 m.

This chapter determines the effects of the various trade parameters on the critical time plots by plotting changes in the cross-over baseline for a mission of ten year duration. Recalling that the critical time plots are derived from the total dry masses and

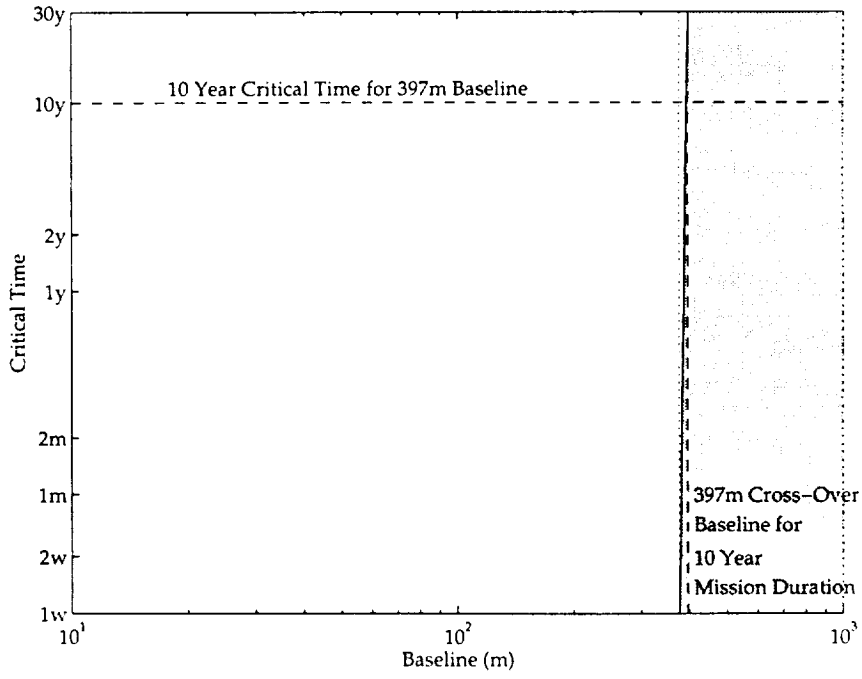


Figure 6-1: Critical Time Plot of Passive Reference Case Showing Ten Year Cross-Over Baseline

average propellant mass rates of the structurally connected and multiple spacecraft interferometers (recall Equation 2.3), a change in the ten year cross-over baseline is indicative of a change in one or both of these quantities.

Therefore, the procedure of this chapter is to first determine if the cross-over baselines of each of the cases in Table 2.3 differ from that of the reference case and, if so, to then explain the reason for the change by describing how the variation of the trade parameter affects the total dry mass and/or the average propellant mass rate.

Before presenting the non-reference cases, it is important to recall some properties of the critical time plots. First, it must be recalled that the equal dry mass and equal mass-rate points set the minimum and maximum baselines of the critical time plot, respectively. This can be seen in Figure 6-1. The second property that must be remembered is the value of the critical time plot, and therefore of the ten year cross-over baseline, is determined by the difference between the MSI and SCI average propellant mass rates.

## 6.2 Various Orbits (Cases 2-4)

This section presents the effects of varying the orbit of the interferometer (Cases 2-4 of Table 2.3). Figure 6-2 presents the ten year cross-over baselines for the four different orbits examined. The structurally connected interferometer is preferable over a smaller range of baselines for Earth-orbiting interferometers than for interferometers in solar orbit. Furthermore, there is an advantage to adding active structural control to interferometers in Earth orbit, but no advantage for solar-orbiting interferometers. These results are explained below.

It is recalled from Chapter 5 that the reference case SCI design in solar orbit at 1 AU is gage limited and the sizing of the attitude control thrusters is dominated by the slew requirements of the interferometer. Since the minimum mass design is neither performance nor frequency limited, there is no advantage to using active structural control.

It can then be reasoned that putting the interferometer in a 5.2 AU solar orbit

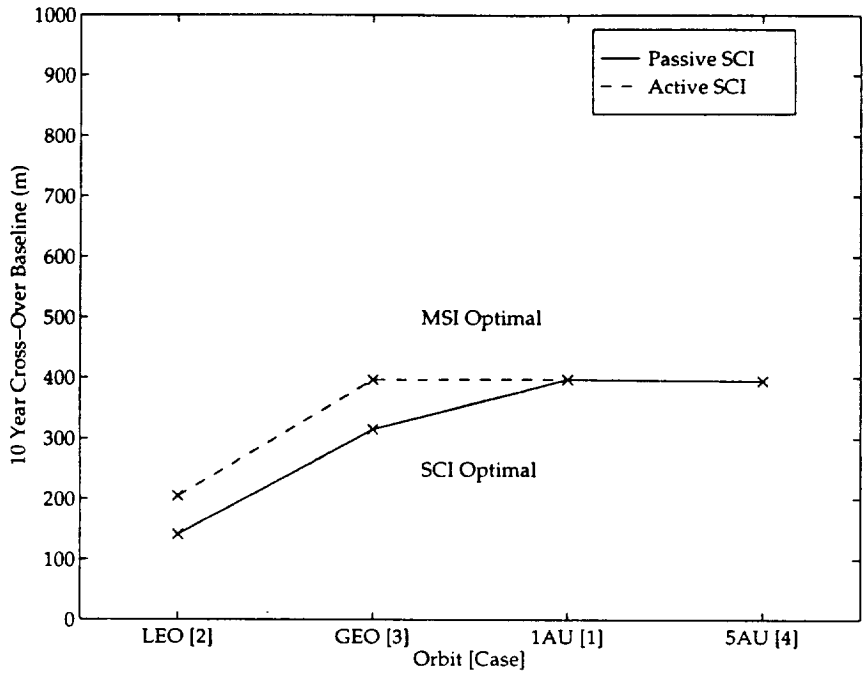


Figure 6-2: 10 Year Cross-Over Baselines for Various Orbits (Cases 2-4)

will not change the minimum mass SCI design. The thrusters are still sized for the slew requirements which are independent of orbit, so the performance and frequency constraints are still not active. Just as in the reference case, the design is gage limited. Therefore, the dry mass versus baseline plots for the two orbits are identical, as can be seen in Appendix A.

Even though the average propellant mass rate curves are different for the two orbits (see Appendix A), this has no effect on the cross-over baseline for practical mission durations (i.e. mission of less than 30 years.) Similar to the reference case, the required mass rates for the 5.2 AU orbit are so small that the equal dry mass point is essentially the cross-over baseline for all practical mission durations. Therefore, the critical time plots of the 1 AU and 5.2 AU orbits are nearly identical and there is no measurable change in the ten year cross-over baseline.

The Earth-orbiting interferometers (Cases 2 and 3) have different cross-over baselines and critical time plots than the reference case because these minimum mass SCI designs are performance limited, not gage limited. The entire minimum mass design of the passive SCI in LEO is presented in Appendix B so the reader can see

how the various design parameters change for a performance limited design. The external/attitude disturbances are greater in Earth orbit and are large enough that disturbance rejection drives the design of the thrusters. These effects are seen in Figures 6-3 and 6-4. In both figures, the baseline at which the curves for the LEO case stop (around 200 m) is the maximum baseline for which all constraints and requirements are met.

Figures 6-3 and 6-4 show the thrust levels and thrust frequencies required for both disturbance rejection and slew requirements for the passive SCI minimum mass designs in LEO and in a 1 AU solar orbit. From these figures, it is clear that the disturbance rejection requirements determine the thruster size and frequency in LEO, whereas the slew requirements determine the thruster size and frequency in solar orbit.

The larger thrusters and the increased frequency of thruster firing cause the performance and frequency constraints to become active in the design of the minimum mass SCI. This is best seen in Figures 6-5 and 6-6, in which the active constraints for a baseline of 100 m as functions of the areal density and aspect ratio are plotted for the structurally passive and active SCI's, respectively. These plots are obtained

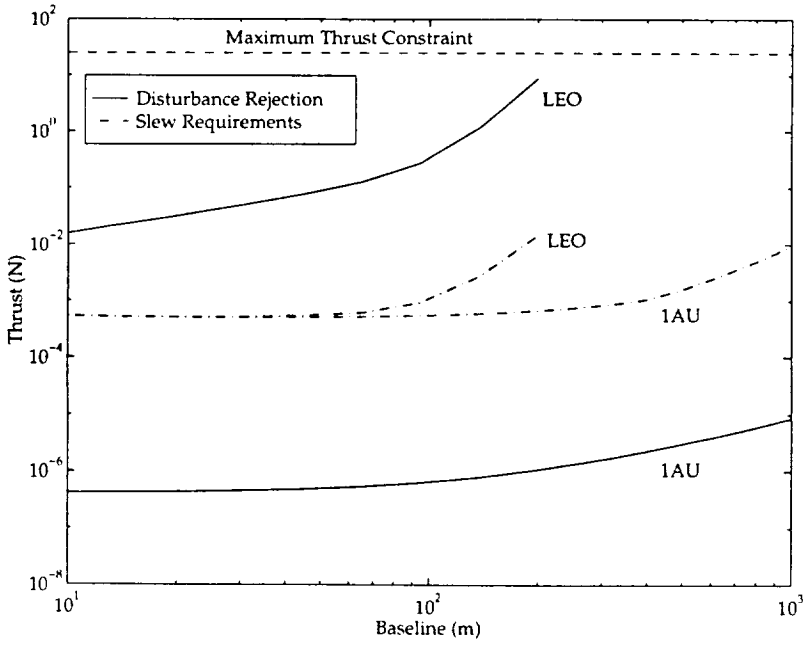


Figure 6-3: SCI Thruster Sizing for LEO

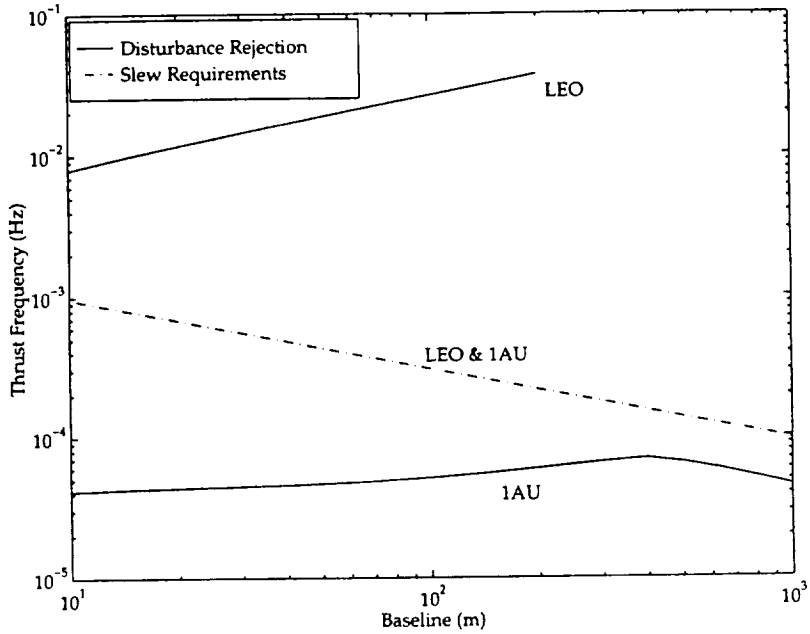


Figure 6-4: SCI Thruster Frequency for LEO

following the procedure described in Section 5.3. Similar plots can be generated for the interferometer in geostationary orbit, but are not presented here. The trends are the same as those described below.

Figure 6-5 reveals that the combinations of areal density and aspect ratio that satisfy all performance requirements and constraints for a passive, 100 m SCI in LEO are bounded by the performance requirement (T9) and the total dry mass constraint (C1).

Figure 6-6 shows the advantage of using active structural control on an SCI whose design is performance limited. The allowable region of areal density and aspect ratio is still bounded by the performance requirement and the dry mass constraint, but by increasing the structural damping of the truss, more combinations of areal density and aspect ratio are enabled. Furthermore, the frequency constraint is no longer a factor.

Since the Earth-orbiting interferometers are performance limited and not gage limited, their dry masses are greater than that of the reference case. Figure 6-7 shows the dry mass plot for the passive LEO interferometer and can be compared

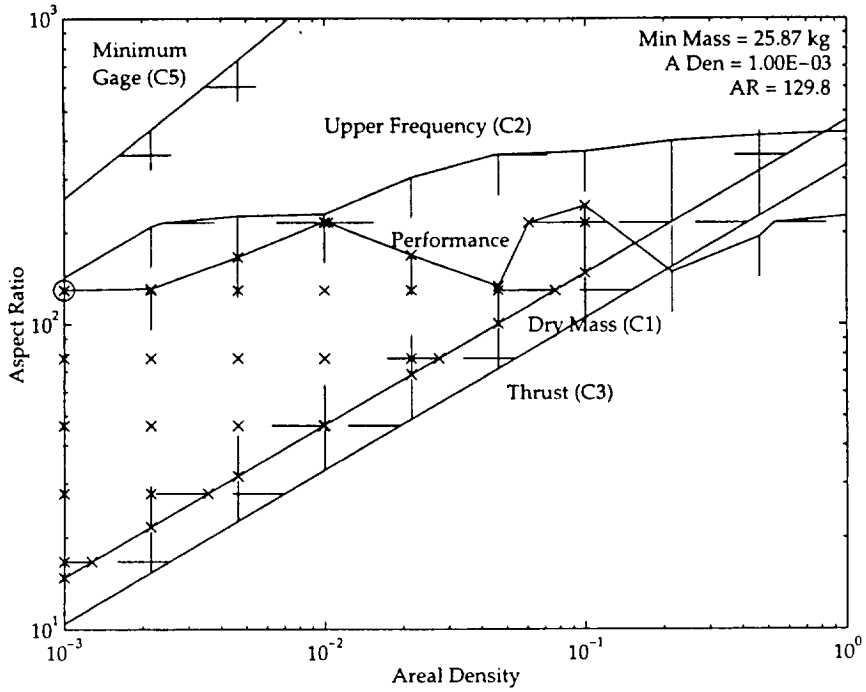


Figure 6-5: Computation of Minimum Mass Passive SCI for a 100 m Baseline in LEO

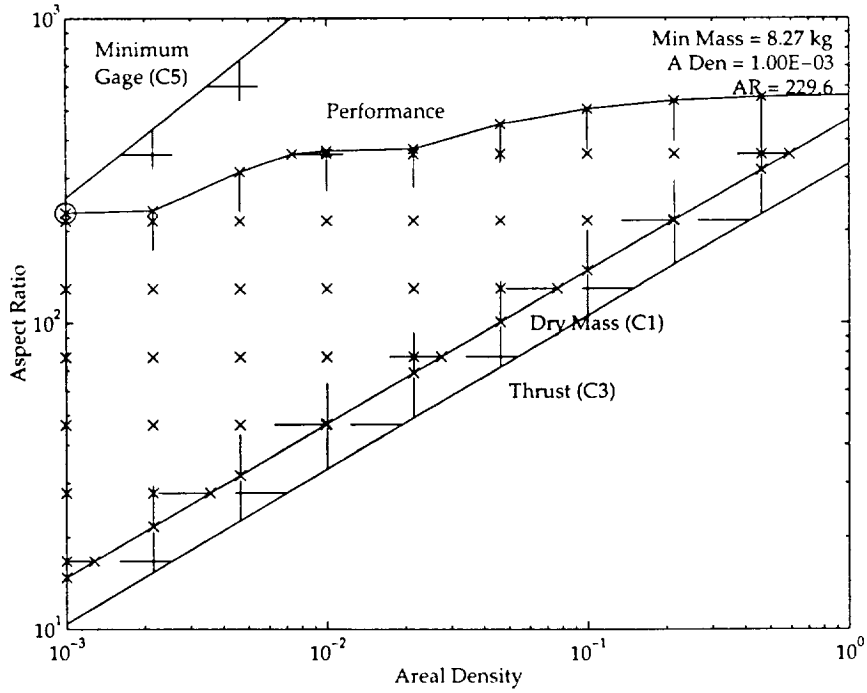


Figure 6-6: Computation of Minimum Mass Active SCI for a 100 m Baseline in LEO

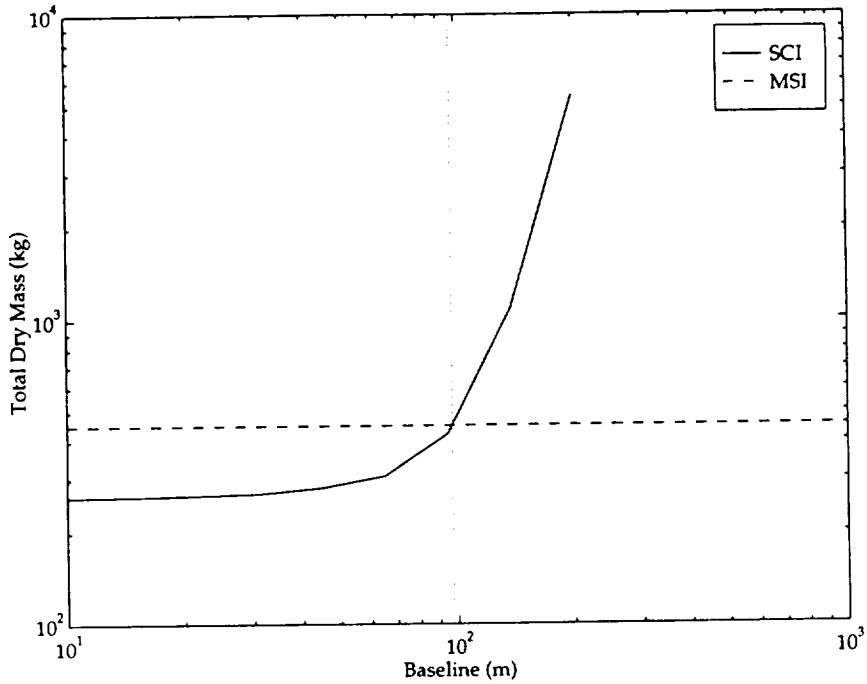


Figure 6-7: Total Dry Masses for Passive Interferometer in LEO

to Figure 5-39. Since the total dry mass of the multiple spacecraft interferometer is assumed constant, the equal dry mass points of the Earth-orbiting interferometers are less than the equal dry mass point of the reference case. Note from Appendix B that for baselines longer than 200 m, the maximum thrust constraint (C3) can not be satisfied by the structurally connected interferometer in low Earth orbit.

The greater attitude disturbances also require greater average propellant mass rates, as can be seen by comparing Figure 6-8 with Figure 5-40. The mass rates are small enough, however, that the decrease in the equal dry mass point causes a decrease in the ten year cross-over baseline. The fact that the Earth-orbiting minimum mass structurally connected interferometers are performance limited then explains the decrease in cross-over baseline as compared to the reference case. This fact also explains the benefit of using active structural control on Earth-orbiting interferometers.

All plots of dry mass, average propellant mass rate, and critical time for Cases 2–4 can be found in Appendix A. As mentioned earlier, the entire minimum mass design of the passive SCI in LEO is also presented in Appendix B. It will be noticed that the performance requirement of the minimum mass passive SCI is not met for

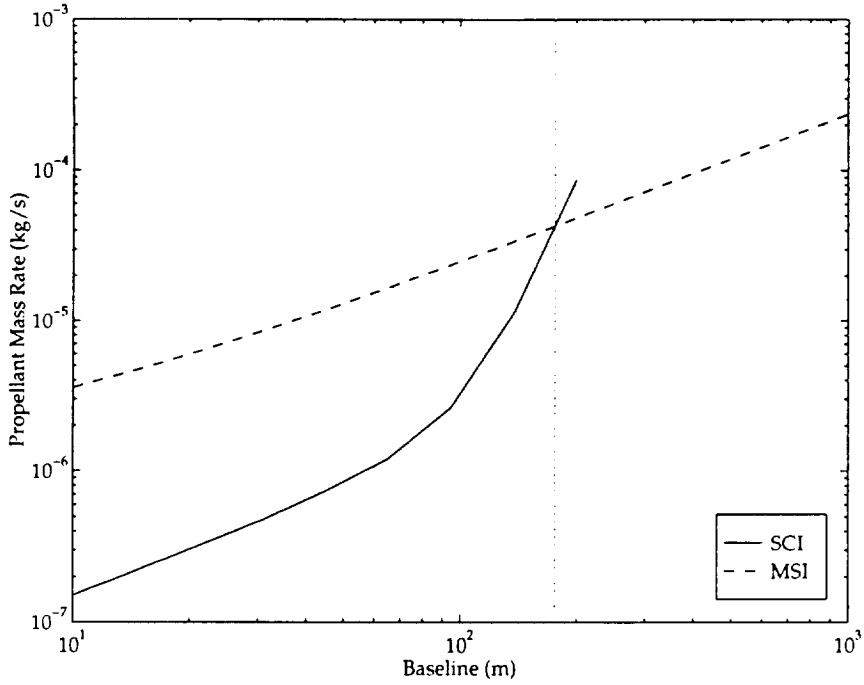


Figure 6-8: Average Propellant Mass Rates for Passive Interferometer in LEO

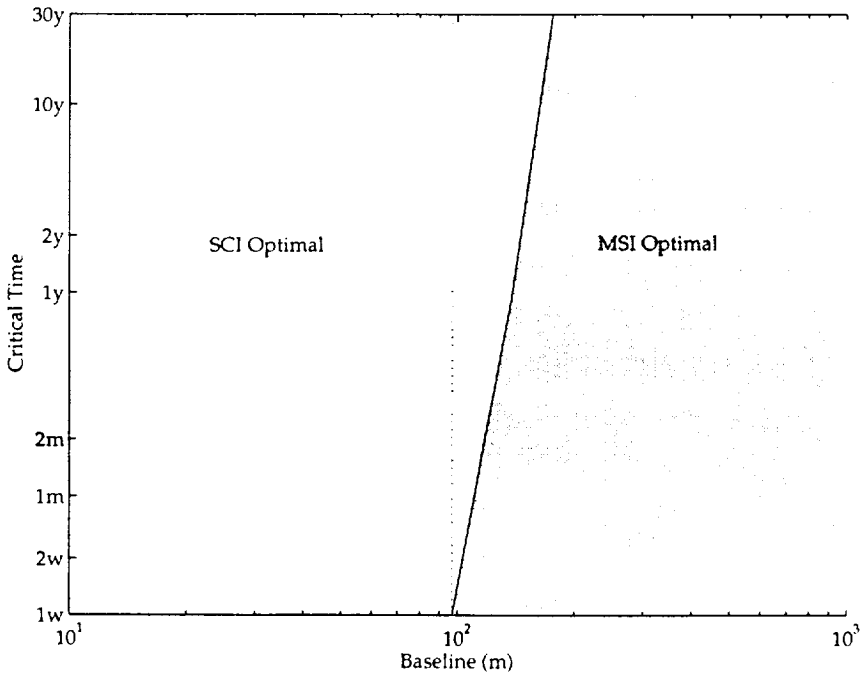


Figure 6-9: Practical Critical Time Plot for Passive Interferometer in LEO

all baselines. This is a consequence of using interpolation to generate the constraint curves of Figures 6-5 and 6-6. When a design is performance limited, the calculation of the minimum mass combination of areal density and aspect ratio selects a point on the interpolated performance curve. Since the performance requirement surface is not as smooth as the other constraint surfaces, the points on this interpolated curve may not actually satisfy the performance requirement. There is, however, a combination of areal density and aspect ratio close to that combination calculated that does satisfy the requirement, so the errors in the calculation of the minimum dry mass and average propellant mass rate are small.

## 6.3 Various Orientations (Cases 5-8)

Figure 6-10 presents the ten year cross-over baselines for various orientations of a non-rotating interferometer in a solar orbit at 1 AU. These are Cases 5-8 of Table 2.3. It is apparent from Figure 6-10 that changing the orientation of the interferometer, does not affect the ten year cross-over baseline. It can be inferred from this that

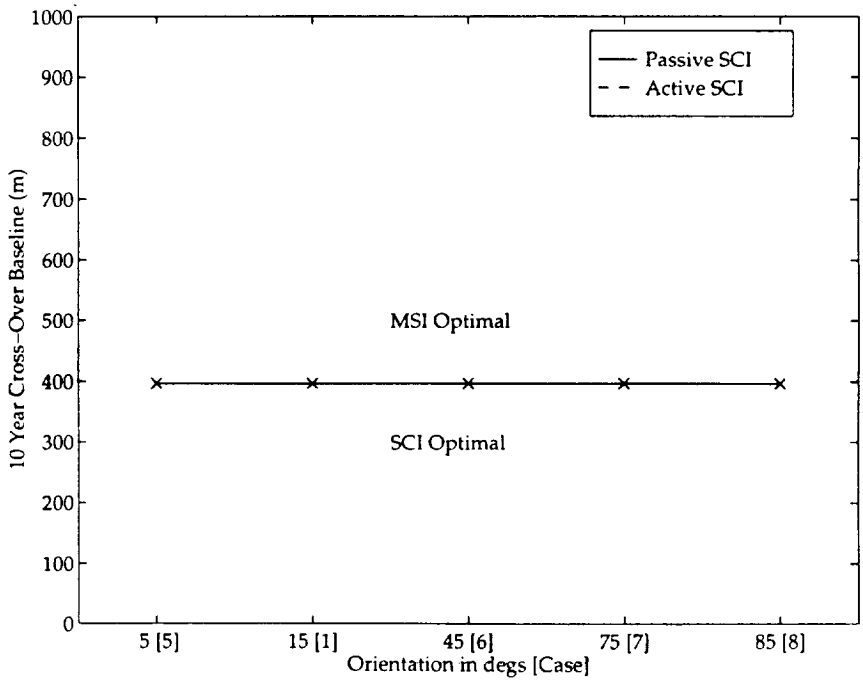


Figure 6-10: 10 Year Cross-Over Baselines for Various Orientations (Cases 5-8)

the critical time plots for the various orientations are similar, and this can be seen in Appendix A. Furthermore, just as in the reference case, adding active structural control to the SCI does not alter the critical time plot.

Changing the orientation of the interferometer does affect the external/attitude disturbance environment, as can be seen in Appendix A. However, none of the active constraints that drive the minimum mass design of the SCI nor the important propellant mass-rate parameters that determine the critical time plot are affected.

The minimum mass SCI is limited, in both the structurally passive and active cases, by the minimum gage constraint (C5). A change in the orientation does affect the thruster size and frequency associated with disturbance rejection, but the thruster design is still dominated by the slew requirements, which are independent of orientation. This can be seen in Figures 6-11 and 6-12. The minimum mass SCI design is therefore gage limited and is the same for all orientations. Consequently, the equal dry mass points of all the critical time plots in Appendix A are the same.

The value of the critical time plot for baselines beyond the equal dry mass point is calculated from Equation 2.3. Since the dry mass plots are the same for all orien-

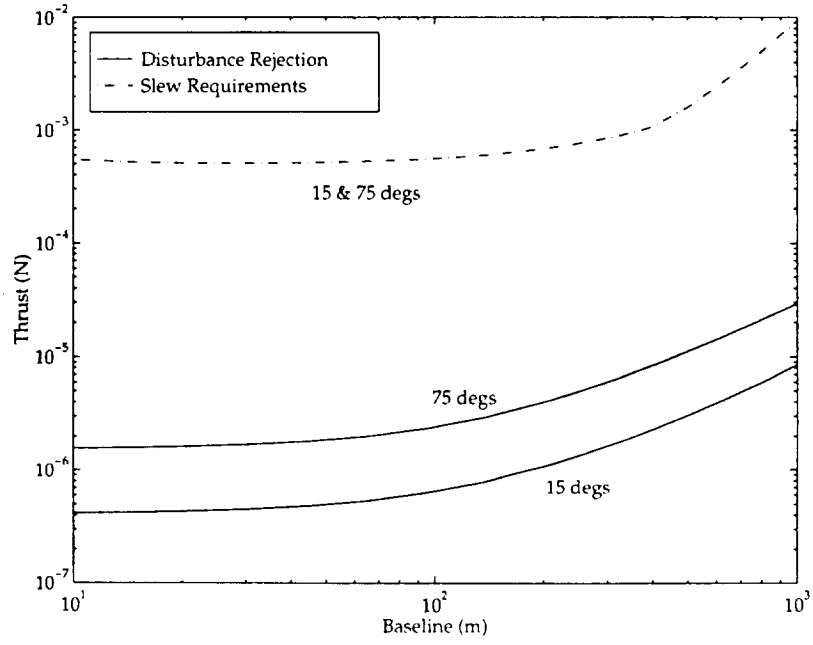


Figure 6-11: Thruster Sizing for Various Orientations

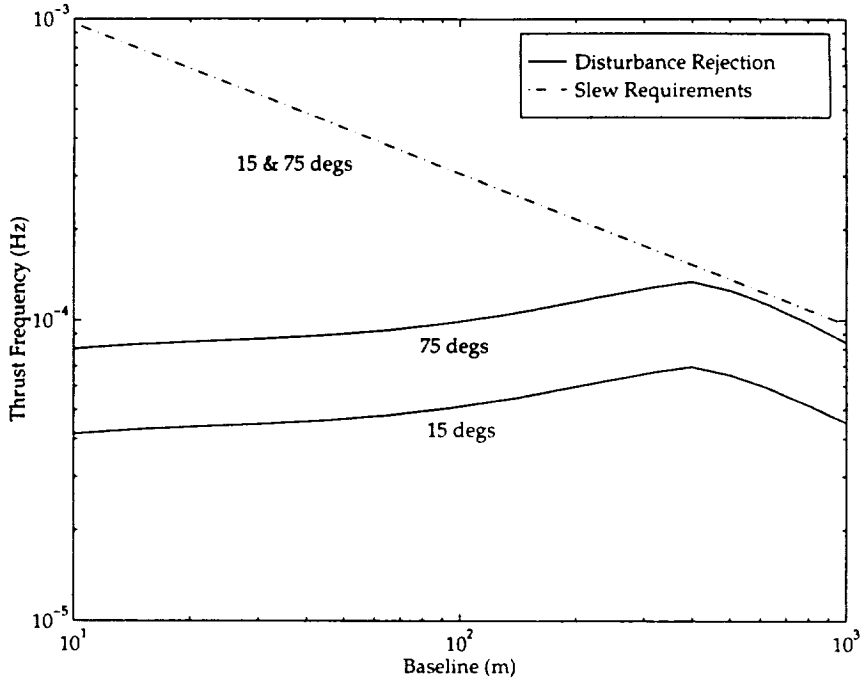


Figure 6-12: Thrust Frequency for Various Orientations

tations, the similarity of the critical time plots (and hence the equivalence of the ten year cross-over baselines) can be explained by examining the average propellant mass rate plots of Appendix A and the reference case, Figure 5-40.

The critical time is a function of the difference between the propellant mass rates of the SCI and MSI. Figure 5-40 illustrates that this difference is dominated by the MSI propellant mass rate. The MSI propellant mass rate is in turn dominated by the compensation of the differential acceleration of the freeflyers caused by solar pressure. (See Figure 5-35.) Since, the differential acceleration due to solar pressure is independent of the orientation of the MSI and dominates the MSI average propellant mass rate for all orientations, the critical time plots of the various orientations are the same.

## 6.4 Interferometer Rotation (Cases 9-12)

Rotating interferometers in different orbits (Cases 9-12 of Table 2.3) are investigated in this section. The critical time plots of these cases are presented in Appendix A while Figure 6-13 presents the ten year cross-over baselines for these cases.

The minimum mass design of the rotating interferometers is assumed to be the same as the minimum mass design of a non-rotating interferometer oriented at 45° to the gravity gradient in the same orbit. From Sections 6.2 and 6.3, it is known that the minimum mass designs of non-rotating interferometers in solar orbit are gage limited, while the minimum mass designs of non-rotating interferometers in Earth orbit are performance limited. Since the rotating interferometers have the same designs as the non-rotating interferometers, the fact that only Earth-orbiting interferometers are performance limited explains why active structural control increases the ten year cross-over baseline only for rotating interferometers in Earth orbit.

The increase in the ten year cross-over baselines for rotating interferometers as

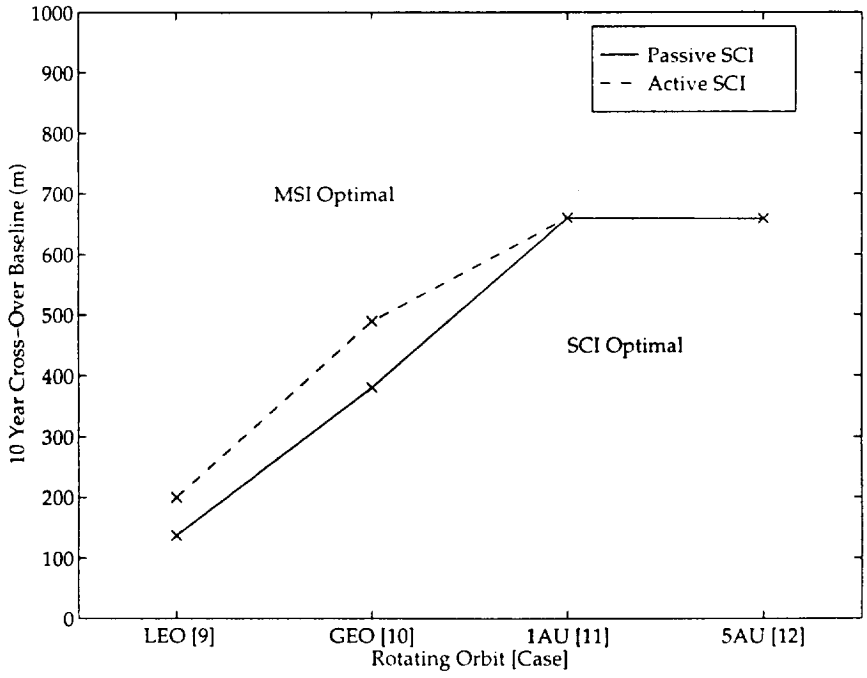


Figure 6-13: 10 Year Cross-Over Baselines for a Rotating Interferometer in Different Orbits (Cases 9-12)

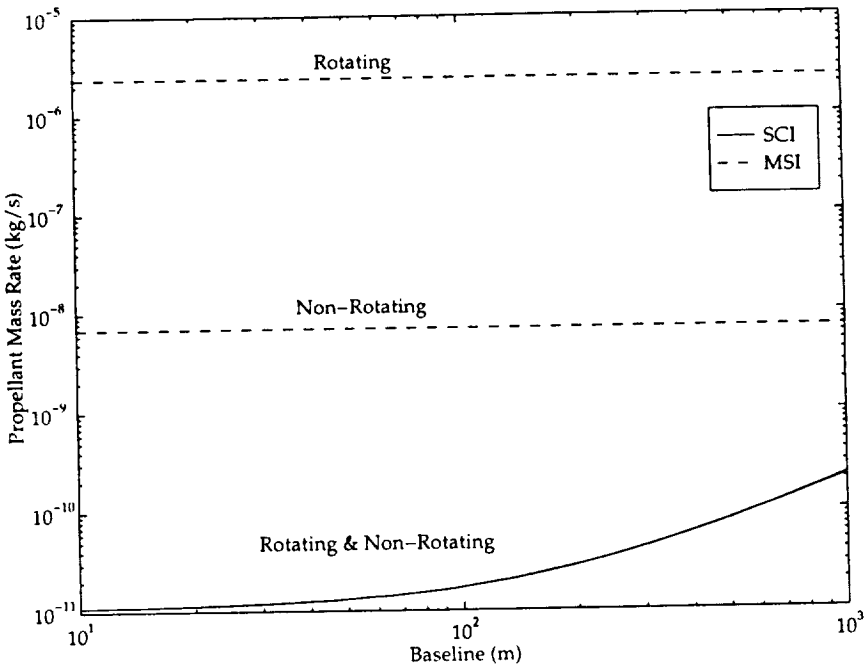


Figure 6-14: Average Propellant Mass Rates for Rotating and Non-Rotating Interferometers in Solar Orbit at 1 AU

compared to non-rotating interferometers is due to the increase in average propellant mass rate required to rotate the multiple spacecraft interferometers. This is shown in Figure 6-14 where the mass rates required for the 1 AU rotating and non-rotating interferometers are compared. For reference, a propellant mass rate of $3 \times 10^{-6}$ kg/s is approximately equal to 100 kg/yr.

## 6.5 Different Materials and Propellants (Cases 13-15)

This section presents the results of changing the truss material to aluminum and using different propellants for attitude control (Cases 13-15 of Table 2.3). The critical time plots of these cases are presented in Appendix A.

Figure 6-15 shows the effect of using aluminum instead of graphite/epoxy as the truss material for the SCI. An aluminum truss is relatively worse than one made of graphite/epoxy and the reason is straightforward. As can be seen in Appendix A, the

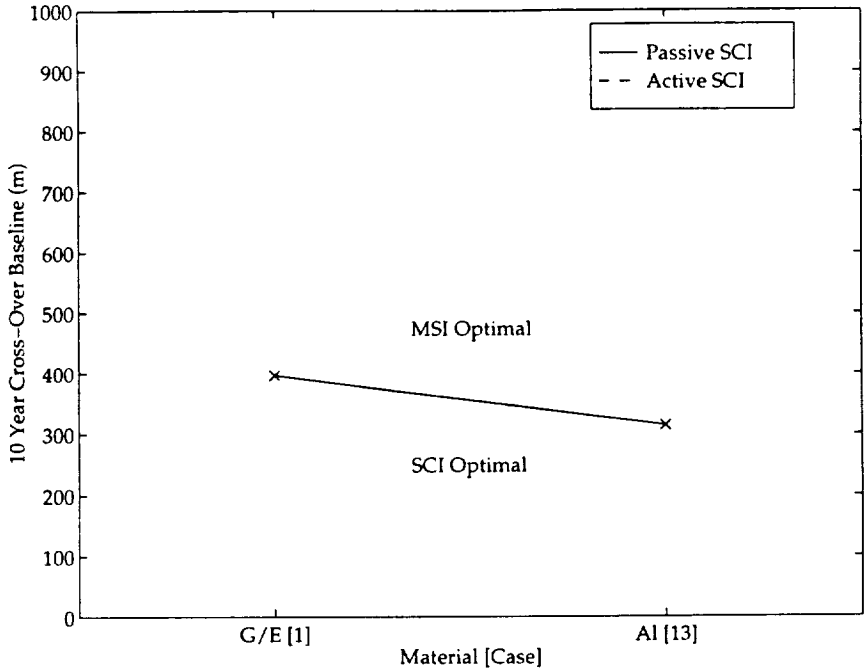


Figure 6-15: 10 Year Cross-Over Baselines for Different Truss Materials (Case 13)

minimum mass SCI design is still gage limited. The geometries of the graphite/epoxy and aluminum trusses are identical, so consequently the SCI with an aluminum truss is more massive. This is shown in Figure 6-16. Once again, since the SCI design is neither performance nor frequency limited, the critical time plots of the structurally passive and active SCI's are the same.

Figure 6-17 shows the lack of effect of using different propellants for attitude control. Changing the propellant affects the average propellant mass rate required because of the change in specific impulse. This is shown in Figure 6-18. The mass rates required, however, are still extremely small so the effect on the cross-over baseline for realistic length missions is negligible.

For this study, the different propellants also had different corresponding maximum allowable thrusts. However, in the 1 AU solar orbit where slew requirements determine thruster size, these maximum thrust levels were only reached for pulsed plasma thrusters (PPT) for baselines beyond 800 m, which is well beyond the ten year or even thirty year cross-over baseline. It must be noted once again that because the SCI design is gage limited, there is no advantage to using active structural control.

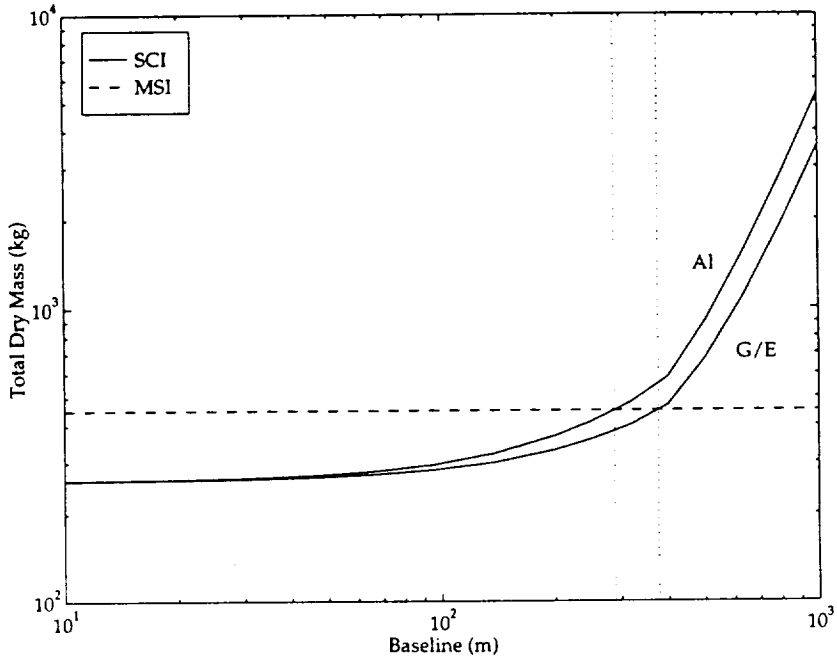


Figure 6-16: Dry Masses of Graphite/Epoxy and Aluminum Truss SCI's

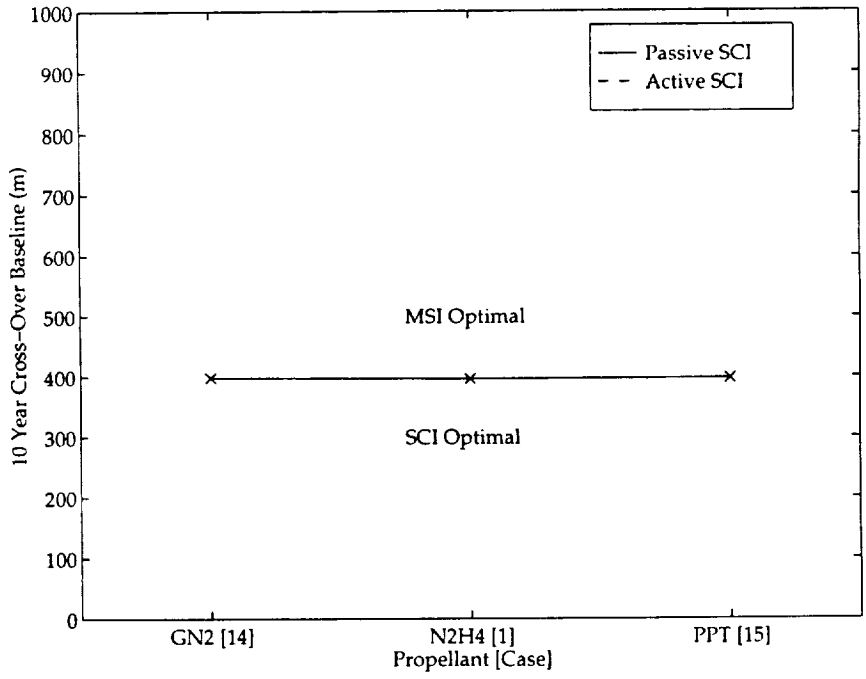


Figure 6-17: 10 Year Cross-Over Baselines for Different Propellants (Cases 14-15)

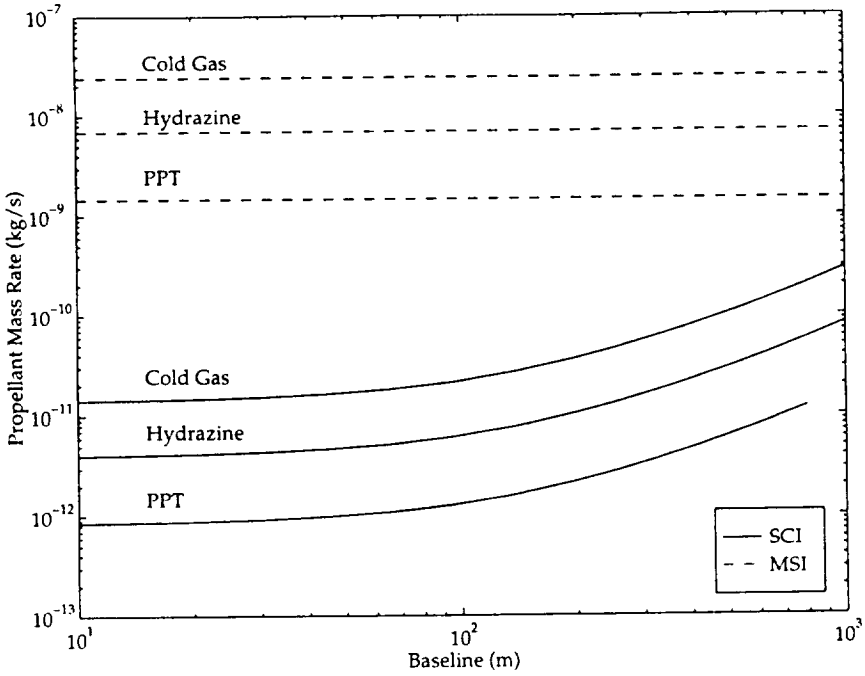


Figure 6-18: Propellant Mass Rates for Various Propellants

## 6.6 Central Spacecraft Thrusters and Thermal Snap (Cases 16-17)

Figure 6-19 presents the results of placing the attitude control thrusters on the central spacecraft and of including thermal snap as a disturbance (Cases 16-17 of Table 2.3). There is no effect on the ten year cross-over baseline if the attitude control thrusters are placed on the central spacecraft instead of at the tips of the truss. The minimum mass SCI design is still gage limited and the SCI propellant mass rate is still much less than the propellant mass rate of the MSI, so the critical time plot is nearly identical to the reference case, Figure 5-41.

The effect of thermal snap is very sensitive to the modeling of the disturbance. Figure 6-20 presents the ten year cross-over baselines for thermal snap forces equal to 10%, 1%, and 0.1% of the strut buckling load.

From Figure 6-20, it is apparent that the minimum mass passive SCI design for a thermal snap force equal to 10% of the buckling load is performance limited. This is so because the active SCI design has a larger cross-over baseline. In fact, as can be

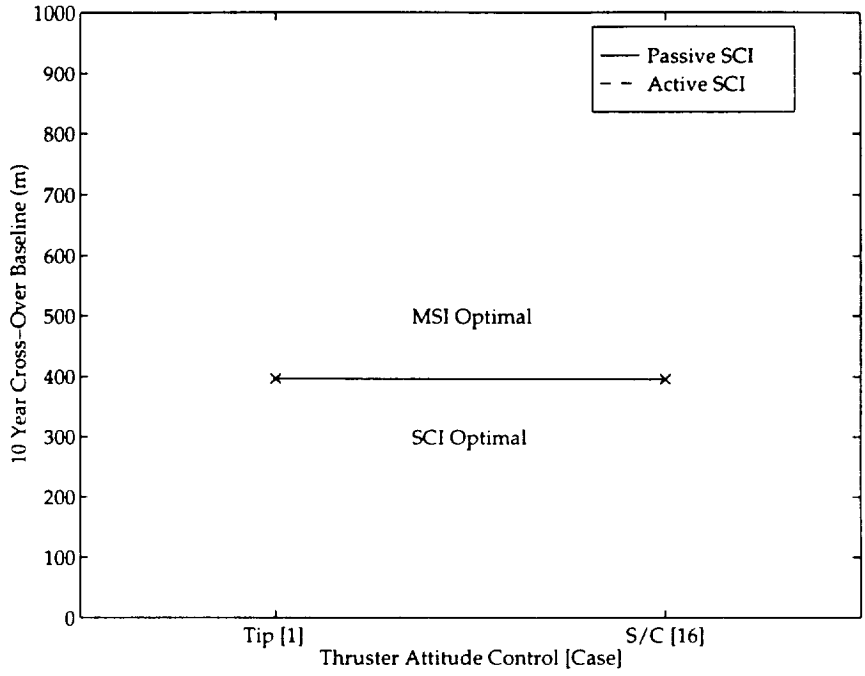


Figure 6-19: 10 Year Cross-Over Baselines for Different Thruster Locations

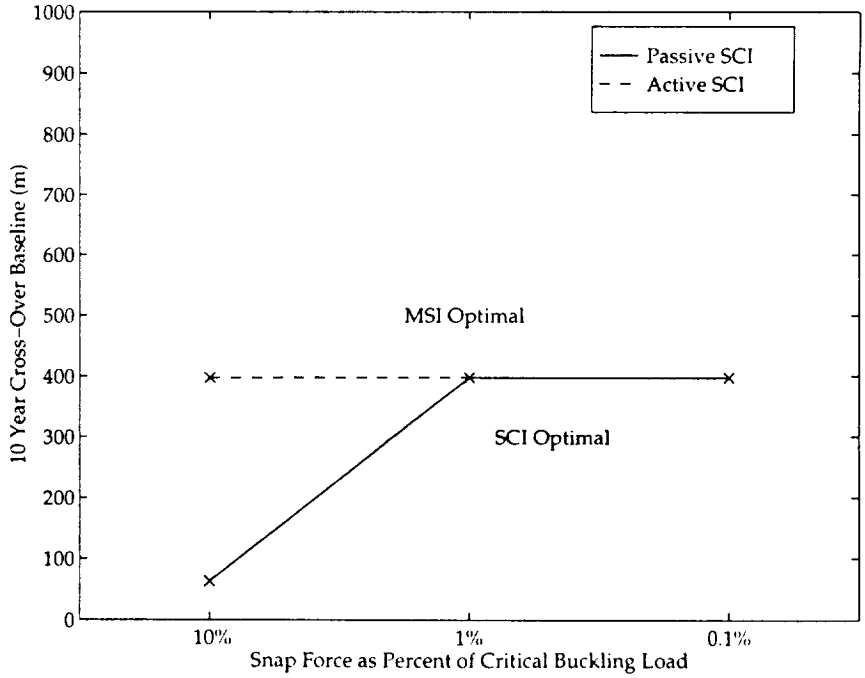


Figure 6-20: 10 Year Cross-Over Baselines for Different Thermal Snap Forces

seen in Appendix A, the passive SCI can not meet the performance requirement for any baseline greater than 130 m. As the thermal snap force becomes smaller, however, the active and passive designs both have the same cross-over baseline as the reference case, implying that both designs are gage limited.

It must be noted that the thermal snap modeling process produces snap forces that are very high. This is shown in Figure 6-21 for the passive SCI. At first glance then, it is surprising that these strong forces don't affect the performance more strongly, and thereby alter the critical time plots. The reason for this is the thermal snap is input to the model as a pair of equal and opposite moments separated by the length of one strut and located roughly one-fourth of the distance between the collector and combiner optics away from one of the tips of the truss. When the length of one strut is very small compared to the distance between the tip and the location of the disturbance, the net effect of these two opposite moments on the displacement of the tip is very small. The ratio of strut length to the distance between the disturbance input and the tip performance output is plotted in Figure 6-22. Additionally, the shorter the strut, the less distance there is between the location of the thermal snap force and the neutral axis of the truss. This causes a reduction in the magnitude of the moment applied to the structure.

Some of the problems of the thermal snap results are the consequence of the interpretation of the modeling of the truss. By interpreting the truss design to be composed of cubic bays, the use of very high aspect ratios produces very short struts. For example, the gage limited reference case design has a constant aspect ratio of 1000 for all baselines, which produces strut lengths of 1–100 cm over the range of baselines. The combination of these strut lengths with the minimum gage constraint and the $\sqrt{L}$ scaling of the strut radius of gyration produces very high critical buckling loads, as can be seen from Figure 5-30. It is also the cause of the small ratio of strut length to separation of snap disturbance and performance.

One possible counter argument to this is that for high aspect ratios and short baselines, the design should not be interpreted as a truss of bay size 1 cm but rather as a single deployable boom, or possibly a tether, with a diameter of 1 cm. If this

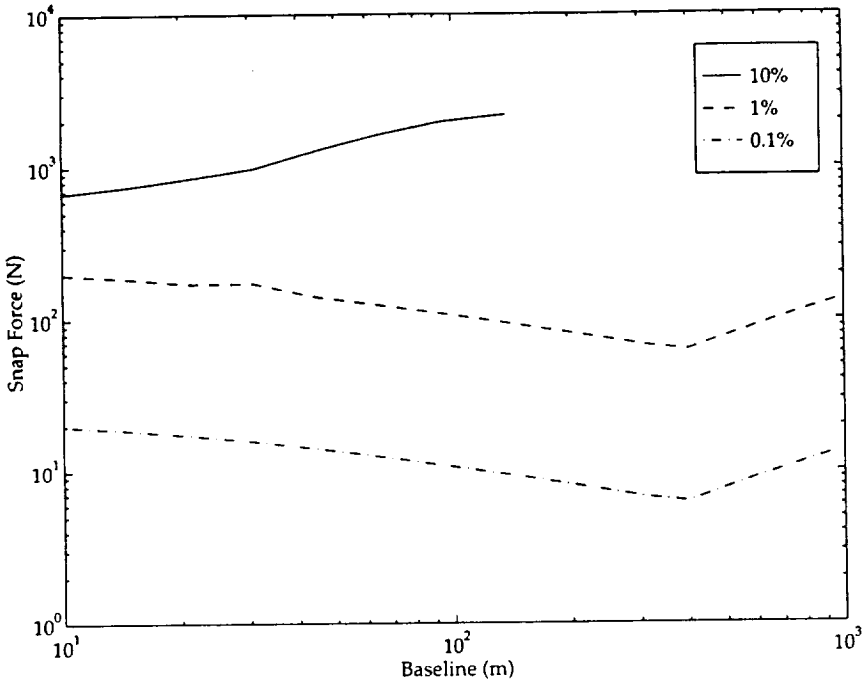


Figure 6-21: Passive SCI Thermal Snap Force

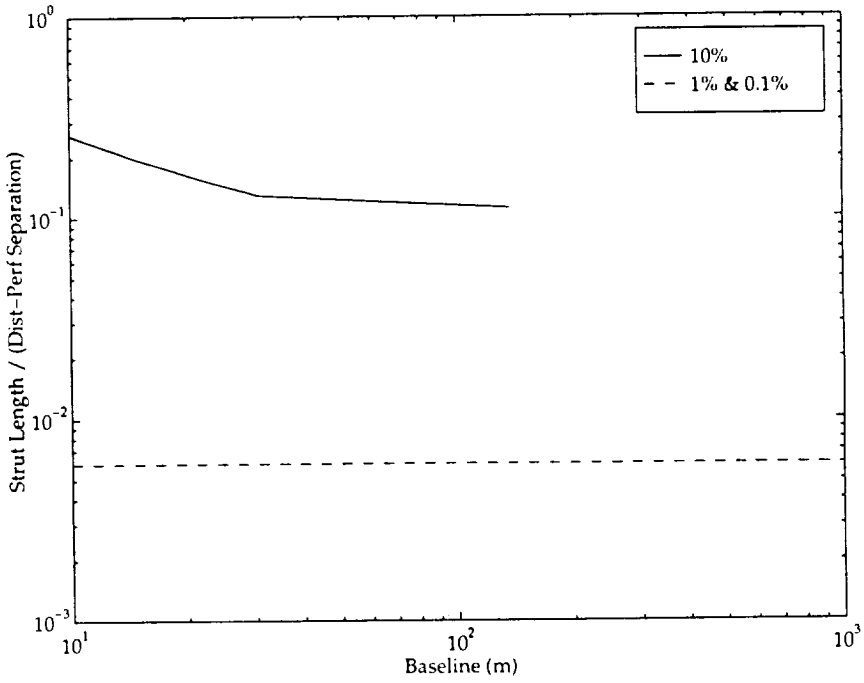


Figure 6-22: Passive SCI Ratio of Strut Length to Separation of Snap Disturbance and Performance

were the case, the modeled mechanism by which thermal snap occurs, the differential heating of different struts in a truss bay, would not apply. It is conceivable that if a single boom were used, thermal snap would not be as large a disturbance as it would be in a truss-like structure, so the conclusion that thermal snap may not have a large effect on the critical time plots may be correct even though the derivation is incorrect. The most important conclusion is that more work needs to be done on the modeling of thermal snap, and specifically, more experimental data needs to be analyzed.

## 6.7 Reaction Wheels as Attitude Control Actuators (Cases 18-20)

This section presents the results of using reaction wheels as the primary source of attitude control (Cases 18-20 of Table 2.3). The critical time plots of these cases are presented in Appendix A. Figure 6-23 presents the ten year cross-over baselines for a non-rotating interferometer with reaction wheels for attitude control and in solar orbit at 1 AU. The two cases presented are distinguished by the location of the thrusters used for desaturation, whether the thrusters are located at the tips of the truss or on the central spacecraft.

Figure 6-23 is identical to Figure 6-19 which indicates that the use of reaction wheels, instead of thrusters, as the primary source of attitude control has little effect on the critical time plots. Even though the reaction wheels introduce different disturbances, these disturbances are not large enough to cause the minimum mass SCI design to be performance limited. The design is still gage limited. The only difference between the critical time plots presented in Appendix A and the critical time plots discussed in Section 6.6, is the SCI can not meet the maximum reaction wheel mass constraint of 100 kg (C4) for baselines beyond 600 m. Figures 6-24 – 6-26 present the design of the reaction wheels for the minimum mass SCI.

The reaction wheels are sized according to the procedure described in Section 3.4.2 and Figures 6-24– 6-26 reveal that very small wheels are required. This indicates that

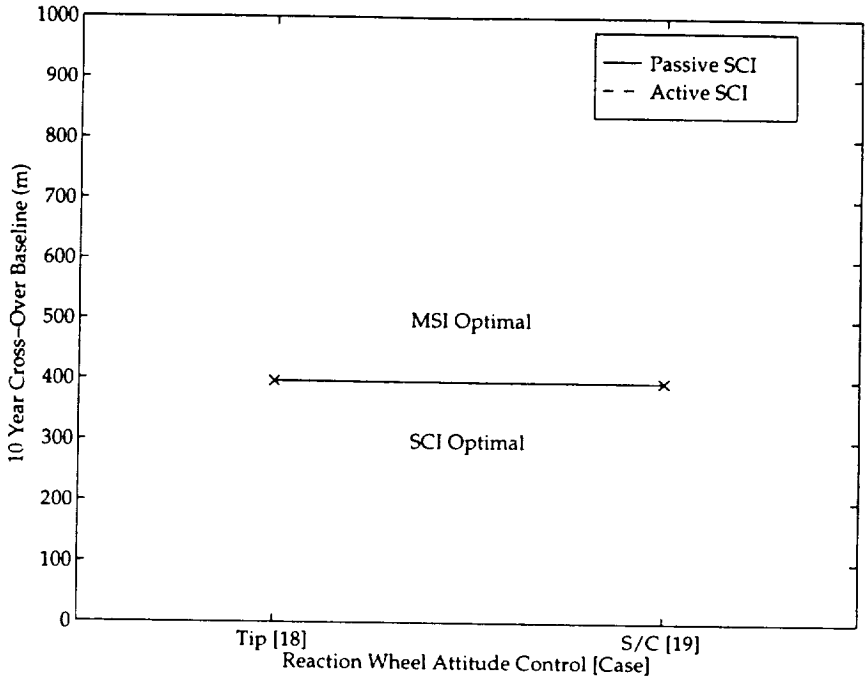


Figure 6-23: 10 Year Cross-Over Baselines for Reaction Wheel Attitude Control (Cases 18-19)

maybe it is not realistic to scale the wheels by keeping the internal stress constant over all sizes. One possibility would be to limit the minimum reaction wheel size to the size of the Hubble wheels and to then scale larger wheels by keeping the stress constant.

The effect of including thermal snap as a disturbance is presented in Figure 6-27 for three different thermal snap force levels. Unlike Figure 6-20, there is no difference between the passive and active SCI designs for any of the force levels. All designs are gage limited. The thermal snap force does not cause the performance requirement to be violated when reaction wheels are used because the stochastic performance requirement, $z_{req}$, associated with reaction wheels is larger than that associated with attitude control thrusters. See Table 3.1. The elimination of the rigid body deadband through the use of reaction wheels allows a greater flexible response.

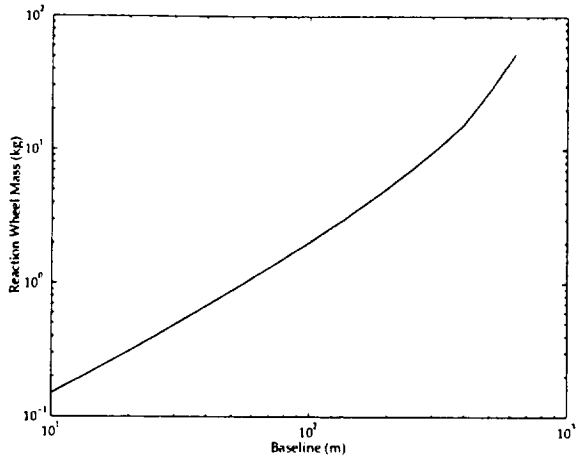


Figure 6-24: Reaction Wheel Mass

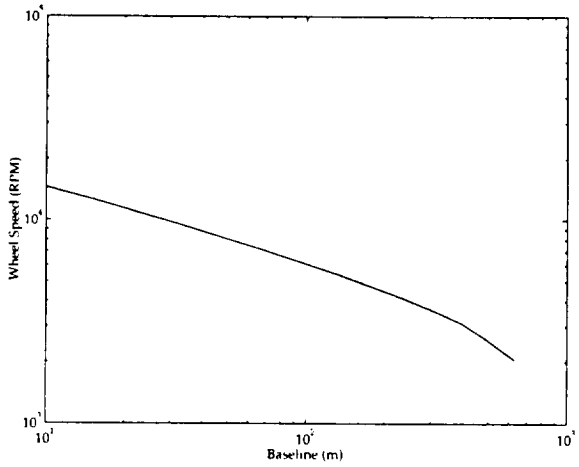


Figure 6-25: Maximum Reaction Wheel Speed

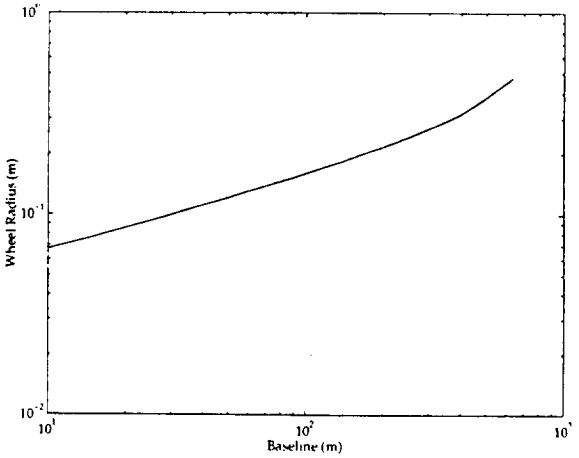


Figure 6-26: Reaction Wheel Radius

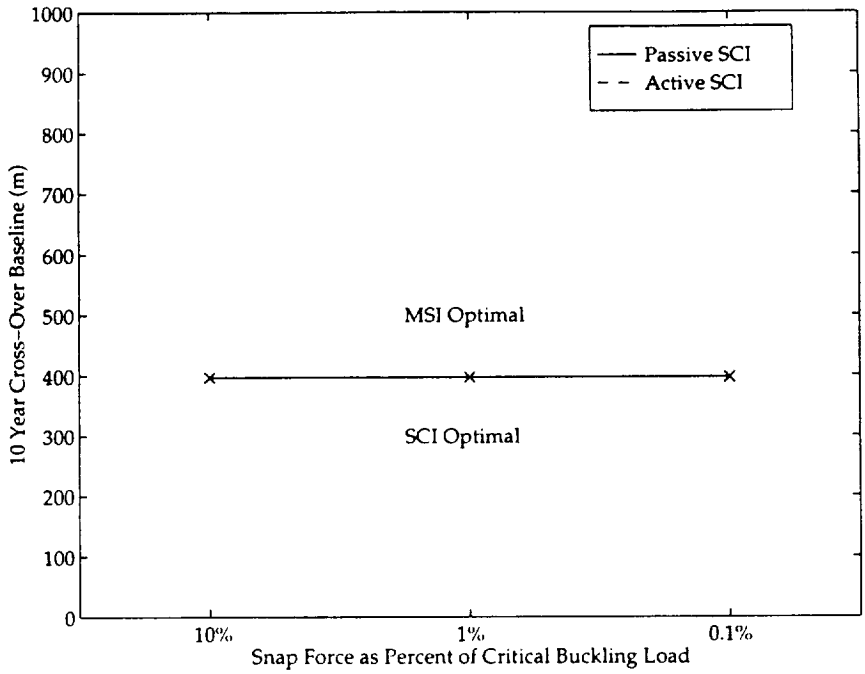


Figure 6-27: 10 Year Cross-Over Baselines for Reaction Wheels with Thermal Snap (Case 20)

## 6.8 Various Performance and Deadband Requirements (Cases 21-22)

Figure 6-28 presents the results of varying the performance requirement, and hence the deadband, of the interferometer (Cases 21-22 of Table 2.3). As expected, since the reference case design is not performance limited, relaxing the performance requirement to 2.50 cm in amplitude does not affect the ten year cross-over baseline nor the critical time plot. Tightening the performance requirement to 0.25 cm in amplitude also does not affect the cross-over baseline nor the critical time plots. This result, however, hides the fact that for short baselines around 10 m, the minimum mass SCI design *is* performance limited, as shown in Figure 6-29. Even though the design is performance limited, the dry mass of the SCI is still less than that of the MSI. For baselines greater than 16 m, the design is again gage limited so the critical time plot shown in Appendix A is nearly the same as that for the reference case.

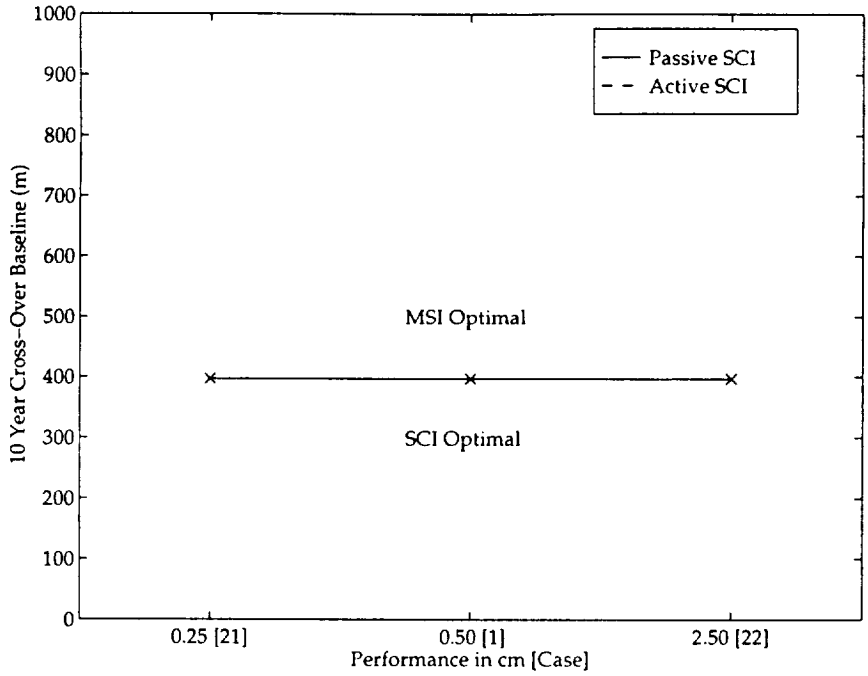


Figure 6-28: 10 Year Cross-Over Baselines for Various Performance Requirements (Cases 21-22)

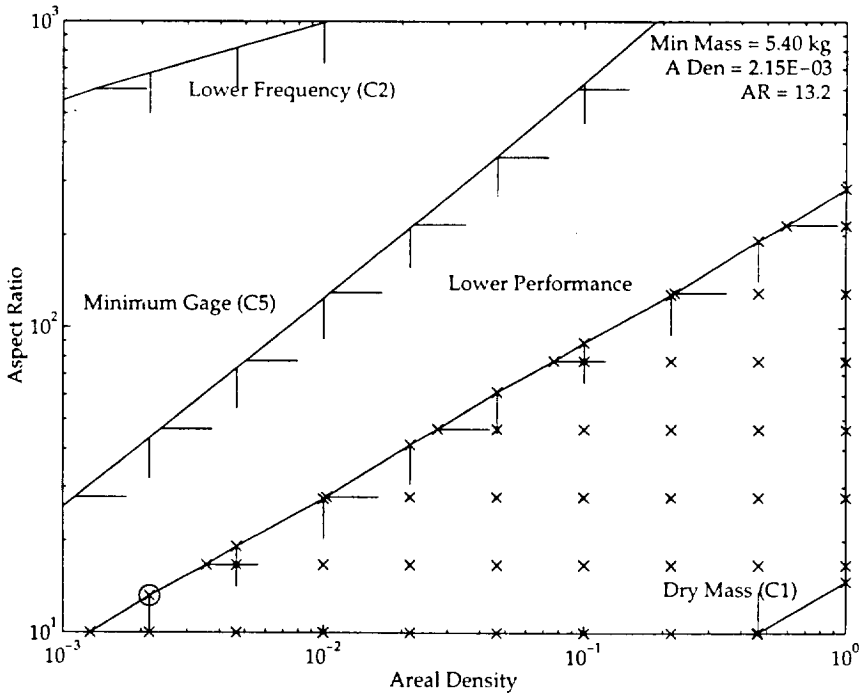


Figure 6-29: Minimum Mass Truss Calculation for 10 m Baseline with 0.25 cm Performance Amplitude (Case 21)

## 6.9 Summary

This chapter described the effects of the various trade parameters on the critical time by explaining the differences between the ten year cross-over baselines of the cases in Table 2.3. All plots of dry mass, average propellant mass rate, and critical time versus baseline can be found in Appendices

It was discovered that the minimum mass SCI designs for all interferometers in solar orbit are gage limited. For non-rotating interferometers, the disturbance levels are extremely small so very little propellant is required to reject them. This causes the critical time plot to have a very steep slope when plotted on the scale of practical mission durations, regardless of orientation, propellant, attitude control actuators, or performance requirement. Only a change of truss material causes a noticeable change in the critical time plot.

It was also discovered that the propellant required to rotate a multiple spacecraft interferometer is very large. This caused an approximate two-thirds increase in the ten year cross-over baseline for solar orbits.

Another important observation was made concerning the effect of thermal snap. When thrusters are used for attitude control, the minimum mass SCI design is sensitive to the modeling of the thermal snap forces. When reaction wheels are used, the minimum mass design is insensitive to the inclusion of thermal snap. This is because the use of thrusters necessitates the budgeting of the performance requirement between rigid-body motion within a deadband and allowable flexible motion. The larger the deadband, the greater the possibility that the vibrations induced by thermal snap will cause the performance requirement to be violated.

# Chapter 7

# Conclusion

## 7.1 Summary and Key Assumptions

This study used the total launched mass of each configuration to compare structurally connected and multiple spacecraft interferometers. To make this comparison, it was assumed that detailed models of the optical subsystems were not necessary. It was assumed that if the absolute positions of the collecting and combining optics were maintained within a specified range, on the order of centimeters, then the optical control subsystem alone would be able to reduce the remaining optical pathlength difference to the required level, on the order of tens to hundreds of nanometers. This corresponded to an assumed gain of 100-120 dB for the optical control system.

Twenty-two different combinations of trade space parameters were used to investigate the effects on the comparison of different orbits, orientations, truss materials, propellants, attitude control actuators, onboard disturbance sources, and performance requirements. Rotating interferometers were also examined in this study. Additionally, this study investigated the advantages of adding active structural control to the SCI in order to keep the collecting and combining optics within the range specified.

The comparison of the structurally connected and multiple spacecraft interferometers was performed through the generation of critical time plots, a process which was described in Chapter 2. Chapter 2 also presented, in block diagram form, the methodology used in this study to compare structurally connected and multiple spacecraft

interferometers. The methodology block diagram, Figure 2-5, graphically illustrates the interactions between the trade space parameters, imposed constraints, and comparison metrics which allows an investigator to qualitatively determine which metrics and constraints are affected by changes in the trade space, *without a large modeling or computational effort.*

The methodology used in this study required the modeling of four areas — the performance, the mission scenario, the plant, and the disturbances. Chapters 3 and 4 described the modeling of these areas and presented the assumptions inherent in each model. Future investigators may use different assumptions or models than those presented, but the interactions of these areas will still be governed by the methodology block diagram, Figure 2-5.

Finally, Chapters 5 and 6 presented the comparisons of the structurally connected and multiple spacecraft interferometers for the 22 different combinations of trade space parameters.

## 7.2 Conclusions

This section summarizes the most important conclusions of this study.

(i) *For non-rotating interferometers, the cross-over baseline is nearly constant over all practical mission durations and parameter variations in solar orbit and is approximately equal to the value of the equal dry mass point.* This corresponds to a cross-over baseline of approximately 400 m for the SCI with a truss constructed of graphite/epoxy and 300 m for an aluminum truss with the assumed dry masses of the other subsystems (optical, thermal, attitude control, etc. as described in Section 2.1) used in this study.

(ii) *The minimum mass SCI designs for all interferometers in solar orbit that do not include thermal snap as a disturbance are gage limited.* This is independent of orientation, truss material, propellant, attitude control actuators, other disturbance sources studied, or performance requirement.

(iii) *There is no benefit to placing the attitude control thrusters at the tips of the connecting truss.* Even though more propellant is required if the thrusters are located on the central spacecraft, the space environment in solar orbit is very benign so the propellant rate required for non-rotating interferometers is very small (less than $10^{-7}$ kg/s.) The savings in propellant mass do not offset the added complexity of locating the thrusters at the tips of the connecting truss. There may, however, be an improvement in response. This study did not address that issue.

(iv) *There is no benefit to adding active structural control to the interconnecting truss for interferometers in solar orbit and* for the formulation of the problem used in this study, *i.e. in order to keep the collecting and combining optics within the range specified.* Since the minimum mass SCI for the non-thermal snap cases are limited by the minimum gage constraint and not by performance or frequency, the addition of active structural control can not reduce the mass of the truss necessary. There may be other reasons for using active structural control which are not apparent in this formulation of the problem. For example, active structural control may be needed to robustify the plant for the optical control system to work.

(v) *The propellant mass required to rotate the multiple spacecraft interferometer is very large.* The ten year cross-over baseline for rotating interferometers in solar orbit is approximately two-thirds larger than that of non-rotating interferometers.

(vi) *The selection of mass as the comparison metric allows the SCI and MSI designs to be compared at a very early stage in the modeling process.* This is illustrated in the methodology block diagram, Figure 2-5. The fact that the SCI and MSI designs can be compared at a very early stage in the modeling process saves the designer time by the elimination of many potential configurations after the calculation of only the external attitude disturbances.

## 7.3 Recommendations for Future Research

This study was a first attempt at determining the cross-over baseline of structurally connected and multiple spacecraft interferometers. It is by no means *the* answer to the question. The results of this study, however, can be used as a guide for future investigators. Obviously, different assumptions regarding parameter values, or even different models of the areas discussed in Chapters 3 and 4, can be used. The following recommendations, however, are those areas of future research that the author believes may contribute significantly to the determination of the cross-over baseline.

(i) More Accurate Modeling of Operational Scenario

A more accurate model of the operational scenario of the interferometer would allow a better estimate of the propellant requirement. This estimate is required for the calculation of the value of the critical time between the equal dry mass and equal mass rate points.

One issue in particular should be looked at — the propellant required for reorientation of the interferometer. This issue requires a more detailed model of the day-to-day operations of the interferometer which includes length of time per measurement, number of measurements per day and average slew distance and time between measurements.

(ii) More Accurate Characterization of Onboard Disturbances

As mentioned in Section 4.2.4, there is very little, if any, experimental data available to characterize the thermal snap disturbance. However, as was seen in this study and in the ISIS performance study [7], thermal snap does have the possibility of greatly affecting the performance of the structurally connected interferometer. Therefore, it is important to characterize this disturbance in order to know if it is necessary to compensate for it. Experiments should be performed to verify analytical models, like that proposed by Kim [30] and summarized in Section 4.2.4. The other solution is to design the connecting truss

so that it doesn't snap, for example, by using a material with a zero coefficient of thermal expansion or by using a tether. (See below.)

Additionally, the reaction wheels sized in this study for the SCI may be too small to be realistic. One possibility is to limit the wheels from being smaller than those used on the Hubble Space Telescope, which would increase the onboard disturbance levels and may cause the SCI design to be performance limited for short baselines.

(iii) Investigation of the Use of Tethers and Other Structural Configurations

The fact that the minimum mass design of the structurally connected interferometer was gage limited in all but one of the solar orbit cases implies that it may be possible to use a tether or some other structural configuration to maintain the separation distance between the combining and collecting optics. A tether would be less massive than an interconnecting truss (although some of the trusses designed in this study are probably best interpreted as single deployable booms) and would still require less propellant than a multiple spacecraft interferometer for station keeping and reorientation. The tether may also act as an isolator between the combining and collecting optics.

(iv) Reduction of the Gain Requirement of the Optical Control System

This study assumed a gain of 100-120 dB for the optical control system. If the real gain of the optical control system is less than that assumed, it is necessary to maintain the position of the combiner and collector optics to more stringent requirements. Studies should be performed to investigate how tightly the position of the optics can be maintained using both passive and active structures in order to reduce the gain required of the optical control system.

(v) Modeling of the Optical Subsystem

The primary assumption of this study was that SCI's and MSI's could be compared to first order without modeling the optical subsystems. It was assumed that if the absolute positions of the combining and collecting optics, treated as

lumped masses, could be maintained within a specified range on the order of centimeters, then the optical control system would handle the rest of the control necessary.

It may be the case, however, that the optical control subsystem is not sufficiently isolated from the structure that the residual structural vibrations, although not the cause of large deformations of the tips of the truss, may interact with the optical subsystem in such a way that prevents the nanometer level performance requirement from being met. Or, as was mentioned above, it may be necessary for active structural control to be used to robustify the plant, thus enabling the performance requirement to be met. A generalized model of the optical subsystem could be devised and then scaled for the different baselines.

On the other hand, it may not be possible to determine if active structural control is necessary without a very detailed model of the layout of the interferometer, which is not available at this stage of decision making. A generalized model may not be good enough because the nanometer level performance requirement is highly dependent on the motion of the individual elements of the optical subsystem. Instead of designing the structure to allow the predetermined optical layout to meet the performance specification, it makes more sense to design the optical layout to meet the performance specification given the structural design.

It may be possible to simultaneously design the structure and the optical subsystem, and in so doing, to design an "optimal" interferometer for a given set of operating conditions and disturbances. Once again, however, this requires extremely detailed models of the structure and optical subsystem which are beyond the level of fidelity available, or even necessary, at this stage of decision making. This optimal integrated design could be performed for the final design of the structurally connected interferometer but is not necessary to determine the cross-over baseline that will be used in making decisions concerning future missions.

Future investigators will have to determine the feasibility and benefits of modeling the optical subsystem.

(vi) Modeling of the Cost

The actual decision as to whether to build and operate a structurally connected or a multiple spacecraft interferometer will be made based on cost, not mass. It was assumed in this study that these two are related, which is true for many space payloads, and to first order would give the same result.

This assumption can, however, be checked by running a standard cost model on both designs. This would, unfortunately, require more detailed models of the two configurations.

(vii) Investigation of Other Structural and Non-Structural Issues

There may be other structural and/or non-structural issues that actually drive the design of the interferometer and that aren't addressed in this study. In that case, the estimates derived here for the cross-over baseline are only upper bounds on the real solution. A simple structural example is the issues involved in deploying a 400 m truss have not been examined here. There may be some reason why this is not feasible (and which may further indicate the advantages of using a tether.)

An example of a possible non-structural issue that may drive the design of the interferometer is the communications bandwidth required for the multiple spacecraft interferometer to control optical elements on different spacecraft. At some point, this issue will have to be resolved in order to operate the thousand kilometer baseline interferometer necessary to map other planets envisioned by the Origins program. Even if this issue is resolved in the future, however, it may be necessary in the near term to only operate structurally connected interferometers.

Additionally, there is the possibility of investigating different configurations of multiple spacecraft interferometers. For example, an interferometer with more

than two collector spacecraft may reduce the total propellant requirement for acquisition of an image. It will also reduce the required time by making multiple measurements simultaneously. The fact that more targets can be imaged or measured in less time may also play a role in decision making.

# References


[1] Kaplan, M., "Origins." Handouts from Origins Technology Workshop, June 4-6, 1996. Provided by Dr. David S. Miller, Director, Space Systems Laboratory, M.I.T.

[2] Dressler, A., *Exploration and the Searth for Origins: A Vision for UltraViolet-Optical-Infrared Space Astronomy*, Association of Universities for Research in Astronomy, Washington, D.C., 1996. Report of the "HST and Beyond" Committee.

[3] "Space Interferometry Mission: Taking the Measure of the Universe," 1996. Final Report of the Space Interferometry Science Working Group.

[4] "The Decade of Discovery in Astronomy and Astrophysics." National Academy Press, Washington, D.C., 1991. National Research Council (U.S.).

[5] "A Road Map for the Exploration of Neighboring Planetary Systems (ExNPS)." Jet Propulsion Laboratory Report No. JPL 96-22, Pasadena, CA, August 1996. Final Report of the ExNPS Team.

[6] Shao, M., M. M. Colavita, B. E. Hines, D. H. Staelin, and D. J. Hutter, "The Mark III Stellar Interferometer," *Journal of Astronomy and Astrophysics*, Vol. 193, 1988, pp. 357–371.

[7] Masters, B. P., M. Ingham, Y. Kim, and D. Surka, "Project ISIS: Pointing & Dynamics." Handouts from Presentation given at JPL, March 6, 1996.

[8] Colavita, M., "New Millenium Interferometer." Handouts from Presentation given, March 25, 1996. Provided by Dr. David S. Miller, Director, Space Systems

Laboratory, M.I.T.

[9] Marzwell, N., J. Cutts, M. Colavita, and E. Mettler, "Multiple Spacecraft Interferometer Constellation (MUSIC)." Handouts from Presentation to NASA Headquarters given, May 2, 1996. Provided by Dr. David S. Miller, Director, Space Systems Laboratory, M.I.T.

[10] Colavita, M., "Optical Interferometry with Separated Spacecraft." Handouts from Presentation given, March 11, 1996. Provided by Dr. David S. Miller, Director, Space Systems Laboratory, M.I.T.

[11] Shao, M. and M. M. Colavita, "Long Baseline Optical and Infrared Stellar Interferometry," *Annual Review of Astronomy and Astrophysics*, Vol. 30, 1992, pp. 457–498.

[12] Hyde, T. T., *Active Vibration Isolation for Precision Space Structures*, Ph.D. thesis, Massachusetts Institute of Technology, 1996.

[13] Spanos, J., R. Z., C. Chu, and J. O'Brien, "Control Structure Interaction in Long Baseline Space Interferometers," in *12th IFAC Symposium on Automatic Control in Aerospace*, (Ottobrunn, Germany), September 1992.

[14] Miller, D. W. and et. al., "Middeck Active Control Experiment (MACE) Summary Report," Tech. Rep. 7-96, Space Engineering Research Center, July 1996.

[15] "Kilometric Baseline Space Interferometry: Comparison of Free-Flyer and Moon-Based Versions." European Space Agency Report No. esa SCI(96)7, Paris, France, June 1996. Report by the Space Interferometry Study Team.

[16] Laskin, R. A., August 13, 1996. Email communication.

[17] Larson, W. J. and J. R. Wertz, *Space Mission Analysis and Design*, Microcosm, Inc., Torrance, CA, 1992.

[18] Olin Aerospace Thruster Spec Sheets. Provided by Adam London, Graduate Student, M.I.T.

[19] Barlow, M. S. and E. F. Crawley, "The Dynamics of Deployable Truss Structures

in Zero-Gravity: The MODE STA Results," Tech. Rep. 1-92, Space Engineering Research Center, Jan. 1992.

[20] Mills, R. A., *Natural Vibrations of Beam-Like Trusses*, Master's thesis, Department of Aeronautics and Astronautics, M.I.T., Cambridge, MA, June 1985.

[21] Colavita, M., June 13, 1996. Email communication.

[22] London, A. P., *A Systems Study of Propulsion Technologies for Orbit and Attitude Control of Microspacecraft*, Master's thesis, Department of Aeronautics and Astronautics, M.I.T., June 1996.

[23] Honeywell Reaction Wheel Spec Sheets, April 1991. Provided by Jim Melody, J.P.L.

[24] Hughes, P. C., *Spacecraft Attitude Dynamics*, John Wiley & Sons, Inc., New York, 1986.

[25] Griffin, M. D. and J. R. French, *Space Vehicle Design*, AIAA Education Series, American Institute of Aeronautics and Astronautics, Washington, DC, 1991.

[26] Eyerman, C. E. and J. F. Shea, "A Systems Engineering Approach to Disturbance Minimization for Spacecraft Utilizing Controlled Structures Technology," Tech. Rep. 2-90, Space Engineering Research Center, June 1990.

[27] Prussing, J. E. and B. A. Conway, *Orbital Mechanics*, Oxford University Press, New York, 1993.

[28] Davis, L., R. E. Wilson, J. E. Jewell, and J. J. Rodden, "Hubble Space Telescope Reaction Wheel Assembly Vibration Isolation System." NASA Marshall Space Flight Center, Huntsville, AL.

[29] Melody, J. W., "Discrete-Frequency and Broadband Reaction Wheel Disturbance Models." Jet Propulsion Laboratory Interoffice Memorandum 3411-95-200csi, June 1995.

[30] Kim, Y. A., "Modeling Thermal Creak." Handouts from Presentation to MIT's Space Systems Laboratory given, Sept. 27, 1996.

# Appendix A

# Total Dry Mass, Average Propellant Mass Rate and Critical Time Plots

This appendix contains the total dry mass, average propellant mass rate and critical time plots versus baseline for all 22 cases in Table 2.3, reproduced here for the reader's convenience. All of the plots for the passive SCI are presented. The plots for the active SCI are presented only if they differ from the passive case, which is true for Cases 1, 2, 3, 9, 10,

For the total dry mass and average propellant mass rate plots, the solid line is the curve for the minimum mass structurally connected interferometer while the dashed line is the multiple spacecraft interferometer curve.

In the critical time plots, the solid line is the critical time, the dashed line is the time at which the propellant mass of the SCI equals 30% of the SCI dry mass at that baseline, and the dash-dot line is the time at which the propellant mass of one of the freeflyers of the MSI equals 30% of its corresponding dry mass. The shaded area represents the combination of mission durations and baselines for which the multiple spacecraft interferometer is optimal.

Table 2.3: Summary of Cases

| Case | T1 - Orientation | | | | | | T2 - Orbit | | | | T3 - Material | | T4 - Propellant | | | T5 - Attitude Control | | T6 - Thruster Location | | T7 - Onboard Disturbances | | | | T9 - Performance | | |
|---|---|---|---|---|---|---|---|---|---|---|---|---|---|---|---|---|---|---|---|---|---|---|---|---|---|---|
| | Rot. | 5° | **15°** | 45° | 75° | 85° | LEO | GEO | **1 AU** | 5.2 AU | **G/E** | Al | GN2 | **N2H4** | PPT | **Thrusters** | RWA | **Tip** | S/C | **Thruster** | RWA | **ODL** | Thermal Snap | 0.25 cm | **0.50 cm** | 2.50 cm |
| 1 | | | X | | | | | | X | | X | | | X | | X | | X | | X | | X | | | X | |
| 2 | | | X | | | | X | | | | X | | | X | | X | | X | | X | | X | | | X | |
| 3 | | | X | | | | | X | | | X | | | X | | X | | X | | X | | X | | | X | |
| 4 | | | X | | | | | | | X | X | | | X | | X | | X | | X | | X | | | X | |
| 5 | | X | | | | | | | X | | X | | | X | | X | | X | | X | | X | | | X | |
| 6 | | | | X | | | | | X | | X | | | X | | X | | X | | X | | X | | | X | |
| 7 | | | | | X | | | | X | | X | | | X | | X | | X | | X | | X | | | X | |
| 8 | | | | | | X | | | X | | X | | | X | | X | | X | | X | | X | | | X | |
| 9 | X | | | | | | X | | | | X | | | X | | X | | X | | X | | X | | | X | |
| 10 | X | | | | | | | X | | | X | | | X | | X | | X | | X | | X | | | X | |
| 11 | X | | | | | | | | X | | X | | | X | | X | | X | | X | | X | | | X | |
| 12 | X | | | | | | | | | X | X | | | X | | X | | X | | X | | X | | | X | |
| 13 | | | X | | | | | | X | | | X | | X | | X | | X | | X | | X | | | X | |
| 14 | | | X | | | | | | X | | X | | X | | | X | | X | | X | | X | | | X | |
| 15 | | | X | | | | | | X | | X | | | | X | X | | X | | X | | X | | | X | |
| 16 | | | X | | | | | | X | | X | | | X | | X | | | X | X | | X | | | X | |
| 17 | | | X | | | | | | X | | X | | | X | | X | | X | | X | | X | X | | X | |
| 18 | | | X | | | | | | X | | X | | | X | | | X | X | | | X | X | | | X | |
| 19 | | | X | | | | | | X | | X | | | X | | | X | | X | | X | X | | | X | |
| 20 | | | X | | | | | | X | | X | | | X | | | X | X | | | X | X | X | | X | |
| 21 | | | X | | | | | | X | | X | | | X | | X | | X | | X | | X | | X | | |
| 22 | | | X | | | | | | X | | X | | | X | | X | | X | | X | | X | | | | X |

Figure A-1: Plots for Passive Case 1 (Reference Case)

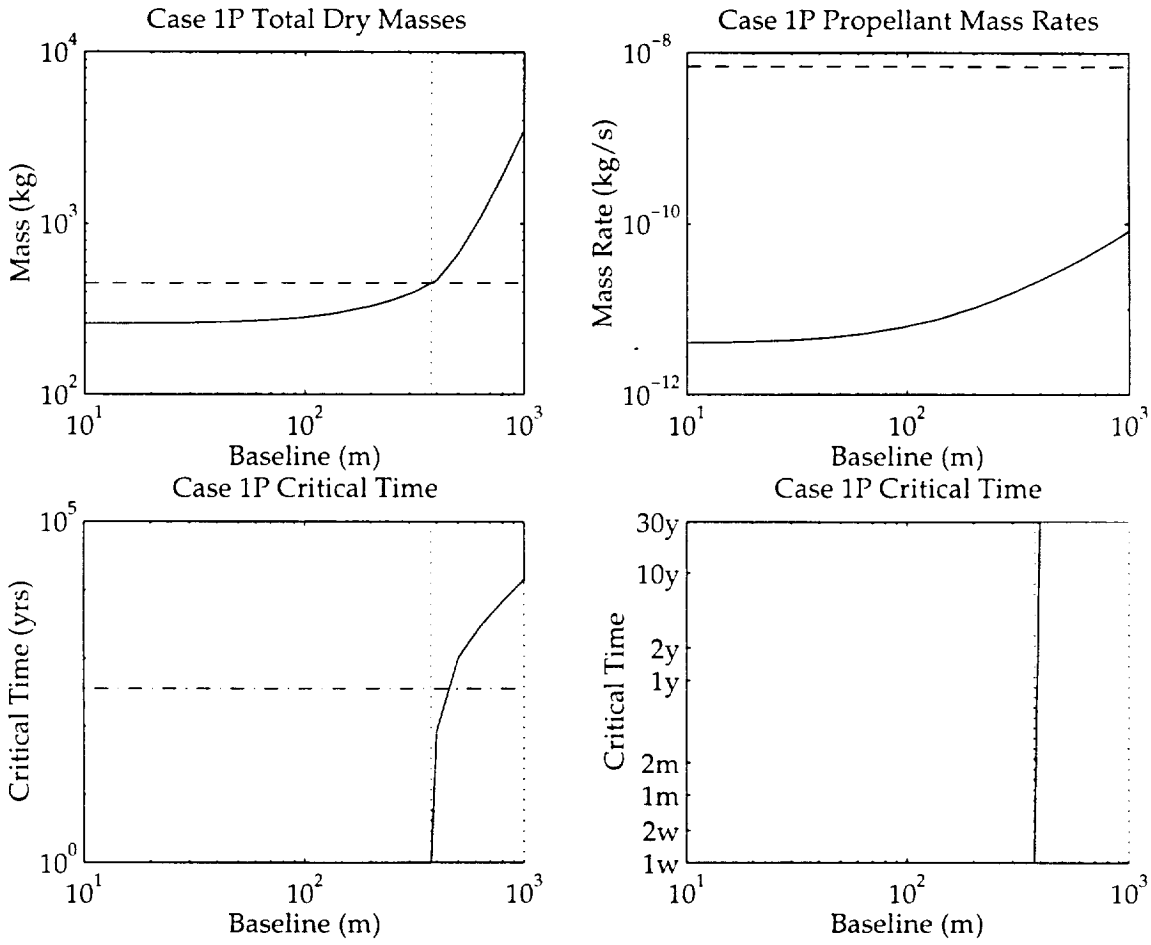

Figure A-2: Plots for Passive Case 2

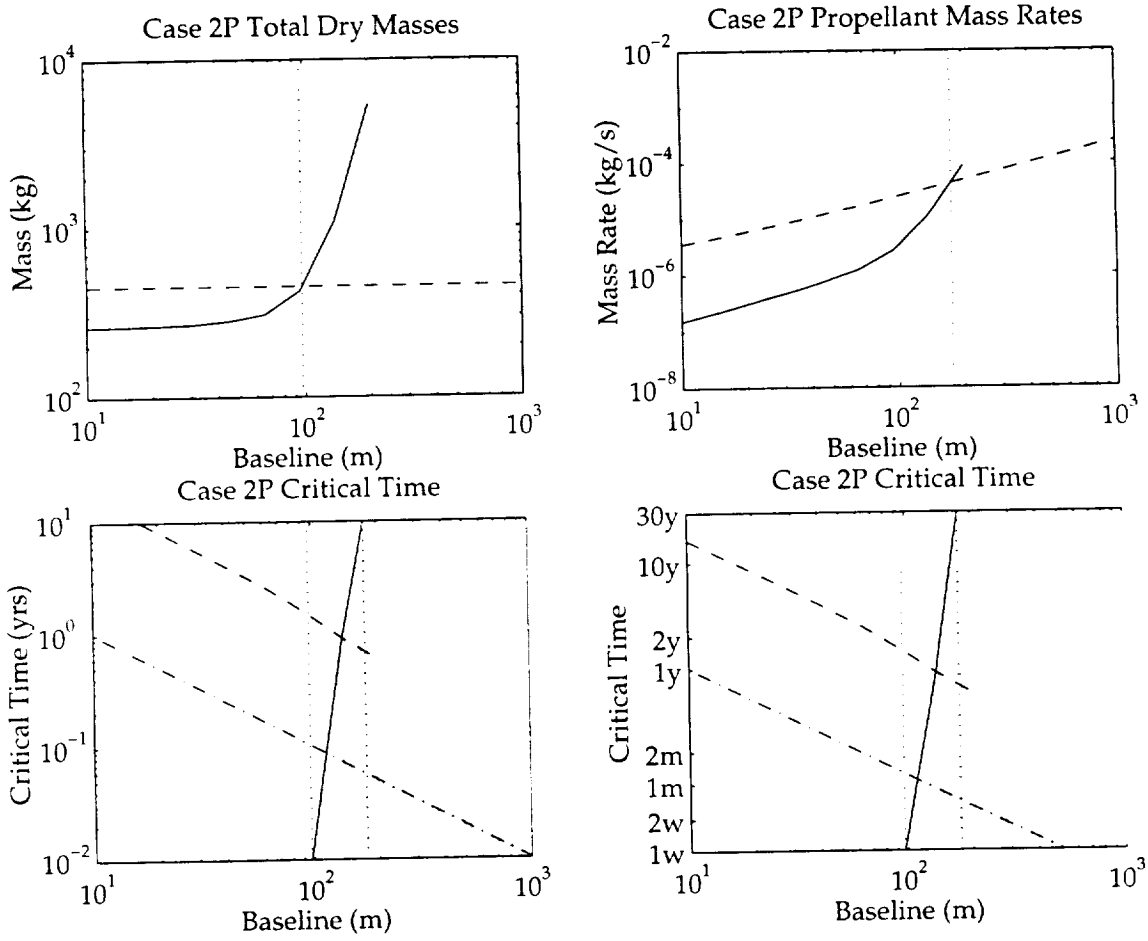

Figure A-3: Plots for Active Case 2

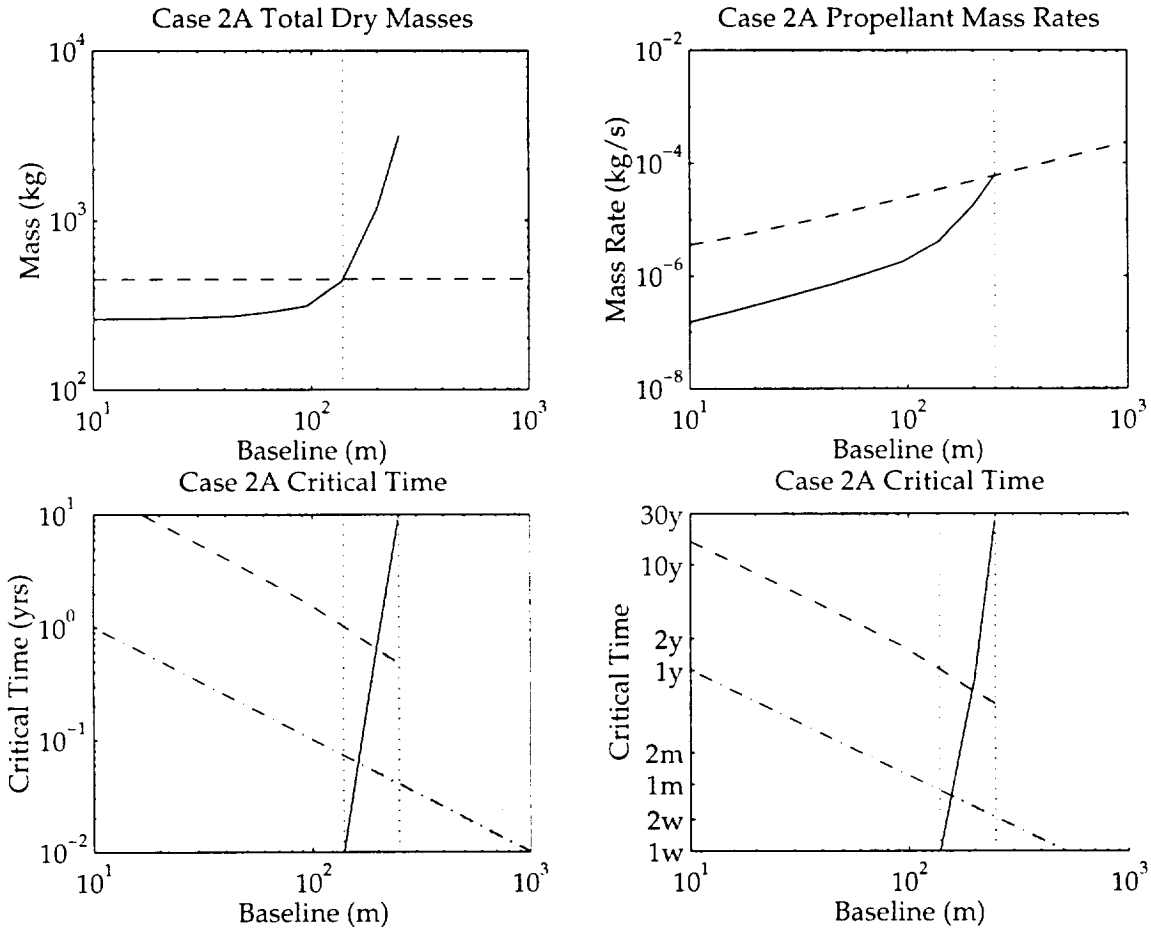

Figure A-4: Plots for Passive Case 3

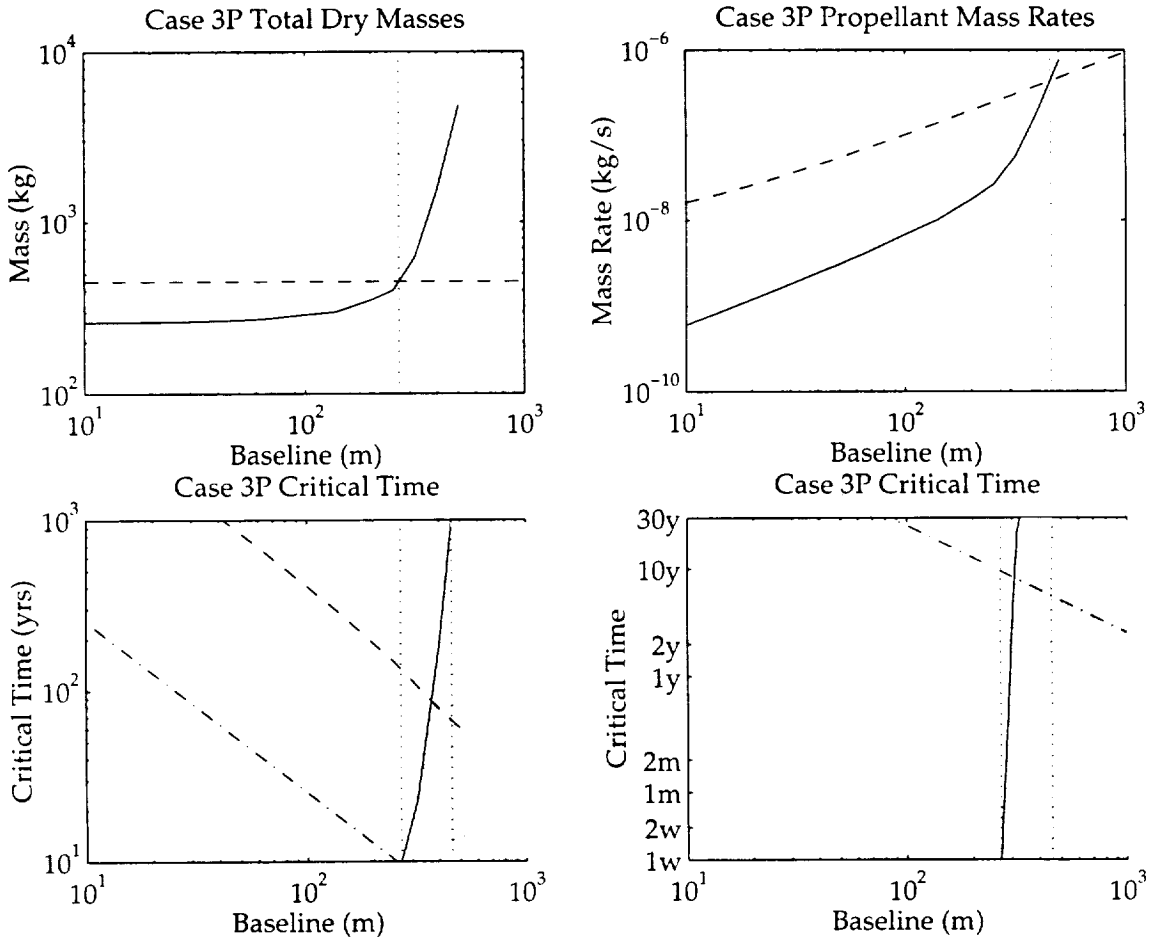

Figure A-5: Plots for Active Case 3

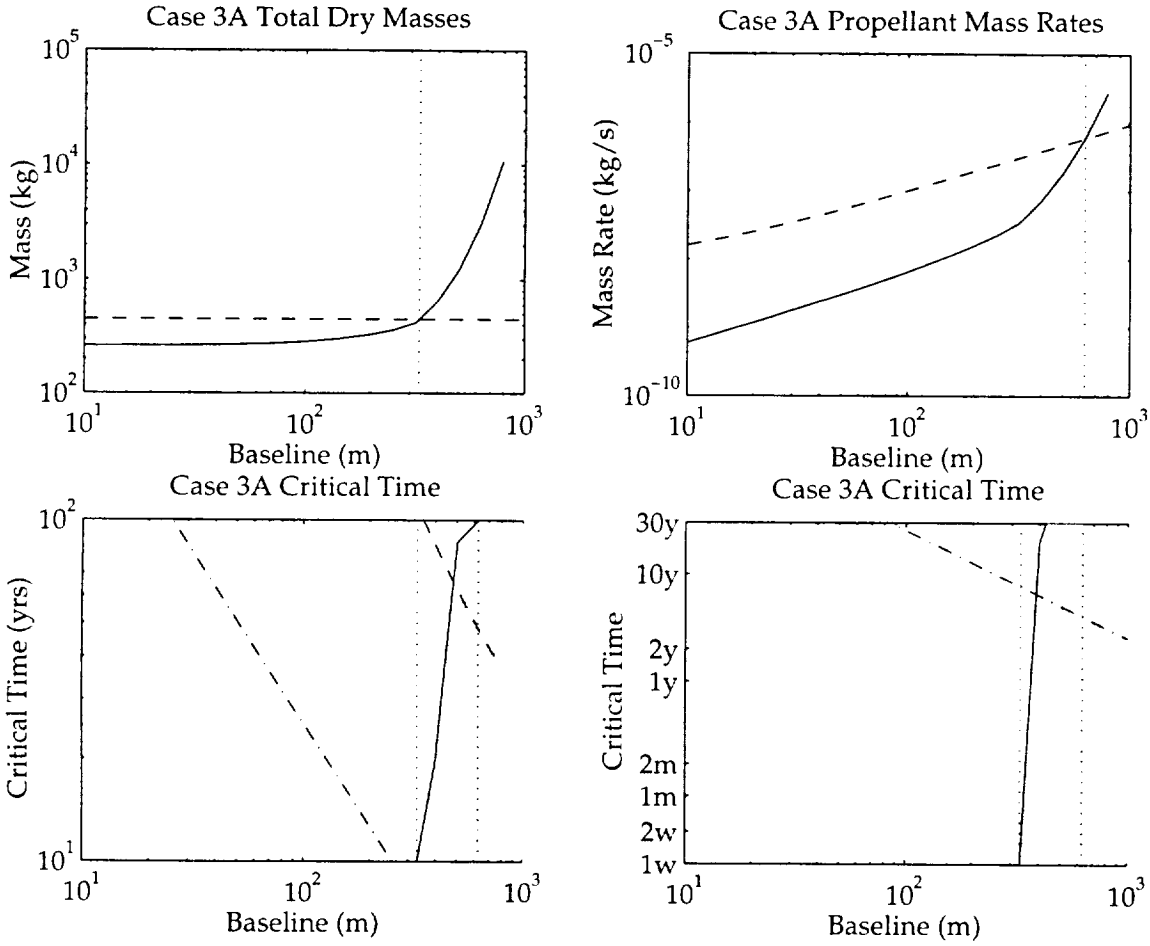

Figure A-6: Plots for Passive Case 4

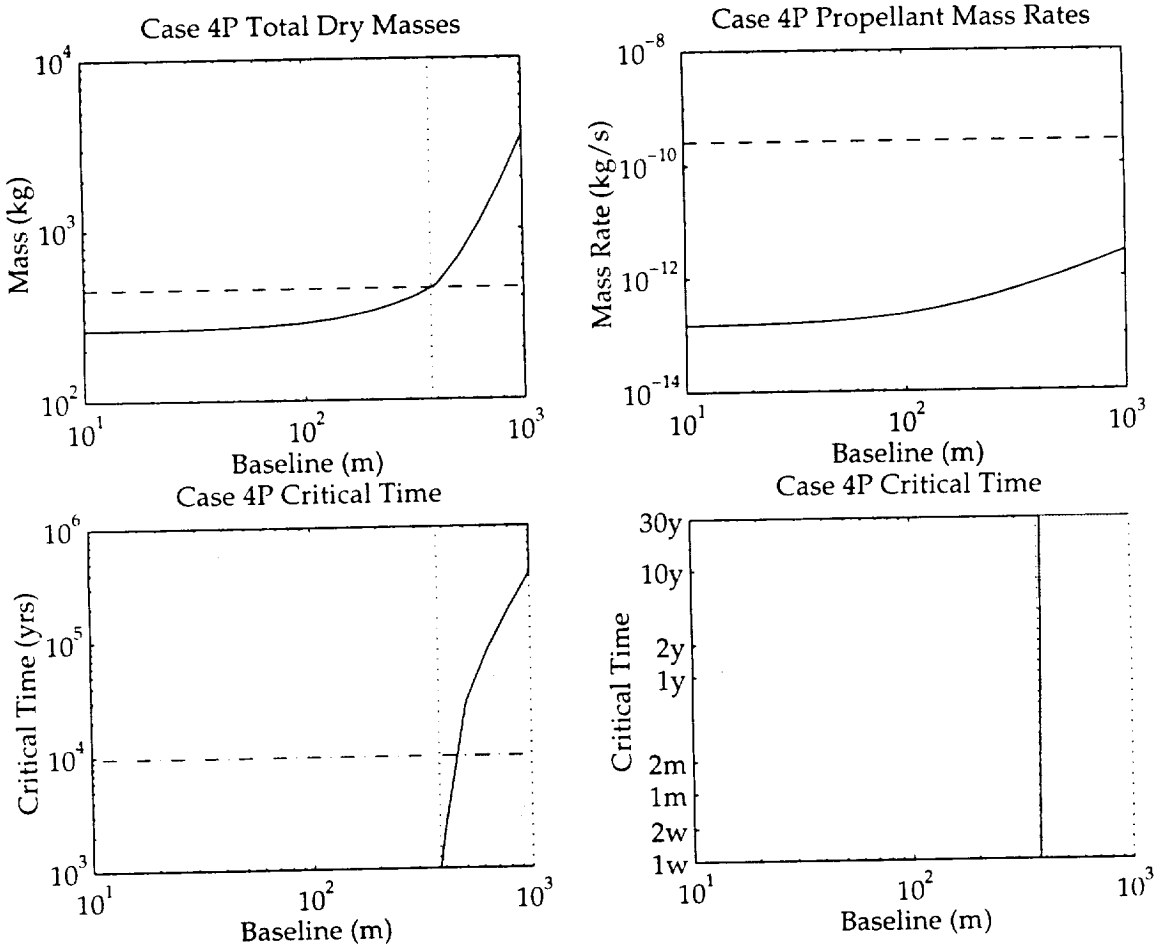

Figure A-7: Plots for Passive Case 5

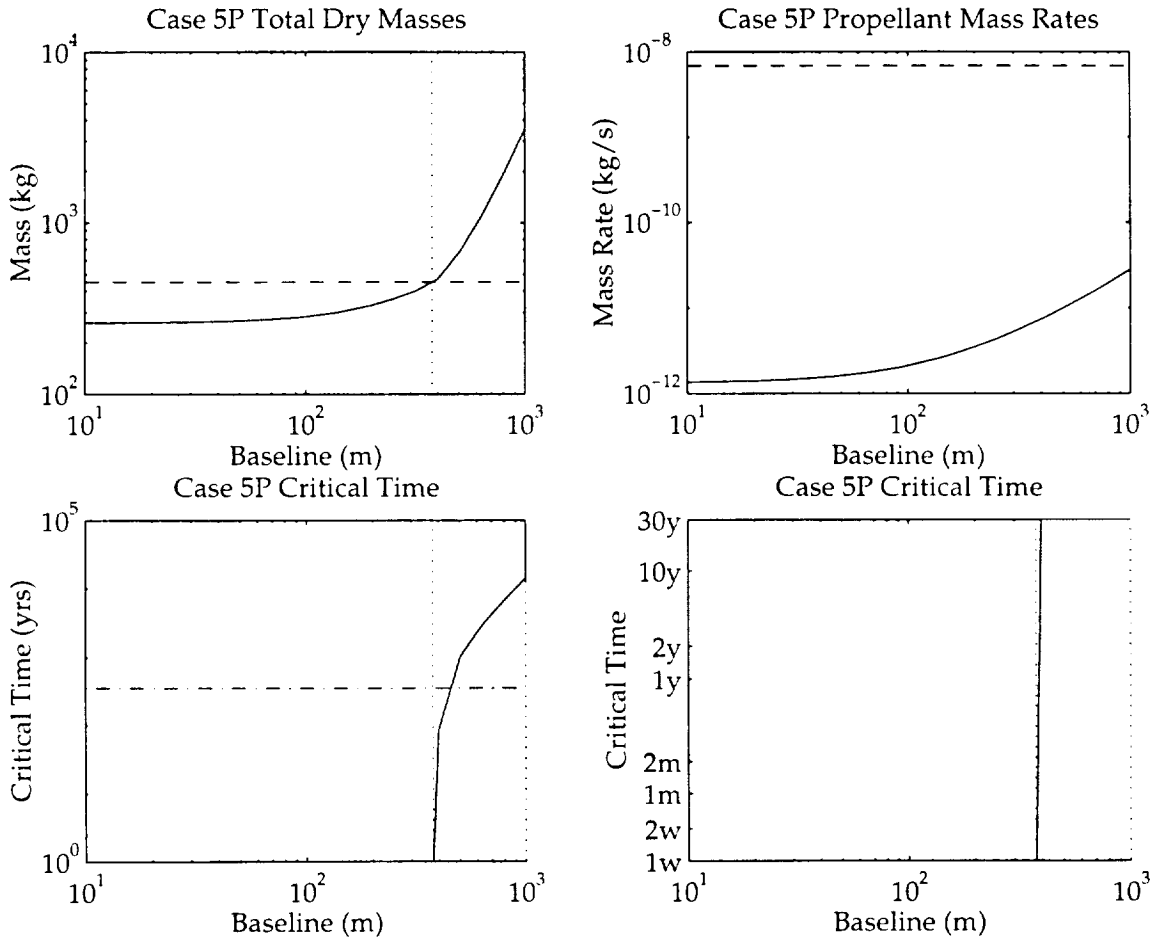

Figure A-8: Plots for Passive Case 6

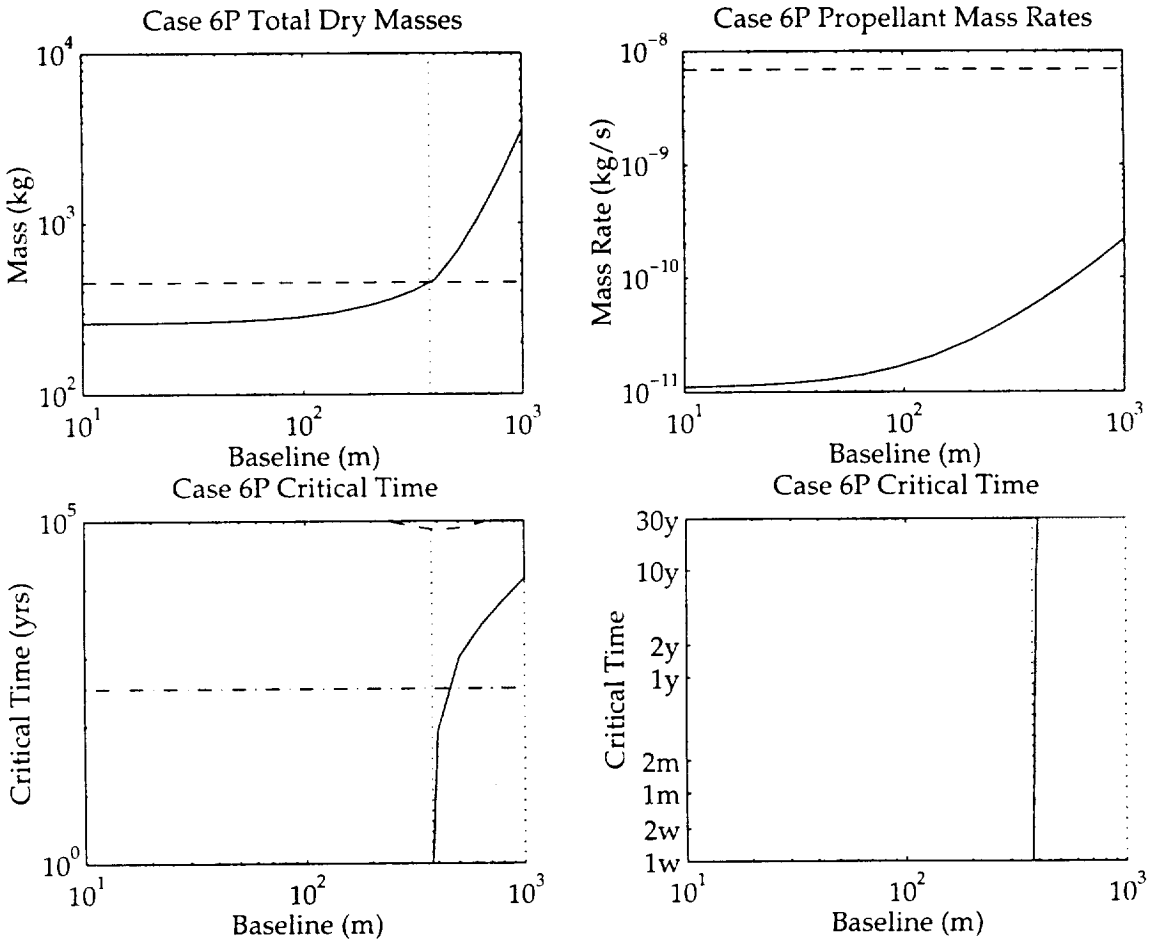

Figure A-9: Plots for Passive Case 7

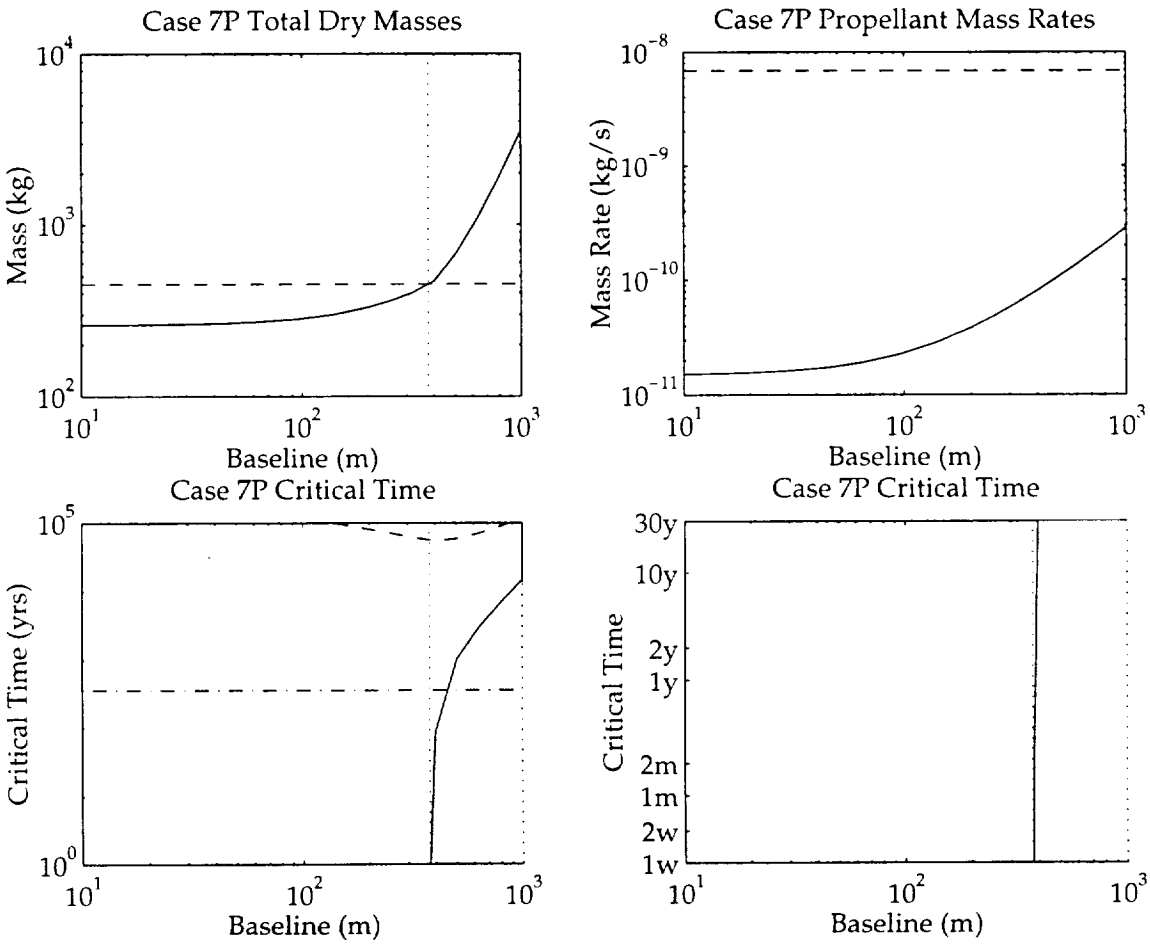

Figure A-10: Plots for Passive Case 8

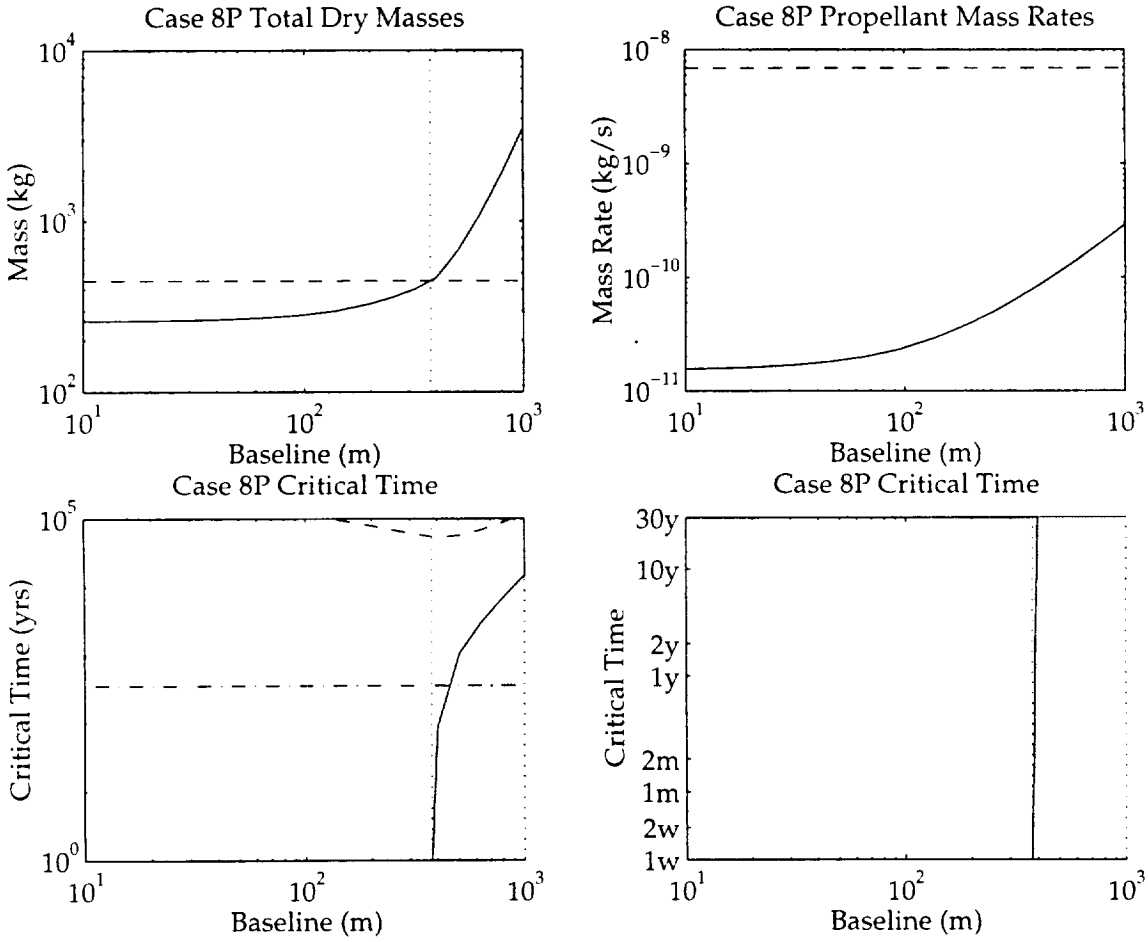

Figure A-11: Plots for Passive Case 9

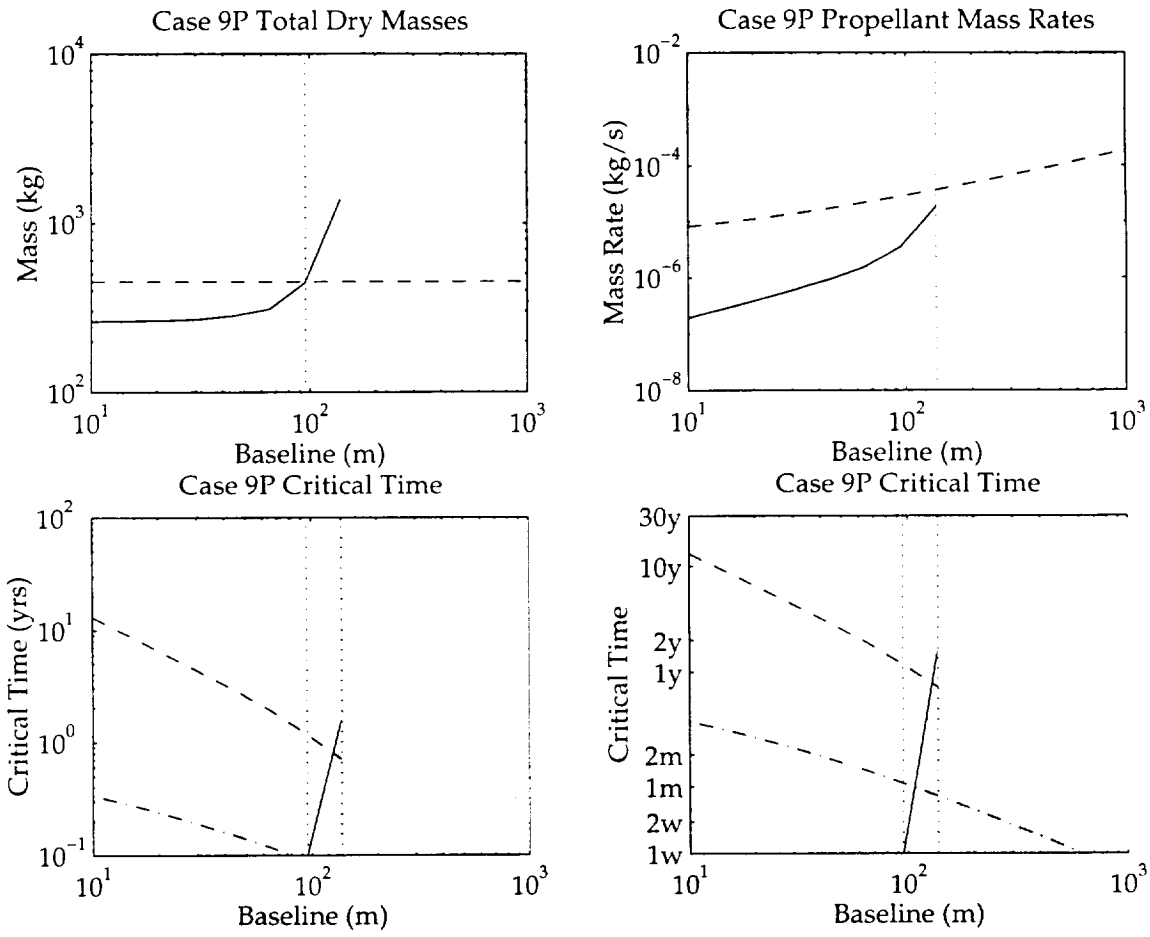

Figure A-12: Plots for Active Case 9

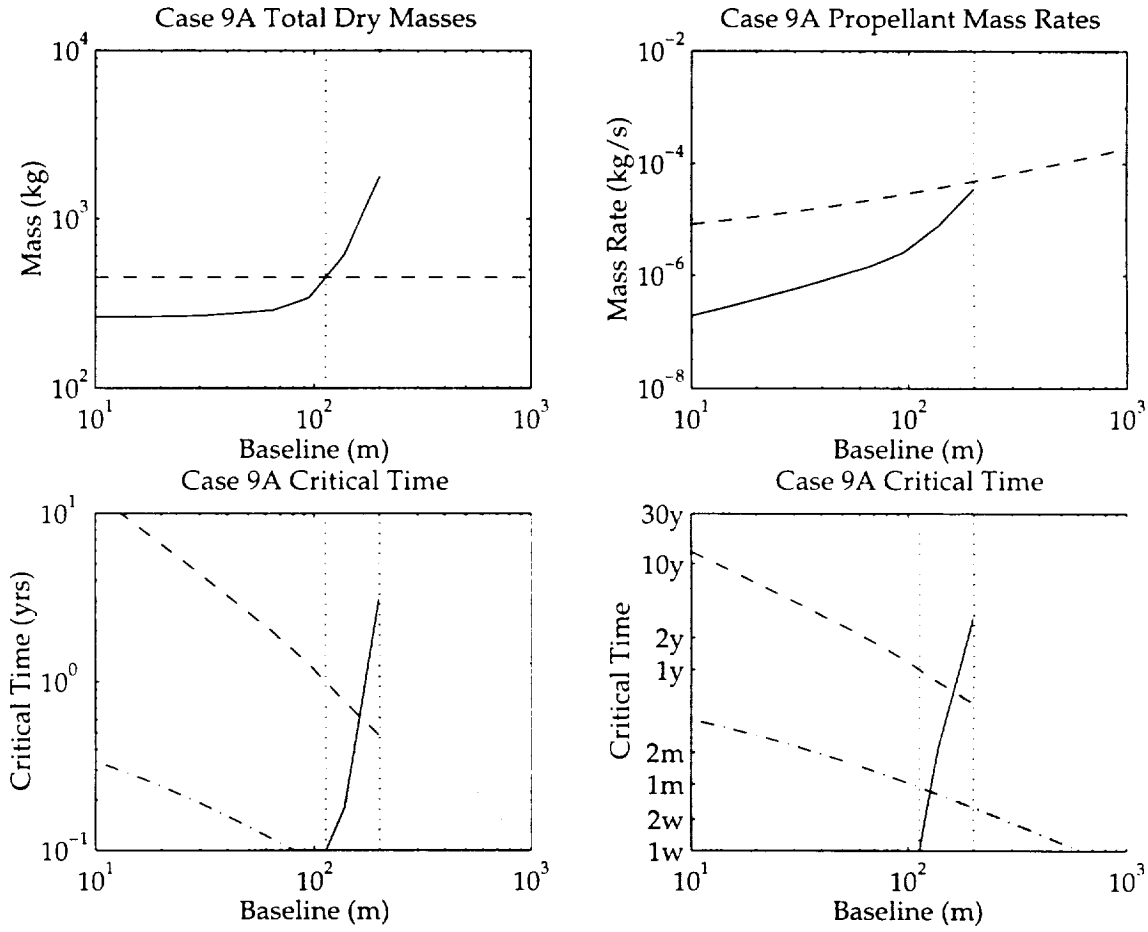

Figure A-13: Plots for Passive Case 10

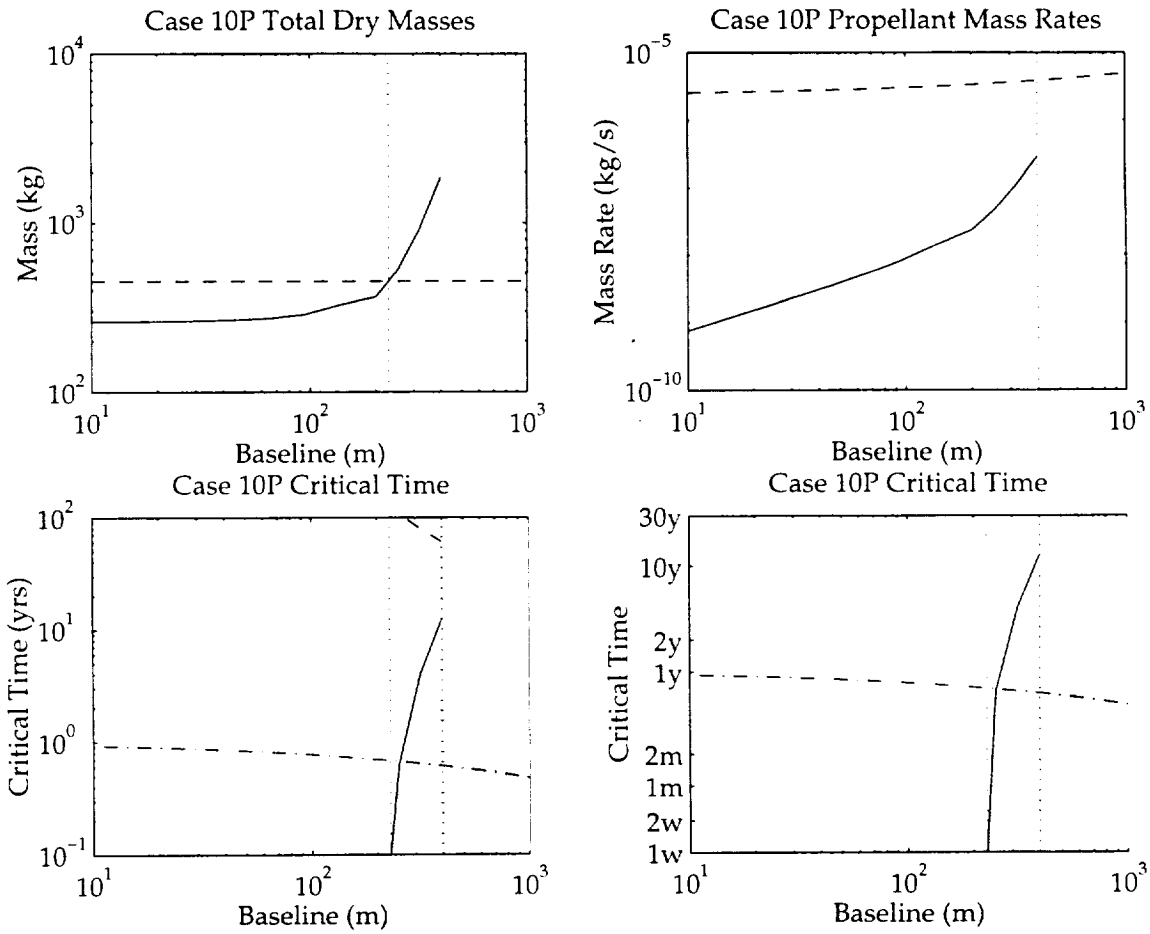

Figure A-14: Plots for Active Case 10

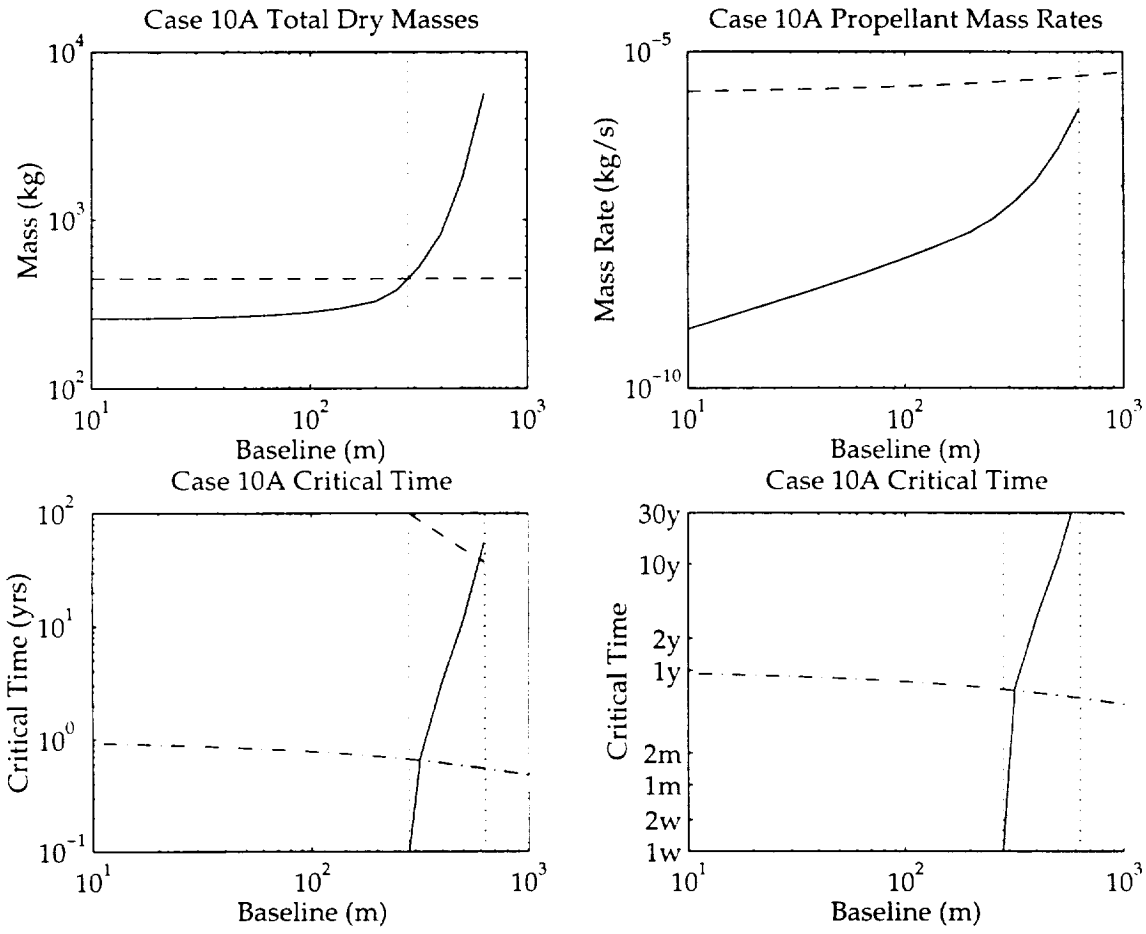

Figure A-15: Plots for Passive Case 11

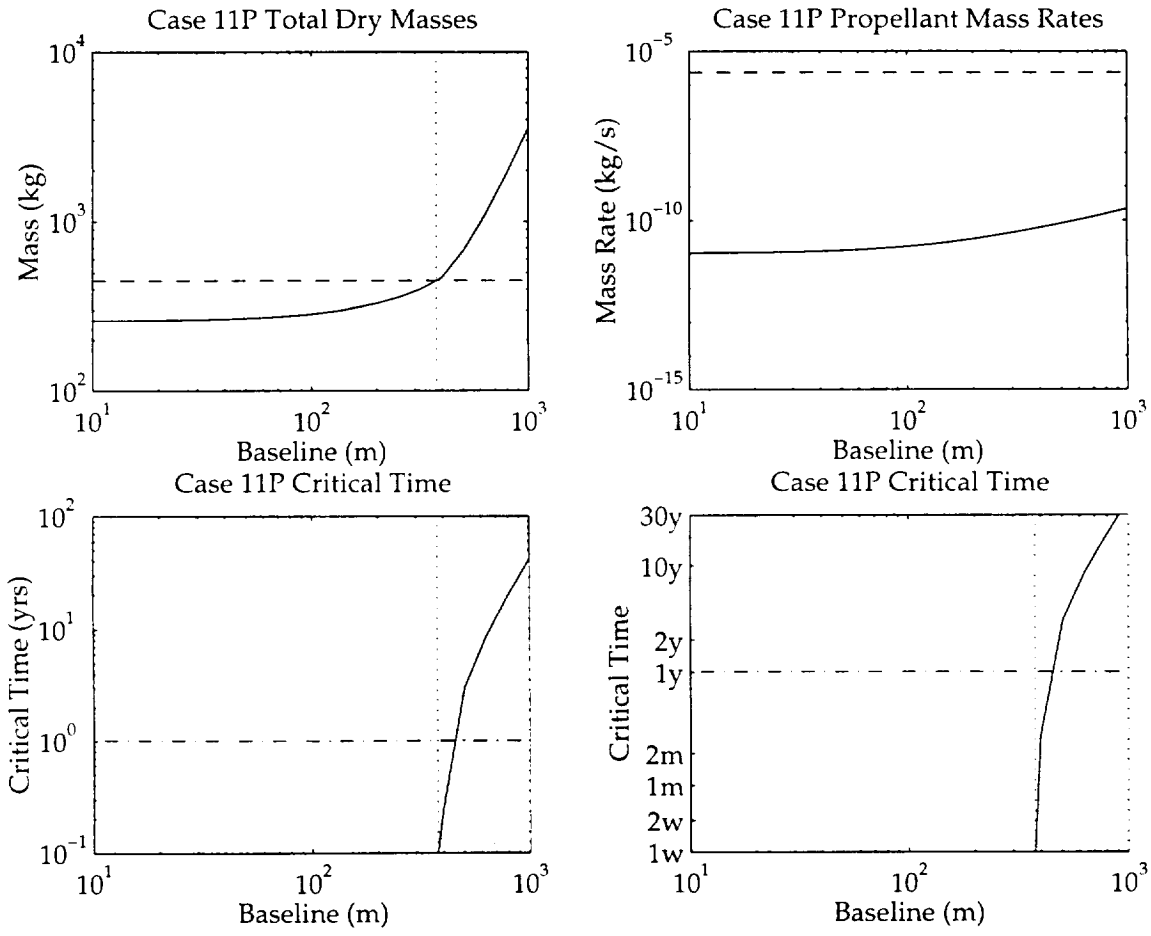

Figure A-16: Plots for Passive Case 12

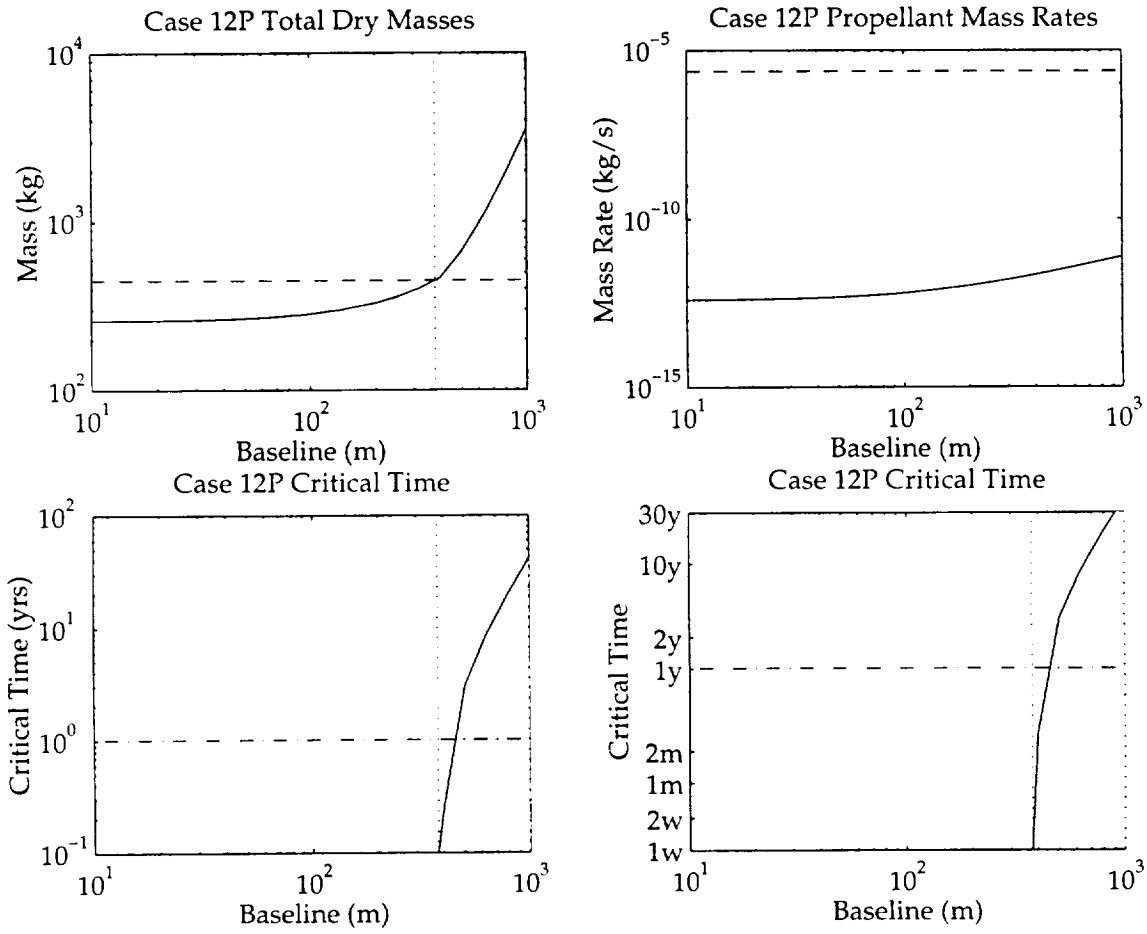

Figure A-17: Plots for Passive Case 13

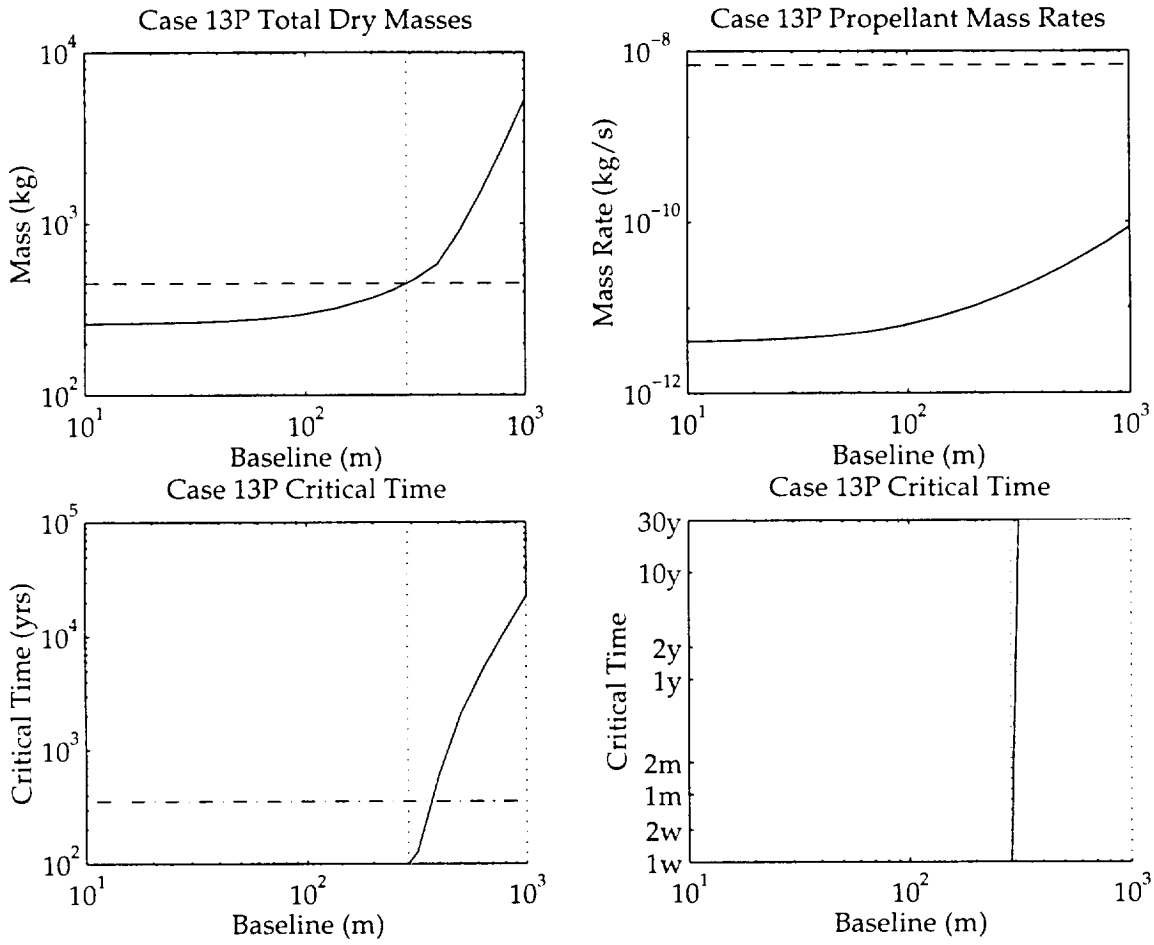

Figure A-18: Plots for Passive Case 14

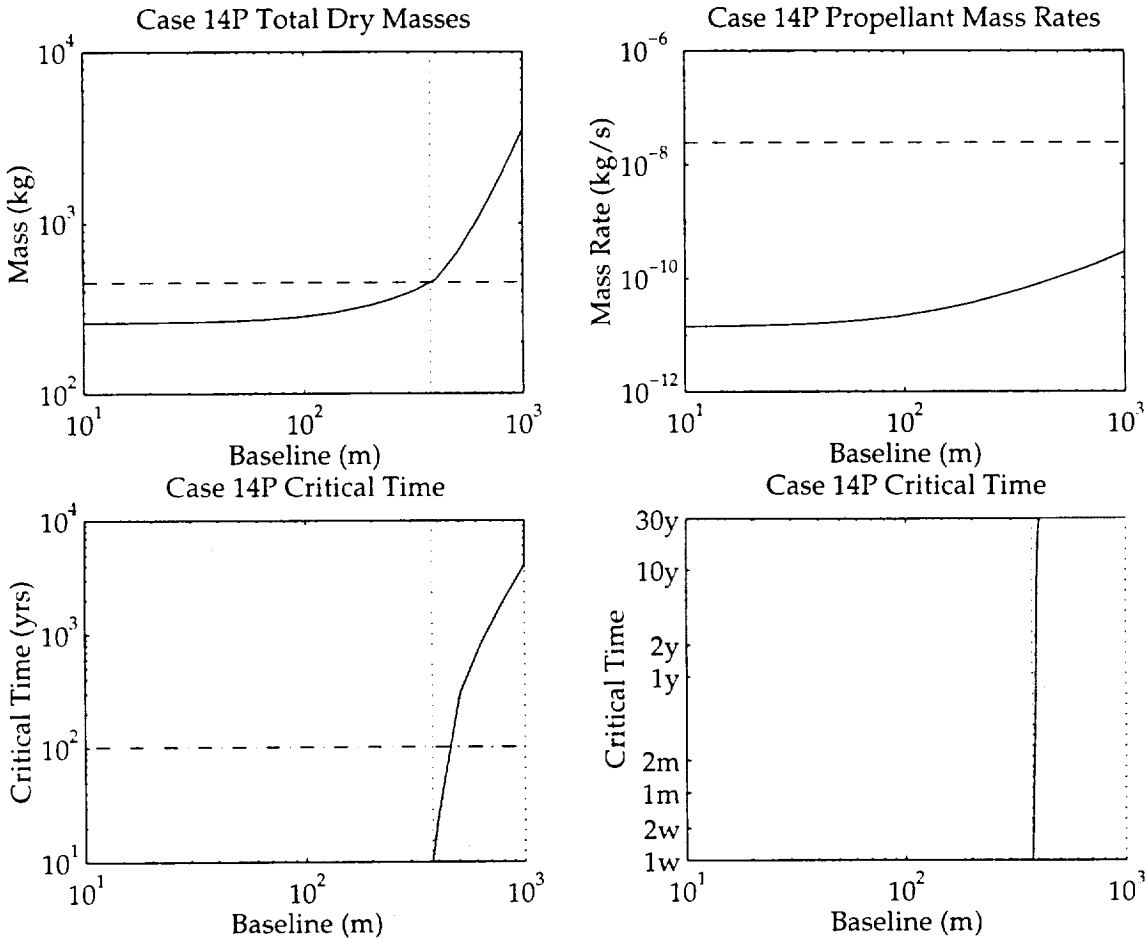

Figure A-19: Plots for Passive Case 15

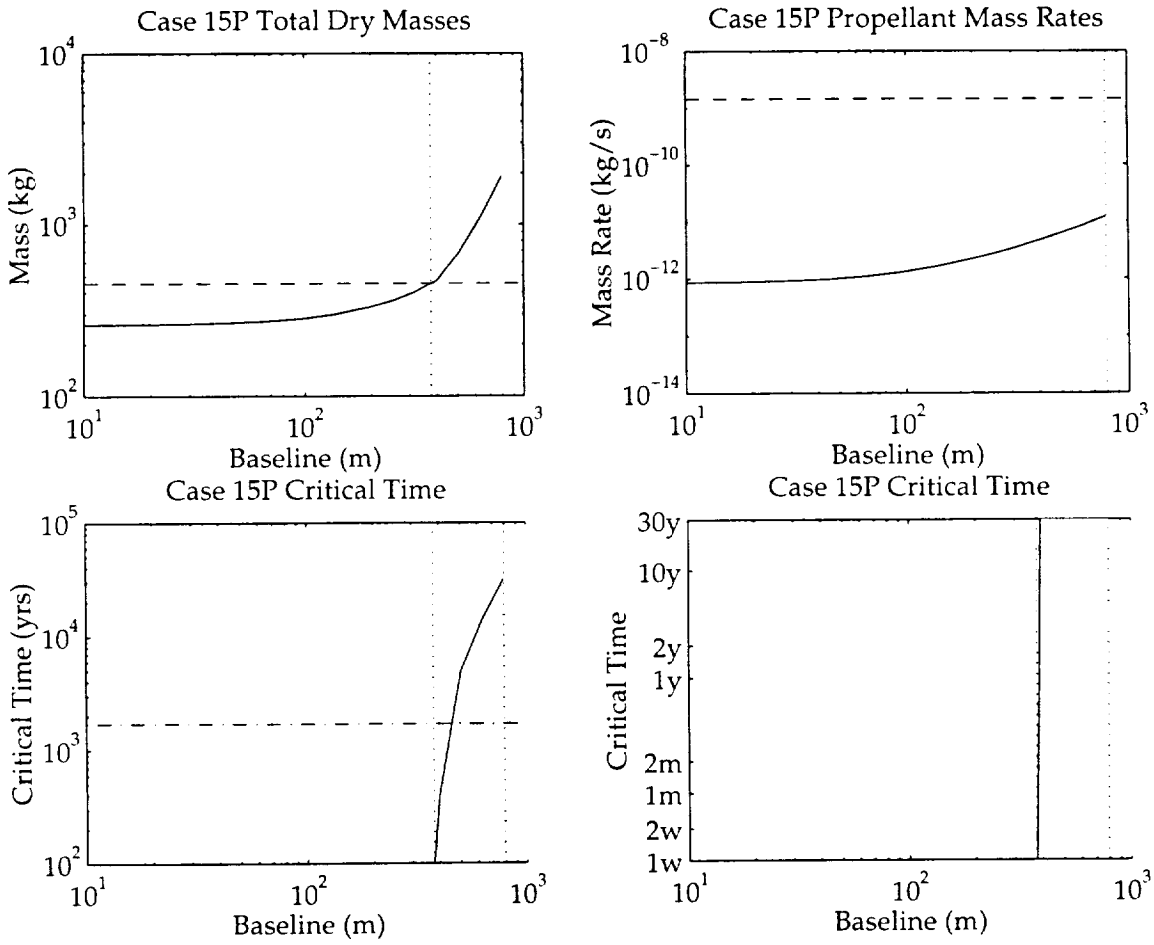

Figure A-20: Plots for Passive Case 16

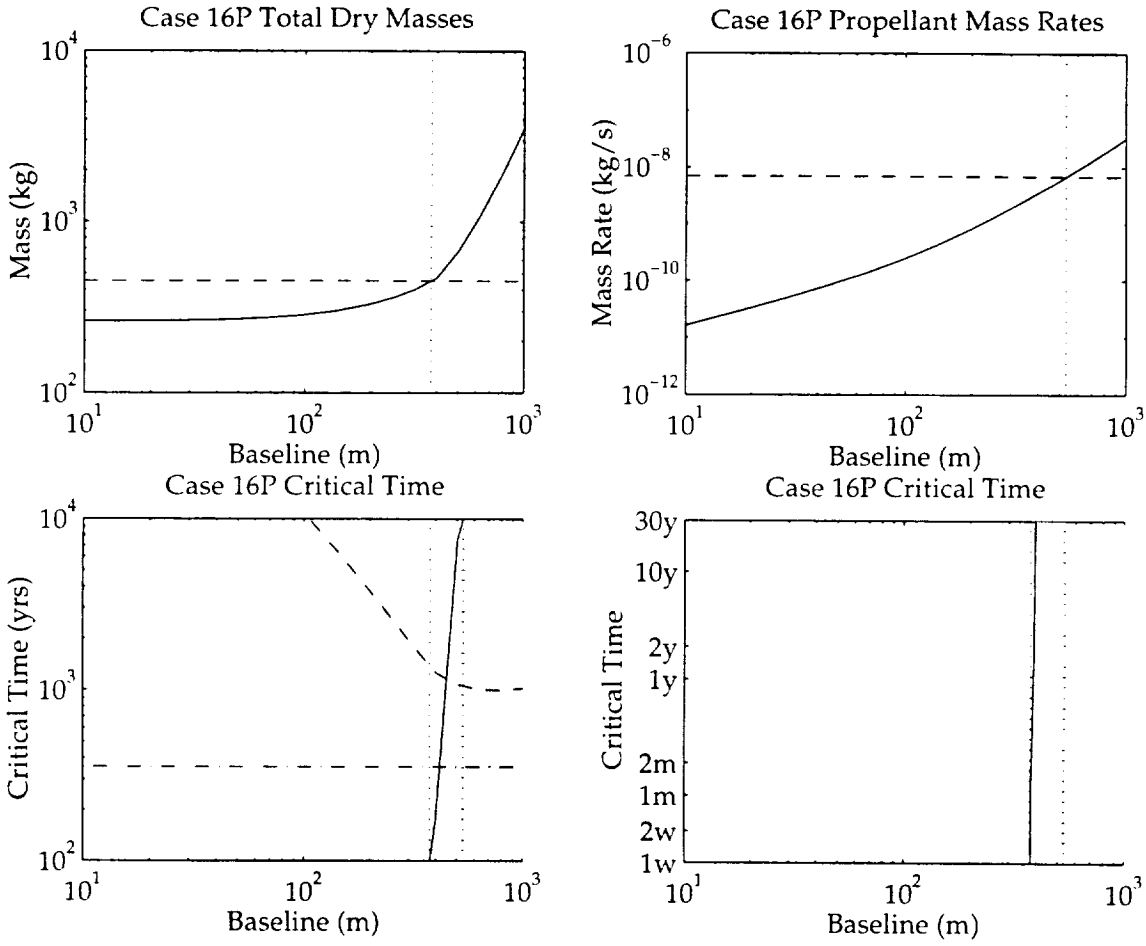

Figure A-21: Plots for Passive Case 17 with Snap Force Equal to 10% Buckling Load

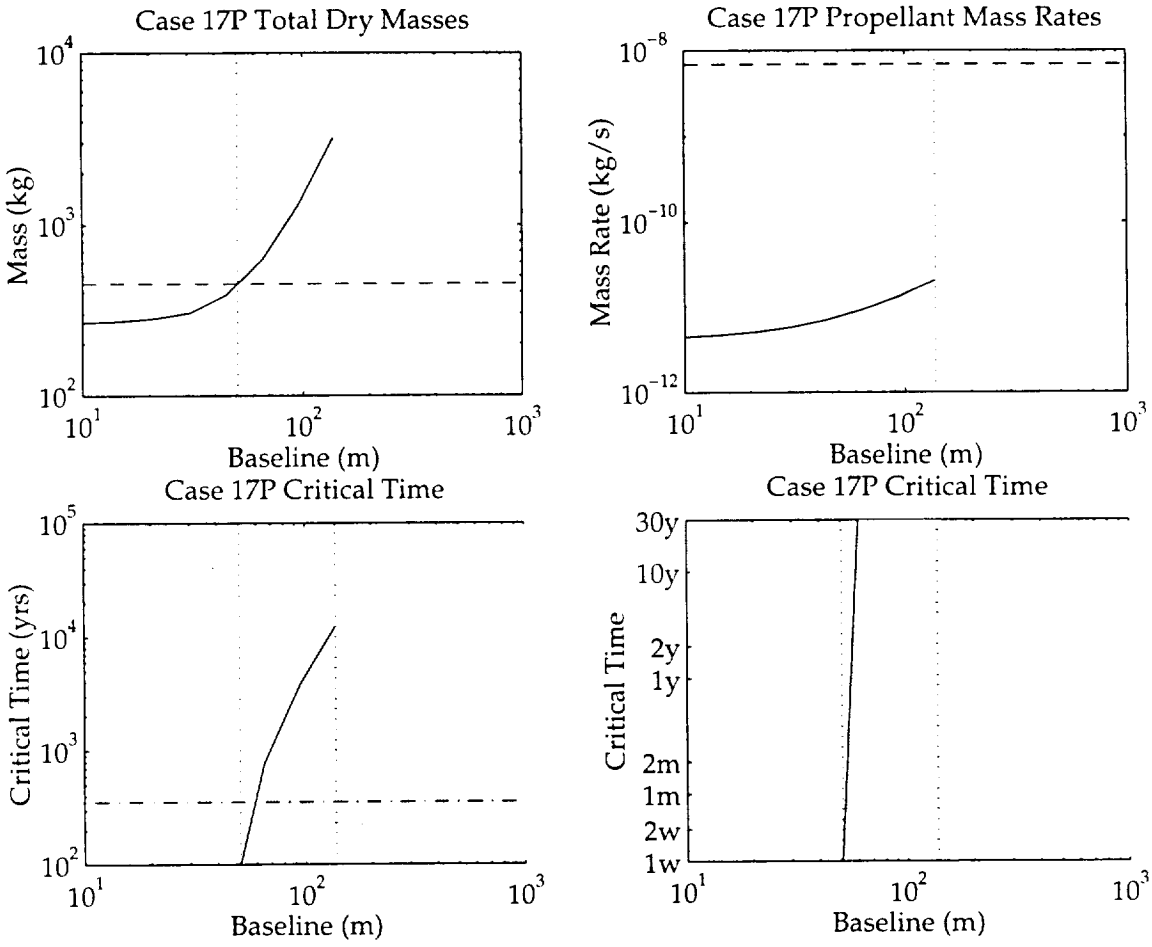

Figure A-22: Plots for Active Case 17 with Snap Force Equal to 10% Buckling Load

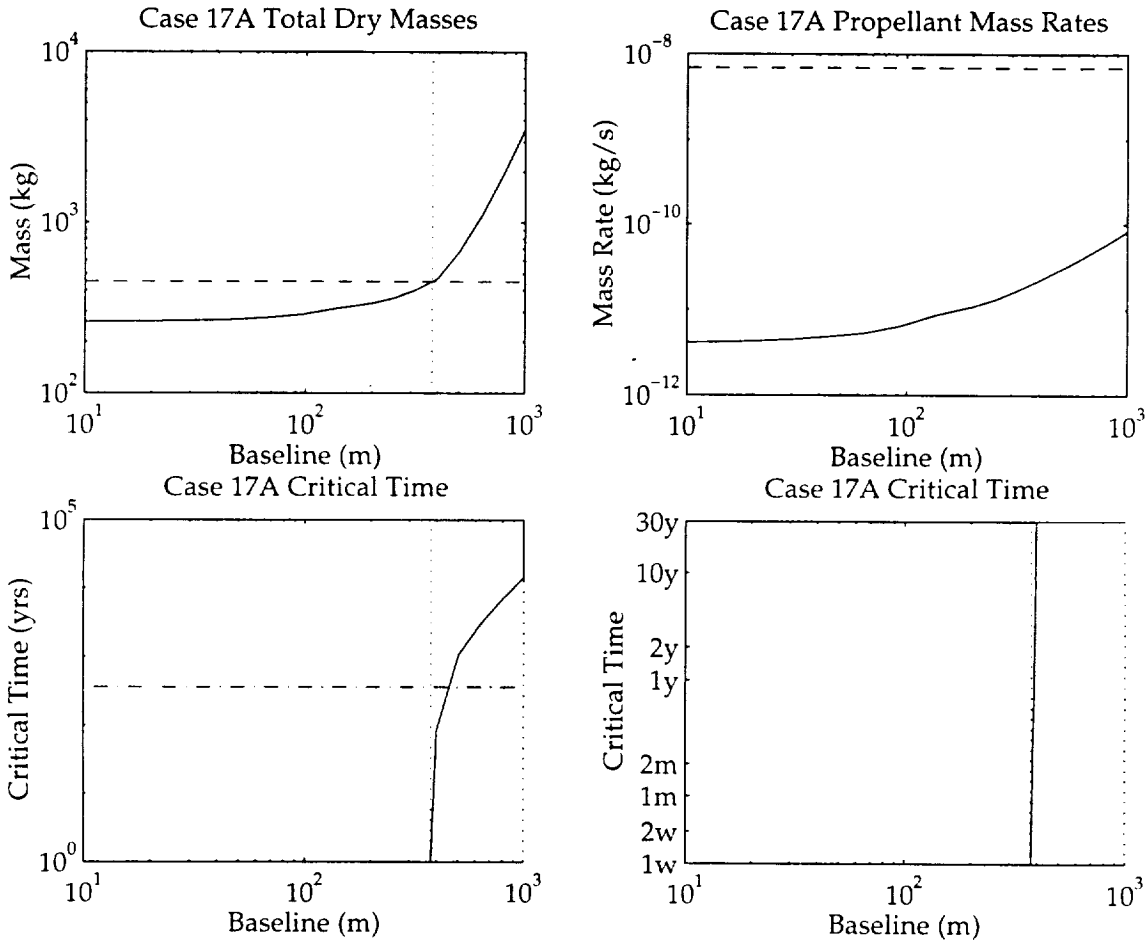

Figure A-23: Plots for Passive Case 17 with Snap Force Equal to 1% Buckling Load

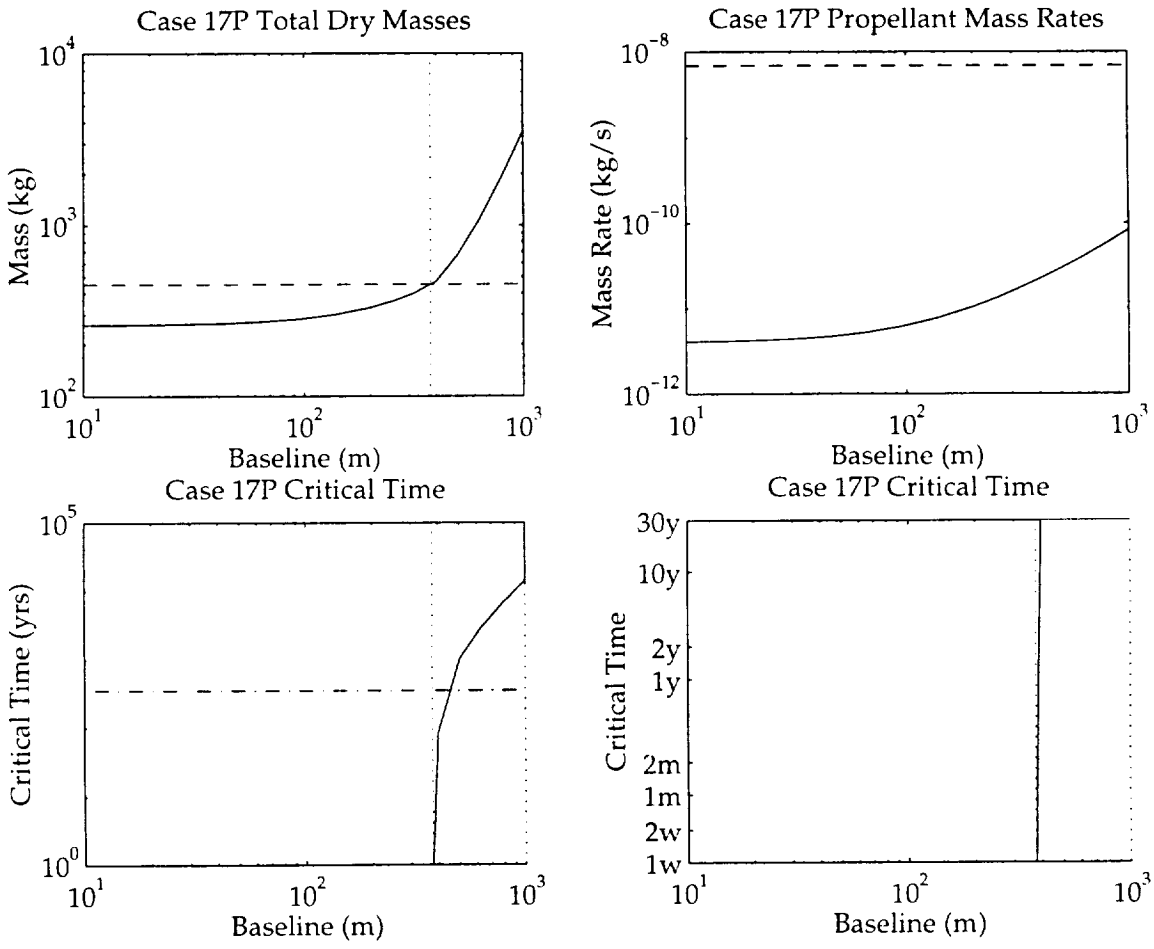

Figure A-24: Plots for Passive Case 17 with Snap Force Equal to 0.1% Buckling Load

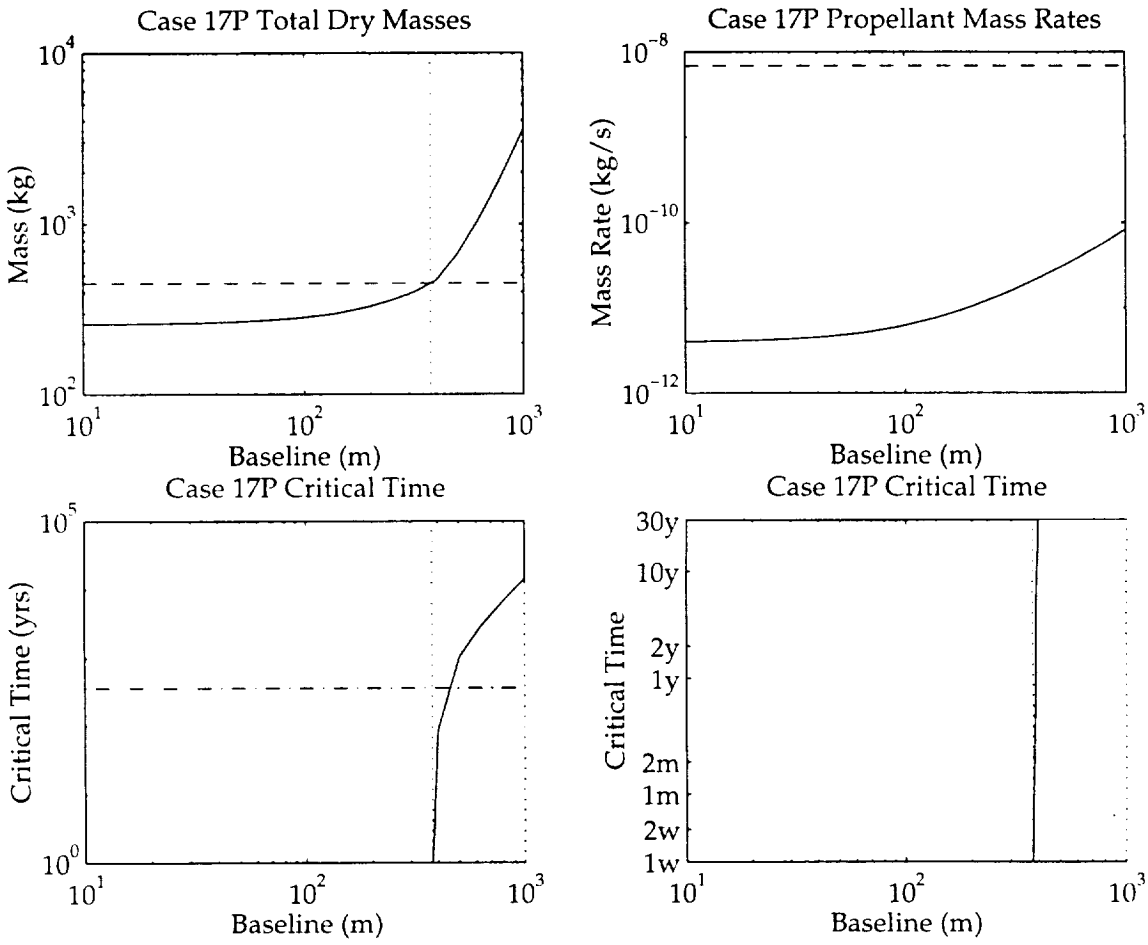

Figure A-25: Plots for Passive Case 18

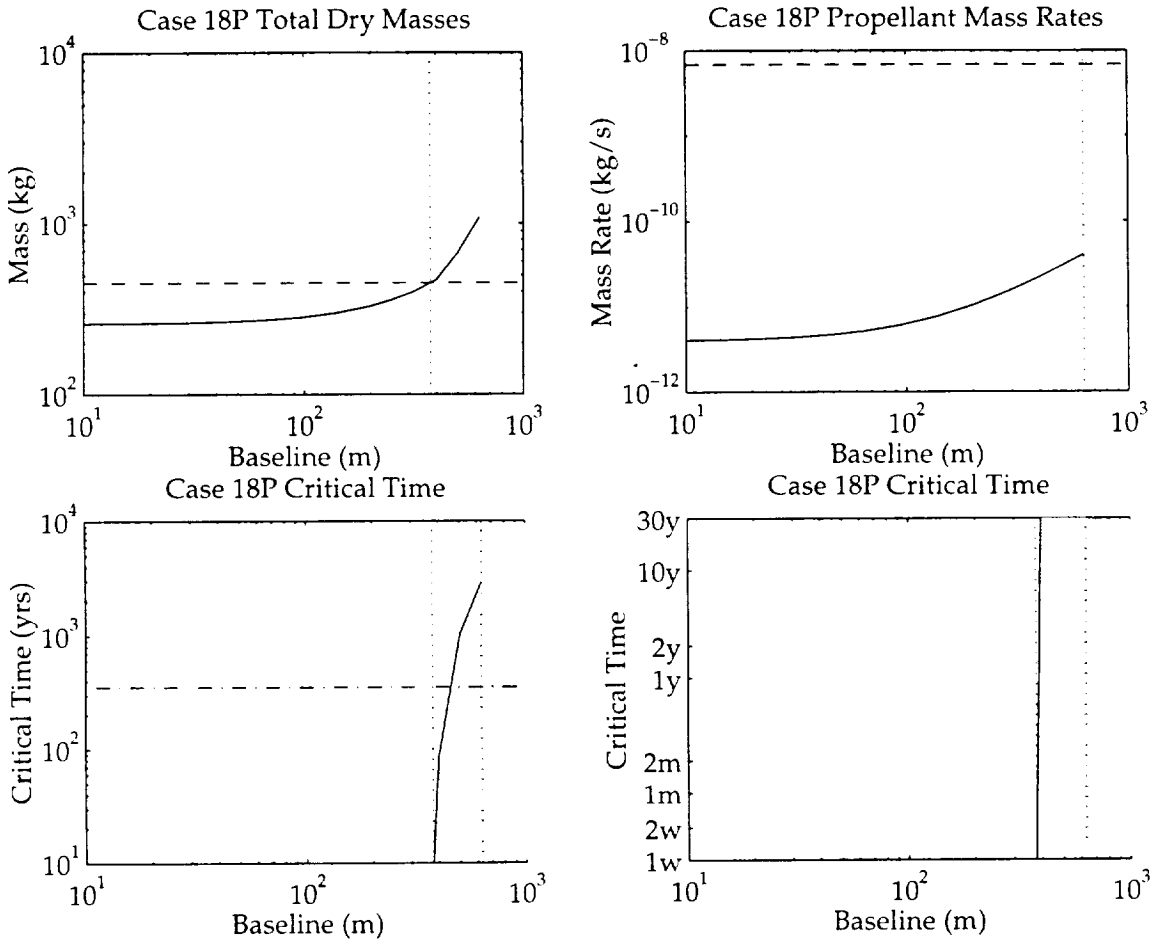

Figure A-26: Plots for Passive Case 19

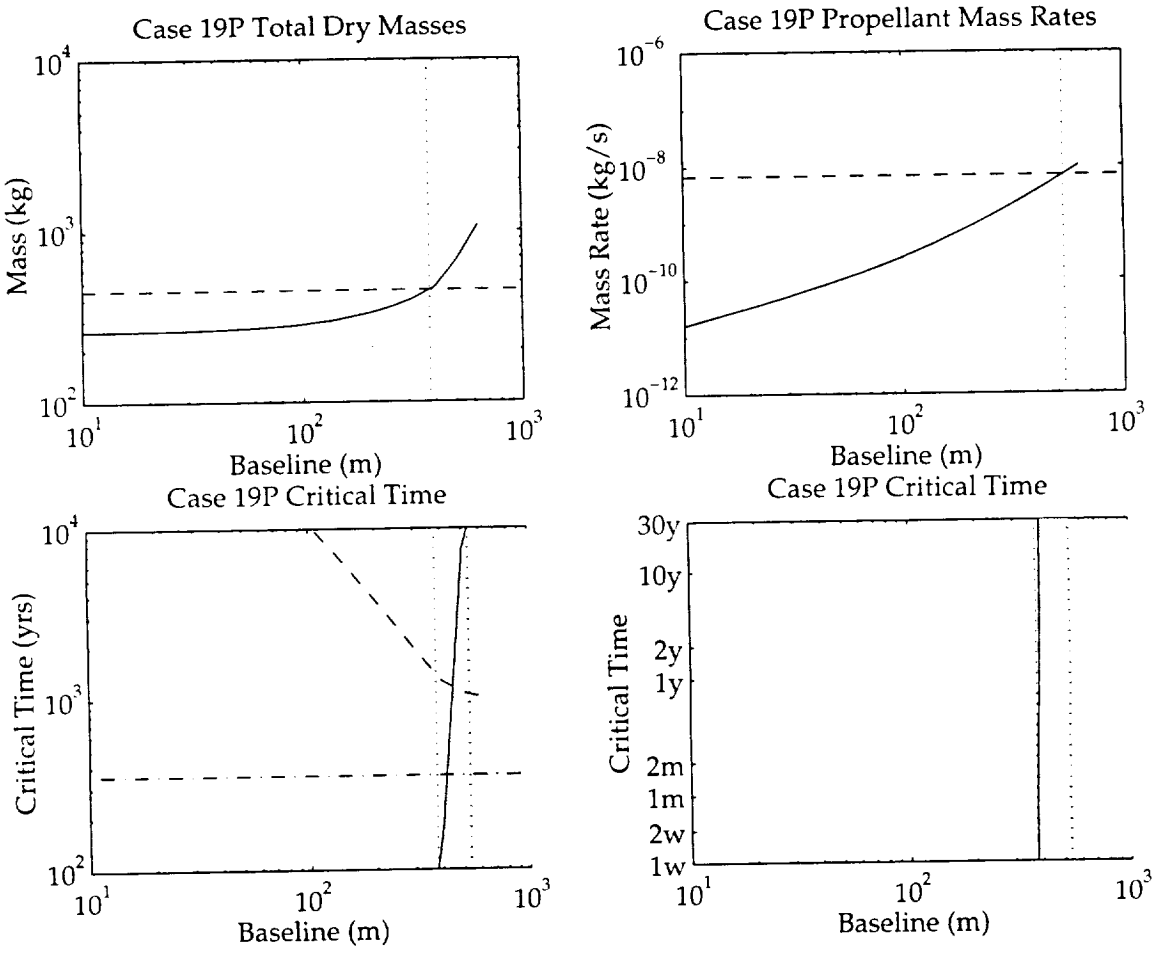

Figure A-27: Plots for Passive Case 20 with Snap Force Equal to 10% Buckling Load

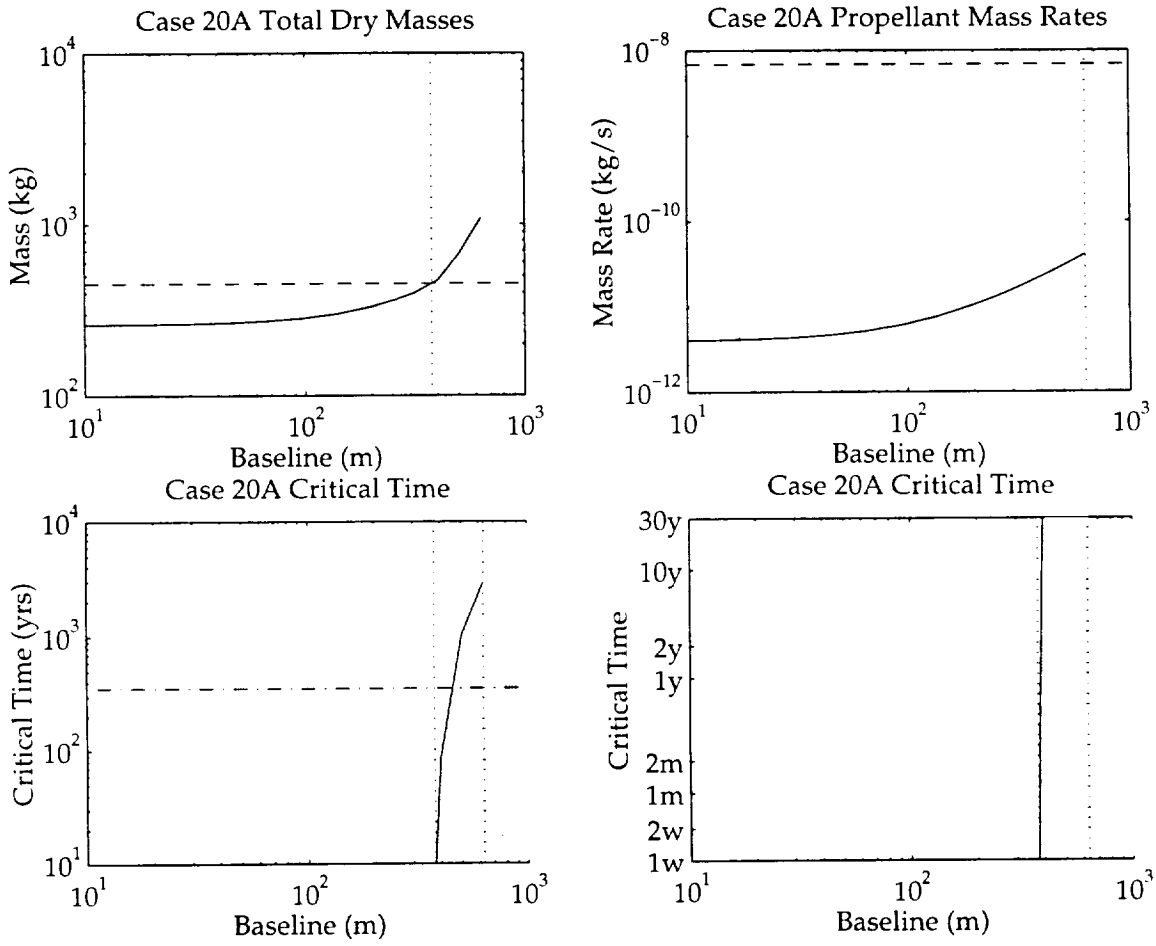

Figure A-28: Plots for Passive Case 20 with Snap Force Equal to 1% Buckling Load

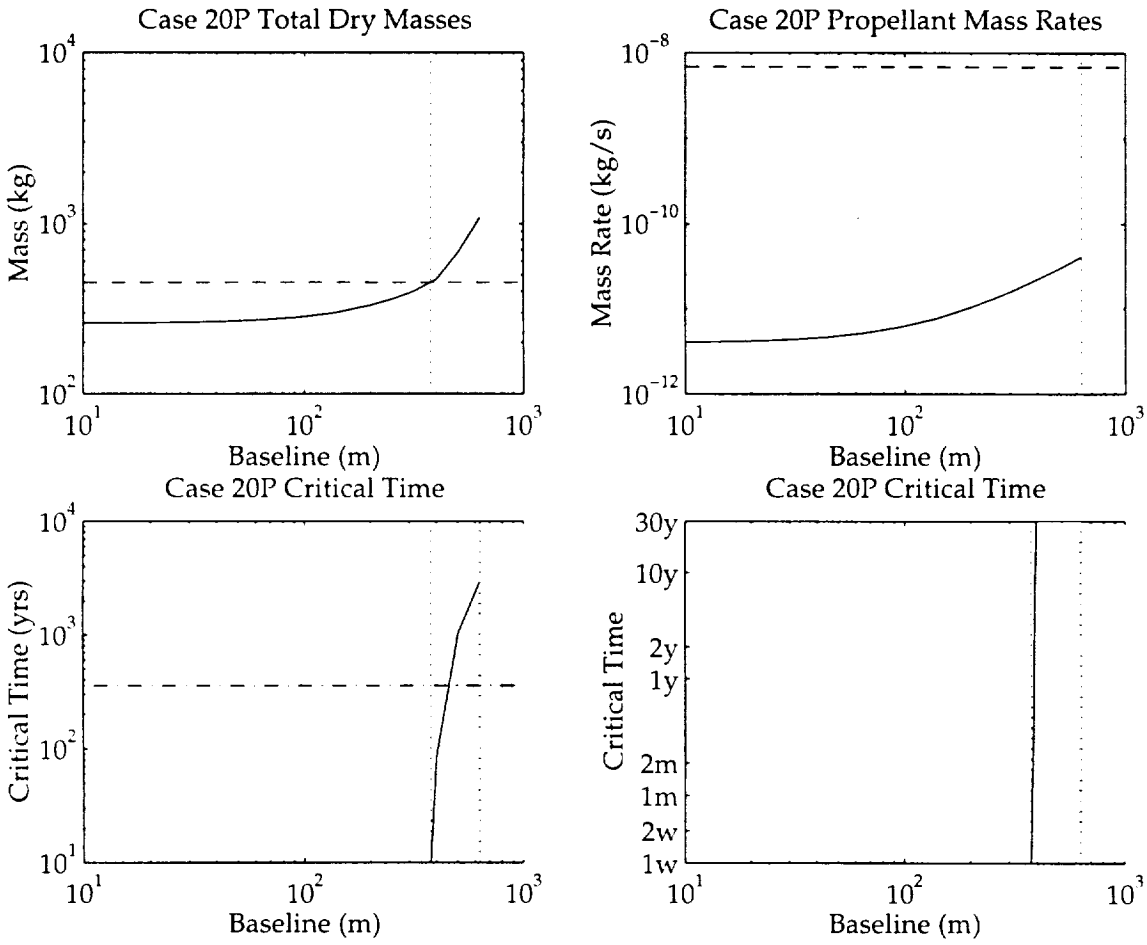

Figure A-29: Plots for Passive Case 20 with Snap Force Equal to 0.1% Buckling Load

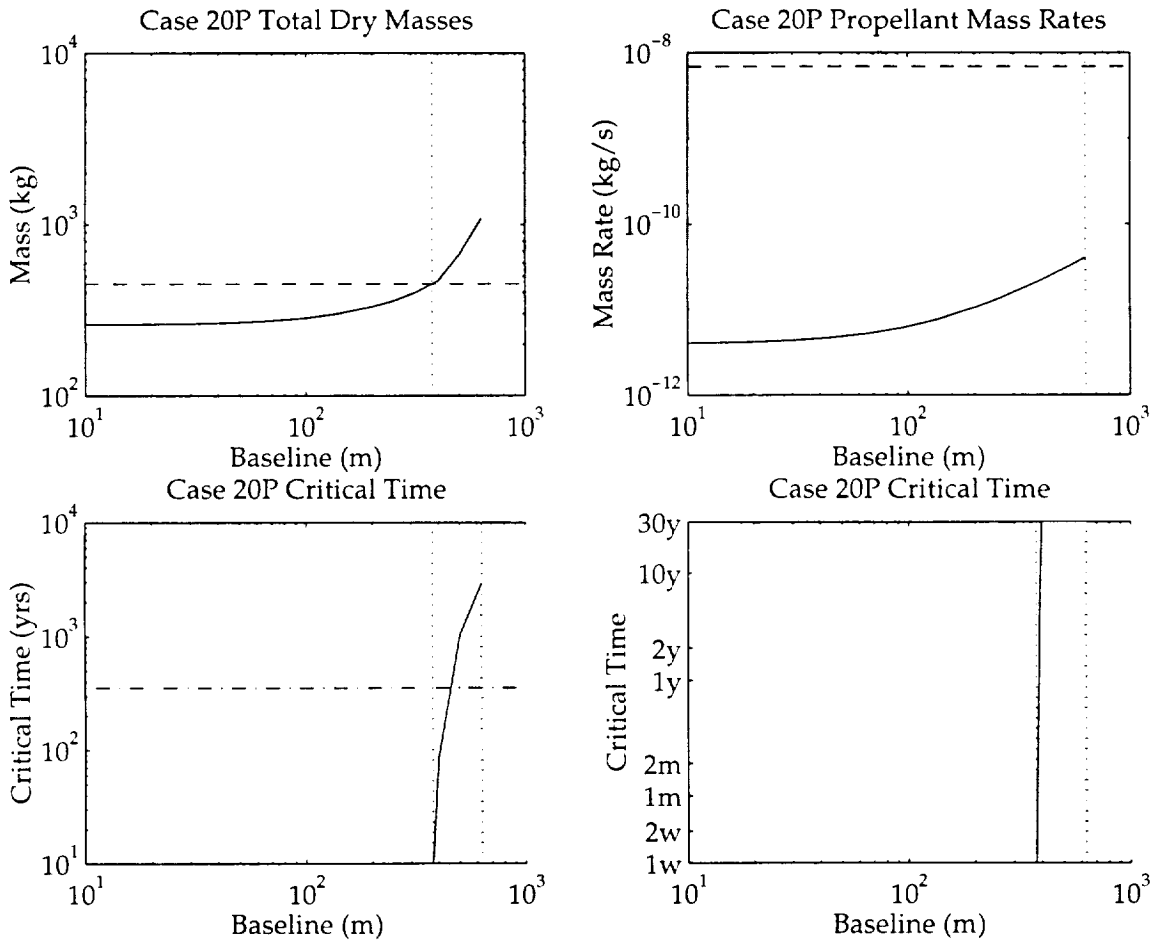

Figure A-30: Plots for Passive Case 21

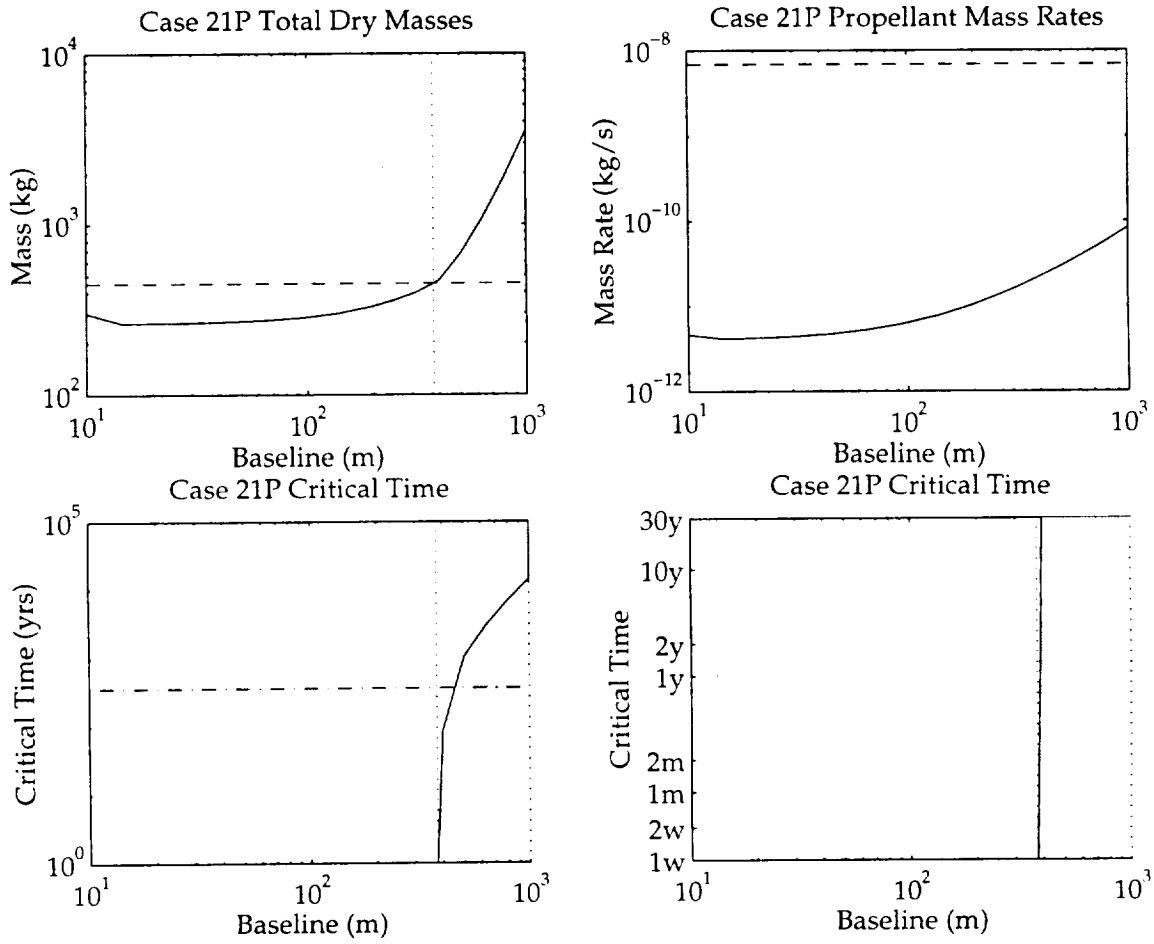

Figure A-31: Plots for Passive Case 22

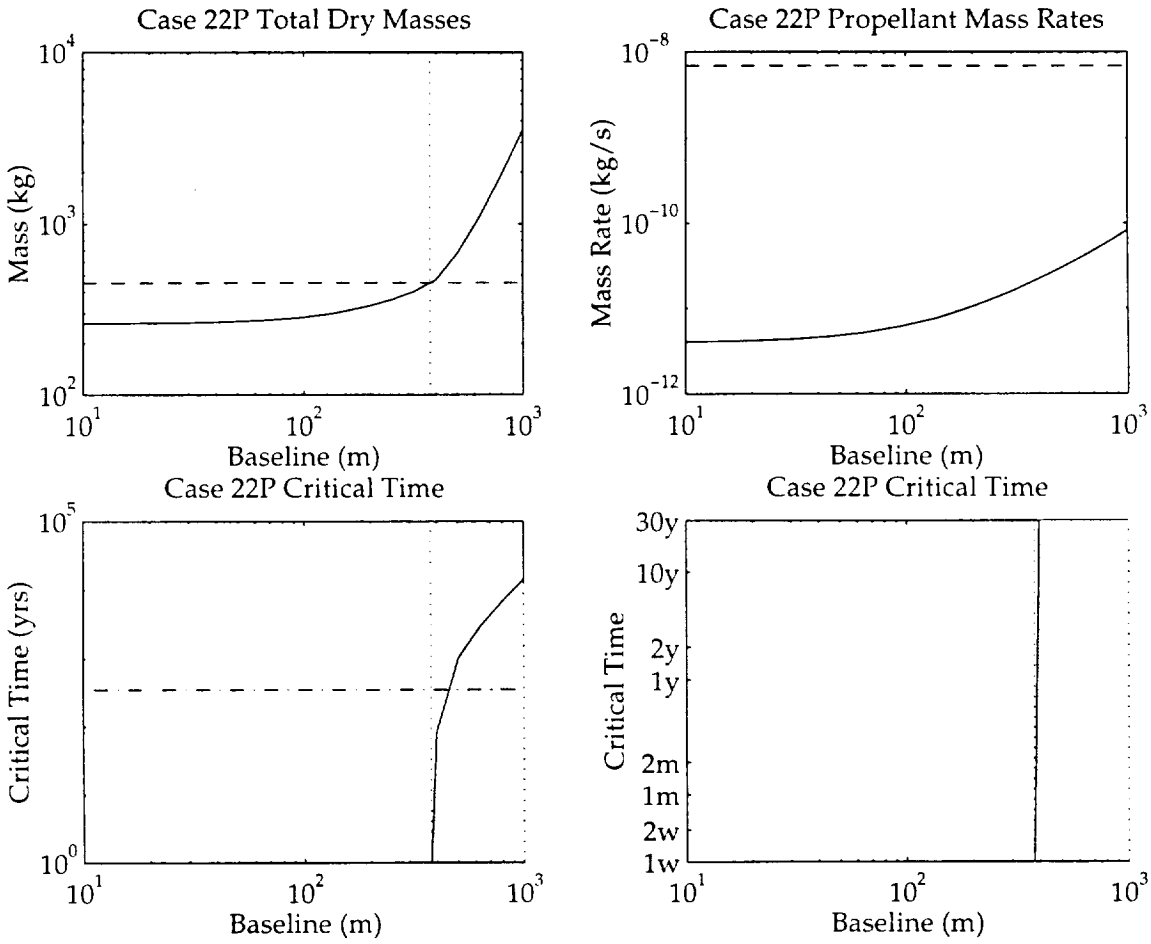

# Appendix B

# Minimum Mass Passive SCI Design for LEO (Case 2)

This appendix presents the plots that characterize the minimum mass design of a passive structurally connected interferometer in Low Earth Orbit. Following the presentation of the minimum mass design are the constraint surface plots used to generate this design. This is an example of a design that is performance limited. If not otherwise indicated, solid lines represent the parameter value and dashed lines represent the constraint value.

It will be noticed that the performance requirement of the minimum mass passive SCI is not met for all baselines. This is a consequence of using interpolation to generate the constraint curves of Figures 6-5 and 6-6. When a design is performance limited, the calculation of the minimum mass combination of areal density and aspect ratio selects a point on the interpolated performance curve. Since the performance requirement surface is not as smooth as the other constraint surfaces, the points on this interpolated curve may not actually satisfy the performance requirement. There is, however, a combination of areal density and aspect ratio close to that combination calculated that does satisfy the requirement, so the errors in the calculation of the minimum dry mass and average propellant mass rate are small.

For the constraint surface plots, the following constraints are satisfied by combinations of areal density, aspect ratio, and baseline that are below the surface — dry

mass (C1), upper frequency (C2), maximum thrust (C3), upper stress (C6), upper buckling (C7) and performance. The following constraints are satisfied by combinations of areal density, aspect ratio, and baseline that are above the surface — lower frequency (C2), minimum gage (C5), lower stress (C6), and lower buckling (C7).

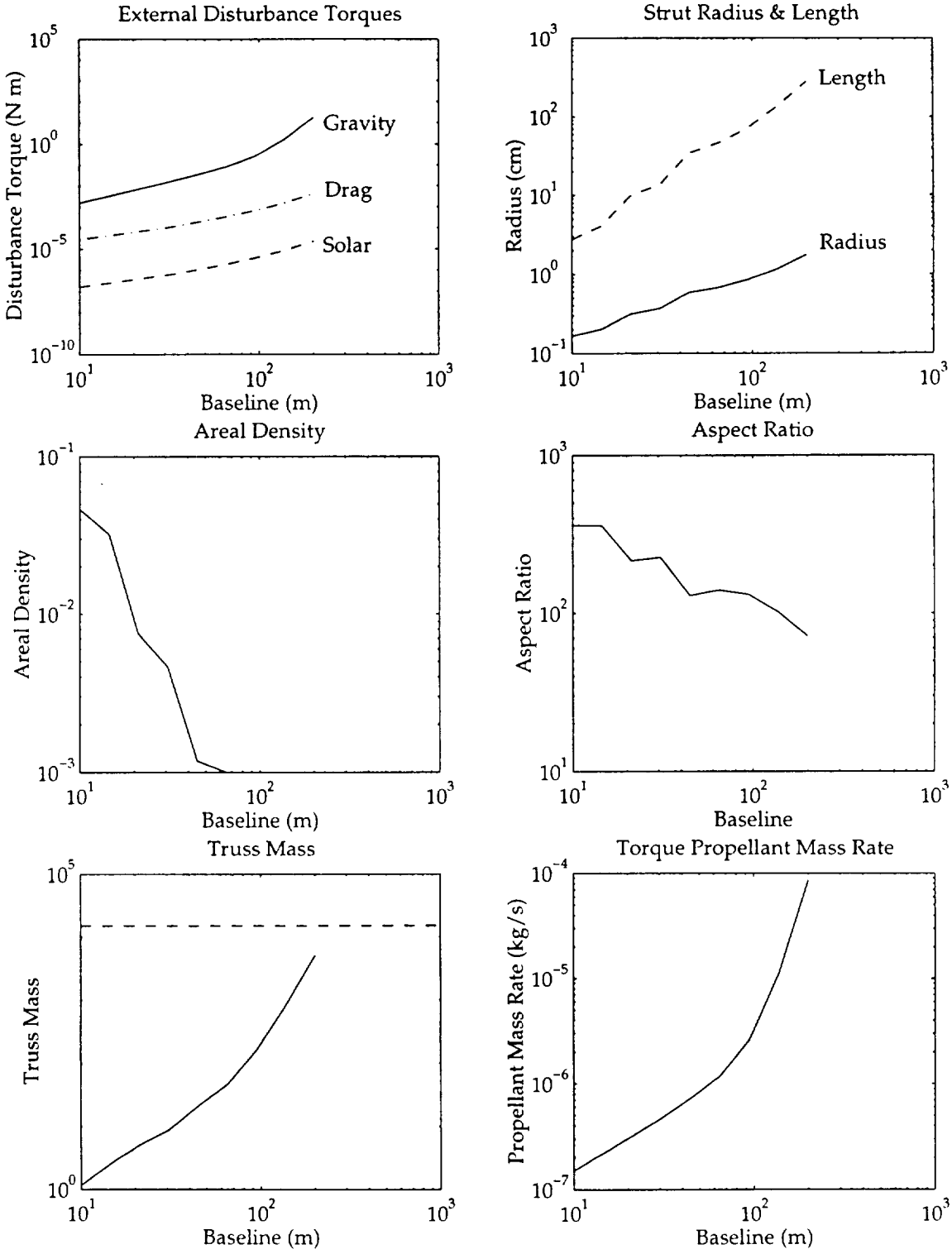
External Disturbance Torques
Disturbance Torque (N m)
Gravity
Drag
Solar
Baseline (m)
Strut Radius & Length
Radius (cm)
Length
Radius
Baseline (m)
Areal Density
Areal Density
Baseline (m)
Aspect Ratio
Aspect Ratio
Baseline
Truss Mass
Truss Mass
Baseline (m)
Torque Propellant Mass Rate
Propellant Mass Rate (kg/s)
Baseline (m)

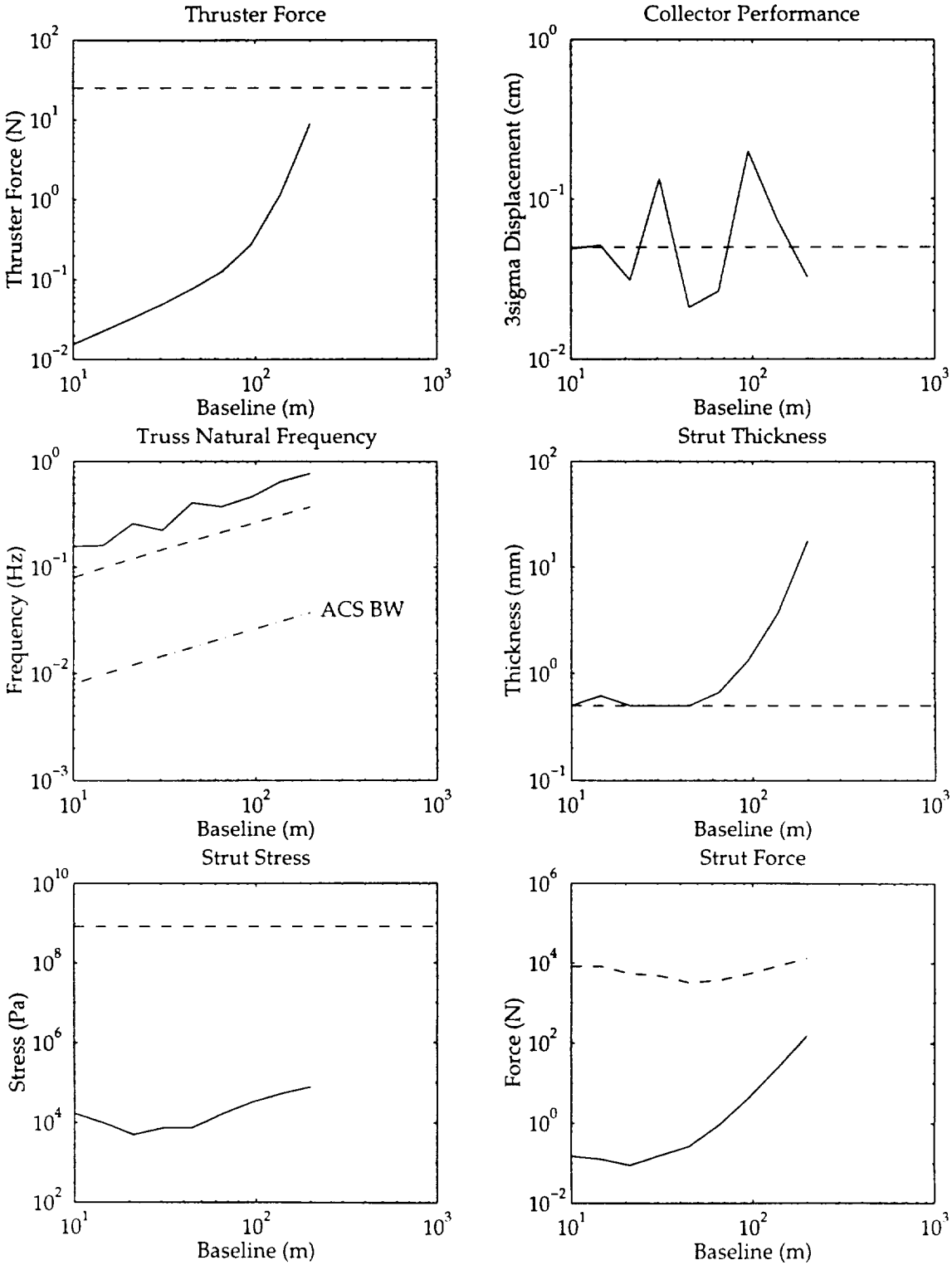
Thruster Force
Thruster Force (N)
Baseline (m)
Collector Performance
3sigma Displacement (cm)
Baseline (m)
Truss Natural Frequency
Frequency (Hz)
ACS BW
Baseline (m)
Strut Thickness
Thickness (mm)
Baseline (m)
Strut Stress
Stress (Pa)
Baseline (m)
Strut Force
Force (N)
Baseline (m)

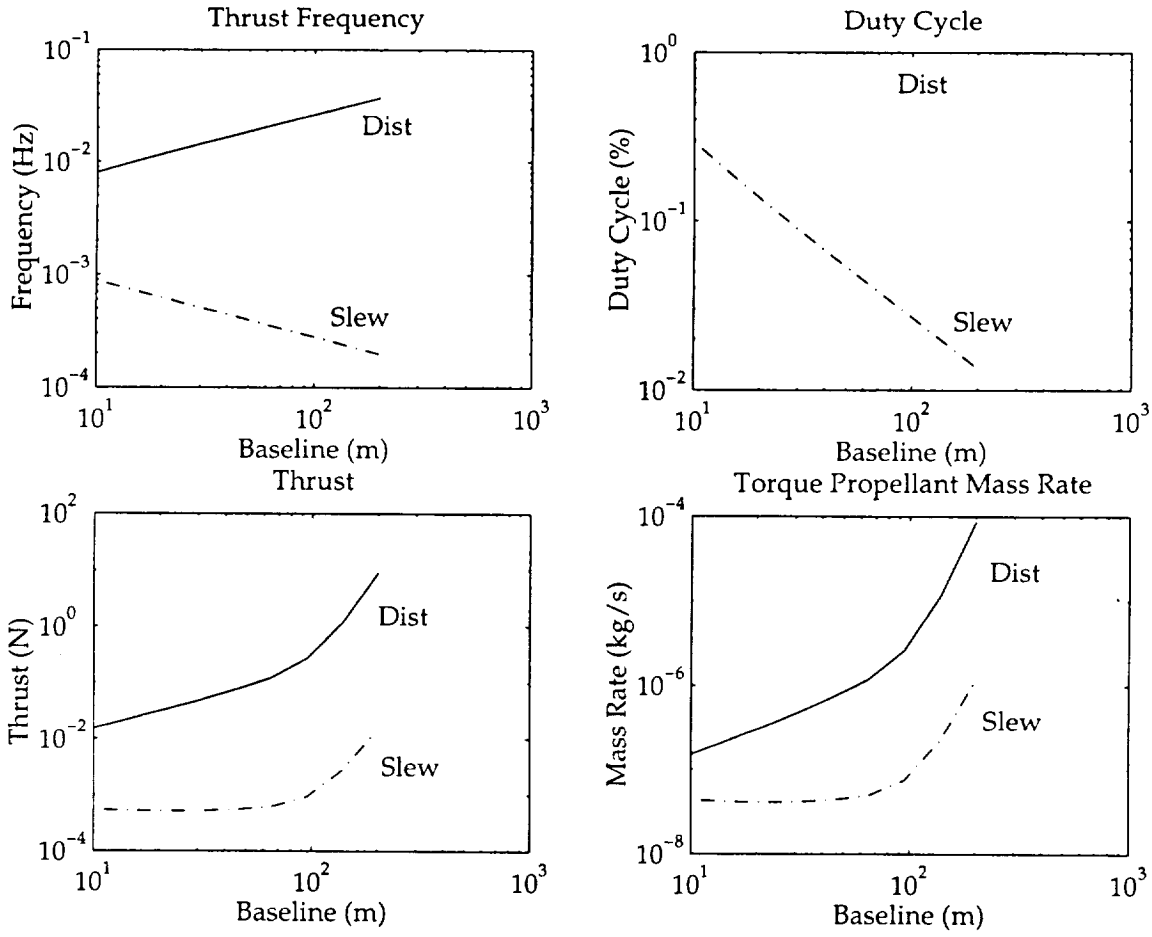
Thrust Frequency
Frequency (Hz)
Dist
Slew
Baseline (m)
Duty Cycle
Duty Cycle (%)
Dist
Slew
Baseline (m)
Thrust
Thrust (N)
Dist
Slew
Baseline (m)
Torque Propellant Mass Rate
Mass Rate (kg/s)
Dist
Slew
Baseline (m)

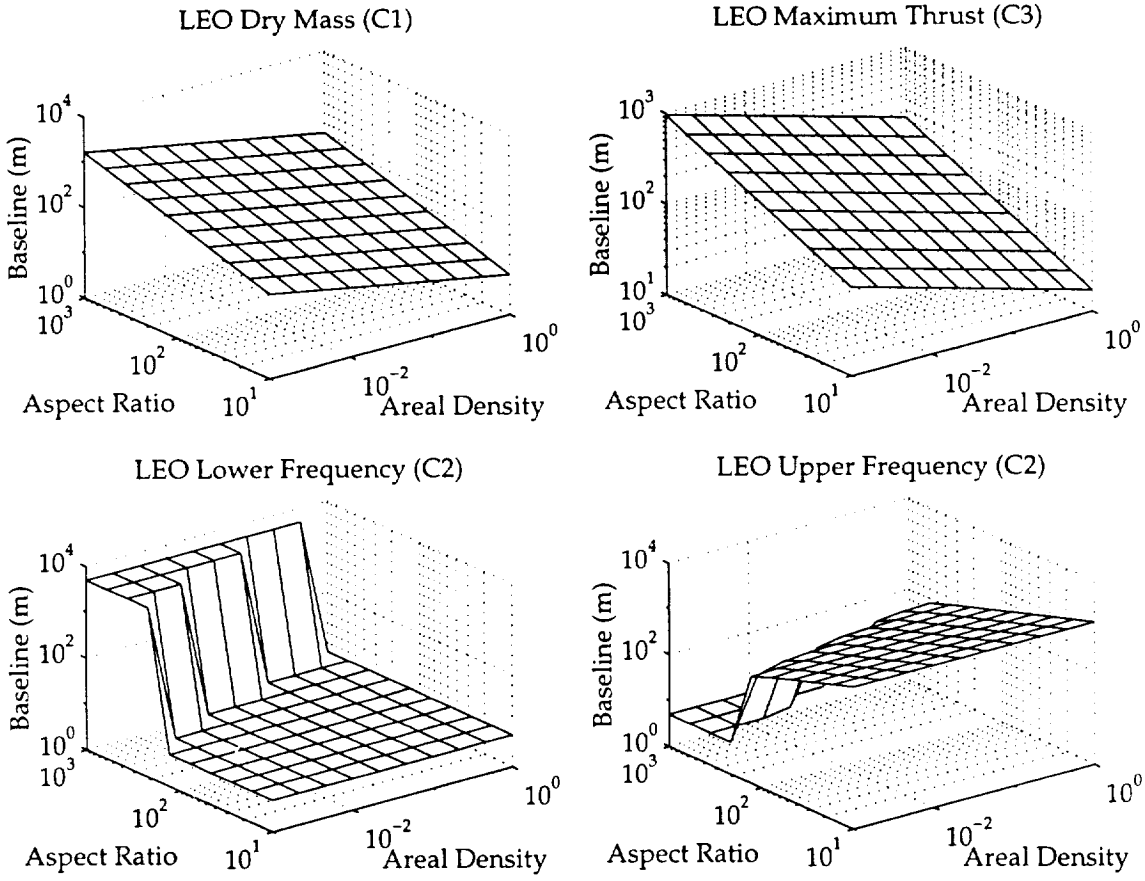
LEO Dry Mass (C1)
LEO Maximum Thrust (C3)
LEO Lower Frequency (C2)
LEO Upper Frequency (C2)
Baseline (m)
Aspect Ratio
Areal Density

LEO Lower Stress (C6)

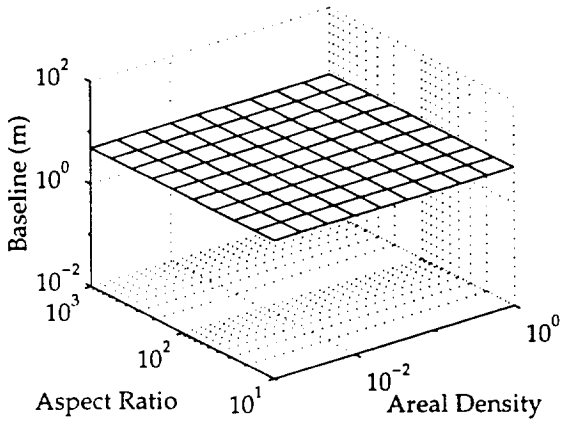


LEO Upper Stress (C6)

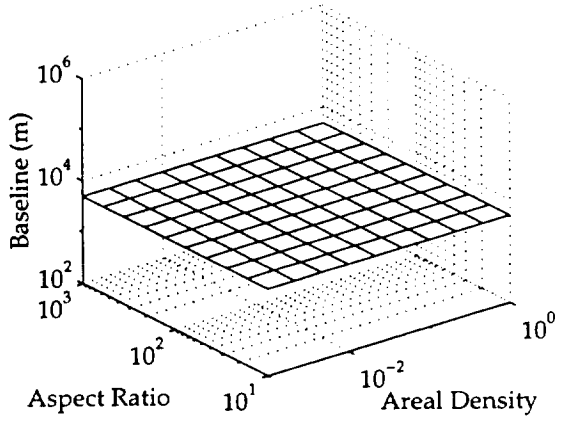


LEO Lower Buckling (C7)

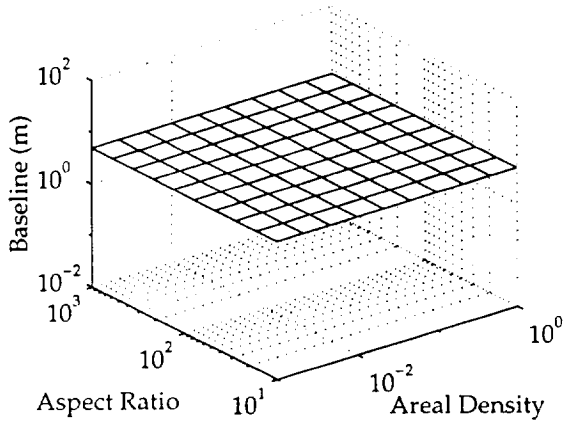


LEO Upper Buckling (C7)

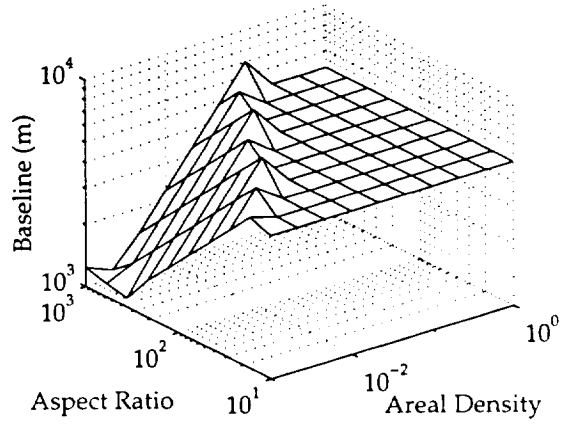


LEO Minimum Gage (C5)

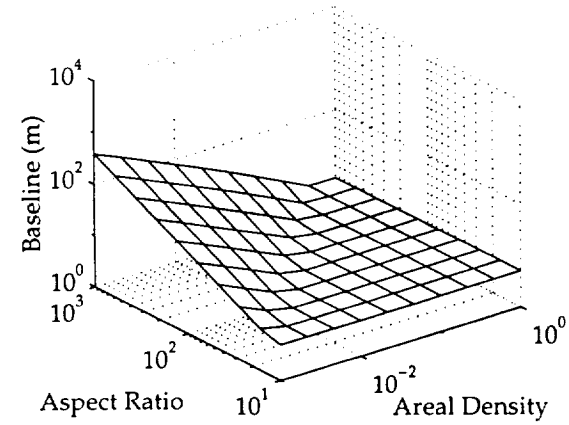


LEO Performance